

UNIVERSIDADE FEDERAL DE UBERLÂNDIA

CARLOS ANTONIO RIBEIRO DUARTE

**Simulation of a new pipe design for erosion
reduction in curves**



Uberlândia – MG – Brasil

31 de Março de 2017

CARLOS ANTONIO RIBEIRO DUARTE

Simulation of a new pipe design for erosion reduction in curves

TESE apresentada ao Programa de Pós-Graduação em Engenharia Mecânica da Universidade Federal de Uberlândia, como parte dos requisitos para a obtenção do título de **DOCTOR EM ENGENHARIA MECÂNICA**.

Área de concentração: Transferência de Calor e Mecânica dos Fluidos

Universidade Federal de Uberlândia – UFU

Faculdade de Engenharia Mecânica

Programa de Pós-Graduação

Supervisor: Prof. Dr. Francisco José de Souza

Uberlândia – MG – Brasil

31 de Março de 2017

Dados Internacionais de Catalogação na Publicação (CIP)
Sistema de Bibliotecas da UFU, MG, Brasil.

D812s Duarte, Carlos Antonio Ribeiro, 1989-
2017 Simulation of a new pipe design for erosion reduction in curves /
Carlos Antonio Ribeiro Duarte. - 2017.
179 f. : il.

Orientador: Francisco José de Souza.
Tese (doutorado) - Universidade Federal de Uberlândia, Programa
de Pós-Graduação em Engenharia Mecânica.
Inclui bibliografia.

1. Engenharia mecânica - Teses. 2. Desgaste mecânico - Teses. 3.
Transporte por tubo pneumático - Teses. I. Souza, Francisco José de,
1973- II. Universidade Federal de Uberlândia. Programa de Pós-
Graduação em Engenharia Mecânica. III. Título.

CDU: 621

CARLOS ANTONIO RIBEIRO DUARTE

Simulation of a new pipe design for erosion reduction in curves

TESE apresentada ao Programa de Pós-Graduação em Engenharia Mecânica da Universidade Federal de Uberlândia, como parte dos requisitos para a obtenção do título de **DOUTOR EM ENGENHARIA MECÂNICA**.

Área de concentração: Transferência de Calor e Mecânica dos Fluidos

Trabalho aprovado. Uberlândia – MG – Brasil, 31 de Março de 2017:

Prof. Dr. Francisco José de Souza
Orientador - UFU

Prof. Dr. Aristeu da Silveira Neto
UFU

Prof. Dr. Sinésio Domingues Franco
UFU

Prof. Dr. Dirceu Noriler
UNICAMP

Prof. Dr. Henry França Meier
FURB

Uberlândia – MG – Brasil
31 de Março de 2017

To my family for always standing by my side.

Acknowledgements

I would like to express my deepest gratitude to my supervisor, Professor Dr. Francisco José de Souza, for his guidance and encouragement during my doctoral study. I would like to thank him for giving me an initial direction for my research, and always giving me freedom to focus on the academic fields of great interest. He always recommended some academic conferences to me for expanding my academic vision. His positive and timely feedback on my manuscripts and reports makes my research progress quite fluent. Every discussion with him is an enjoyable time.

My research is carried out with the "in-house" CFD code UNSCYFL3D providing a reliable and powerful framework for the simulations. My special thanks go to its principal developer, Professor Dr. Francisco José de Souza, for making UNSCYFL3D available to me and continuously maintaining its high quality.

I would also like to thank my parents, Maria Beatriz and José Carlos for the support they provided me through my entire life, my brother Lucas Eduardo for the friendship and in particular, I must acknowledge my wife and best friend, Larissa, without whose love, encouragement and patience, I would not have finished this thesis.

In conclusion, I recognize that this research would not have been possible without the financial assistance of Petróleo Brasileiro (PETROBRAS¹), the National Counsel of Technological and Scientific Development (CNPq²) , the Federal University of Uberlândia and the Department of Mechanical Engineering, and express my gratitude to those agencies.

¹ PETROBRAS <<http://www.petrobras.com.br/>>

² CNPq <<http://cnpq.br/>>

*"The heart of the wise is in the house of mourning,
but the heart of fools is in the house of mirth."*

Ecclesiastes 7:4

Abstract

Pneumatically conveyed particles are commonly responsible for triggering the erosion process by impacts on the wall. Those impacts result from the fluid-particle interaction and understanding its mechanisms is the key to mitigate the erosion damage in engineering applications. In general, erosion due to particle impingement, which can occur in a variety of practical cases, is often the key factor in pipeline failure. Parts such as elbows, for instance, are particularly prone to erosion issues. In the first part of this thesis, the Unsteady Reynolds Averaged Navier-Stokes (URANS) equations are combined with a stochastic Lagrangian particle tracking scheme considering all relevant elementary processes (drag and lift forces, particle rotation, inter-particle collisions, particle-wall interactions, coupling between phases) to numerically predict the erosion phenomenon on a 90° elbow pipe. After a detailed validation of the erosion model based on the experimental data of [Solnordal et al. \(2015\)](#), several cases regarding the wall roughness and static and dynamic coefficients of friction are analysed to elucidate the nature of the erosive process. For such analysis, more fundamental variables related to particle-wall interactions (impact velocity, impact angle, impact frequency) were used to scrutinize the basic erosion mechanisms. Finally, to prove the importance of inter-particle collision on elbow erosion, different mass loadings are additionally simulated. Especially for the high mass loading cases, interesting results about the role of the inter-particle collisions on elbow erosion are enlightened. In a second step, we propose a novel pipe wall design in order to reduce the erosion on a 90° elbow. This design consists of twisting the pipe wall along the flow streamwise direction. Basically, such configuration generates a swirling motion of the flow upstream of the elbow and consequently re-disperse the transported particles, preventing them to focus on a single point at the elbow. Based on a four-way coupled simulation, the simulations were run for the new pipe wall design. To understand the nature of the erosive process on the new pipe wall design, the above-mentioned variables regarding the particle-wall interaction were evaluated. In general, it was found that the changes in the multiphase flow promoted by the twisted pipe wall are effective for reducing elbow erosion. The numerical simulations reveal that the pipeline equipped with a twisted pipe wall reduces the peak of erosion depth up to 33% on the elbow when compared to the conventional pipe.

Keywords: Eulerian-Lagrangian URANS approach, One-way, two-way and four-way coupling, Elbow erosion modeling, Particle impact angle, Particle impact velocity, Cushioning effect, Innovative pipe wall, Erosion mitigation, Air-sand erosion.

Resumo

Partículas transportadas pneumáticamente são comumente responsáveis por desencadear o processo de erosão por impactos na parede. Esses impactos resultam da interação fluido-partícula e a compreensão de seus mecanismos é a chave para mitigar os danos causados pela erosão em aplicações de engenharia. Em geral, a erosão causada por impacto de partículas, que pode ocorrer em uma variedade de casos práticos, é frequentemente o fator principal na falha de tubulações. Acessórios como cotovelos, por exemplo, são particularmente propensos a problemas de erosão. Na primeira parte desta tese, as equações médias de Reynolds transiente (URANS) são combinadas com um modelo lagrangeano estocástico de rastreamento de partículas considerando todos os processos elementares relevantes (forças de arrasto e sustentação, rotação das partículas, colisões entre partículas, interações partícula-parede, acoplamento entre as fases) para prever numericamente o fenômeno erosivo em um cotovelo de 90° . Após uma validação detalhada do modelo de erosão com base nos resultados experimentais de [Solnordal et al. \(2015\)](#), vários outros casos com diferentes rugosidades na parede e coeficientes de atrito estático e dinâmico são apresentados para elucidar a natureza do processo erosivo. Para tal análise, foram utilizadas variáveis mais fundamentais e que estão relacionadas às interações partícula-parede (velocidade de impacto, ângulo de impacto, frequência de impacto) para examinar os mecanismos básicos de erosão. Finalmente, para provar a importância da colisão entre partículas na erosão do cotovelo, diferentes cargas mássicas são simuladas. Especialmente para os casos com carga mássica elevada, resultados interessantes sobre a importância das colisões entre partículas na erosão do cotovelo são abordados. Em uma segunda etapa, propomos um novo design para a parede da tubulação com o intuito de reduzir a erosão no cotovelo de 90° . Esta concepção consiste em torcer a parede do tubo ao longo do sentido principal do escoamento. Basicamente, tal configuração gera a rotação do fluido a montante do cotovelo e, conseqüentemente, re-dispersa as partículas transportadas, evitando que se concentrem diretamente em um único ponto no cotovelo. Com base em simulações com quatro vias de acoplamento, simulações são feitas para a configuração proposta. Para compreender a natureza do processo erosivo na nova geometria, as variáveis relativas as interações partícula-parede que foram mencionadas anteriormente também foram avaliadas. Em geral, verificou-se que as alterações no escoamento multifásico promovidas pela parede torcida são efetivas na redução da erosão no cotovelo. As simulações numéricas revelam que a tubulação equipada com o tubo torcido reduz o pico de profundidade de erosão no cotovelo em até 33% quando comparado ao tubo convencional.

Palavras-chaves: Abordagem Euler-Lagrange URANS, Uma via, duas vias e quatro vias de acoplamento, Modelagem da erosão em cotovelos, Ângulo de impacto, Velocidade de impacto, Efeito de amortecimento, Parede de tubo inovadora, Mitigação de erosão, Erosão ar-areia.

List of Figures

Figure 1 – Erosive wear inside an 90° elbow pipe.	30
Figure 2 – Methodology used to reach the research objective.	35
Figure 3 – Flowchart illustrating the relationship between operating conditions and type of wear (Stachowiak and Batchelor (2013).)	38
Figure 4 – Schematic of a jet of abrasive particles hitting a surface at a high velocity. (Bhushan (2013).)	39
Figure 5 – Sections through impact sites formed by hard particles on a ductile metal, showing typical shapes (Hutchings (1992).)	40
Figure 6 – Effect of the flow on impingement angle by erosive particles. Adapted from (Hojo et al. (1986).)	41
Figure 7 – Effect of the flow on erosive wear. Adapted from (Dosanjh and Humphrey (1985).)	42
Figure 8 – Variation of erosion with impact angle for various surface materials. Adapted from (Tilly (1979).)	43
Figure 9 – Variation of erosion with impact velocity for various surface materials. Adapted from (Tilly and Sage (1970).)	44
Figure 10 – The influence of particle size and velocity on erosion. Adapted from (Tilly (1969).)	45
Figure 11 – Variation of erosive wear resistance with indentation hardness for various surface materials. Adapted from (Finnie and McFadden (1978).)	46
Figure 12 – Variation of specific erosion with impact angle for 'as received' and heat treated alloy tool steel. Adapted from (Mills and Mason (1987).)	47
Figure 13 – Example of a 90 degree elbow.	48
Figure 14 – The influence of elbow geometry on the erosive wear of pipeline elbows. Adapted from Tong et al. (1980).	49
Figure 15 – The influence of elbow geometry on particle impact angle. Adapted from Tong et al. (1980).	50
Figure 16 – Wear back methods of elbow reinforcement: (a) concrete filled channel and (b) pressure-tight sleeve over elbow. Adapted from Mills (2004).	51
Figure 17 – Elbow protection by use of sacrificial inserts in preceding straight pipeline. Adapted from Mills (2004).	52

Figure 18 – Streamlines of the velocity field with twisted tape insert. Adapted from Santos et al. (2016).	52
Figure 19 – Some special elbows developed for pneumatic conveying systems: (a) the blind tee, (b) the Booth elbow, (c) the vortice ell or vortex chamber elbow, (d) the flow bow, (e) the expanded elbow and (f) the gamma elbow. Adapted from Mills (2004).	53
Figure 20 – The effect of loading and gas velocity on flow patterns in a blind tee (horizontal-vertical orientation). Adapted from Dhodapkar et al. (2009).	54
Figure 21 – Streamlines of the fluid velocity field inside the vortex chamber elbow. Adapted from Duarte et al. (2016).	55
Figure 22 – A "vortex chamber" creates a circulating flow pattern or a pocket of material, which cushions the impact on incoming stream. Adapted from Dhodapkar et al. (2009).	55
Figure 23 – In the gamma elbow design, accumulation of material in the primary impact zone prevents direct impact of material on the elbow wall, reducing erosive damage to the pipe. Adapted from Dhodapkar et al. (2009).	56
Figure 24 – Distribution of gas abrasive wear rate I along the length of the elbow l determined by angle α at various velocities V and stream concentrations. ($R_{av} = 128$ mm and $d = 50$ mm): 1) $V = 33.1$ m/sec, $\mu = 4.35$ kg/kg; 2) $V = 39.2$ m/sec, $\mu = 3.01$ kg/kg; 3) $V = 50$ m/sec, $\mu = 2.93$ kg/kg; and 4) $V = 54.8$ m/sec, $\mu = 2.10$ kg/kg. Adapted from Bikbaev et al. (1972).	57
Figure 25 – Effect of gas velocity on rate of erosion for ASTM 234. Grade WPB Ells with $r/d = 1.5$ (Number 2 Blasting Sand). Adapted from Bourgoyne (1989).	57
Figure 26 – Thickness loss profile of elbow specimen at different gas velocities, horizontal, $V_s l = 0.03$ m/s. Adapted from Mazumder et al. (2008).	58
Figure 27 – Colour contour plots of experimentally determined erosion depth profile after 200 kg passage of sand; graphical representation of erosion depth profiles after 200 kg passage of sand. Adapted from Solnordal et al. (2015).	59
Figure 28 – Predicted variation of volume removal with angle for a single abrasive grain. Experimental points for erosion by many grains (\triangle copper, \square SAE 1020 steel, \circ aluminum) are plotted so that the maximum erosion is the same in all cases. Adapted from Finnie (1960).	61
Figure 29 – Erosion tests on glass. $K = 318.7$ cm/sec; $V = 990.6$ cm/sec; X value used for calculating ε ; — theoretical curve; \boxplus test results (probability 95%). Adapted from Bitter (1963b).	61

Figure 30 – Predicted erosion rates at various particle impingement angles using the modified S–K model: at 98 m s ⁻¹ particle impact velocity. Adapted from Nsoesie et al. (2014)	74
Figure 31 – The turbulent kinetic energy distributed over eddies of different sizes (Fröhlich and Terzi (2008)).	78
Figure 32 – Control volume for a finite volume discretization.	91
Figure 33 – Flowchart solution of SIMPLE method implemented in UNSCYFL3D.	94
Figure 34 – Flow chart of fully coupled Euler-Lagrange calculations (Laín and Sommerfeld (2013)).	96
Figure 35 – Experimental configuration according to Solnordal et al. (2015) and the profiles used for comparison in the present work.	100
Figure 36 – (a) Grid of the elbow, perspective view. (b) Grid cross section upstream of the elbow. (c) Grid of the fluid and particle inlet regions.	103
Figure 37 – Mean and RMS normalized particle velocity profiles after a conveying distance of 8 m, numerical computations versus experiments of Huber and Sommerfeld (1998)	105
Figure 38 – Normalized particle mass flux after a conveying distance of 8 m, numerical computations versus experiments of Huber and Sommerfeld (1998)	106
Figure 39 – Normalized particle mean diameter after a conveying distance of 8 m, numerical computations versus experiments of Huber and Sommerfeld (1998)	106
Figure 40 – Contours of the erosion-related variables for mass loading $\eta = 3.846\%$. From left to right: one-way, two-way and four-way coupling. From top to bottom: erosion depth, impact velocity, impact angle and impact frequency.	108
Figure 41 – Erosion-related variables extracted from profile A for one, two and four-way coupling. (a) Erosion depth, (b) impact velocity, (c) impact angle and (d) impact frequency. Mass loading $\eta = 3.846\%$	110
Figure 42 – Particles concentration inside the elbow for: (a) one, (b) two and (c) four-way coupling. Mass loading $\eta = 3.846\%$	111
Figure 43 – Particle concentration upstream of the elbow. Mass loading $\eta = 3.846\%$	112
Figure 44 – Particle concentration upstream of the elbow with and without Saffman lift force. Mass loading $\eta = 3.846\%$	113
Figure 45 – Erosion-related variables extracted from profile C for one, two and four-way coupling. (a) Erosion depth, (b) impact velocity, (c) impact angle and (d) impact frequency. Mass loading $\eta = 3.846\%$	114
Figure 46 – Location of extracted profiles for mass loading $\eta = 3.846\%$. (a) One-way, (b) two-way and (c) four-way coupling.	114

Figure 47 – Erosion-related variables extracted from profile E for one, two and four-way coupling. (a) Erosion depth, (b) impact velocity, (c) impact angle and (d) impact frequency. Mass loading $\eta = 3.846\%$	116
Figure 48 – Erosion depth contours for mass loading $\eta = 3.846\%$ for four-way coupling. (a) $\Delta\gamma = 3.0^\circ$, (b) $\Delta\gamma = 5.0^\circ$, (c) $\Delta\gamma = 7.0^\circ$ and (d) $\Delta\gamma = 9.0^\circ$	118
Figure 49 – Erosion-related variables extracted from profile A for four-way coupling. (a) Erosion depth, (b) impact velocity, (c) impact angle and (d) impact frequency. Mass loading $\eta = 3.846\%$	119
Figure 50 – Erosion depth contours for mass loading $\eta = 3.846\%$ for four-way coupling. (a) $\mu_d = 0.45$ and $\mu_s = 0.6$, (b) $\mu_d = 0.3$ and $\mu_s = 0.45$, (c) $\mu_d = 0.3$ and $\mu_s = 0.15$, (d) $\mu_d = 0.15$ and $\mu_s = 0.15$	120
Figure 51 – Erosion-related variables extracted from profile A for four-way coupling. (a) Erosion depth, (b) impact velocity, (c) impact angle and (d) impact frequency. Mass loading $\eta = 3.846\%$	121
Figure 52 – Erosion-related variables extracted from profile C for four-way coupling. (a) Erosion depth, (b) impact velocity, (c) impact angle and (d) impact frequency. Mass loading $\eta = 3.846\%$	122
Figure 53 – Erosion depth contours for mass loadings: (a) $\eta = 3.846\%$, (b) $\eta = 10.0\%$, (c) $\eta = 30.0\%$, (d) $\eta = 50.0\%$, (e) $\eta = 70.0\%$ and (f) $\eta = 90.0\%$	124
Figure 54 – Particle concentration contours for mass loadings: (a) $\eta = 3.846\%$, (b) $\eta = 10.0\%$, (c) $\eta = 30.0\%$, (d) $\eta = 50.0\%$, (e) $\eta = 70.0\%$ and (f) $\eta = 90.0\%$	125
Figure 55 – Erosion-related variables extracted from profile A for four-way coupling. (a) Erosion depth, (b) impact velocity, (c) impact angle and (d) impact frequency.	126
Figure 56 – Scheme representing the cushioning effect caused at high mass loadings.	127
Figure 57 – Erosion-related variables extracted from profile C for four-way coupling. (a) Erosion depth, (b) impact velocity, (c) impact angle and (d) impact frequency.	128
Figure 58 – Erosion-related variables extracted from profile E for four-way coupling. (a) Erosion depth, (b) impact velocity, (c) impact angle and (d) impact frequency.	129
Figure 59 – Schematics of the proposed pipe wall with 4 undulations.	132
Figure 60 – Schematics of the proposed pipe wall with 8 undulations.	132
Figure 61 – Schematic representation of the transition between the untwisted and twisted wall pipe.	133
Figure 62 – (a) Grid of the untwisted pipe, perspective view. (b) Detail view of the untwisted pipe. (c) Grid cross section upstream of the elbow.	134

Figure 63 – (a) Grid of the twisted wall pipe with 4 undulations, perspective view. (b) Detail view of the twisted pipe. (c) Grid cross section upstream of the elbow.	134
Figure 64 – (a) Grid of the twisted wall pipe with 8 undulations, perspective view. (b) Detail view of the twisted pipe. (c) Grid cross section upstream of the elbow.	134
Figure 65 – Contours of the erosion-related variables for the untwisted pipe. (a) Erosion depth, (b) impact velocity, (c) impact angle and (d) impact frequency.	136
Figure 66 – Erosion-related variables extracted from the elbow extrado of symmetry plane. (a) Erosion depth, (b) impact angle, (c) impact velocity and (d) impact frequency.	138
Figure 67 – Streamlines of the velocity field. (a) Untwisted pipe, (b) 4-spiral pipe and (c) 8-spiral pipe.	139
Figure 68 – Velocity magnitude along each pipe type. (a) Untwisted pipe, (b) 4-spiral pipe and (c) 8-spiral pipe.	140
Figure 69 – Contours of the erosion-related variables for the 4-spiral pipe. (a) Erosion depth, (b) impact velocity, (c) impact angle and (d) impact frequency.	142
Figure 70 – Contours of the erosion-related variables for the 8-spiral pipe. (a) Erosion depth, (b) impact velocity, (c) impact angle and (d) impact frequency.	143
Figure 71 – Erosion depth contours for each pipe type with the magnitude fixed for the untwisted pipe.	144
Figure 72 – Influence of the pipe wall type on the erosion-related variables. (a) Erosion depth, (b) impact angle, (c) impact velocity and (d) impact frequency. Profiles extracted from the elbow extrados of symmetry plane.	145
Figure 73 – Influence of the pipe wall type on the particle concentration. (a) Un- twisted pipe, (b) 4-spiral pipe and (c) 8-spiral pipe.	147
Figure 74 – Particle concentration along the center line of each pipe wall type. . . .	148
Figure 75 – Influence of the pipe wall type on the particle mean diameter. (a) Untwisted pipe, (b) 4-spiral pipe and (c) 8-spiral pipe.	149
Figure 76 – Particle mean diameter along the center line of each pipe wall type. . .	149
Figure 77 – Static pressure profile extracted from the center line of each pipe type. Continuous line is the single phase flow and dashed line is the two-phase flow.	150
Figure 78 – Erosion depth contours for each pipe wall type. (a) Untwisted pipe, (b) 4-spiral pipe and (c) 8-spiral pipe.	151
Figure 79 – Schematic representation of the location where the erosion-related vari- ables were extracted at the pipe wall.	152
Figure 80 – Erosion-related profiles comparing each pipe wall type.	153

List of Tables

Table 1 – Expenses with wear based on the Brazilian gross national product (GNP). Source: < https://goo.gl/hCsZN6 >.	31
Table 2 – Parameters for the erosion model (Oka and Yoshida (2005)).	72
Table 3 – Experimental facility dimensions (Solnordal et al. (2015)).	101
Table 4 – Experimental conditions.	102
Table 5 – Particle size distribution of sand.	102
Table 6 – Simulation conditions.	103
Table 7 – Mesh resolutions and y^+ average values.	107
Table 8 – Abbreviation of the computed cases.	120
Table 9 – Parameters for the erosion model.	135
Table 10 – Simulation conditions.	135
Table 11 – Integral value of each erosion depth curve normalized by the maximum curvature angle ($\pi/2$).	146

List of abbreviations and acronyms

CFD	Computational Fluid Dynamics
DES	Detached Eddy Simulation
DNS	Direct Numerical Simulation
FVM	Finite Volume Method
LES	Large Eddy Simulation
MFlab	Laboratory of Fluid Mechanics
NSE	Navier Stokes Equation
NPS	Nominal Pipe Size
PETROBRAS	Petróleo Brasileiro
RANS	Reynolds-Averaged Navier–Stokes equations
RMS	Root Mean Square
SIMPLE	Semi-Implicit Method for Pressure-Linked Equations
TKE	Turbulence Kinetic Energy

List of symbols

δ_{ij}	Kronecker delta
g_i	Gravity component

Contents

1	INTRODUCTION	29
2	THESIS SCOPE	33
2.1	Research objective	33
2.2	Relevance	34
2.3	Methodology	34
3	BACKGROUND THEORY	37
3.1	Types of wear	37
3.1.1	Erosion due to particles	39
3.1.2	Erosion mechanisms	40
3.1.3	Influence of the flow in the erosion	41
3.2	Erosive wear in pipeline systems	42
3.2.1	Variables involved	43
3.2.1.1	Impact angle	43
3.2.1.2	Impact velocity	44
3.2.1.3	Particle size	44
3.2.1.4	Particle hardness	45
3.2.1.5	Surface material	46
3.2.1.6	Particle concentration	47
3.2.1.7	Particle shape	47
3.3	Elbow fitting	47
3.3.1	Influence of elbow geometry on erosion	48
3.3.1.1	Long radius elbows	49
3.3.1.2	Short radius elbows	50
3.3.2	Methods to mitigate elbow erosion	51
3.3.2.1	Wear back methods	51
3.3.2.2	The use of inserts	52
3.3.2.3	Special elbows	53
3.3.3	Experimental work in elbows in air-sand flows	56
3.4	Solid particle erosion modeling	59
3.4.1	Erosion equations review	60
3.4.2	Particle wall rebound models	75
3.4.3	Coefficients of friction	76
4	MATHEMATICAL MODELS	77

4.1	Gas phase equations	77
4.1.1	Unsteady Reynolds Averaged Navier Stokes simulations	79
4.1.2	Turbulence closure model	80
4.1.2.1	Two layer $k - \epsilon$ closure model	81
4.1.2.2	Reynolds stress closure model	82
4.2	Particle motion equations	84
5	FINITE VOLUME DISCRETIZATION	89
5.1	Finite Volume Method	89
5.2	Numerical discretization	90
5.3	Pressure-velocity coupling	92
5.4	Solution procedure	92
5.5	Solver UNSCYFL3D	93
6	PARTICLE PHASE ALGORITHM	95
6.1	Coupling procedure	95
6.2	Particle-tracking algorithm	97
7	THE ROLE OF INTER-PARTICLE COLLISIONS ON ELBOW ERO-	
	SION	99
7.1	Test case description	99
7.1.1	Description of the experimental set-up	100
7.1.2	Description of the numerical set-up	102
7.1.2.1	Domain size and grid	102
7.1.2.2	Boundary conditions	103
7.1.2.3	Statistics	104
7.2	Results and discussions	104
7.2.1	Two-phase flow validation	104
7.2.2	Erosion computations	107
7.2.2.1	Mesh independence study	107
7.2.2.2	Erosion model validation - one, two and four-way couplings	107
7.2.2.3	Influence of the surface roughness on the penetration depth	117
7.2.2.4	Influence of the static and dynamic coefficients of friction in the penetration depth	119
7.2.2.5	Influence of the mass loading in the penetration depth	123
7.3	Chapter conclusions	129
8	INNOVATIVE PIPE WALL DESIGN TO MITIGATE ELBOW ERO-	
	SION	131
8.1	Pipe wall design proposal	131
8.1.1	Geometries and grids	133
8.1.2	Boundary conditions	135

8.2	Results and discussions	135
8.2.1	Erosion model validation - Standard 90° elbow pipe	135
8.2.2	Influence of the pipe design on the fluid flow	139
8.2.3	Influence of the pipe design on the elbow erosion	141
8.2.4	Particle dynamics inside each pipe design	146
8.2.5	Erosion analysis	150
8.2.6	Practicality of the twisted pipe wall for fabrication and testing	154
8.3	Chapter conclusions	155
9	THESIS CONCLUSIONS	157
10	FUTURE RESEARCH	161
	BIBLIOGRAPHY	163
	APPENDIX	175
APPENDIX A	– LIST OF PUBLICATIONS	177
APPENDIX B	– CURRICULUM VITAE	179

Chapter 1

Introduction

Erosive wear due to particle impingement is a typical multiphase flow configuration relevant for a variety of practical applications involving particle-laden flows especially for pipeline systems. The surface damage is caused by the repeated application of high localized stresses (Cousens (1984)). In particular, erosion causes severe problems in pneumatic and hydraulic transport systems (Bikbaev et al. (1972), Bikbaev et al. (1973)). In this sense, pipe fittings such as elbows, for instance, are prone to wear during the abrasive particle conveying (Duarte et al. (2016)). While usually considered undesirable, erosion has useful application in processes such as sand blasting, abrasive deburring and the erosive drilling of hard materials (Finnie (1960), Neilson and Gilchrist (1968)). In this regard, the necessity to model and predict detailed information about these kind of flows became a persistent issue in the study of multiphase flows over the past few decades. By understanding the dynamics of motion, it is possible to make improvements and increase the safety during the operation of these systems.

Throughout the 60's a new theoretical approach has been developed, the Computational Fluid Dynamics (CFD). The Computational Fluid Dynamics aims to simulate flow through numerical methodologies designed to represent a physical phenomenon. Although its development begun over 50 years ago, only in the 90's it started to have greater acceptance in the industry, especially in aeronautical projects. Nowadays, the Computational Fluid Dynamics has become an important tool to study flow problems, helping designers to optimize single and multiphase systems. In wear-related problems, the CFD is used as a tool for predicting the wear in various environments and due to its complexity unfeasible the use of empirical correlations.

In this context, constant effort has been put in the accurate prediction of the erosion effects. Until now, many aspects of the erosion process are still too complex to model and innovative experimental and theoretical developments are needed. Furthermore, the precise measurements of some important parameters is of paramount importance. These parameters are basically related to inter-particle collisions and particle-surface interactions,

such as rebounding (impact angle) and impact velocity.

In many industrial processes, the erosive wear arises from the impingement of solid particles against the surface and have noticeable consequences on equipment reliability and safety. The erosive wear can be a problem in cyclones separators, propellers and pumps, but in pneumatic conveying systems (*cf.* Fig. 1) erosive wear can be even more serious (Mills (2004)).



Figure 1 – Erosive wear inside an 90° elbow pipe.

Source: <<http://goo.gl/tkrCpb>>

Generally speaking, erosive wear is a problem which industry has learned to live. Although there are many ways to reduce the magnitude of the problem, relate the conveyed material and the system itself requires a large number of variables to be taken into account. In addition, maintenance time and operating costs are also important factors that lead companies to decide which is the best method for the reduction of erosion in their equipment. For an entire pipeline plant, the effects of different elements (*e.g.*, constrictions, pipe shapes and pipe fittings) have to be considered. Due to the nature of the transport process, piping systems are willing to wear when abrasive particles have to be conveyed. When particles are carried in suspension through the air, high conveying air velocities are required to keep the material moving, in order to prevent pipeline obstruction. In this context, pipe fittings provide pneumatic conveying systems with their flexibility in change the flow direction, however, these spots become more susceptible to repeatedly collisions and rapid wear can occur. In terms of economics, the cost of wear (*e.g.*, abrasion, erosion, cavitation and others) has been estimated as ranging from 1% to 4% of the gross national product (GNP) of an industrialized nation. The effect of erosion is particularly evident in the industrial areas of agriculture, mining, mineral processing, and earth moving (Bayer (2002)). Table 1 shows the wear expenses based on the Brazilian gross national product. Clearly, the costs with wear are pretty high. This implies in a necessity of more studies

about the theme, aiming the reduction of such values.

Table 1 – Expenses with wear based on the Brazilian gross national product (GNP). Source: <<https://goo.gl/hCsZN6>>.

Year	Gross National Product (R\$)	Wear expenses (R\$)
2015	5,90 trillion	2,36 billion
2014	5,52 trillion	2,20 billion
2013	5,31 trillion	2,12 billion
2012	4,80 trillion	1,92 billion

The goal of this thesis is to support oil and gas industry by analyzing the mechanisms responsible for the erosion reduction in elbows promoted by a novel pipe wall design. In agreement with the supervisor from the university, and supported by the acquired knowledge during the literature review, it was decided to focus the research on the erosion reduction by generating a swirling flow upstream of the elbow.

The present thesis is organized as follows: Chapter 2 discusses the objective and the method to reach it. In chapter 3, the background theory is presented as well as an overview of the elbows studied. Chapter 4 presents an overview of the relevant equations for gas/particle phase and erosion prediction. Chapters 5 and 6 describes the type of discretization and the particle phase algorithm, respectively. Chapter 7 presents a summary of the first part of this thesis which include validations and parametric variations of the erosion-related variables in a standard pipeline configuration. In chapter 8, the twisted pipe wall configuration is proposed and its benefits regarding the erosion reduction at the elbow are enlightened. The thesis is concluded in Chapter 9.

Chapter 2

Thesis scope

After an exhaustive literature review, for a successful and fulfillment of the doctoral thesis, it is of extreme importance to define the goal and a method to reach it. Both are elaborate in this chapter. First Section 2.1 presents the research objective, after which a few words are spend on the relevance of the project in Section 2.2. Finally, in Section 2.3, a methodology is presented in order to reach the objective.

2.1 Research objective

There are two factors that directly influenced the definitive research objective of the current thesis. Besides the literature acquired during the literature research, the suggestions and advices from the university supervisor are taken into account. PETROBRAS project suggestions are focused on solve problems related to wear in oil and gas industry, whereas my supervisor also draw attention to the scientific value of the research. For this reason, the research objective is divided into a primary and secondary objective.

The first objective relates to the research from a scientific perspective. This objective forms the basis to complete the research.

Carry out a detailed investigation to elucidate the nature of the erosive process of a ninety-degree-elbow, by simulating the elbow with an in-house CFD code.

The reason for focusing on the ninety-degree-elbow is related to validate the erosion prediction model with experiments, scrutinize the basic erosion mechanisms using more fundamental variables related to particle-wall interactions (impact velocity, impact angle and impact frequency), implement it in the code and analyze its capacity to deal with a variety of erosion problems in engineering with sufficient accuracy.

The second objective covers the part of the research that is of particular interest for industry.

Propose a novel pipe wall design which consists of twisting a pipe wall along the flow streamwise direction in order to reduce the erosion on a ninety-degree-elbow and verify its benefits when compared with the standard pipe geometry.

The reduction of erosion in pipeline systems and cyclones separators are of particular interest for the company. For engineering purpose they require to know the magnitude of erosion acting on the equipment surface and the effects of the mass loading on the erosive process.

Both objectives are fulfilled simultaneously throughout this thesis, whereas the final conclusions can be found in Chapter 9.

2.2 Relevance

For this research, the only available simulation tool is CFD. Unfortunately erosion experimenting and measuring are not feasible due to facility limitations. During the literature survey no example of solely the application of CFD onto a twisted pipe was found. Hence it would be rather novel to produce useful results using solely CFD. The ninety-degree-elbow validation process will form one of the key parts in successfully acquiring these results. So besides the benefits for industry, the research will also contribute to the scientific community.

2.3 Methodology

Knowing the research objectives it is possible to outline an initial methodology. This process is devised with the knowledge obtained during the literature review. It is schematically showed in Fig. 2 by placing the various steps in blocks and connecting them via arrows.

Two phases can be distinguished; a validation phase and an analysis phase. The goal of the validation phase is to come up with a simulation setup that provides sufficiently accurate results in order to be used for the standard elbow simulations. In the analysis phase, both standard and twisted pipes are simulated for different situations. The next lines explain both phases in details.

Validation phase

For the validation phase of the present study, an initial simulation setup is created based on literature and different erosion prediction models are tested. After finding the best model, the simulation is ran and the resulting erosion profile is compared to existing experimental data. Depending on the outcome, the setup is updated in order to match

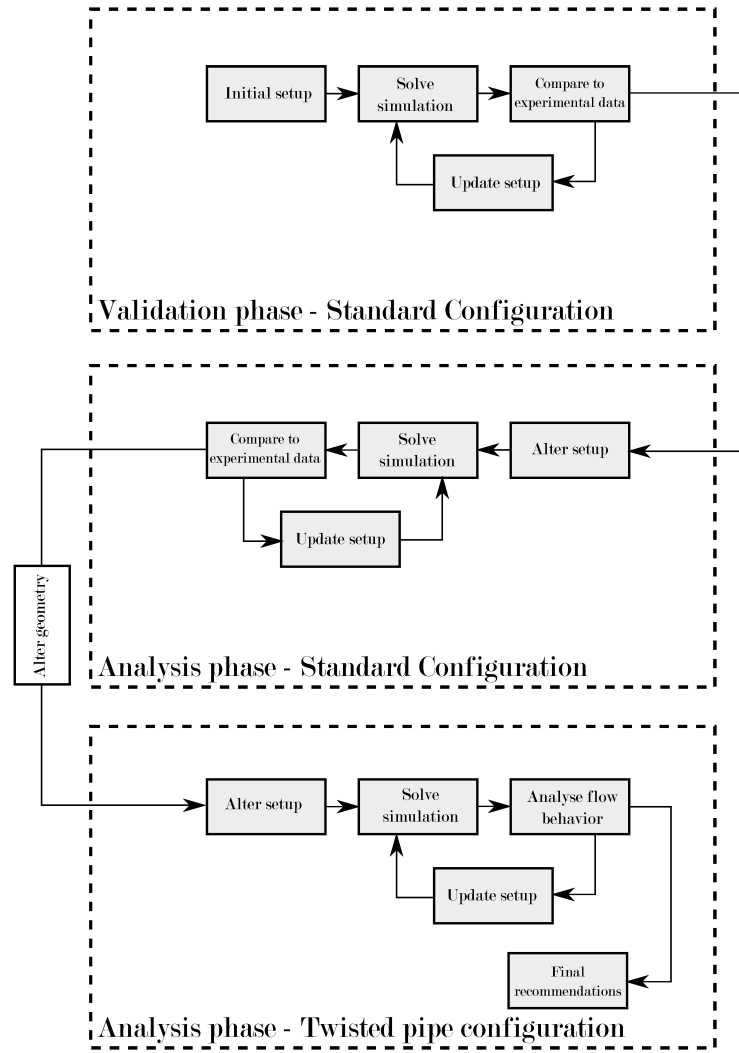


Figure 2 – Methodology used to reach the research objective.

both data sets more closely. Note that the updates are based on acquired literature and preserves the experimental characteristics. The complete validation phase is covered in Chapter 7 of this thesis.

Analysis phase

Once the simulation shows good agreement with the experimental data, the setup is altered such that it solves the flow and the erosion for different wall roughness, static and dynamic coefficients of friction and mass loadings. The resulting simulations can provide important insight into the changes of the erosion profile due to such variations. After this stage, the twisted pipe wall is conceived and the validate standard elbow simulation setup serves as an initial setup for the twisted pipe simulations.

Finally, the twisted pipe is simulated with two different configurations while using the best known simulation setup employed for the standard elbow. By analyzing

the resulting dataset, it becomes possible to obtain remarkable results on both elbows simulations. The complete analysis phase is covered in Chapter 7 and Chapter 8 of this thesis.

However, before elaborating the research objective, first some background theory is required. This should provide the reader with a basic understanding of erosion wear and numerical techniques to compute them. The following set of chapters, bundled in Chapters 3 to 6, presents this theory.

Chapter 3

Background theory

Several characteristics make the erosion profile inside pipelines and elbows significantly different. Hence the Computational Fluid Dynamical (CFD) techniques required to simulate the flow differ as well. This part of the thesis will present the background theory required to understand the basic erosion phenomena occurring inside pipes and the CFD techniques employed to simulate them.

3.1 Types of wear

As described in many books, (*e.g.*, [Gahr \(1987\)](#) and [Hutchings \(1992\)](#)), different types of wear may be separated by referring to the basic material removal mechanisms, the wear mechanisms, that cause the wear on a microscopic level. There are many attempts to classify wear by wear mechanisms, but a commonly accepted first order classification distinguishes between *adhesive wear*, *abrasive wear*, *wear caused by surface fatigue*, and *wear due to tribochemical reactions*. Very commonly, the damage observed on a tribologically loaded surface is a result of two or more coexisting or interacting surface damage types. Interacting damage types may lead to unproportionally high wear rates, as for example in oxidation-enhanced surface cracking; adhesive wear may however also be suppressed by oxidation ([Askeland et al. \(2010\)](#)).

According to [Bhushan \(2013\)](#), each type of wear occurs by mechanical and/or chemical means and is usually speeded by frictional heating or some kind of thermal means. In addition, [Bhushan \(2013\)](#) indicates that wear can be divided into six different phenomena. They are: adhesive, abrasive, fatigue, impact by erosion and percussion, chemical and electrical. However, all of them has one thing in common: the subtraction of solid material from rubbing surfaces.

Even though the division proposed by [Gahr \(1987\)](#) and [Hutchings \(1992\)](#) presents the basis of the wear classes. There is another classification proposed by [Stachowiak and Batchelor \(2013\)](#) which come up with a dependence of wear on various operating conditions.

Such dependence of wear on various operating conditions can be summarized in a flowchart shown in Fig. 3.

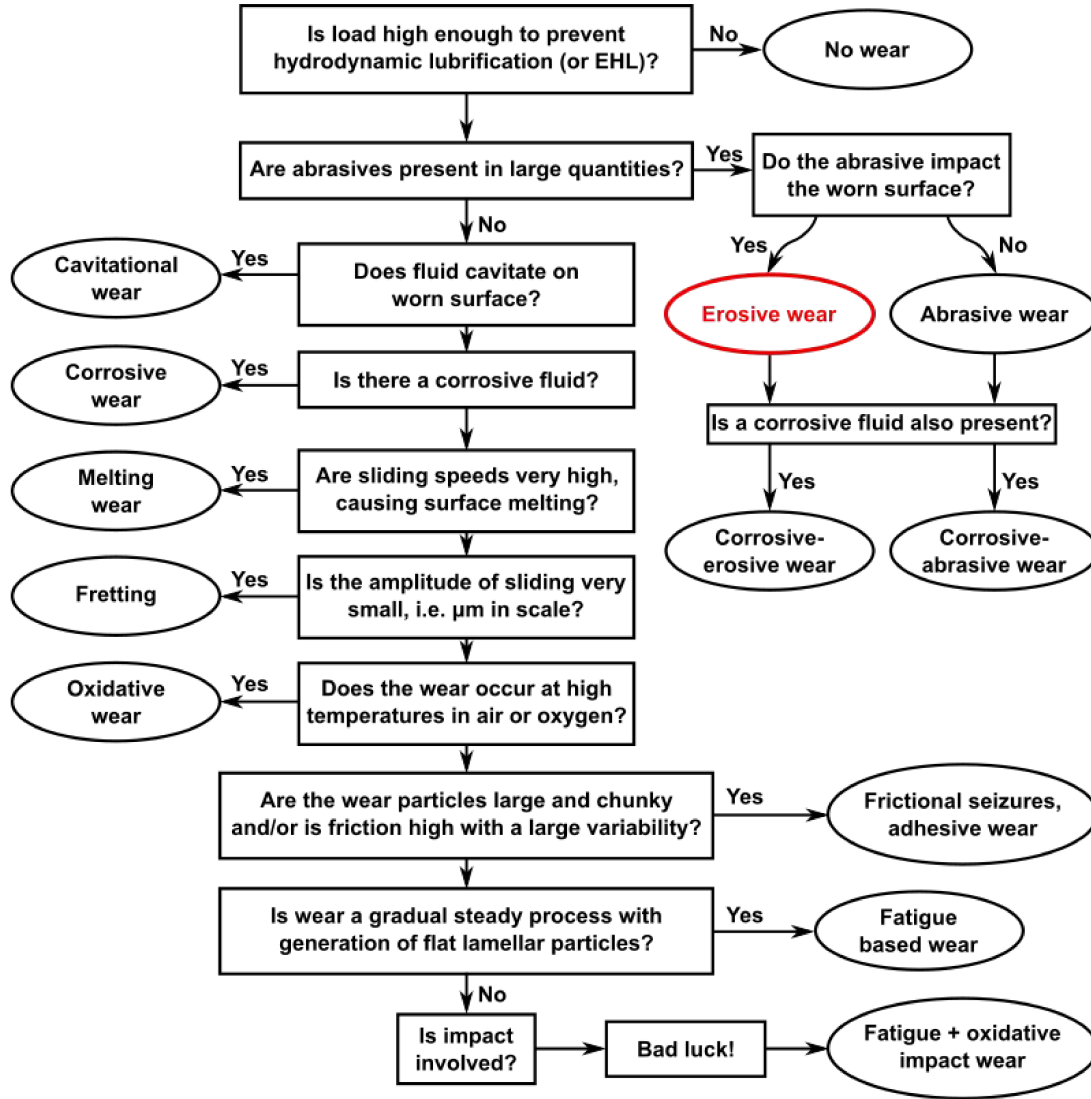


Figure 3 – Flowchart illustrating the relationship between operating conditions and type of wear (Stachowiak and Batchelor (2013).)

In this context, the present thesis will exclusively focus on the erosion due to particles impingement. It is known that other types of wear can coexist, however, carry out a study with more than one type of wear at the same time can significantly increase the difficulty to find accurate mathematical models. Due to this fact, all the geometries studied in this report as well as the experimental database have their surface damaged preferentially by erosion, avoiding the interference of other types of wear and facilitating an accurate analysis of the models used in the simulations.

3.1.1 Erosion due to solid particles

Erosion is defined as the wear resulted by the interaction between a solid surface and a fluid flow containing abrasive particles with a certain speed, or the impact of free moving liquid (or solid) particles on a solid surface (Finnie (1960)). We can divide the understanding of erosion in two major parts, the first being the determination of the fluid flow conditions of the number, direction, and velocity of the particles striking the surface. The second part may be defined as the calculation of surface material removed, with the data acquired from the first part. Clearly, the first part of the erosion process is characterized as a fluid mechanics problem, with the fluid flow transporting the particles into the surface, which defines the erosion wear (Pereira et al. (2014)).

Erosion wear is dependent of the number of particles striking a surface, as well as the physical quantities associated with it, such as particle velocity and their direction relative to the surface to be struck. It is known that these quantities are noticeably determined by the flow conditions. In other words, any minor change in the flow conditions such as viscous regime or temperature might bring large variations in the erosion rate. For example, in operations where the flow direction changes quickly such as turbine blade erosion is usually more severe than in a straight run of piping. Other erosion-increasing factor is the local turbulence generated from roughened surface or misaligned parts (Finnie (1960)).

According to Bhushan (2013), erosion is a form of abrasion that is generally treated rather differently because the contact stress arises from the kinetic energy of particles flowing in an air or liquid stream as it encounters a surface (Fig. 4). The particle velocity and impact angle combined with the size of the abrasive give a measure of the kinetic energy of the impinging particles, that is, of the square of the velocity. Wear debris formed in erosion occurs as a result of repeated impacts.

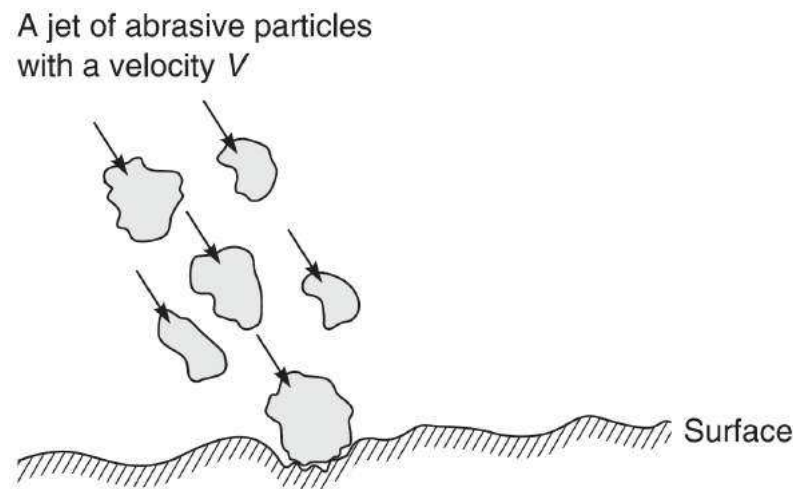


Figure 4 – Schematic of a jet of abrasive particles hitting a surface at a high velocity. (Bhushan (2013).)

3.1.2 Erosion mechanisms

According to the literature, there are several ways to describe the mechanism of erosion, as provided from different authors. Therefore, it is difficult to establish only one mechanism as the most reliable and real mechanism. The most used in the literature are the ones proposed by [Finnie \(1960\)](#) and [Hutchings \(1992\)](#).

[Finnie \(1960\)](#) proposed a mechanism of erosion in which the particle acts as a miniature machine tool in which the surface material is cut, generating a chip. Also, for the erosion of ductile metals, at oblique impact, this mechanism happens irrespective of its shape and size.

[Hutchings \(1992\)](#) proposed a similar mechanism. However, he split the cutting action into three different types, relying on the shape and the orientation of the eroding particle. The first type occurs when there is erosion by oblique impact of spherical particles, and the material is removed by a *ploughing* action (Fig. 5a), moving materials to the front and side of the particle. The second and third types occur when there is the collision of angular shaped particles, and they differ from each other in the orientation of the erodent particle as it strikes the target surface, as well as the direction of the particle during the contact with the surface; in other words, if the particle rolls forward or backward during contact. Type I cutting (Fig. 5b) is defined when the particle rolls forward during the contact, and material is removed by repeated impacts on a prominent lip formed by the indenting angular particle. Type II cutting (Fig. 5c) is defined when the particle rolls backward, and the material is removed as if the erosion was a machining operation, with the material being removed as a chip due to the fact that there's a sharp tip of the erodent particle, working as a machining tool ([Hutchings \(1992\)](#)).

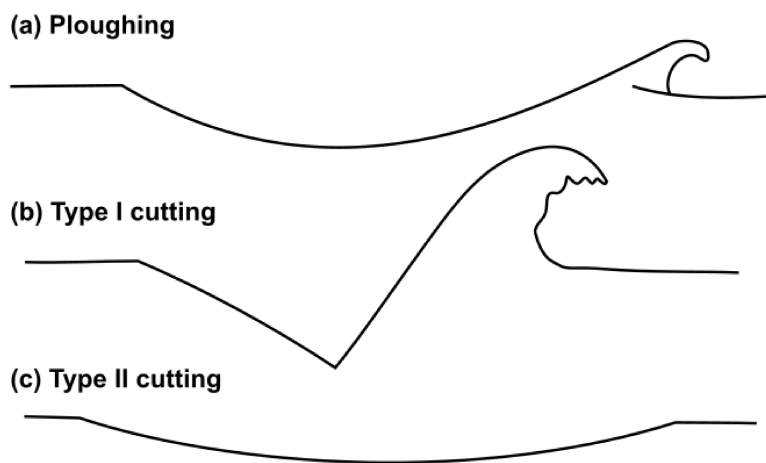


Figure 5 – Sections through impact sites formed by hard particles on a ductile metal, showing typical shapes ([Hutchings \(1992\)](#)).

3.1.3 Influence of the flow in the erosion

Most erosive agents are conveyed by a flow, e.g., water or air. A mixture of erosive particles and liquid flow is known as a slurry. The characteristics of the flow have a surprisingly strong effect on the final wear rate. Controlling factors relate to the bulk properties of the flow, i.e., viscosity, density and turbulence, and to its microscopic properties such as corrosivity and lubrication capacity. It has been shown that small additions of lubricants to erosive slurries can significantly reduce wear (Levy and Hickey (1987), Levy et al. (1987)). The ability of the liquid medium to provide cooling during particle impingement is also important (Levy and Hickey (1987), Levy et al. (1987)).

In terms of bulk properties, the drag forces imposed by a viscous slurry on the erosive particles can affect wear by altering the impingement angle. This is demonstrated schematically in Fig. 6.

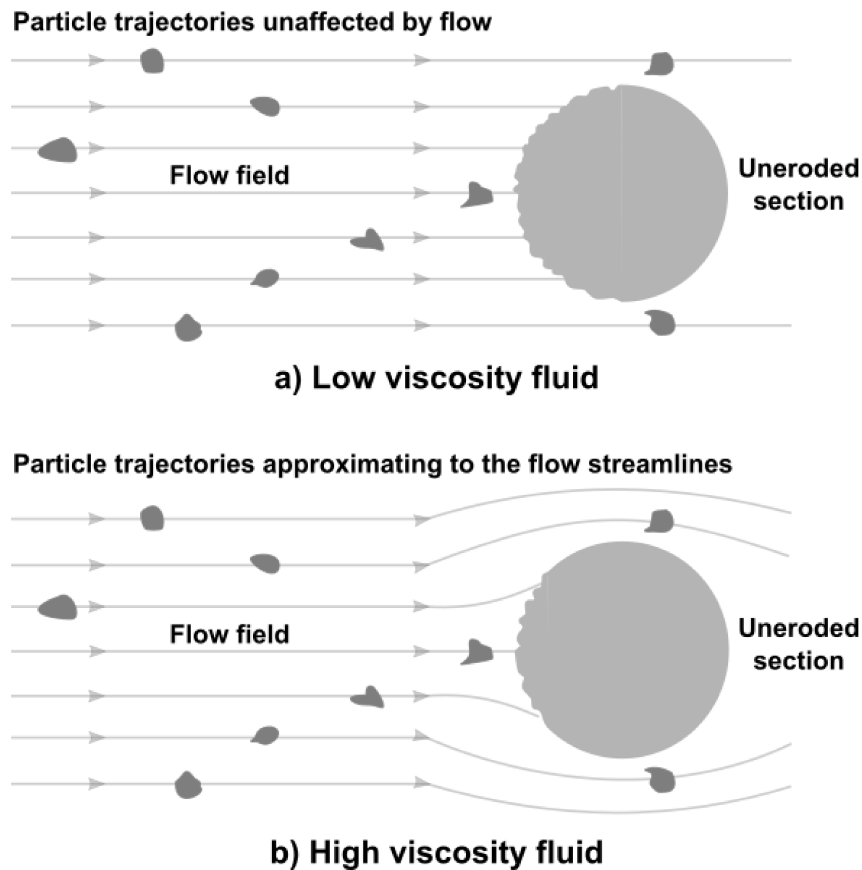


Figure 6 – Effect of the flow on impingement angle by erosive particles. Adapted from (Hojo et al. (1986).)

It can be seen that the increased particle drag forces imposed by the more viscous flow shift particle impingement to the sides of the eroding cylinder. The effect of the flow is to alter the location and form of wear since the impingement angle is reduced by the shift to the cylinder sides. The flow-induced reduction in impingement angle causes an increase in abrasion-type mechanisms of erosive wear. If an estimation of wear rates in a

real machine is required then a comprehensive analysis of particle trajectories is essential (Hojo et al. (1986)).

The flow turbulence accelerates erosive wear as particle impingement is more likely to occur in turbulent flow than in laminar flow where the flow tends to draw the particles parallel to the surface (Dosanjh and Humphrey (1985)). The difference between particle behavior in laminar and turbulent flow of the medium is illustrated in Fig. 7.

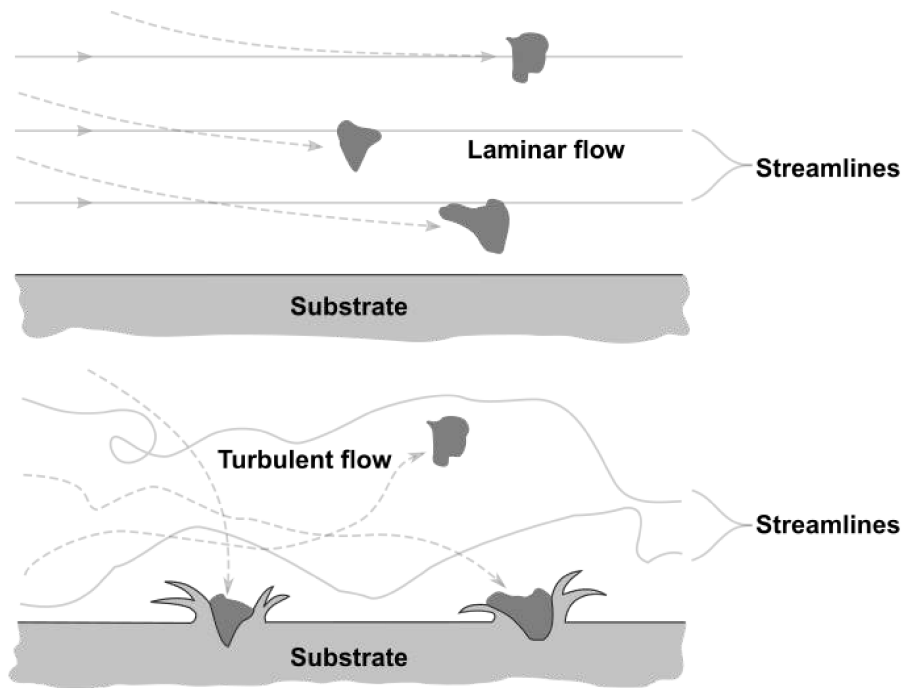


Figure 7 – Effect of the flow on erosive wear. Adapted from (Dosanjh and Humphrey (1985)).

An exception to this rule is where the laminar flow is directed normally to the surface which is the case when a jet of fluid impinges against a surface. In this case, wear is concentrated directly beneath the jet and a relatively unworn annular area surrounds the wear scar. This phenomenon is known as the 'halo effect'. The effect of increasing turbulence with distance from the jet is outweighed by the concentration of erosion directly beneath the jet (Dosanjh and Humphrey (1985)).

3.2 Erosive wear in pipeline systems

Erosion represents a major problem, not only in bulk solids handling plant, but in many other areas. Both pneumatic and hydraulic conveying of particulate materials in pipelines can result in severe erosion problems, and aircraft, rockets and missiles are eroded by rain drops and ice particles. The area that has probably received most attention, however, is aircraft engines, and in particular helicopters, for dust ingestion can cause

considerable damage, and has resulted in several catastrophic failures in service (Mills (2004)).

In pneumatic conveying, in particular, erosion can be a severe problem because of the high velocities required for conveying bulk particulate materials. The erosion of surfaces by solid particles in a fluid stream is probably the main reason why industry is often reluctant to install pneumatic conveying systems, particularly when abrasive materials have to be handled. In several other areas, however, erosion has many practical uses and advantages, such as in erosive cleaning of surfaces and erosive drilling and cutting.

3.2.1 Variables involved

There are many parameters associated with both the impacting particles and the surface material that will have an effect on erosive wear. In some cases the variables are inter-related and so need to be considered in groups in these situations. All these variables are presented below.

3.2.1.1 Impact angle

A curve presented by Tilly (1979) and shown in Fig. 8 illustrates the variation of erosion with impact angle for two different surface materials and is typical of the early work carried out to investigate the influence of these variables.

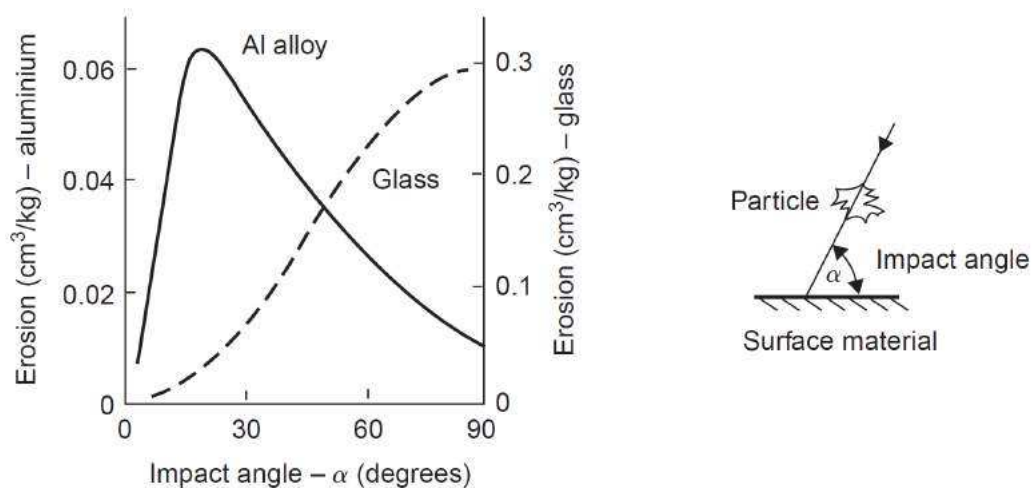


Figure 8 – Variation of erosion with impact angle for various surface materials. Adapted from (Tilly (1979).)

Both materials showed very significant differences in both erosion rate and the effect of impact angle. These materials do, in fact, exhibit characteristic types of behavior that are now well recognized. The aluminum alloy is typical of ductile materials: it suffers maximum erosion at an impact angle of about 20° and offers good erosion resistance to

normal impact. The glass is typical of brittle materials: it suffers severe erosion under normal impact but offers good erosion resistance to low angle, glancing impact.

The influence of impact angle and the different response of ductile and brittle materials to erosive wear is an aspect of the problem that will be considered at many different points. The relationships can be used to explain a number of observed phenomena in erosive wear, and are particularly useful in predicting the possible behavior in new and untried situations.

3.2.1.2 Impact velocity

Of all the variables that influence the problem of erosive wear, velocity is probably the most important of all (Mills (2004)). It is generally recognized that erosive wear is dependent upon a simple power of velocity, such as:

$$\text{Erosion} = \text{constant} \times (\text{velocity})^n \quad (3.1)$$

There is no certainty about the value of the exponent, and values of n ranging from 2–6 have been reported. Tilly and Sage (1970) tested a wide range of different materials and obtained very good agreement with respect to the exponent, n , in each case. Their results are reproduced in Fig. 9. This is a log plot and the slope of all the lines was approximately 2.3. The velocities, of course, are well above those generally encountered in pneumatic conveying systems, even at the lower end of their range.

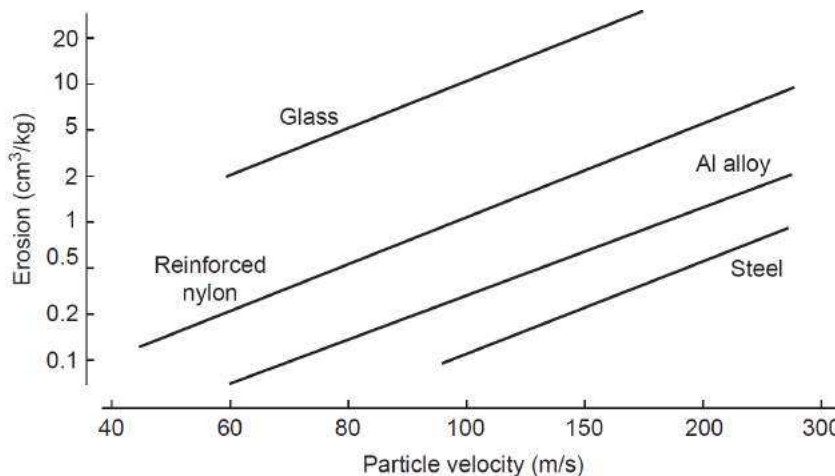


Figure 9 – Variation of erosion with impact velocity for various surface materials. Adapted from (Tilly and Sage (1970).)

3.2.1.3 Particle size

The general consensus regard to particle size is that there is a threshold value of wear rate which, for velocities appropriate to pneumatic conveying, occurs at a particle

size of about $60\ \mu\text{m}$ (Tilly (1969)). Below this size wear rate reduces, but for particle sizes greater than $60\ \mu\text{m}$ it remains constant.

Figure 10 shows that the threshold value increases with increase in velocity. The work was carried out by Tilly (1969) considering the erosion of aircraft engines, which explains the high velocity range. A shot blast type of test rig, in which abrasive particles were impacted against flat plates, was used for the purpose.

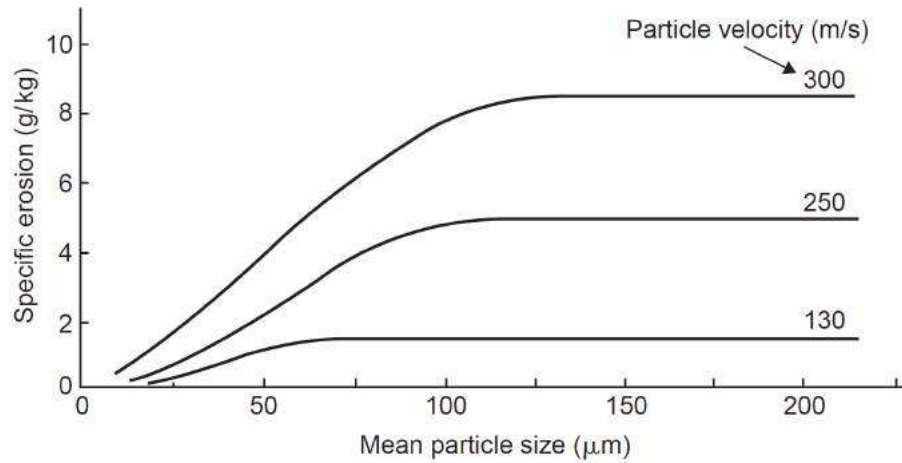


Figure 10 – The influence of particle size and velocity on erosion. Adapted from (Tilly (1969)).

Wear rate here is expressed in specific terms, that is the mass (or volume) of surface material eroded per unit mass of particles impacted. In a given mass of particles, the number of particles will reduce as the particle size increases, and so although the specific erosion remains constant with increase in particle size, the erosive wear per particle will increase approximately with the cube of the particle size. Little work has been undertaken with particles much larger than about 1 mm in size and so it is not known to what particle size the threshold value remains constant (Mills (2004)).

3.2.1.4 Particle hardness

The particle hardness of the material being conveyed is the major indicator of the potential erosiveness of the material. Goodwin et al. (2006) investigated the influence of particle hardness on erosive wear with a rig in which abrasive particles were impacted against test plates. They found that erosion is related to hardness by the expression:

$$\text{Erosion} = \text{constant} \times H_p^{2.4} \quad (3.2)$$

where H_p is the particle hardness (kg/mm^2).

It is generally considered, however, that there is a threshold value of particle hardness beyond which erosion remains essentially constant. This occurs at a particle

hardness of about 800 kg/mm^2 , and so materials with hardness values much greater than this would not be substantially more erosive than sand particles (Goodwin et al. (2006)).

3.2.1.5 Surface material

There is a wealth of information in the field of abrasive wear and the relationship between surface material hardness and wear resistance for metals. Finnie (1962) was the first to show that such a relationship might exist in the field of erosive wear, but Finnie and McFadden (1978) were the first to produce a hardness to wear resistance relationship similar to those presented for abrasive wear. Results of their work are presented in Figure 11. The range of materials that they considered was rather limited but the shape and trends of the curves were similar.

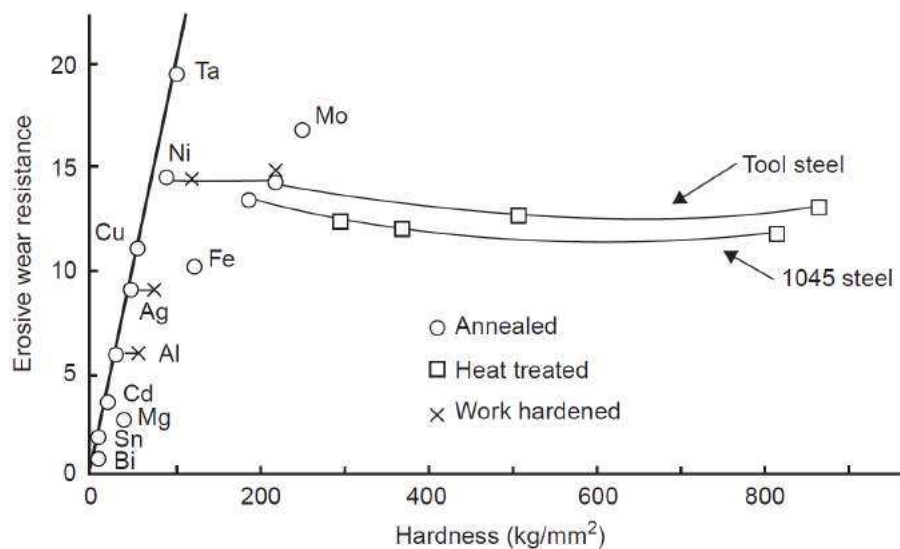


Figure 11 – Variation of erosive wear resistance with indentation hardness for various surface materials. Adapted from (Finnie and McFadden (1978).)

Mills and Mason (1987) also carried out tests to determine the influence of surface hardness on erosive wear resistance. An acceleration tube device was used, with silica as the abrasive material. The surface material employed was an alloy tool steel and this was hardened, and tempered over a range of temperatures, to produce a range of surface hardness values up to 830 kg/mm^2 . In the annealed, or 'as received', condition the steel had a Vickers hardness of about 230 kg/mm^2 .

A comparison of the two hardness extremes, with respect to impact angle, is presented in Figure 12. This clearly shows an impact angle effect and reinforces the point that the reference conditions for any comparison with respect to erosive wear performance should always be clearly stated.

Although there is little or no difference in wear rate at very high values of impact angle, at low impact angles the heat treated material shows a significant improvement.

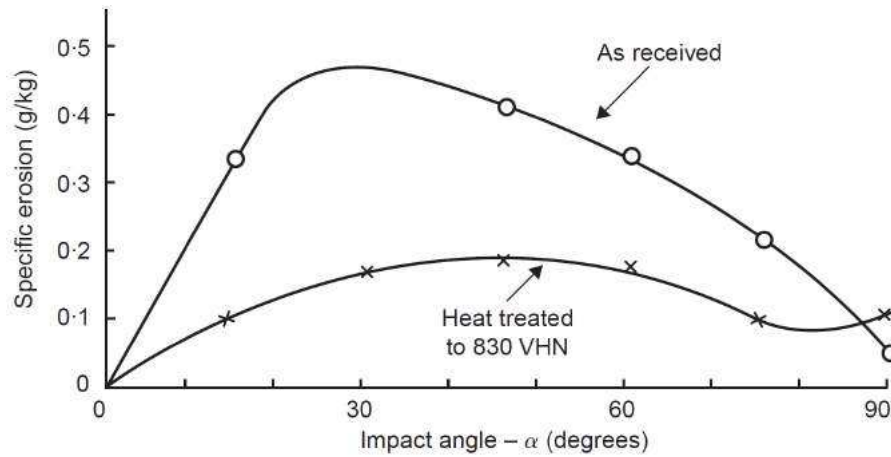


Figure 12 – Variation of specific erosion with impact angle for 'as received' and heat treated alloy tool steel. Adapted from (Mills and Mason (1987).)

3.2.1.6 Particle concentration

Particle concentration is a variable that has received little attention in basic research work on the subject (Duarte et al. (2015)). Concentrations investigated, however, have generally been very much lower than those encountered in pneumatic conveying, even with dilute phase conveying. In pneumatic conveying, the term used for particle concentration is generally solids loading ratio or mass loading. The mass loading is defined as $\eta = \dot{m}_p / \dot{m}_f$ where \dot{m}_p and \dot{m}_f are respectively the particle and fluid mass fluxes through the domain. Its particular advantages over particle concentration are that it is a dimensionless quantity and that its value does not vary with conveying air velocity or pressure, so that it remains essentially constant along the length of a pipeline.

3.2.1.7 Particle shape

The influence of particle shape on mass eroded has been reported by many researchers. The result is much as one might expect, for smooth and rounded particles do not cause as much erosion as sharp angular particles, under similar conditions of impact velocity and surface and particle hardnesses. For test work on the erosive wear of pipe bends in pneumatic conveying system pipelines there is generally a need to re-circulate the conveyed material. As a result of re-circulating the material, it degrades and the sharp angular corners and edges of the fresh material are gradually worn away, and they become more rounded and hence significantly less erosive (Mills and Mason (1977)). This is a major problem when test facilities are used to assess component life.

3.3 Elbow fitting

An elbow is a pipe fitting installed between two lengths of pipe or tubing to allow a change of direction, usually a 90° or 45° angle. A 90 degree elbow (Fig. 13) is also called

a "90 bend" or "90 ell" but in this thesis the name "standard elbow" is used in order to facilitate the treatment between the two pipelines studied. It is a fitting which is bent in such a way to produce 90 degree change in the direction of flow in the pipe. It is used to change the direction in piping and is also sometimes called a "quarter bend" (Mills (2004)). A 90 degree elbow attaches readily to plastic, copper, cast iron, steel and lead. It can also attach to rubber with stainless steel clamps. It is available in many materials like silicone, rubber compounds, galvanized steel, aluminum, etc. The main application of a standard elbow is to connect hoses to valves, water pressure pumps, and deck drains.



Figure 13 – Example of a 90 degree elbow.

Source: <<http://goo.gl/UznH03>>

Elbows are often used in oil and gas production systems, and they cause redistribution of gas and liquid which can affect distribution of corrosion inhibitors within and downstream of the bends. Elbows are also a location susceptible to the impact of particles along the outer radius (Vieira et al. (2014)).

By the very nature of the transport process, pipelines used for pneumatic conveying systems are prone to wear when abrasive materials have to be conveyed. In dilute phase, materials are conveyed in suspension in the air, and a high conveying air velocity must be maintained in order to keep the material moving, and so avoid pipeline blockage. The main problem relates to the wear of elbows in the pipeline, and any other surfaces where particles are likely to impact as a result of a change in flow direction. Elbows provide pneumatic conveying systems with their flexibility in routing, but if the material is abrasive and the velocity is high, rapid wear can occur.

3.3.1 Influence of elbow geometry on erosion

Elbows are available in a wide range of geometries, in terms of elbow curvature, from long radius elbows to tight elbows and mitered elbows. As elbows are so vulnerable

to wear, there have been many developments and innovations for reducing the problem (Santos et al. (2016)). Some authors have researched the subject over the years (Dutta et al. (2016), Ono et al. (2011), Tong et al. (1980)). Tong et al. (1980) investigated a wide range of elbow diameter ratio (D/d , where D is the elbow diameter and d is the pipe diameter) for a 90° mild steel elbows. The results are shown in Fig. 14. The elbows were eroded by sand, conveyed at a mass loading of two and with a conveying air velocity of 25 m/s .

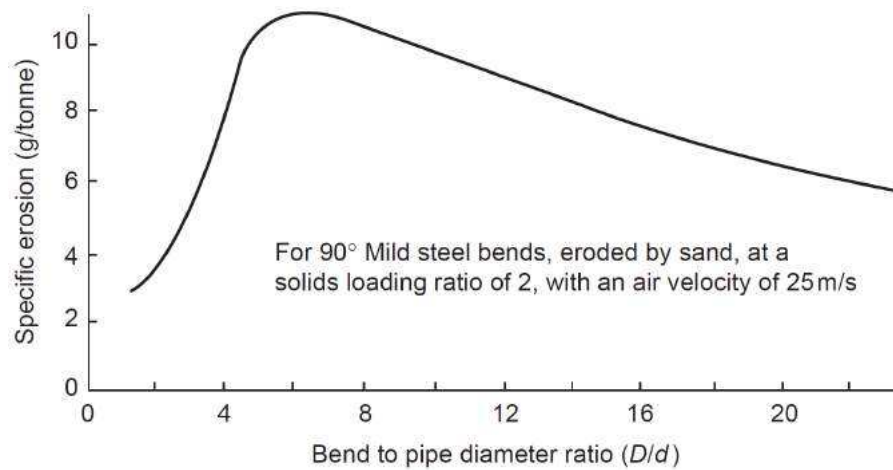


Figure 14 – The influence of elbow geometry on the erosive wear of pipeline elbows. Adapted from Tong et al. (1980).

With sharp bends, having a low D/d ratio, the majority of the particles will impact against the bend wall at a fairly steep angle. At a high impact angle erosive wear will not be too severe for a ductile material and so it can be expected that the bend will not wear too rapidly.

An elbow with a D/d ratio of about 6 corresponds closely to the worst case from the data in Fig. 14. The majority of the particles will impact against the bend wall at an angle of about 20° . For a ductile material this will result in maximum erosion and so the elbow can be expected to fail quickly. Particle impact against the wall for elbows with a D/d ratio greater than about 20 is at a much shallower angle. If the impact angle is relatively small the erosion will not be too severe, and so for this case also it can be expected that the elbow will not wear too rapidly.

3.3.1.1 Long radius elbows

Low impact angles is an essential pre-requisite for minimizing erosion, particularly in the case of brittle surface materials. In the case of ductile materials, because of the remarkably steep increase in erosion with very small increase in impact angle, as shown in Fig. 8, exceptionally long radius bends would be required (Zahedi et al. (2016)). It is possible to calculate the relationship between the elbow geometry (D/d) and the impact

angle (Tong et al. (1980)). The results of such an analysis are given in Fig. 15 and this clearly shows the nature of the problem.

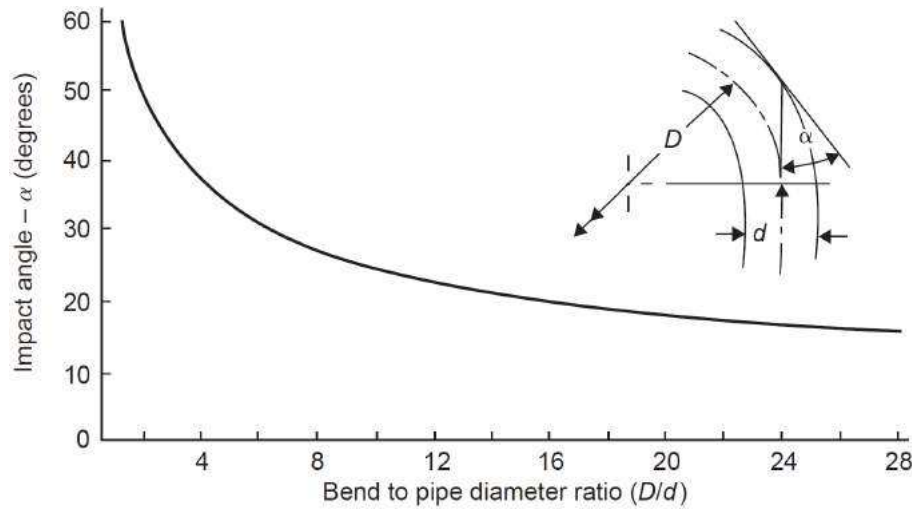


Figure 15 – The influence of elbow geometry on particle impact angle. Adapted from Tong et al. (1980).

For ductile materials long radius elbows are not likely to be a viable proposition. For brittle materials, however, such as basalt and cast iron, they are essential. A common method of providing a long radius elbows is to make the elbow in segments. By this means the elbow will be lighter and much easier to fit into the pipeline. Since the majority of the wear will be at the primary impact point only one or two sections need to be replaced should the elbow fail. It is also possible to reverse and interchange segments and so extend the overall life of the elbow.

3.3.1.2 Short radius elbows

In very short radius elbows, the angle at which the material impacts against the elbow wall will be fairly high, as shown in Fig. 15. Although this will not be suitable for brittle surface materials, ductile materials, because of their improved erosion resistance at high impact angle often gives reasonable service in use, if the conveyed materials is not too abrasive.

Two major problems have to be taken into account, however, before using very short radius and similar elbows (Mills (2004)). A short radius elbow will probably increase the conveying line pressure drop, which will mean that the material mass flow rate will have to be reduced to compensate. In addition, a very short radius elbow that are designed to trap the conveyed material, may require a slightly higher value of conveying line inlet air velocity to ensure that the pipeline does not block.

3.3.2 Methods to mitigate elbow erosion

The mitigation of the wear magnitude proven to be one of the critical factors for some machinery components. Erosive wear is frequently a key factor in defining or restricting the proper lifetime of a component. In addition, maintenance time and operating costs are also important factors that lead companies to decide on the best method for minimizing erosion in their equipment. With this in mind, some alternatives to the traditional elbow geometry are presented below.

3.3.2.1 Wear back methods

Wear back methods are potentially the cheapest and most effective means of suppressing erosion. A channel welded to the back of an elbow and filled with concrete, as shown in Fig. 16a, is probably the most common method adopted ([McKetta \(1995\)](#)). When the outer surface of the original steel elbow erodes, the concrete will generally extend the life of the elbow for a reasonably long time. It is essential however, that the wear back covers as much as possible of the outer elbow surface, for bends can be holed over a wide range of both elbow and pipe angles.

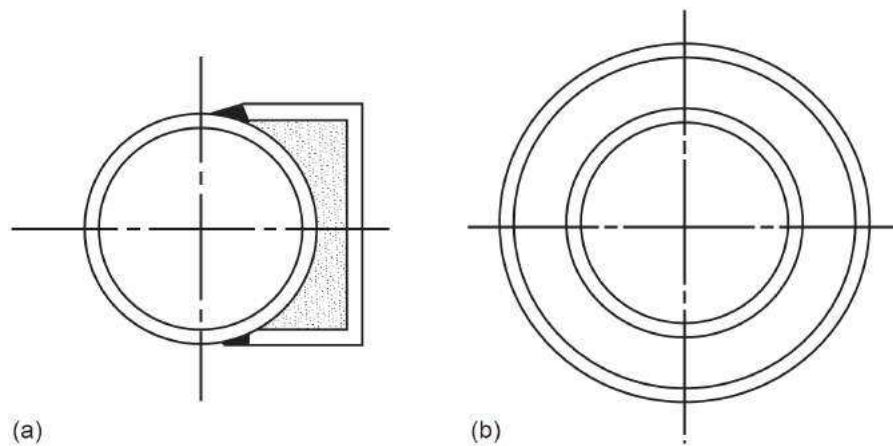


Figure 16 – Wear back methods of elbow reinforcement: (a) concrete filled channel and (b) pressure-tight sleeve over elbow. Adapted from [Mills \(2004\)](#).

The only problem with this type of solution is that when a primary wear point is established in the concrete at the initial impact point, deflection of particles can result, and these may cause erosion of the inside surface of the bend. The bend may well fail through erosion of the inside surface long before the material has penetrated the concrete. Secondary and tertiary wear pockets in long radius bends may also cause the material to be deflected against the wall of the following straight length of pipe and cause this to fail. A similar method of prolonging bend life is to sleeve the main elbow with another pressure-tight elbow, which is shown in Fig. 16b. When the inner bend fails the space will fill with the material being conveyed.

3.3.2.2 The use of inserts

Considerable protection can be provided for an elbow by positioning a sacrificial insert in the pipeline just prior to the elbow. An insert made of a flat strip twisted through 180° , for example, and shown in Fig. 17, will ensure that the material impacts against the insert prior to impact against the elbow. The velocity of the particles will be reduced after impact with the strip and the presence of the strip will prevent the particles from focusing on a small area of the bend. Such a strip should offer little resistance to flow and should last for a reasonable period of time, since the wear would be very evenly distributed over the entire surface of the strip ([Agarwal and Mills \(1989\)](#)).

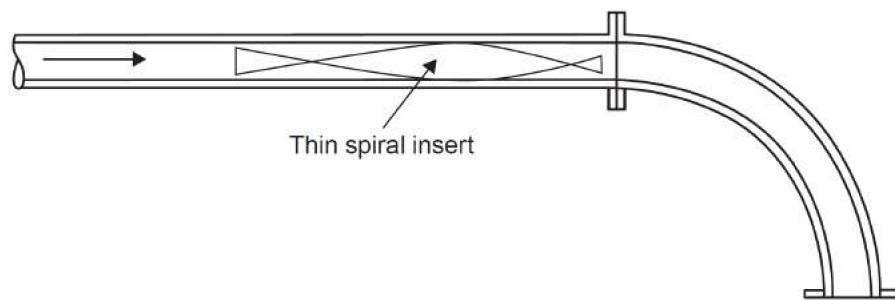


Figure 17 – Elbow protection by use of sacrificial inserts in preceding straight pipeline. Adapted from [Mills \(2004\)](#).

Recently, the insertion of a twisted tape upstream of the elbow was numerically investigated by the authors ([Santos et al. \(2016\)](#)). Fig. 18 shows the streamlines for the clean air flow. Clearly, a well-defined, swirling flow is generated by the insert.

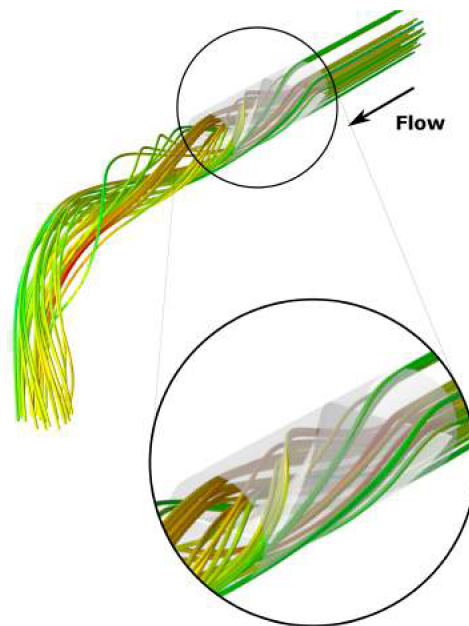


Figure 18 – Streamlines of the velocity field with twisted tape insert. Adapted from [Santos et al. \(2016\)](#).

In this case, the swirling motion imparted to the particles by the twisted tape reduces the maximum penetration ratio in the elbow. Despite the apparent advantage of the twisted tape regarding elbow erosion, the results show that the twisted tape itself becomes more susceptible to erosion.

3.3.2.3 Special elbows

Numerous different bends are available, to minimize erosion-related problems. Many of these are made of, or lined with, basalt, cast iron, rubber, etc, and some have a constant bore and a constant radius, as with conventional elbows. Another group of elbows that have been developed, specifically for pneumatic conveying system pipelines, have neither constant bore nor constant radius. Some of these bends are shown in Fig. 19. Care must be taken in selecting such bends, for account must be taken of their suitability for the material being conveyed and the pressure drop across the bend with that material (Agarwal and Mills (1989)).

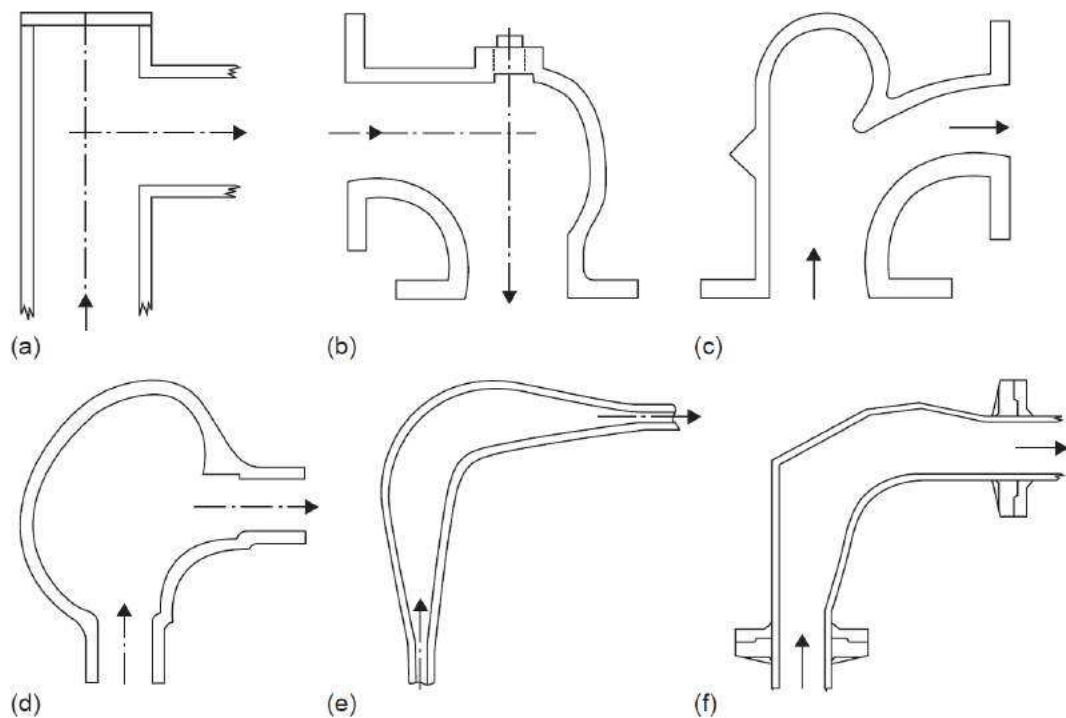


Figure 19 – Some special elbows developed for pneumatic conveying systems: (a) the blind tee, (b) the Booth elbow, (c) the vortice ell or vortex chamber elbow, (d) the flow bow, (e) the expanded elbow and (f) the gamma elbow. Adapted from Mills (2004).

With an abrasive material, the simple blind tee bend shown in Fig. 19a will probably last 100 times longer than an equivalent radiused elbow. It will ultimately fail around the inside corner due to turbulence. For abrasive materials, therefore, it is extremely effective, and can even be made out of scrap material. The blind end of the bend traps the conveyed material and so the oncoming material impacts against other material (Fig. 20), instead

of the bend, and thereby protects it. The penalty, however, is in the increased pressure drop that can result. Another problem with this type of bend is that the material that is trapped in the dead end of the bend may take a long time to be purged from the bend at the end of a conveying run. It could not, therefore, be used in pipelines required for the conveying of perishable and other time limited materials.

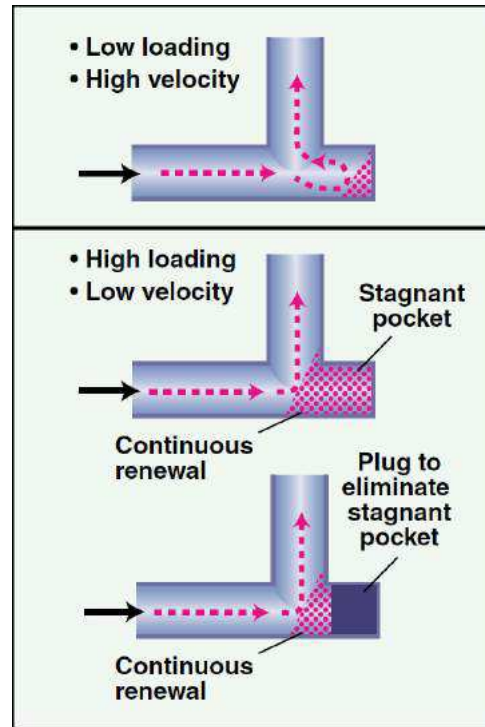


Figure 20 – The effect of loading and gas velocity on flow patterns in a blind tee (horizontal-vertical orientation). Adapted from [Dhodapkar et al. \(2009\)](#).

Figure 19b shows a more sophisticated version of the blind tee bend that was developed in the early 1970s and is known as the Booth bend after its originator. This is a very short radius cast elbow that incorporates a shallow depression. This allows material to collect in the bend and so subsequent material flowing through the pipeline will impact against itself. At the end of a conveying cycle the trapped material will be readily purged from the shallow depression in this elbow. A pipe plug is provided in the back of the elbow as it was well recognized that it is usually at elbows that pipelines become blocked.

Another, more recent version, shown in Fig. 19c, is the short radius bend with a large recessed chamber in the area of the primary wear point ([Paulson and Hess \(1983\)](#), [Hess \(1991\)](#)). It is claimed that this acts as a vortice and that material is constantly on the move in this pocket, thereby providing a cushioning effect to oncoming material that should reduce problems of erosive wear and material degradation. In a previous work, the authors investigated the use of a vortex chamber ([Duarte et al. \(2016\)](#)). Basically, it was found that the rotating fluid motion within the chamber (Fig. 21) maintains the particulate material continuously moving, thus protecting the elbow from direct particle

impacts.

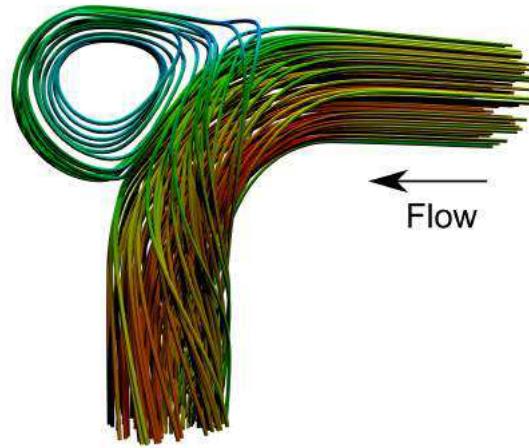


Figure 21 – Streamlines of the fluid velocity field inside the vortex chamber elbow. Adapted from [Duarte et al. \(2016\)](#).

The penetration ratio is decreased by a protecting layer of particles adjacent to the chamber wall, which absorbs the incoming particle impacts (Fig. 22). The vortex chamber elbow is an effective option, but depending on the application, the constant contact between the particles can increase the conveyed material breakup, which may not be interesting for moist, sticky and cohesive materials, for instance.

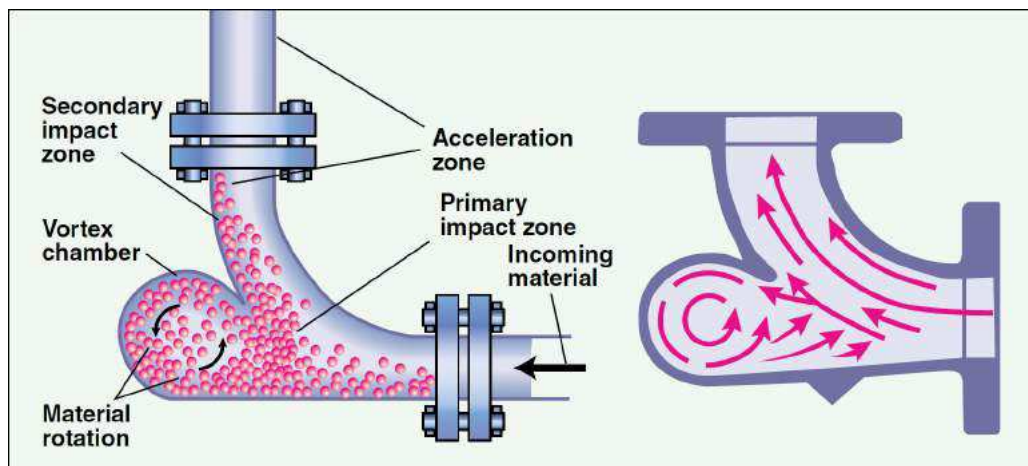


Figure 22 – A "vortex chamber" creates a circulating flow pattern or a pocket of material, which cushions the impact on incoming stream. Adapted from [Dhodapkar et al. \(2009\)](#).

It is suggested that the expanded elbow ([Paulson \(2005\)](#)), shown in Fig. 19e, will also help to reduce erosive wear and particle degradation ([Agarwal et al. \(2000\)](#)). Both of these operational problems are very significantly influenced by velocity. With the expansion to a larger section at the elbow the air velocity is significantly reduced, with a consequent

reduction in impact velocity of the particles against the elbow wall. The turbulence in the bend is so great that even if the velocity falls well below the minimum value for the material, the pipeline is unlikely to block, but material may be deposited in the bend and this will be difficult to purge clear.

Finally, the gamma elbow ([Storf and Lang \(1994\)](#)) in Fig. 19f was specifically developed to minimize the problems of "angel hair" formation that can occur with materials such as nylons and polymers when they slide around the wall of a conventional radiused elbow (Fig. 23).

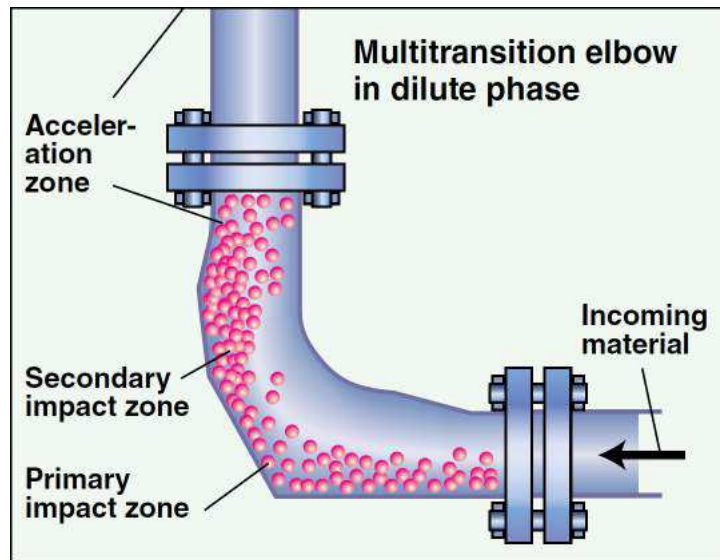


Figure 23 – In the gamma elbow design, accumulation of material in the primary impact zone prevents direct impact of material on the elbow wall, reducing erosive damage to the pipe. Adapted from [Dhodapkar et al. \(2009\)](#).

3.3.3 Experimental work in elbows in air-sand flows

There is not a large amount of published data on erosion problems in the field. Therefore, it becomes necessary to design and build experimental facilities to understand erosion phenomena under controlled conditions and develop and improve erosion prediction models ([Vieira et al. \(2016\)](#)).

The erosion of bends conveying a gas–solid mixture has been investigated by many researchers. Earlier experimental studies were carried out by [Bikbaev et al. \(1972\)](#). Basically, they found that the erosion rate increases as the inlet gas velocity and curvature ratio increase (Fig. 24).

They observed that higher particle velocities result in sharply increased gas abrasive wear rate even when particle concentration is reduced. This indicates the dominant role of particle velocity on wear rate of elbows.

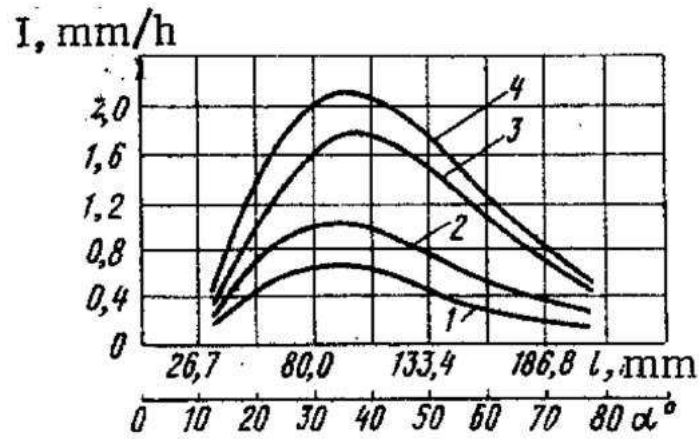


Figure 24 – Distribution of gas abrasive wear rate I along the length of the elbow l determined by angle α at various velocities V and stream concentrations. ($R_{av} = 128$ mm and $d = 50$ mm): 1) $V = 33.1$ m/sec, $\mu = 4.35$ kg/kg; 2) $V = 39.2$ m/sec, $\mu = 3.01$ kg/kg; 3) $V = 50$ m/sec, $\mu = 2.93$ kg/kg; and 4) $V = 54.8$ m/sec, $\mu = 2.10$ kg/kg. Adapted from [Bikbaev et al. \(1972\)](#).

[Tolle and Greenwood \(1977\)](#) studied the flow of gas/sand mixtures in tubulars for gas velocities of up to 30 m/s. Both high and low sand concentrations in air were used at different velocities in 50.8 mm standard elbows.

[Bourgoyne \(1989\)](#) studied experimentally the effect of flow velocity, liquid content, and sand concentration in standard elbows (Fig.25).

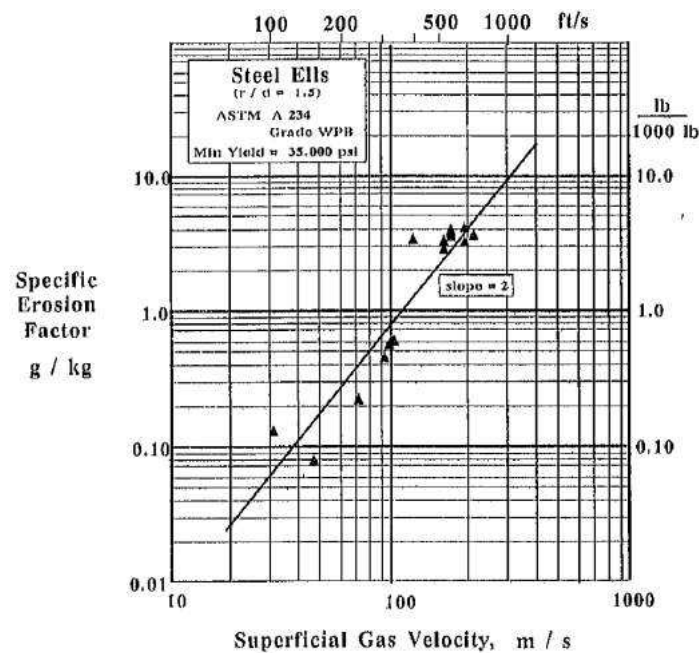


Figure 25 – Effect of gas velocity on rate of erosion for ASTM 234. Grade WPB Ells with $r/d = 1.5$ (Number 2 Blasting Sand). Adapted from [Bourgoyne \(1989\)](#).

[Chen et al. \(2004a\)](#) performed experimental erosion tests as well as numerical

simulations in an elbow and a plugged tee with 25.4 mm diameter. They found that the particle rebound model may have a significant impact on the particle trajectories as well as the erosion profile. For cases where the strong particle recirculation potentially occurs, such as in a plugged tee, the application of the stochastic particle rebound model is required to acquire realistic simulation results of erosion.

Mazumder et al. (2008) investigated the location and magnitude of maximum erosion in single-phase flows in a 25.4 mm elbow using aluminum and stainless steel specimens at different fluid velocities. The maximum erosion ratio at 34.1 m/s for 150 μm sand particles was measured at 55° from the inlet of the elbow.

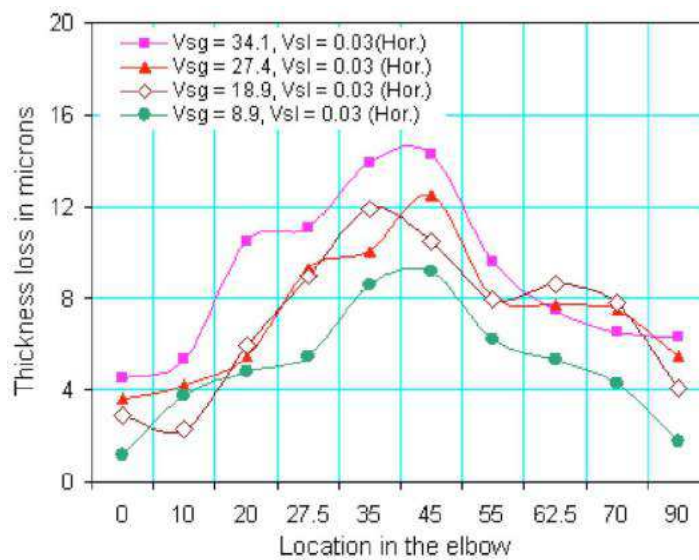


Figure 26 – Thickness loss profile of elbow specimen at different gas velocities, horizontal, $V_{sl} = 0.03$ m/s. Adapted from Mazumder et al. (2008).

They concluded that higher liquid velocity, the entrainment is higher in the gas core of annular flow. Therefore, a large number of sand particles entrained in the gas core impacts the elbow specimen surface at high velocity. The effect of this higher impact velocity is more significant than the assumed dampening provided by the thicker liquid film, resulting in higher erosion.

Evans et al. (1978) carried out an erosion study in high velocity gas systems at high pressure (6.89 MPa) in 101.6 mm long-radius elbows. Intrusive Electrical Resistance (ER) Probes were installed where the centerline of the elbow inlet intersects with the elbow surface. Similarly, extensive empirical information has been gathered at The Tulsa University Sand Management Projects (TUSMP) for examining sensitivity of ER probes in air flow with sand at atmospheric pressure conditions in 50.8mm ID and 76.2mm and 101.6mm elbows. In all of these experiments, standard elbow measurements were conducted at 45° and 90° to the flow orientation using 150 μm and 300 μm sand. Although these ER probe experiments provide valuable information for erosivity trend for many conditions,

all these experiments used ER probes at a fixed location. Also, the intrusive effect of ER probes could affect gas flow parameters inside the elbow.

Eyler (1987) studied the erosion pattern generated for gas-sand flow along the long bend of an elbow with $r/D = 3.25$ in a one dimensional sense. Ultrasonic and caliper instruments were used to obtain readings from 19 locations along the elbows long bend. Maximum wall loss was measured at the 35° position from the inlet to the elbow. Deng et al. (2005) studied erosion patterns on bends of pneumatic conveyors and utilized a handheld ultrasonic probe to determine the extent of wall loss. Measurements were obtained in a two-dimensional pattern instead of a one-dimensional line along the elbow's long bend. Kesana (2013) used a novel non-intrusive temperature compensated ultrasonic device to measure the metal loss at 16 different locations inside an elbow. Initially, experiments were performed with a single-phase carrier fluid (gas-sand) moving in a horizontal pipeline. Next, experiments were extended to the horizontal multiphase slug flow regime.

Solnordal et al. (2015) developed a new experimental procedure and presented the detailed surface map of erosion depth in a standard elbow by measuring hundreds of points with a surface profiler (Fig. 27).

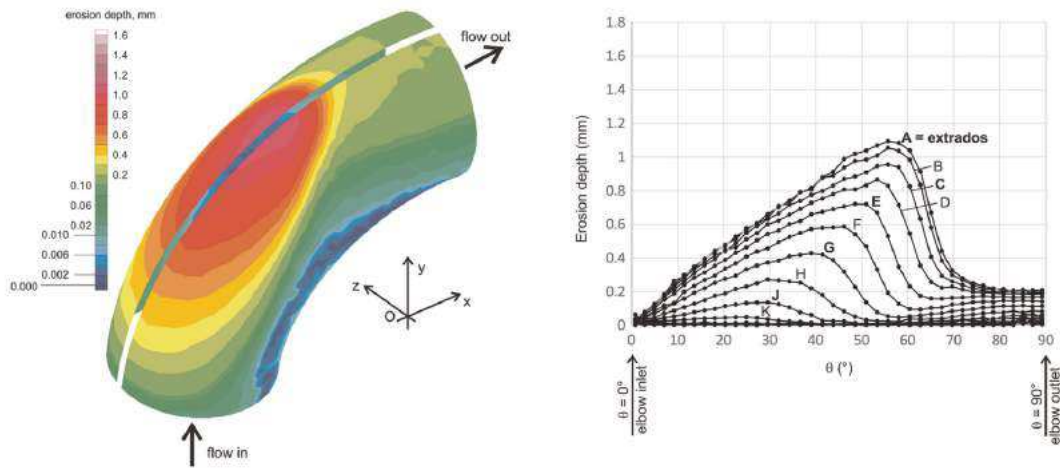


Figure 27 – Colour contour plots of experimentally determined erosion depth profile after 200 kg passage of sand; graphical representation of erosion depth profiles after 200 kg passage of sand. Adapted from Solnordal et al. (2015).

3.4 Solid particle erosion modeling

Due to industrial importance, there have been many studies regarding solid particle erosion available in the literature. While some of these studies investigated the phenomena experimentally, there are other studies which tried to describe solid particle erosion mathematically by proposing models. A complete review of the erosion equations developed over the years are presented below.

3.4.1 Erosion equations review

Most of the equations presented in this section have a large number of variables. Only the most important equations, from the author's point of view, will have such variables defined. If the reader has an interest in delving into a specific equation, he can access the original work through the citation markers. Such position will be adopted in order to maintain a pleasant reading of the thesis without losing the focus of the review.

[Finnie \(1960\)](#) proposed one of the earliest erosion equations that rather fundamentally investigated the erosion of solid particles on a material surface. In his study, he stated that erosion on surface of a material struck by solid particles depends on the motion of the particles and the material properties. He divided material into two categories: ductile where erosion is caused by plastic deformation and brittle where intersection of cracks is the main reason of erosion. Based on some assumptions, he proposed two equations to predict volume of removed material by a single abrasive grain for low and high particle striking angles as follows:

$$Q = \frac{mV^2}{p\psi K} \left(\sin(2\alpha) - \frac{6}{K} \sin^2(\alpha) \right) \text{ if } \tan(\alpha) \leq \frac{K}{6}$$

$$Q = \frac{mV^2}{p\psi K} \left(\frac{K \cos^2(\alpha)}{6} \right) \text{ if } \tan(\alpha) \geq \frac{K}{6}$$
(3.3)

For developing these equations, the following assumptions were made: i) the ratio of the depth of contact to the depth of cut is constant, ii) the width of particle cutting face is uniform and is large compared to the depth of cut, iii) constant plastic flow is reached upon impact of particles. This model predicts no erosion would occur for normal impingement of particles. [Finnie \(1960\)](#) also compared the predicted volume removal for a single abrasive grain with experimental data by many grains (Fig. 28) and stated that the single grain analysis can be used to predict erosion caused by many grains for low angle erosion.

[Bitter \(1963a\)](#) proposed repeated deformation and cutting as two mechanisms for erosion and developed two models to predict erosion rate caused by these two mechanisms for ductile and brittle materials. In the first part of his study, he developed an equation, based on balance of energy for a plastic-elastic collision, to predict erosion caused by the deformation mechanism:

$$W_D = \frac{1}{2} \frac{M(V \sin(\alpha) - K)^2}{\epsilon}$$
(3.4)

in which W_D is erosion in units volume loss, M and V are respectively total mass and velocity of impinging particles, (α is impact angle, K is a constant, which can be calculated

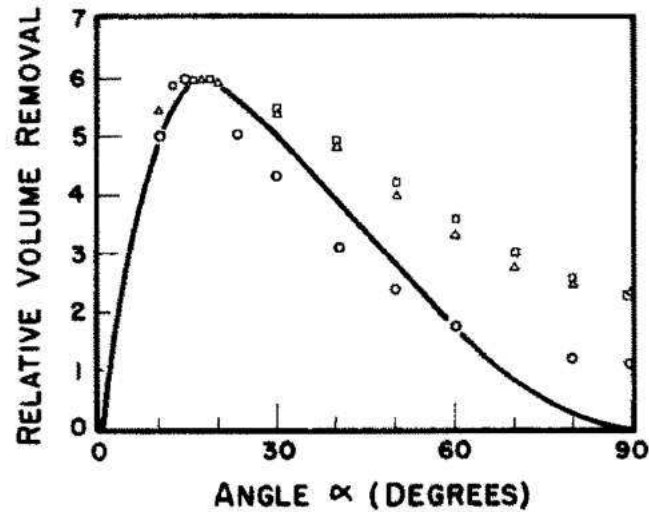


Figure 28 – Predicted variation of volume removal with angle for a single abrasive grain. Experimental points for erosion by many grains (\triangle copper, \square SAE 1020 steel, \circ aluminum) are plotted so that the maximum erosion is the same in all cases. Adapted from [Finnie \(1960\)](#).

from mechanical and physical properties and expresses the particle velocity at incipient erosion. ε represents the energy needed to remove a unit volume of material from the body surface and describes the plastic-elastic behavior of the substance.

He compared the model prediction with experimental data (Fig. 29) and reported that there is good agreement between the model prediction and the erosion data for brittle substances at different impact angles.

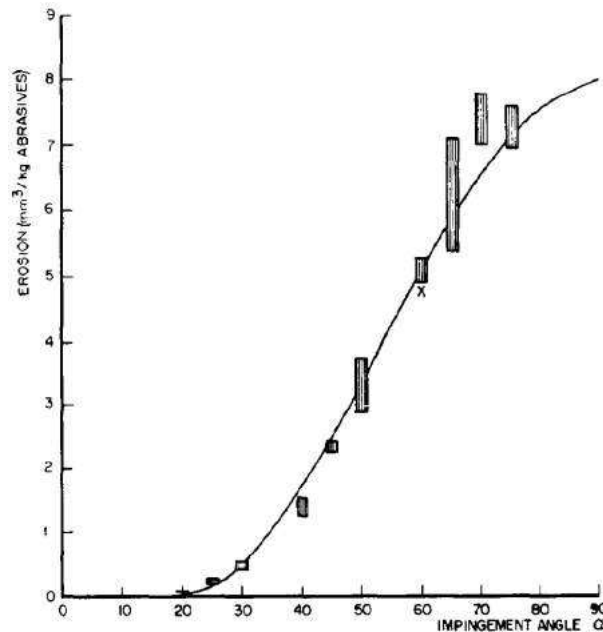


Figure 29 – Erosion tests on glass. $K = 318.7$ cm/sec; $V = 990.6$ cm/sec; X value used for calculating ε ; — theoretical curve; \boxplus test results (probability 95%). Adapted from [Bitter \(1963b\)](#).

In the second part of his study ([Bitter \(1963b\)](#)), he considered two scenarios for impacting particles including particles that still have a horizontal velocity component when they leave the body surface and particles with zero horizontal velocity component during the collision. He proposed two models for the cutting mechanism based on these scenarios as:

$$\begin{aligned}
 W_{C1} &= 2M \frac{C(V \sin(\alpha) - K)^2}{\sqrt{V \sin(\alpha)}} \left[V \cos(\alpha) - \frac{C(V \sin(\alpha) - K)^2}{\sqrt{V \sin(\alpha)}} \varrho \right] \text{ if } \alpha \leq \alpha_0 \\
 W_{C2} &= \frac{\frac{1}{2}M[V^2 \cos^2(\alpha) - K_1(V \sin(\alpha) - K)^{3/2}]}{\varrho} \text{ if } \alpha \geq \alpha_0
 \end{aligned} \tag{3.5}$$

Total erosion rate is the summation of erosion caused by these two mechanisms (repeated deformation and cutting):

$$W_t = W_D + W_{C1} \tag{3.6}$$

or

$$W_t = W_D + W_{C2} \tag{3.7}$$

[Neilson and Gilchrist \(1968\)](#) proposed two models for erosion prediction of particles at small and large angles of attack based on previous work by [Finnie \(1960\)](#) and [Bitter \(1963b\)](#). It was suggested that the normal component of kinetic energy of impacting particles causes deformation wear while the parallel component of kinetic energy causes cutting wear. He introduced deformation and cutting wear factors and suggested that total erosion on a surface is equal to the summation of erosion due to deformation and cutting mechanisms. In the following equations, the first term and the second term on the right hand side of the equations represent erosion caused by cutting and deformation, respectively.

$$\begin{aligned}
 W &= \frac{\frac{1}{2}MV^2 \cos^2(\alpha) \sin(n\alpha)}{\phi} + \frac{\frac{1}{2}M(V \sin(\alpha) - K)^2}{\varepsilon} \text{ if } \alpha < \alpha_0 \\
 W &= \frac{\frac{1}{2}MV^2 \cos^2(\alpha)}{\phi} + \frac{\frac{1}{2}M(V \sin(\alpha) - K)^2}{\varepsilon} \text{ if } \alpha > \alpha_0
 \end{aligned} \tag{3.8}$$

He concluded that further study is needed to define deformation and cutting wear factors.

[Finnie \(1972\)](#) modified his previous model ([Finnie \(1960\)](#)) to predict erosion for ductile metals. In that study, the parameters that may affect ductile erosion were listed and it was stated that not all these parameters can be implemented in a model (some of them are not controllable or measurable). He solved the equation of motion of an abrasive grain and proposed the following equation for erosion rate prediction:

$$V = \frac{cMU^2}{4p \left(1 + \frac{mr^2}{I}\right)} \left[\cos^2(\alpha) - \left(\frac{\dot{x}_t'}{U} \right) \right] \quad (3.9)$$

$$\dot{x}_t' = U \cos(\alpha) - \frac{2U}{P} \sin(\alpha) \quad (3.10)$$

[Finnie \(1972\)](#) discussed two possibilities that cease the cutting mechanism. The first possibility is that cutting terminates when the horizontal velocity component of particle tip is zero. The other possibility is that the particle leaves the surface while the tip is still moving horizontally. Based on these two possibilities, he further simplified the above equation to:

$$V = \frac{cMU^2}{4p \left(1 + \frac{mr^2}{I}\right)} [\cos^2(\alpha)] ; \dot{x}_t' = 0 \quad (3.11)$$

$$V = \frac{cMU^2}{4p \left(1 + \frac{mr^2}{I}\right)} \frac{2}{P} \left[\sin(2\alpha) - 2 \frac{\sin^2(\alpha)}{P} \right] ; \dot{x}_t' \text{ for } y_t = 0$$

This model has low accuracy as contact angle approaches 90°.

In another study, [Sheldon and Kanhere \(1972\)](#) developed an erosion model based on indentation hardness characteristics of materials for single particles. He used an empirical correlation between applied load and diameter of indentation proposed by [Meyer \(1908\)](#). It was assumed that this correlation is valid for erosion at low velocities and normal impact angle. By equating maximum value of kinetic energy to the work expended during indentation and using some algebraic simplifications and experimental data, he proposed the simple following model to predict material removal:

$$w = \frac{D^3 V^3 (\rho_p)^{3/2}}{H_v^{3/2}} \quad (3.12)$$

By comparing this model to experimental data it was claimed that the velocity exponent of 3 obtained in his model, matches more closely to experimental data rather than an exponent of 2 obtained by considering kinetic energy.

[Tilly \(1973\)](#) suggested a two-stage mechanism for erosion of ductile materials. The first stage of the erosion mechanism occurs when particles impact the target surface and

cut chips from it. The second stage of erosion is caused by particles impacting a target and they break up into small fragments around the primary scar caused by the first stage. The extent of fragmentation is a function of particle size and velocity, and based on that he introduced a particle size and velocity threshold below which no erosion occurs. For the primary erosion (stage one), he proposed a model based on an energy balance between the energy required to produce erosion, energy to produce elastic deformation and initial kinetic energy as follows:

$$\varepsilon_1 = \hat{\varepsilon}_1 \left(\frac{V}{V_r} \right)^2 \left[1 - \left(\frac{d_0}{d} \right)^{3/2} \left(\frac{V_0}{V} \right) \right]^2 \quad (3.13)$$

Tilly (1973) assumed that secondary erosion only happens when particles break up, and the extent of it is proportional to the extent of fragmentation and particle initial kinetic energy.

$$\varepsilon_2 = \hat{\varepsilon}_2 \left(\frac{V}{V_r} \right)^2 F_{d,v} \quad (3.14)$$

$$F_{d,v} = \frac{W_0 - W}{W_0} \quad (3.15)$$

Therefore, total erosion is a summation of erosion in stages one and two:

$$\hat{\varepsilon} = \varepsilon_1 + \varepsilon_2 \quad (3.16)$$

$$\hat{\varepsilon} = \hat{\varepsilon}_1 \left(\frac{V}{V_r} \right)^2 \left[1 - \left(\frac{d_0}{d} \right)^{3/2} \frac{V_0}{V} \right]^2 + \hat{\varepsilon}_2 \left(\frac{V}{V_r} \right)^2 F_{d,v} \quad (3.17)$$

Jennings et al. (1976) experimentally reported that melting of the target surface is a major mechanism of ductile material erosion. Based on this hypothesis, he employed dimensional analysis to develop a mathematical model considering the factors that resist and drive erosion phenomena:

$$\varepsilon = \frac{K_T^{5/2}}{R} \frac{G^{1/3}}{\rho_t^{1/3} k T_m \Delta H_m} \quad (3.18)$$

Hutchings et al. (1976) performed a series of experiments using steel spheres impacting mild steels and reported that their experimental test results successfully simulated erosion of sand particles on metals. They investigated the dependence of crater dimension to impact velocity and angle. A high speed photography technique was also employed to study the energy balance during an impact.

It was found that at 30° impact angle the mass of material removed varies according to the relation $W = 5.82 \times 10V^{2.9}$ where W is the mass removed (kg) per kg of impacting particles and V is the impact velocity (m s⁻¹).

Evans et al. (1978) studied the impact damage in brittle materials in the elastic-plastic response regime. They analyzed radial cracks (surface extension), lateral cracks (penetration) and fracture thresholds using a simplified discussion of impact dynamic features and fracture mechanics in order to characterize the fracture caused by the impact. They also proposed an erosion model by finding a relation between radial crack formation and fracture toughness of the target materials:

$$\hat{v}_1 \propto \frac{v_0^{19/2} R_p^{11/3} \rho_p^{1/4}}{K_c^{4/3} H^{1/4}} \quad (3.19)$$

A semi-empirical model to predict erosion rate at different impact angles and velocities was developed by Tabakoff et al. (1979). They assumed that the erosion process can be characterized by two mechanisms at small and large impingement angles. It was pointed out that the proposed model is applicable to small, intermediate and large impact angles as well as a combination of them. In their model, the effect of particle tangential restitution coefficient as a parameter that affects the erosion rate was taken into account:

$$\varepsilon = K_1 f(\beta_1) V_1^2 \cos^2(\beta_1) (1 - R_T^3) + f(V_{IN}) \quad (3.20)$$

$$R_T = 1 - 0.0016 V_1 \sin(\beta_1) \quad (3.21)$$

$$f(\beta_1) = [1 + CK \{K_{12} \sin(90/\beta_0) \beta_1\}]^2 \quad (3.22)$$

$$f(V_{IN}) = K_3 (V_1 \sin(\beta_1))^4 \quad (3.23)$$

where ε is the erosion per unit mass of impacting particles, β_1 the relative angle between particle path and specimen surface, β_0 the angle of maximum erosion, V_1 the particle velocity, R_T the tangential restitution ratio, $CK = 1$ for $\beta_1 \leq 3\beta_0$, and $CK = 0$ for $\beta_1 > 3\beta_0$.

Another mechanistic model to predict erosion rate for the erosion of metals impacted by spherical particles at normal angle was developed by Hutchings (1981). He proposed the

following model by formulating an energy balance equation between impacting particles and the metal surface:

$$E = 0.033 \frac{\alpha \rho \sigma^{1/2} v^3}{\varepsilon_c^2 P^{3/2}} \quad (3.24)$$

In this equation the properties of the target material are described by three quantities: the density, the dynamic hardness and ε_c , which may be called the "erosion ductility". The dynamic hardness of a metal may be calculated from measurements of indentations made by single spheres impacting at a suitable velocity and is therefore amenable to independent measurement, but the erosion ductility ε_c is not readily measured and must be derived, together with the ratio α , from experimental measurements of the erosion rate. The factor α/ε_c is therefore the only term in Eq. 3.24 which cannot be measured independently. It was also concluded that although dynamic hardness and ductility are included in the above equation, more investigation is needed to obtain their values and incorporate them in Eq. 3.24.

[Sundararajan and Shewmon \(1983\)](#) proposed an analytical expression for the erosion rate based on a localization concept. The localization concept suggests that there is strain at which plastic deformation on the target surface localizes causing lip formation called critical strain which in turn leads to material removal from the target surface or erosion. In the first step, they developed an expression for critical impact number by conducting algebraic calculations. There are four undetermined parameters in their erosion equation including critical strain (ε_f), mean strain increment ($\Delta\varepsilon_m$), deforming volume and an exponent. A constitutive equation for flow stress as a function of critical strain was proposed. They further simplified the constitutive equation using experimental data and finally proposed an equation for critical strain as a function of target specific heat and melting point. The [Tabor \(1951\)](#) relation was used to obtain an equation for mean strain increment. They also assumed that the plastic deforming volume is proportional to the crater volume and proposed the following erosion equation:

$$E = \frac{0.085 v^{2.5} \rho_b^{1/4} \rho_t^{1-q} \alpha (t+1)^{5a} \{1 - (t+1)/(t+2)\} F(t)}{6.06^q (1 - CT_c)^{1.25} \{n_c C_p T_m^{0.75} (1 - 436/T_m)^{0.75}\}^q (AH_s)^{1.25-q}} \quad (3.25)$$

where

$$q = (1 + 5a)P \quad (3.26)$$

and

$$a = \frac{0.25 n_c^{1-PS} (t+1)^S (AH_s)^{PS}}{\{6.06 \rho_t C_p T_m^{0.75} (1 - 436/T_m)^{0.75}\}^{PS}} \quad (3.27)$$

They also proposed an alternative form of the erosion model by using the critical number of impacts equation suggested by [Hutchings \(1981\)](#):

$$E_2 = \frac{3.6 \times 10^{-3} v^{3.0} \rho_b^{0.5} \alpha (t+1)^{6a} \rho_t^{1-u}}{(6.06)^u (1 - CT_c)^{1.5} \{N_c C_p T_m^{0.75} (1 - 436/T_m)^{0.75}\}^u (AH_s)^{1.5-u}} \quad (3.28)$$

where $u = (2 + 6a)P$.

They compared their model with experimental data, [Mamoun \(1975\)](#) and the [Hutchings \(1981\)](#) model (fatigue model) and reported that erosion rate predictions by the localization model are more accurate as compared to fatigue models. A simplified form of their erosion model was also proposed as

$$E \approx \frac{6.5 \times 10^{-3} v^{3.5} \rho_b^{0.25}}{C_p T_m^{0.75} H_s^{0.25}} \quad (3.29)$$

[Reddy and Sundararajan \(1986\)](#) conducted experiments on two ductile materials at a constant velocity of 40 m/s and three impact angles of 30, 60 and 90°. They reported that lip formation and fracture are the main erosion mechanisms based on scanning electron microscope (SEM) image analyses. It was shown that in contrast with previous studies, their results show maximum erosion at the normal impact angle. They also used a localization model to show that erosion rate is proportional to

$$E \propto \frac{L^3 \Delta \varepsilon_m}{\varepsilon_c} \quad (3.30)$$

[Johansson et al. \(1987\)](#) developed a statistical model to predict erosion rate of brittle single-crystal materials. He stated that the material removal caused by impact of solid particles on the surface of such materials is controlled by brittle fracture. Taking that into account, he recognized two different types of spalling mechanisms: lateral spalling and median spalling. When a particle impacts a surface, the spalled volume depends on spalled area and depth. Therefore, he assumed that the spalled areas and spalling depth is proportional to the plastic zone depth for lateral spalling and proportional to median crack extension for median spalling. The average spalled volume is equal to the summation of fraction of mass loss due to median spalling and lateral spalling. He developed a correlation between median crack size and plastic zone depth with material properties and proposed the following equation for the erosion rate. In this equation, maximum impact force is correlated to particle properties as

$$e = (1 - f) Y_4 \frac{\rho_t \rho_p^{2/9} E^{2/3} v_0^2 D^{2/3}}{H^{5/9} K_{Ic}^{4/3}} + f Z_4 \frac{\rho_t \rho_p^{1/3} E v_0^{8/3} D}{H^{1/3} K_{Ic}^2} \quad (3.31)$$

[Sundararajan \(1991\)](#) proposed a model to predict the erosion rate for ductile materials for all impact angles and different particle shape. The basic idea behind localization of plastic deformation is that there is a critical strain (ε_c) that causes lips to be formed on the surface rather than fracture. Therefore, erosion happens when this critical strain equals the critical strain for material removal. He suggested that for normal impact angle, the plastic work in the plastic zone is equal to the incident energy absorbed in plastic deformation based on a balance of energy in the plastic zone. He proposed the following equation for dimensionless erosion under normal impact by implementing the constitutive equation for plastic deformation:

$$E_n = \left(\frac{2^n C}{nC_p} \right) F(t) V^2 \sin^2(1 - e^2) \quad (3.32)$$

where e can be expressed as:

$$e = \frac{1.9H^{5/8}}{E_e^{1/2} \rho_p^{1/8} V^{1/4}} \quad (3.33)$$

He utilized the energy absorption relations developed by [Brach \(1988\)](#) into his previous localized plastic deformation model in order to predict erosion rate for oblique impact. Based on a balance of energy, it was suggested that the amount of dissipated energy in the shear zone caused by incident kinetic energy of an impacting particle is equal to plastic work which is required to strain lip volume from zero to the critical strain value (required to cause erosion). He used the dissipated energy equation proposed by [Brach \(1988\)](#) and obtained the following equation for erosion rate under oblique impact conditions:

$$V_{lip} = \left\{ \frac{C(m+1)mV^2}{2^{2-n}n\rho C_p(1+\lambda)} \right\} \left(\frac{\mu}{\mu_c} \right) \left(2 - \frac{\mu}{\mu_c} \right) \cos^2(\alpha) \quad (3.34)$$

Finally, it was suggested that the overall erosion rate is the summation of erosion rate at normal (Eq. 3.50) and oblique (Eq. 3.34) impact angles as:

$$E = \left(\frac{2^n C V^2 \sin^2 \alpha F(t)}{nC_p} \right) \left[1 + \left\{ \frac{(n+1) \left(\frac{\mu}{\mu_c} \right) \left(2 - \frac{\mu}{\mu_c} \right)}{4(1+\lambda) \tan^2 \alpha F(t)} \right\} - e^2 \right] \quad (3.35)$$

An empirical correlation to predict erosion rate for carbon steel with dry or wet surface was proposed at the University of Tulsa, Erosion/Corrosion Research Center (E/CRC) in 1994 by [Ahlert \(1994\)](#). The model is based on a series of direct impact

experiments for different particle shapes and impact angles for calculating the erosion ratio:

$$\varepsilon_m = 2.17 \times 10^{-7} \times (BH)^{-0.56} F_s V_p^{2.41} F(\alpha) \quad (3.36)$$

According to [Zhang et al. \(2007\)](#) particle impact angle function is defined as:

$$F(\alpha) = \sum_{i=1}^5 A_i \alpha^i \quad (3.37)$$

where the values of A_i and F_s and are suggested empirically.

A study of erosion in choke valves, which are widely used in oil and gas industry, was performed by [Haugen et al. \(1995\)](#). They used a general correlation of erosion and empirically determined the coefficients of the equation:

$$E = M_p K F(\alpha) V_p^n \quad (3.38)$$

They examined 28 different material types, and for each they varied impact speed and angle of attack and obtained empirical coefficients. Using the coefficients obtained for steel, a numerical simulation of the flow with Lagrangian particle tracking of sand particles was also performed. Good agreement between the proposed model and numerical simulation was reported in this study.

[Chen et al. \(1997\)](#) proposed a model for erosion at normal impacts based on a residual tensile stress mechanism. They assumed that residual tensile stresses cause material removal from the crater region and developed an equation for the ratio of removed volume to indentation volume. In the next step, based on the assumed mechanism for erosion, they used the [Johnson and Cook \(1985\)](#) fracture model to define the critical strain for erosion. They also used random walk theory along with an empirical correlation to estimate the mean number of impacts needed to cause material removal. Finally, inserting all the obtained equations into the [Hutchings \(1981\)](#) erosion model, the following equation was proposed to estimate erosion rate:

$$E = 0.064 \frac{\rho_t \rho^{1/2} V_0^3}{p^{-3/2} [D_1 + D_2 \exp D_3 \sigma^*]^2 [1 + D_4 \ln \varepsilon^*]^2 [1 + D_5 T^*]^2} \quad (3.39)$$

[Chen et al. \(1998\)](#) suggested a computational model to predict erosion rate using a general impact friction model. In fact, based on previous experimental studies of friction coefficient, they proposed a mathematical model to calculate friction coefficient called "general impact friction model". They modified the suggested governing equations of oblique impacts based on [Hutchings \(1981\)](#) study and combined them with the general

impact friction model. The modified equations were numerically solved to calculate velocity components and the critical impact angle. Having those parameters, they proposed the following equations to calculate deforming, cutting and total erosion rates:

$$E_D = \frac{T_y}{m_p \delta} = \frac{\sum m_p V_{pn} \Delta V_{pn}}{m_p \delta} \quad (3.40)$$

$$E_C = \frac{T_x}{m_p \chi} = \frac{\sum m_p V_{pt} \Delta V_{pt}}{m_p \chi} \quad (3.41)$$

$$T_t = T_x + T_y \quad (3.42)$$

$$E_v = E_C + E_D \quad (3.43)$$

Levin et al. (1999) proposed a model for solid particle erosion of ductile alloys. He stated that an accurate model to represent the mechanism of material removal, should take into account the effect of mechanical properties of the target and erodent, as well as the work hardening effect during the erosion process. As a result, it was stated that the portion of initial kinetic energy causing plastic deformation of the target material is a function of the ratio of particle rebound velocity to particle impact velocity called coefficient of restitution. This coefficient is also a function of mechanical properties of target material and particles. He proposed an erosion parameter based on energy loss during erosion incorporating mechanical properties of the alloys as well as the evolution of these properties during deformations.

$$E_m \propto E_{parameter} = \frac{m_p V_p^2}{2} \left\{ \frac{\left[1 - \left(\frac{3.05 H_t^{5/4}}{\rho_p V_p^{1/2}} \right) \left(\frac{1 - \mu_t^2}{E_t} + \frac{(1 - \mu_p^2)}{E_p} \right) \right]}{T L_v} \right\} \quad (3.44)$$

Oka et al. (2005) also proposed an empirical correlation similar to the E/CRC erosion equation. They modified the basic equation of dependence of erosion to impact velocity at the normal angle to take into account the effect of target material hardness, particle diameter and particle properties. The erosion rate is defined as the mass of removed material per unit of area per unit of time. It is calculated on the walls by accumulating the damage that each particle causes when colliding against the wall surface. It is given by:

$$E_f = \frac{1}{A_f} \sum_{\pi(f)} \dot{m}_\pi e_r \quad (3.45)$$

where A_f is the face area, \dot{m}_π is the particle mass flow rate represented by each computational particle that collides with the face and e_r is the erosion ratio, which is the ratio

of mass of eroded material over mass of erodent material, and must be computed by a correlation.

The erosion is formulated in terms of the penetration ratio according to the expression:

$$\text{Penetration Ratio} = \frac{E_f}{\dot{m}_p \rho} \quad (3.46)$$

where \dot{m}_p is the inlet sand mass flow rate (kg/s) and ρ is the eroded material density (kg/m³). The penetration ratio represents the thickness of material removed from the wall based on the mass of sand injected into the elbow.

The predictive equation for erosion damage proposed by [Oka et al. \(2005\)](#) can be written as:

$$E(\alpha) = g(\alpha) E_{90} \quad (3.47)$$

$E(\alpha)$ and E_{90} denote a unit of eroded material per mass of particles (mm³/kg). $g(\alpha)$ is the impact angle dependence expressed by two trigonometric functions and by the initial eroded material Vickers hardness number (Hv) in GPa, as in Eq. (3.48):

$$g(\alpha) = (\sin \alpha)^{n_1} (1 + \text{Hv} (1 - \sin \alpha))^{n_2} \quad (3.48)$$

n_1 and n_2 are exponents determined by the eroded material hardness and other impact conditions, such as particle properties and shape. These exponents show the effects of repeated plastic deformation and cutting action, and for particles of SiO₂-1 are expressed by:

$$n_1 = 0.71 (\text{Hv})^{0.14} \quad (3.49)$$

$$n_2 = 2.4 (\text{Hv})^{-0.94} \quad (3.50)$$

The reference erosion ratio E_{90} (erosion damage at normal impact angle) is related to the impact velocity, particle diameter and eroded material hardness, and can be expressed as follows:

$$E_{90} = K (a \text{ Hv})^{k_1 b} \left(\frac{u_p}{u_{ref}} \right)^{k_2} \left(\frac{D_p}{D_{ref}} \right)^{k_3} \quad (3.51)$$

u and D are the impact velocity (m s⁻¹) and particle diameter (μm), respectively, and u_{ref} and D_{ref} are the reference impact velocity and the particle diameter used in the

experiments by [Oka et al. \(2005\)](#). k_3 is an exponent which takes an arbitrary unit and is determined by the properties of the particle. The exponent k_2 can be determined by the eroded material Vickers hardness and the particle properties, as shown in Eq. (3.52)

$$k_2 = 2.3 (\text{Hv})^{0.038} \quad (3.52)$$

According to [Oka and Yoshida \(2005\)](#) the term $K (a \text{ Hv})^{k_1 b}$ is highly dependent on the type of the particle and eroded material Vickers hardness, which are not correlated with the impact conditions and other factors. The present work used the experimental data from [Oka and Yoshida \(2005\)](#) to derive a function and obtain the relationship between eroded material Vickers hardness and E_{90} at the reference impact velocity. The function obtained by the curve fitting shown in Fig. 11 of [Oka and Yoshida \(2005\)](#) for the pair SiO₂-aluminum is provided below:

$$K (a \text{ Hv})^{k_1 b} \approx 81.714 (\text{Hv})^{-0.79} \quad (3.53)$$

Is important to emphasize that this function holds for the pair sand-aluminum and may change for other materials. As a result, E_{90} can be expressed as follows:

$$E_{90} = 81.714 (\text{Hv})^{-0.79} \left(\frac{u_p}{u_{ref}} \right)^{k_2} \left(\frac{D_p}{D_{ref}} \right)^{k_3} \quad (3.54)$$

The purported theoretical strength of the [Oka and Yoshida \(2005\)](#) model is that the coefficients for a particular combination of eroded material and eroding material can be derived from more fundamental coefficients, which are specific to either the eroded material or the eroding material. Hence, the fundamental coefficients for sand can serve as a basis for both sand-steel erosion and sand-aluminum erosion, for instance. The fundamental coefficients for the eroding material, in turn, are shown to be derivable from measurable properties such as its Vickers hardness. Table 2 summarizes all [Oka and Yoshida \(2005\)](#) constants used in this work.

Table 2 – Parameters for the erosion model ([Oka and Yoshida \(2005\)](#)).

Eroded material type	Aluminum (6061-T6)
Eroded material Vickers hardness (H_v)	1.049 Gpa
Particle type	Angular SiO ₂ -1
Reference impact velocity (u_{ref})	104 m/s
Reference particle diameter (D_{ref})	326 μm
k_2	2.3042
k_3	0.19
n_1	0.7148
n_2	2.2945

A phenomenological model for erosion was proposed by [Huang et al. \(2008\)](#). They pointed out that particle impact on a target produces normal and tangential directions which cause deformation. They considered the normal component of the force being responsible for "deformation damage removal" and tangential component for "cutting removal". Considering the normal force, they found equations for maximum width and depth of indentation using the equation of motion in the normal direction. Having those parameters, an equation to calculate elementary indentation volume was suggested. They also derived an equation to calculate the average strain introduced into the surface by normal impact. On the other hand, a cutting profile to calculate cutting volume caused by the tangential force as a function of maximum cutting width, depth and length was suggested. They used the [Coffin \(1954\)](#) and [Manson \(1953\)](#) equation along with a critical strain equation to calculate the deformation damage removal:

$$\varepsilon_{VD} = C_1 \frac{m_p \rho_p^{\frac{1}{4b}} (V_p \sin(\alpha))^{(2+\frac{1}{2b})}}{\varepsilon_C^{1/b} P^{(1+\frac{1}{4b})}} \quad (3.55)$$

For real cutting removal by a particle, they assumed it is proportional to the cutting volume but inversely proportional to the material ductility:

$$\varepsilon_{VC} = \frac{C_2 m_p^{(1+\frac{3(1-n_s)}{4})} V_p^{(2+\frac{3(1-n_s)}{2})} (\cos(\alpha))^2 (\sin(\alpha))^{\frac{3(1-n_s)}{2}}}{d_p^{\frac{(1-n_s)}{4}} \varepsilon_0^i p_t P_n^{\frac{3(1-n_s)}{4}}} \quad (3.56)$$

They finally suggested the following equation to predict total volume loss by summing the deformation damage removal and cutting removal as

$$\varepsilon_{VT} = \varepsilon_{VC} + \varepsilon_{VD} \quad (3.57)$$

It was emphasized that the proposed erosion takes into account the effect of particle mass, size, shape and speed as well as impact angle and target material properties. A simplified version of Eq. 3.56 was also proposed for situations where solid transport impact angle is small and cutting wear is the dominant erosion mechanism as

$$\varepsilon_V = \frac{\varepsilon_{VT}}{m_p} \approx C_2 \rho_p^{0.1875} d_p^{0.5} V_p^{2.375} (\cos(\alpha))^2 (\sin(\alpha))^{0.375} \quad (3.58)$$

[Nsoesie et al. \(2014\)](#) using experimental data modified the previous model of [Sheldon and Kanhere \(1972\)](#) which is based on indentation hardness theory. They experimentally investigated the erosion rate for five Stellite alloys at two different impingement angles and two velocities (Fig. 30).

Their experimental measurements showed a higher rate of erosion for Stellite alloys in comparison to [Sheldon and Kanhere \(1972\)](#) model predictions. It was reported that

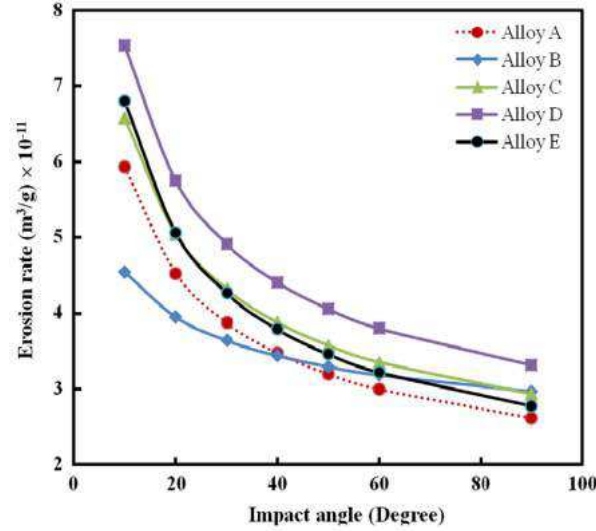


Figure 30 – Predicted erosion rates at various particle impingement angles using the modified S-K model: at 98 m s⁻¹ particle impact velocity. Adapted from Nsoesie et al. (2014).

since the Sheldon and Kanhere (1972) model was developed based on experimental data of aluminum and aluminum is more ductile than Stellite alloys, it under predicts critical velocity for Stellite alloys. Based on these observations, they introduced an order correction factor in the model. They also further modified the model to take into account the effect of impingement angle. The impingement angle correction factor includes two empirical constants called shifting coefficient (A) and shifting exponent (B) which are target material dependent. The final form of their equation is

$$w_1 = \frac{C1D^3(V(A(\sin(\alpha/2))^{1/3})^B)^3\rho_p^{3/2}}{H_v^{3/2}} \quad (3.59)$$

While some of these models have been validated with solid particle erosion data, many of these models did not consider sand erosion. It is noted from the above, that none of these models address the effects of the carrier fluid. The presence of sand particles in fluids is the primary cause of erosion damage and the reduction of production rate is one of the management methods used to avoid erosion damage. In this case, the maximum velocity is restricted to a threshold value called erosional velocity (the velocity above which excessive erosion may occur). As a result, sand production rate and impact velocities decrease likewise the erosion rate. Obviously, decreasing the production rate involves financial consequences.

Among all the erosion models presented during this revision, it is important to note that the erosion model proposed by Oka and Yoshida (2005) can take into account, for instance, the particle shape (see Eqs. 3.49 and 3.50) and diameters (see Eq. 3.51), differing from other models. In this sense, the authors believe that this erosion model

will be able to accurately reproduce complex erosive situations once improvements on non-spherical particle modeling interactions are feasible. In addition, previous works from [Pereira et al. \(2014\)](#) and [Duarte et al. \(2015\)](#) showed that the model proposed by [Oka and Yoshida \(2005\)](#) for the erosion ratio is the most suitable for the erosion prediction when the pair sand-aluminum is dealt with. Therefore, this model will be used in the present thesis working alongside the fluid and the particle models.

3.4.2 Particle wall rebound models

Incorporating a particle-wall rebound model is essential in erosion simulations, since a particle can impact a wall multiple times. Researchers proposed different correlations for the coefficients of restitution based on the particle characteristics and the impact conditions. In order to obtain an accurate prediction of the particle trajectories, it is necessary to select a particle restitution model. Conversely, knowledge on how particles behave after collisions with walls is needed. Upon collision, the particle loses energy, and the rebound velocity is lower than the particle incident velocity. This effect is taken into account through the coefficients of restitution. In this work, three different models were used, all of them being derived from experimental studies.

The model proposed by [Forder et al. \(1998\)](#) for the normal and parallel coefficients of restitution is given, respectively, by:

$$e = 0.988 - 0.78\alpha + 0.19\alpha^2 - 0.024\alpha^3 + 0.0027\alpha^4 \quad (3.60)$$

$$e_{par} = 1 - 0.78\alpha + 0.84\alpha^2 - 0.21\alpha^3 + 0.028\alpha^4 - 0.022\alpha^5 \quad (3.61)$$

where α is the particle incidence angle in radians.

[Grant and Tabakoff \(1975\)](#) proposed the model after treating the post collisional particle movement dynamics in a statistical approach. Based on experimental data on aluminum and sand, they proposed the following coefficients:

$$e = 0.993 - 1.76\alpha + 1.56\alpha^2 - 0.49\alpha^3 \quad (3.62)$$

$$e_{par} = 0.998 - 1.66\alpha + 2.11\alpha^2 - 0.67\alpha^3 \quad (3.63)$$

[Sommerfeld and Huber \(1999b\)](#) proposed a model for the normal coefficient of restitution only, regarding the parallel component equal to one. The reason for that is the

low contribution of the parallel component on the reflection of particles after collision. The correlation for the normal restitution coefficient is given by:

$$e = \max(1 - 0.013\alpha, 0.7) \quad (3.64)$$

Since the present study deals with sand-aluminum material pair, the most suitable coefficient of restitution model is the one proposed by [Grant and Tabakoff \(1975\)](#). Obviously, if another pair of materials is considered in the simulations, such model need to be changed.

3.4.3 Coefficients of friction

Friction is another important effect to be accounted in particle-wall interactions. Depending on the static (μ_s) and dynamic (μ_d) coefficients, particles can lose energy and momentum, directly affecting the erosion. For validation purposes, $\mu_s = 0.45$ and $\mu_d = 0.30$ were adopted, as it was seen to provide the best fit to the experimental results. A detailed revision of the effects regarding the friction modification will be presented in Sec. 7.2.2.4.

Chapter 4

Mathematical models

It is clear that many different simulations techniques are available for the present study. However not every technique is suitable for the type of flow being solved. Based on the type of flow, assumptions can be made that simplify the flow equations. This leads to a set of equations that should resolve the flow field with sufficient accuracy while using the computational resources as effective as possible.

This chapter presents the mathematical models that should be sufficient for the current study. For the gas phase solution, the URANS method with a Reynolds Stress model and a two-layer k-epsilon turbulence models is employed. The particulate phase is treated in a Lagrangian framework, having the equation of motion based on Newton's second law. Every technique and model will be detailed separately.

The chapter is structured as follows. First, Section 4.1 presents the flow equations. Finally, Section 4.2 shows the particle motion equations.

4.1 Gas phase equations

Simulations of fluids are based on the Navier Stokes Equations (NSE). In index notation the continuity and Cauchy momentum equation are respectively,

$$\frac{\partial \rho}{\partial t} + \frac{\partial(\rho u_i)}{\partial x_i} = 0 \quad (4.1)$$

$$\frac{\partial(\rho u_i)}{\partial t} + \frac{\partial(\rho u_i u_j)}{\partial x_j} = -\frac{\partial p}{\partial x_i} + \frac{\partial \tau_{ij}}{\partial x_j} + f_i \quad (4.2)$$

where p is the pressure, ρ is the fluid density, u_i represents the i component of the velocity vector, τ_{ij} denotes the molecular viscous tensor and f_i is the component i of the source term.

For a Newtonian fluid, where ν represents the the kinematic viscosity of the fluid, the tensor is modeled with the Stokes model of viscous stress,

$$\tau_{ij} = \nu \left(\frac{\partial u_i}{\partial x_j} + \frac{\partial u_j}{\partial x_i} \right) - \frac{2}{3} \mu \delta_{ij} \vec{\nabla} \cdot \vec{V} \quad (4.3)$$

For the present study, a unsteady-state and incompressible flow is assumed. External forces such as gravity forces and source terms due to phase interaction (Su_{ip}) are added to the momentum equation. Now, the continuity and momentum equations are,

$$\frac{\partial(\rho u_i)}{\partial x_i} = 0 \quad (4.4)$$

$$\frac{\partial(\rho u_i)}{\partial t} + \frac{\partial(\rho u_i u_j)}{\partial x_j} = -\frac{\partial p}{\partial x_i} + \frac{\partial}{\partial x_j} \left[\nu \left(\frac{\partial u_i}{\partial x_j} + \frac{\partial u_j}{\partial x_i} \right) \right] + Su_{ip} + \rho g_i \quad (4.5)$$

The above presented set of equations allows the assessment of the flow behavior. Hence the flow contains turbulent kinetic energy (E) that is distributed over eddies with varying sizes. When all the turbulence is resolved, the mesh should be fine enough to capture even the smallest eddies. This technique is called Direct Numerical Simulation (DNS). However with the current available hardware this is only possible with very simple geometries and low Reynolds number flows. In order to get a clearer view of which eddies are resolved using various methods, a logarithmic plot of this energy with respect to the reciprocal of the Eddy size, the wavenumber (k), is given in Fig. 31.

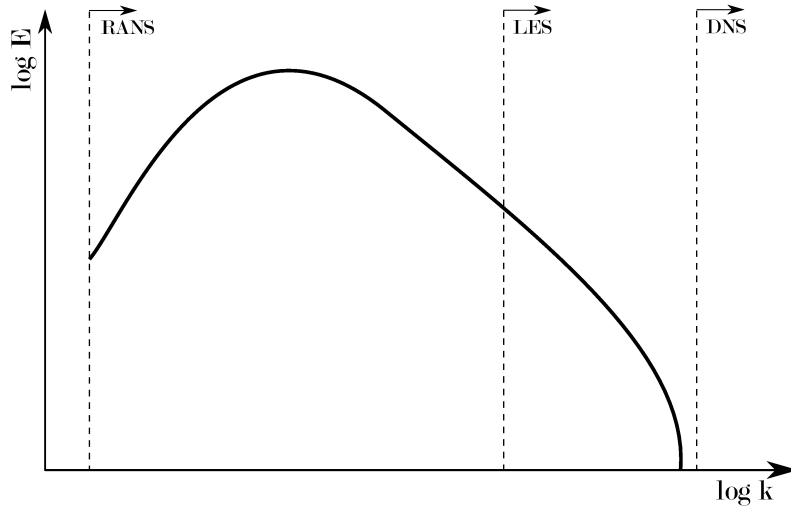


Figure 31 – The turbulent kinetic energy distributed over eddies of different sizes ([Fröhlich and Terzi \(2008\)](#)).

From this figure it can be seen that DNS resolves all the turbulent kinetic length scales and thus all the turbulence. On the other hand RANS simulations model all the

turbulence and thus non of the eddies are resolved. It can be seen that most of the kinetic energy is located in the large eddies. Large Eddy Simulation (LES) is based on this fact and resolves the large scales while the small scales are approximated using mathematical models. In some regions of a flow field, like the boundary layer, the large eddies become very small as well, requiring very small cell sizes.

For the current study, a confined flow is considered. Since high Reynolds number is present and complex flow phenomena occur, DNS is not an option for solving the flow. LES is also discarded as an option due to its high computational costs. Since URANS uses the least computational resources while still providing sufficiently accurate results, the main focus lies on this technique. The next section shows more detail about this method.

4.1.1 Unsteady Reynolds Averaged Navier Stokes simulations

Reynolds (1895) derived a statistical approach to approximate the Navier Stokes Equations. By time averaging the equations, only the mean properties of the flow remain. According to Reynolds, for most turbulent flows only these averages characteristics are of interest. The quantities present in the NSE are split into a mean and a fluctuating component. For the velocity this yields in index notation the following,

$$u_i(\vec{x}_i, t) = \bar{u}_i(x_i) + u'_i(x_i, t) \quad (4.6)$$

for which holds that,

$$\overline{u'_i}(x_i, t) = 0 \quad (4.7)$$

Replacing all time varying quantities in the simplified NSE, as derived in the previous section, with this definition and rearranging the terms yields for the continuity and momentum equation in index notation,

$$\frac{\partial \bar{u}_i}{\partial x_i} = 0 \quad (4.8)$$

$$\frac{\partial (\bar{u}_i \bar{u}_j)}{\partial x_j} = -\frac{1}{\rho} \frac{\partial \bar{p}}{\partial x_i} + \frac{\partial}{\partial x_j} \left[\nu \left(\frac{\partial \bar{u}_i}{\partial x_j} + \frac{\partial \bar{u}_j}{\partial x_i} \right) - \overline{u'_i u'_j} \right] + S u_{ip} \quad (4.9)$$

From the equations above it can be seen that for three-dimensional flow, four equations and ten unknowns are present. Besides three unknown velocity components and the pressure, the later equation contains an additional six unknowns. These are included in the Reynolds stress tensor,

$$\overline{\tau_{ij}} = -\overline{u'_i u'_j} \quad (4.10)$$

The Reynolds stress tensor has to be modeled in order to solve the URANS equations, which is also known as turbulence modeling. The quality of solution depends largely on the quality of the applied turbulence model. Section 4.1.2 describes the models employed for the current research.

4.1.2 Turbulence closure model

The Reynolds stress tensor, $\overline{\tau_{ij}}$, is often approximated by the Boussinesq (1877) hypothesis in order to link the Reynolds stresses with the mean velocity gradients. This approximation is formulated as follows,

$$\overline{\tau_{ij}} = -\nu_t \left(\frac{\partial \bar{u}_i}{\partial x_j} + \frac{\partial \bar{u}_j}{\partial x_i} \right) + \frac{2}{3} k \delta_{ij} \quad (4.11)$$

In this equation both the kinematic Eddy viscosity, ν_t and the turbulent kinetic energy, k , are unknown. Closure models provide a means to compute these extra quantities by introducing extra equations. The models can be classified into four different types; algebraic models, one equation models, two equation models and second moment closure models. Thereof, according to Wilcox (1994), for URANS simulations the two equation models are the most popular. On the other hand, when a Detached Eddy Simulation (DES) simulation is performed, often a one equation model is employed. The term one or two equation turbulence model implies that one or two extra transport equations are used for the formulation that are related to ν_t and k .

For URANS simulations the best choice is to use the $k - \epsilon$ or the $k - \omega$ turbulence model. These models solve two extra transport equations. One for k and one for ϵ or ω . These extra variables relate to ν_t for the $k - \epsilon$ model as,

$$\nu_t = C_\mu \frac{k^2}{\epsilon} \quad (4.12)$$

and for $k - \omega$ as,

$$\nu_t = \frac{k}{\omega} \quad (4.13)$$

On the other hand, the Reynold's Stress Models (RSM), also known as the Reynold's Stress Transport (RST) models, are higher level, elaborate turbulence models. The method of closure employed is usually called a *Second Moment Closure*. This modeling approach originates from the work by Launder and Sharma (1974). In RSM, the Reynolds stresses are directly computed. The exact Reynolds stress transport equation accounts for the directional effects of the Reynolds stress fields.

For this thesis, a Reynolds stress model (Chapter 8) and a variation of the $k - \epsilon$ (Chapter 7) are used. Both will be discussed in details in the following subsections.

4.1.2.1 Two layer $k - \epsilon$ closure model

The most famous model of the two is the $k - \epsilon$ model of which the standard is set by [Jones and Launder \(1972\)](#). In this formulation the second transport variable used is the turbulent kinetic energy dissipation ϵ . In literature the method is often referred to as the Standard $k - \epsilon$ model. When applying the Standard $k - \epsilon$ model, usually the closure coefficients published in [Launder and Sharma \(1974\)](#) are used.

The two layer $k - \epsilon$ model is employed, as it can handle well both the core flow and the near wall region. Essentially, it consists in solving the standard model for the turbulent flow region and a one equation model for the region affected by the viscosity. In the one equation $k - \epsilon$ model, the balance equation for k is retained, whereas ϵ is computed from,

$$\epsilon = \frac{k^{3/2}}{l_\epsilon} \quad (4.14)$$

The length scale that appears in Eq. (4.14) is computed from,

$$l_\epsilon = y C_l (1 - e^{-Re_y/A_\epsilon}) \quad (4.15)$$

In Eq. (4.15), Re_y is the turbulent Reynolds number, defined as:

$$Re_y = \frac{\rho y \sqrt{k}}{\mu} \quad (4.16)$$

where y is the distance from the wall to the element centers. This number is the demarcation of the two regions, fully turbulent if $Re_y > Re_y^*$, $Re_y^* = 200$ and viscosity-affected, $Re_y < 200$. For the one equation model, the turbulent viscosity is computed from,

$$\mu_{t,2layer} = \rho C_\mu l_\mu \sqrt{k} \quad (4.17)$$

The length scale in the equation above is computed as below:

$$l_\mu = y C_l (1 - e^{-Re_y/A_\mu}) \quad (4.18)$$

In UNSCYFL3D code, both the standard $k - \epsilon$ and the one equation model described above are solved over the whole domain, and the solutions for the turbulent viscosity

and the turbulence kinetic energy dissipation rate provided by both models are smoothly blended,

$$\mu_t = \lambda_\epsilon \mu_{t,standard} + (1 - \lambda_\epsilon) \mu_{t,2layer} \quad (4.19)$$

A blending function, λ_ϵ , is defined in such a way that it is equal to unity far from walls and is zero very near walls. The blending function used here is,

$$\lambda_\epsilon = \frac{1}{2} \left[1 + \tanh \left(\frac{Re_y - Re_y^*}{A} \right) \right] \quad (4.20)$$

The constant A determines the width of the blending function,

$$A = \frac{0.20 Re_y^*}{\text{artanh}(0.98)} \quad (4.21)$$

The purpose of the blending function λ_ϵ is to prevent solution divergence when the solution from both the standard and the one-equation models do not match. The constants in the length scale formulas, Eqs. (4.15) and (4.18), are taken from:

$$C_l = 0.4187 C_\mu^{-3/4} \quad A_\mu = 70 \quad A_\epsilon = 2C_l \quad (4.22)$$

Since no wall-functions are used, it is very important to refine the grid so as to have $y^+ < 1$ in the first element away from the wall and ensure accurate results for the fluid flow.

4.1.2.2 Reynolds stress closure model

The most physical URANS turbulence models are the Reynolds Stress Transport Models (RSTM). These models are based on the exact transport equation for the Reynolds stress tensor, which is given by

$$\begin{aligned} \frac{\partial(\overline{\rho u'_i u'_j})}{\partial t} + \frac{\partial(\overline{\rho u'_k u'_i u'_j})}{\partial x_k} = & -\frac{\partial}{\partial x_k} [\overline{\rho u'_i u'_j u'_k} + \overline{p(\delta_{kj} u'_i + \delta_{ik} u'_j)}] + \frac{\partial}{\partial x_k} \left[\mu \left(\frac{\partial \overline{u'_i u'_j}}{\partial x_k} \right) \right] \\ & - \rho \left(\overline{u'_i u'_k} \frac{\partial \overline{u'_j}}{\partial x_k} + \overline{u'_j u'_k} \frac{\partial \overline{u'_i}}{\partial x_k} \right) + \overline{p \left(\frac{\partial u'_i}{\partial x_j} + \frac{\partial u'_j}{\partial x_i} \right)} - 2\mu \overline{\frac{\partial u'_i}{\partial x_k} \frac{\partial u'_j}{\partial x_k}} \end{aligned} \quad (4.23)$$

Each term in the above equation represents a physical transport process, disregarding the first term, which is the local time derivative. From left to right: local time derivative, advection, turbulent diffusion, molecular diffusion, stress production, pressure-strain, and turbulent dissipation.

Some terms in the equations of the Reynolds stresses need to be modeled, since the solution is very complex. The modeling of turbulent diffusion, which is a third-order moment, produces a fourth-order moment. The modeling of a fourth order moment produces a fifth order moment, and so on. In this context, the turbulent diffusion transport can be modeled as follows (Lien and Leschziner (1994)),

$$\frac{\partial}{\partial x_k} [\overline{\rho u'_i u'_j u'_k} + \overline{p(\delta_{kj} u'_i + \delta_{ik} u'_j)}] = \frac{\partial}{\partial x_x} \left[\frac{\mu_t}{\sigma_k} \left(\frac{\partial \overline{u'_i u'_j}}{\partial x_k} \right) \right] \quad (4.24)$$

where μ_t is the turbulent viscosity and $\sigma_k = 0.82$.

The pressure-strain term is responsible for balancing the turbulent energy between all the terms of the Reynolds tensor, and can be modeled as follows (Gibson and Launder (1978), Launder (1989)):

$$\overline{p \left(\frac{\partial u'_i}{\partial x_j} + \frac{\partial u'_j}{\partial x_i} \right)} = \phi_{ij,1} + \phi_{ij,2} + \phi_{ij,w} \quad (4.25)$$

where $\phi_{ij,1}$ is the term of return to isotropy, $\phi_{ij,2}$ is the fast term and $\phi_{ij,w}$ is the wall reflection term.

$$\phi_{ij,1} = C_1 \frac{\varepsilon}{k} \left[\overline{u'_i u'_j} - \frac{2}{3} \delta_{ij} k \right] \quad (4.26)$$

$$\phi_{ij,2} = C_2 \left[(P_{ij} - A_{ij}) - \frac{2}{6} \delta_{ij} P_{ij} \right] \quad (4.27)$$

$$\begin{aligned} \phi_{ij,w} = & C'_1 \frac{\varepsilon}{k} \left(\overline{u'_k u'_m n_k n_m} \delta_{ij} - \frac{3}{2} \overline{u'_i u'_k n_j n_k} - \frac{3}{2} \overline{u'_j u'_k n_i n_k} \right) \frac{k^{3/2}}{C_l \varepsilon d} \\ & + C'_2 \left(\phi_{km,2} n_k n_m \delta_{ij} - \frac{3}{2} \phi_{ik,2} n_j n_k - \frac{3}{2} \phi_{jk,2} n_i n_k \right) \frac{k^{3/2}}{C_l \varepsilon d} \end{aligned} \quad (4.28)$$

where ε is the turbulent dissipation, k is the turbulent kinetic energy, δ is the Kronecker delta, P_{ij} and A_{ij} are the productive and convective terms of Eq. 4.23, n_k is the unitary component of direction x_k normal to the wall and d is the distance to the wall.

The values of the constants are: $C_1 = 1.8$, $C_2 = 0.6$, $C'_1 = 0.5$, $C'_2 = 0.3$, $C_l = C_\mu^{3/4}/k$ with $C_\mu = 0.09$ and $k = 0.4167$ (Von Kármán constant).

The dissipation rate, ε , is modeled by the following transport equation:

$$\frac{\partial(\rho\varepsilon)}{\partial t} + \frac{\partial}{\partial x_i} (\rho\varepsilon u_i) = \frac{\partial}{\partial x_j} \left[\left(\mu + \frac{\mu_t}{\sigma_\varepsilon} \right) \frac{\partial k}{\partial x_j} \right] \frac{C_{\varepsilon 1} \varepsilon P_{ii}}{2k} - \frac{C_{\varepsilon 2} \rho \varepsilon^2}{k} \quad (4.29)$$

where $\sigma_k = 0.82$, $\sigma_\varepsilon = 1.0$, $C_{\varepsilon 1}$ and $C_{\varepsilon 2} = 1.92$.

The turbulent viscosity can be calculated as follows:

$$\mu_t = \rho C_\mu \frac{k^2}{\varepsilon} \quad (4.30)$$

Replacing the proposed models in Eq. 4.23, we have the equation for the six terms of the Reynolds tensor:

$$\begin{aligned} \frac{\partial(\overline{\rho u'_i u'_j})}{\partial t} + \frac{\partial(\overline{\rho u'_k u'_i u'_j})}{\partial x_k} = & -\frac{\partial}{\partial x_k} \left[\frac{\mu_t}{\sigma_k} \left(\frac{\partial \overline{u'_i u'_j}}{\partial x_k} \right) \right] + \frac{\partial}{\partial x_k} \left[\mu \left(\frac{\partial \overline{u'_i u'_j}}{\partial x_k} \right) \right] \\ & - \rho \left(\overline{u'_i u'_k} \frac{\partial \overline{u_j}}{\partial x_k} + \overline{u'_j u'_k} \frac{\partial \overline{u_i}}{\partial x_k} \right) + \phi_{ij,1} + \phi_{ij,2} + \phi_{ij,w} - \varepsilon \end{aligned} \quad (4.31)$$

4.2 Particle motion equations

As mentioned in Section 4, the dispersed phase is treated in a Lagrangian framework, in which each particle is tracked through the domain and its equation of motion is based on Newton's second law. The trajectory, linear momentum and angular momentum equations for a rigid, spherical particle can be written, respectively,

$$\frac{dx_{pi}}{dt} = u_{pi} \quad (4.32)$$

$$m_p \frac{du_{pi}}{dt} = m_p \frac{3\rho C_D}{4\rho_p d_p} (u_i - u_{pi}) + F_{si} + F_{ri} + \left(1 - \frac{\rho}{\rho_p} \right) m_p g_i \quad (4.33)$$

$$I_p \frac{d\omega_{pi}}{dt} = T_i \quad (4.34)$$

In the above equations, $u_i = \overline{u_i} + u'_i$ are the components of the instantaneous fluid velocity. The average fluid velocity $\overline{u_i}$ is interpolated from the resolved flow field, whereas the fluctuating component u'_i is calculated according to the Langevin dispersion model proposed by Sommerfeld (2001). d_p is the particle diameter and $I_p = 0.1 m_p d_p^2$ is the moment of inertia for a sphere. Unlike most commercial CFD codes, UNSCYFL3D solves for the particle rotation. This is particularly important when dealing with large particles, which frequently collide with walls.

The empirical correlation proposed by Schiller and Naumann (1935) is used to evaluate the drag coefficient past each particle:

$$C_D = 24 Re_p^{-1} (1 + 0.15 Re_p^{0.687}) \text{ if } Re_p < 1000 \quad (4.35)$$

$$C_D = 0.44 \text{ if } Re_p > 1000$$

In Eqs. (4.35), Re_p is the particle Reynolds number $Re_p = \rho d_p |\vec{u} - \vec{u}_p| / \mu$.

The calculation of the shear-induced lift force is based on the analytical result of [Saffman \(1965\)](#) and extended for higher particle Reynolds numbers according to [Mei \(1992\)](#):

$$\vec{F}_s = 1.615 d_p Re_s^{1/2} C_{ls} [(\vec{u} - \vec{u}_p) \times \vec{\omega}] \quad (4.36)$$

$\vec{\omega}$ is the vorticity, $Re_s = \rho d_p^2 |\vec{\omega}| / \mu$ is the particle Reynolds number of the shear flow and $C_{ls} = F_{ls} / F_{ls, Saff}$ represents the ratio of the extend lift force to the Saffman force:

$$C_{ls} = (1 - 0.3314 \beta^{0.5}) e^{-0.1 Re_p} + 0.3314 \beta^{0.5} \text{ if } Re_p < 40 \quad (4.37)$$

$$C_{ls} = 0.0524 (\beta Re_p)^{0.5} \text{ if } Re_p > 40$$

β is a parameter $\beta = 0.5 Re_s / Re_p$ which varies with $0.005 < \beta < 0.4$.

The rotation-induced lift is computed based on the relation given by [Rubinow and Keller \(1961\)](#), which was extended to account for the relative motion between particle and fluid:

$$\vec{F}_r = \frac{\pi}{8} \rho d_p^3 \frac{Re_p}{Re_r} C_{lr} \frac{[\vec{\Omega} \times (\vec{u} - \vec{u}_p)]}{|\vec{\Omega}|} \quad (4.38)$$

In Eq. (4.38), $\vec{\Omega} = 0.5 \vec{\nabla} \times \vec{u} - \vec{\omega}_p$ and $Re_s = \rho d_p^2 |\vec{\Omega}| / \mu$. The lift coefficient C_{lr} is obtained from the correlation proposed by [Lun and Liu \(1997\)](#):

$$C_{lr} = \frac{Re_r}{Re_p} \text{ if } Re_p < 1 \quad (4.39)$$

$$C_{lr} = \frac{Re_r}{Re_p} (0.178 + 0.822 Re_p^{-0.522}) \text{ if } Re_p > 1$$

Also, the rotating particle experiences torque from the fluid flow. The correlation of [Rubinow and Keller \(1961\)](#) was extended to account for the relative motion between fluid and particle at higher Reynolds number:

$$\vec{T} = C_r \frac{\rho d_p^5}{64} |\vec{\Omega}| \vec{\Omega} \quad (4.40)$$

The coefficient of rotation, C_r , was obtained from the following correlation, derived from and the direct numerical simulations of [Dennis et al. \(1980\)](#):

$$C_r = \frac{64\pi}{Re_r} \text{ if } Re_r < 32$$

$$C_r = \frac{12.9}{\sqrt{Re_r}} + \frac{128.4}{Re_r} \text{ if } Re_r > 32 \quad (4.41)$$

Forces such as Basset and virtual mass have been neglected. This is a reasonable assumption since the particle material density is over 1000 times the gas density ([Crowe et al. \(1997\)](#), [Crowe \(2005\)](#)).

The extension of the Euler/Lagrange approach to unstructured meshes requires the use of accurate interpolation schemes, since in the above equations the continuous phase properties must be determined at the particle center. A few interpolation schemes have been tried out, and the best compromise between accuracy and cost was obtained with the Sheppard's scheme. Basically, the velocity and vorticity components at the particle position are calculated by weighing the neighboring element values with their inverse distances from their centers to the particle position. For integrating the ordinary differential equations (4.32), (4.33) and (4.34), the analytical scheme was used for the linear and angular velocities.

Upon a particle colliding with a wall, the new particle linear and angular velocities after rebound are calculated according to the following conservation equations ([Breuer et al. \(2012\)](#)):

Nonsliding collision:

$$\vec{u}_p^+ = \vec{u}_p^- - (1 + e_{par}) \frac{2}{7} \vec{u}_{pr}^- - (1 + e) (\vec{u}_p^- \cdot \vec{n}) \vec{n} \quad (4.42)$$

$$\vec{\omega}_p^+ = \vec{\omega}_p^- - \frac{10}{7} \frac{1 + e_{par}}{d_p} \vec{n} \times \vec{u}_{pr}^- \quad (4.43)$$

Sliding collision:

$$\vec{u}_p^+ = \vec{u}_p^- - (1 + e) (\vec{u}_p^- \cdot \vec{n}) \left[\mu_d \frac{\vec{u}_p^-}{|\vec{u}_p^-|} + \vec{n} \right] \quad (4.44)$$

$$\vec{\omega}_p^+ = \vec{\omega}_p^- - \frac{5}{d_p} (1 + e) (\vec{u}_p^- \cdot \vec{n}) \frac{\mu_d}{|\vec{u}_p^-|} \vec{n} \times \vec{u}_{pr}^- \quad (4.45)$$

In the above equations, the superscripts $-$ and $+$ denote values prior to and after the collision, respectively, e_{par} is the parallel restitution coefficient, e is the normal restitution coefficient and μ_d is the dynamic friction coefficient. \vec{n} is the normal unit vector pointing outwards of the element face being impacted. \vec{u}_{rp} is the relative velocity at the contact point:

$$\vec{u}_{pr} = \vec{u}_p - (\vec{u}_p \cdot \vec{n}) \vec{n} + \frac{d_p}{2} \omega_p \times \vec{n} \quad (4.46)$$

Inter-particle collisions are modeled with a stochastic, hard-sphere model. As described by [Oesterle and Petitjean \(1993\)](#) and [Sommerfeld \(2001\)](#), for each computational particle, a fictitious collision partner is generated, and the probability of a collision is checked based on an analogy with kinetic theory of gases. This in turn requires that the average and RMS linear and angular velocities, as well as the particle concentration in each control volume, be sampled and stored every Lagrangian calculation. Although demanding a lot of memory, the method is rather economical and effective, and avoids the use of a deterministic collision model, which is quite expensive computationally.

In this context, it is important to use a number to identify the relation between the gas phase and the particulate one. The mass loading, η , is defined as the ratio of solid phase mass flow rate to gas phase mass flow rate. This relation determines the impact of the interaction between the phases. The density of the phases as well as the inter-particle spaces provides essential information for determining how the dispersed phase is treated. Depending on the mass loading, the degree of interaction between the phases can be interpreted in three different ways:

- **One-way coupling:** Very low mass loadings ($\eta \ll 1$), the gas phase affects the motion of the particles via drag and other forces and the particles do not influence the carrier fluid. This condition is commonly called "dilute phase".
- **Two-way coupling:** Intermediate mass loadings ($\eta \approx 1$), the gas phase influences the motion of the particles, however, particles influence back the carrier fluid by attenuating the mean moments and turbulence effects.
- **Four-way coupling:** High mass loadings ($\eta \gg 1$), this type of flow, besides the two-way coupling, also consider inter-particle collisions. Usually treated as "dense

phase", it shows many different forms, making it difficult to obtain a neat definition of the particle behavior. This is probably the difficulty encountered when performing experiments at high mass loadings. On the other hand, CFD offers the possibility to analyze these phenomena separately, something impossible to be done experimentally.

Numerous experimental studies have shown evidence that wall roughness is important in the particle behavior. Therefore, their influence must be included in the modeling. As demonstrated by [Lain et al. \(2002\)](#) and [Benson et al. \(2004\)](#), the wall roughness plays a vital role in the dispersion of particles in pneumatic transport systems. In order to account for such effects, we implemented the model proposed by [Sommerfeld and Huber \(1999a\)](#), to represent the effects of surface asperities on the particle flow. In summary, the wall roughness is simulated by assuming that the effective impact angle $\alpha_{geometric}$ is composed of the geometric impact angle $\alpha_{geometric}$ added to a stochastic contribution due to wall roughness.

$$\alpha = \alpha_{geometric} + \xi \cdot \Delta\gamma \quad (4.47)$$

This stochastic contribution is sampled from a Gaussian distribution with a standard deviation $\Delta\gamma$, which depends on the structure of wall roughness and particle size. Unfortunately, the value of $\Delta\gamma$ must be calibrated so as to provide the best agreement between the experimental and simulated pressure losses.

When a structured grid is used, it is simple to determine the element hosting the particle, as there exists a straightforward relationship between the element index and its physical location. Because an unstructured grid is used in this work, there is the need for a specific algorithm to locate the particle after its final position is calculated by the integration of Eq. (4.32). For that purpose, the particle-localization algorithm proposed by [Haselbacher et al. \(2007\)](#) is used and will be detailed in Section 6.

Chapter 5

Finite volume discretization

For the current research the UNSCYFL3D code is employed. UNSCYFL3D, amongst many other CFD packages, uses a Finite Volume Method (FVM) in order to resolve a flow field depending on its geometrical boundaries and their respective boundary conditions. For this approach the equations presented in the previous chapter have to be discretized in space and time.

This chapter presents a brief overview of the discretization methods employed for the current research. It is largely based on the information in the Fluent [Guide \(2005\)](#), supplemented with the work of [Ferziger and Peric \(2002\)](#) and [Mathur and Murthy \(1997\)](#). The methods outlined below may not be optimal, but they have proven to deliver sufficiently accurate results within a reasonable amount of time for the problem at hand.

Section 5.1 introduces the FVM. Then Sections 5.2 present the numerical discretization. The pressure-velocity coupling is presented in Section 5.3 and the solution procedure is elaborated in Section 5.4.

5.1 Finite Volume Method

The Finite Volume Method (FVM) is a method for representing and evaluating partial differential equations in the form of algebraic equations ([LeVeque \(2002\)](#), [Toro \(2009\)](#)). Similar to the finite difference method or finite element method, values are calculated at discrete places on a meshed geometry. In the finite volume method, volume integrals in a partial differential equation that contain a divergence term are converted to surface integrals, using the divergence theorem. These terms are then evaluated as fluxes at the surfaces of each finite volume. Because the flux entering a given volume is identical to that leaving the adjacent volume, these methods are conservative. Another advantage of the finite volume method is that it is easily formulated to allow for unstructured meshes ([Versteeg and Malalasekera \(2007\)](#)).

5.2 Numerical discretization

The balance equations for the continuity, velocity components and for the turbulence variables in unsteady state can be written generically as:

$$\frac{\partial \rho \phi}{\partial t} + \frac{\partial}{\partial x_j} (\rho u_j \phi) = \frac{\partial}{\partial x_j} \left(\Gamma \frac{\partial \phi}{\partial x_j} \right) + S_\phi \quad (5.1)$$

By integrating the general conservation Eq. 4.3 over the control volume V , we obtain:

$$\int_V \frac{\partial \phi}{\partial t} dV + \oint_A \rho \phi \vec{V} \cdot d\vec{A} = \oint_A \Gamma \text{grad} \phi \cdot d\vec{A} + \oint_V S_\phi dV \quad (5.2)$$

Note that, for the terms involving surface integrals in Eq. 5.2, the Gauss Divergence Theorem was applied to convert the volume integrals into surface integrals ([Ferziger and Peric \(2002\)](#)):

$$\int_V \frac{\partial \phi}{\partial x_i} dV = \oint_A \phi \vec{l}_i \cdot d\vec{A} \quad (5.3)$$

For the element L shown in Fig. 32, and located at the LHS of face f , the discretization of Eq. 5.3 yields:

$$\left(\frac{\partial \rho \phi}{\partial t} \right)_L \Delta V_L + \sum_f J_f \phi_f = \sum_f D_f + (S_\phi \Delta V)_L \quad (5.4)$$

in which J_f is the mass flow rate, $(\rho_f \vec{V}_f \cdot \vec{A}_f)$, across face f , Γ_f the diffusion coefficient at the that face and $D_f = \Gamma_f (\text{grad} \phi)_f \cdot \vec{A}_f$ is the diffusive flux across face f . The summations above apply to all the faces of element L . \vec{A}_f is the normal area vector of face f , which is directed from the element L to the element R . Next, the discretization of each term of Eq. 5.5 is detailed.

The temporal term

The time derivative of Eq. 5.1 was discretized using the second-order three-level method ([Ferziger and Peric \(2002\)](#)):

$$\left(\frac{\partial \rho \phi}{\partial t} \right)_L = \frac{3(\rho_L \phi_L)^{n+1} - 4(\rho_L \phi_L)^n + (\rho_L \phi_L)^{n-1}}{2\Delta t} \quad (5.5)$$

The discretizations are implicit, so the other terms of Eq. 5.1 are evaluated at time $n + 1$ and algebraic systems are produced.

The advection term

Regarding the advective term in Eq. 5.5, when the first-order upwind scheme is employed, ϕ_f is assigned the value of the element center at element L if J_f is positive. Otherwise, the value of element R is set to the face. Because first-order schemes are usually very diffusive for many applications of interest, a second-order upwind scheme was used in this work:

$$\phi_f = \phi_L + (\text{grad}\phi)_{rL} \cdot \vec{dr}_L \quad (5.6)$$

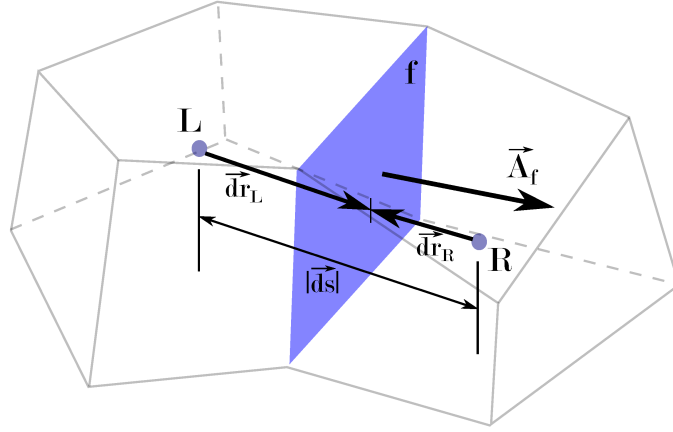


Figure 32 – Control volume for a finite volume discretization.

if $J_f > 0$. If $J_f < 0$ applies Eq. 5.6 considering the element to the right of the face f , R . In the above equation, the value of the variable in the face is obtained by extrapolation of the second order from the value in the *upwind*. The vector \vec{dr}_L is directed from the geometric center of element L to the face f center. $(\text{grad}\phi)_{rL}$ is the reconstructed gradient at element L , which is again computed by means of the Gauss Divergence Theorem:

$$(\text{grad}\phi)_r = \frac{1}{\Delta V} \sum_f (\bar{\phi}_f \vec{A}_f) \quad (5.7)$$

where $\bar{\phi}_f$ is the average of ϕ the element centers sharing face f .

The first term on the right side of Eq. 5.7 is always implicitly treated, whereas the second term is treated as source term and therefore calculated explicitly.

The diffusion term

It can be proven that the diffusive flux for face f is given by [Mathur and Murthy \(1997\)](#):

$$D_f = \Gamma_f \frac{(\phi_R - \phi_L)}{|\vec{ds}|} \frac{\vec{A}_f \cdot \vec{A}_f}{\vec{A}_f \cdot \vec{e}_s} + \Gamma_f \left[\overline{\text{grad}\phi} \cdot \vec{A}_f - \overline{\text{grad}\phi} \cdot \vec{e}_s \frac{\vec{A}_f \cdot \vec{A}_f}{\vec{A}_f \cdot \vec{e}_s} \right] \quad (5.8)$$

In Eq. 5.8, \vec{e}_s is the unit vector connecting the centers of elements R e L , $\vec{e}_s = \frac{\vec{ds}}{|\vec{dr}|}$. The first term at the RHS of Eq. 5.8 is treated implicitly, whereas the remaining terms, which represent the secondary diffusion, are calculated explicitly and therefore incorporated into the source-term S in Eq. 5.5. The secondary diffusion is null for hexahedra for instance, because vectors \vec{A}_f and \vec{e}_s are collinear. The gradient at face f , $\overline{\text{grad}\phi}$, is calculated as the average of the gradients at the adjacent elements. The treatment above is equivalent to the application of the second-order, centered differencing scheme in structured meshes and is advantageous in the sense that it does not depend on the element shape.

5.3 Pressure-velocity coupling

So far, it was proved that the momentum equations can be discretized via finite volume in unstructured meshes. Note that the set of Eqs. 4.1 and 4.2 forms a system of four equations (continuity, momentum for u , v and w) and four unknowns (u , v , w and p), thereby forming a given system. The velocity components must be determined by the respective conservation equations, but restricted with the imposed continuity. There is no explicit equation for the pressure, which requires the deduction of an equation for this variable so a segregated method of solution can be employed. The UNSCYFL3D uses the SIMPLE method (Semi-Implicit Pressure-Linked Equations, (Ferziger and Peric (2002))) to generate this equation and ensure that the continuity equation is also satisfied.

In the SIMPLE method, the procedure solution of the equations for u , v , w and p is said segregated, which means that a system of linear equations for each of these variables are resolved independently by linear system solution methods, and sequentially. The process is repeated until all the standard equations residues is reduced until the specified tolerance. Several global iterations, with the solution of linear systems for u , v , w and p , may be necessary due to the nonlinear nature of the Navier-Stokes equations and the coupling between the variables. Since the variables converge at different speeds, it is necessary under-relaxed the system solutions. For the case of transient problems, global iterations should be performed at each time step, and the process is repeated at each time step.

A more detailed discussion on pressure-velocity coupling can be found in Ferziger and Peric (2002).

5.4 Solution procedure

For the current study, only unsteady simulations are performed. For unsteady simulations the SIMPLE algorithm by V. Patankar (1980) is employed and briefly discussed below.

The SIMPLE algorithm can be summarized as follows:

1. Start-up the values of the velocities components and pressure in the elements and the mass flow rates across the faces of the calculation area, including the boundaries. These fields do not necessarily satisfy the conservation equations;
2. solves the linear system of equations for each component of the velocity vector, this corresponds to the predictor step. UNSCYFL3D uses biconjugated gradient method;
3. with the predicted velocity field, the mass flow rates is calculated on the faces of all the elements. It is then solved the linear system for the pressure correction. Normally, it is necessary to use an efficient solver based on multigrid methods, for example;
4. by knowing the pressure correction, the mass flow rates are corrected on the faces, the pressure in each element, and the velocity components in each element;
5. evaluate the residues and the momentum equations after the corrector step and if they are satisfied according to the tolerance specified by the user, declares the convergence of the set of equations. Due to the couplings between the variables, a global iteration of SIMPLE is usually not sufficient to ensure that all equations are satisfied simultaneously. In this case, the solver returns to the step 2 and the process continues until the convergence of all the equations.

It is important to remember that for transient problems, the above procedure is performed for each time step. The flowchart solution of SIMPLE method is shown in Fig. 33:

5.5 Solver UNSCYFL3D

The UNSCYFL3D is an "in-house" code developed in the Laboratory of Fluid Mechanics (MFlab) from the Federal University of Uberlândia in partnership with PETROBRAS. The code is capable of simulating laminar and turbulent flows with particles. In UNSCYFL3D, the Navier-Stokes equations in the incompressible formulation are solved numerically using the finite volume method of [Ferziger and Peric \(2002\)](#) in unstructured meshes, which can be composed of hexahedra, tetrahedra, prisms, pyramids and wedges. For the disperse phase modeling, a Lagrangian formulation is employed, where the particles are individually tracked in the flow. For the pressure-velocity coupling, the SIMPLE algorithm is used. Flow in both permanent and transient regimes can be simulated, and 6 boundary conditions can be prescribed: imposed velocity, symmetry, outflow, non-slip, imposed pressure and frequency.

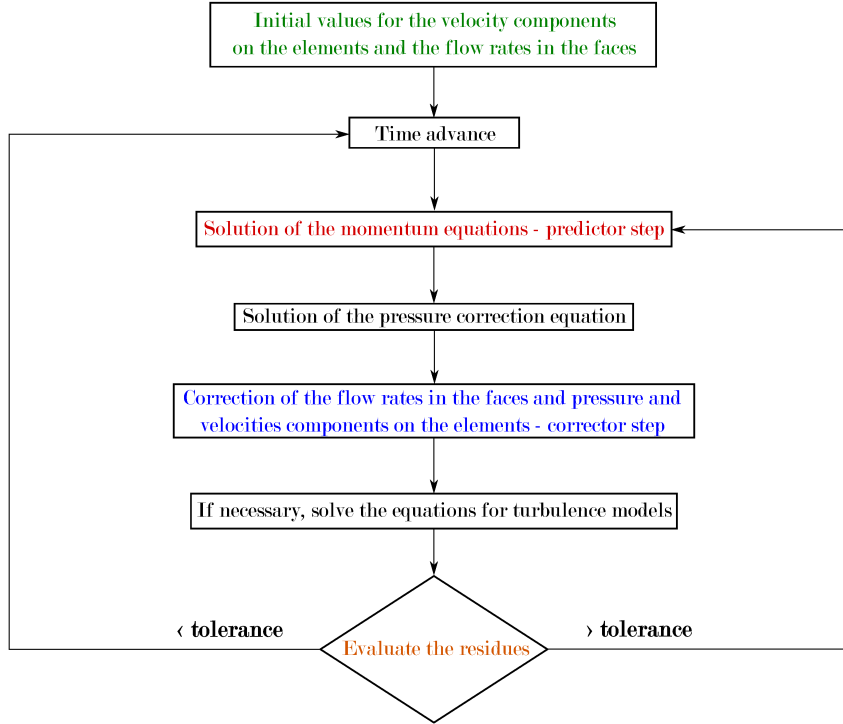


Figure 33 – Flowchart solution of SIMPLE method implemented in UNSCYFL3D.

The diffusive terms are discretized by 2^{nd} order centered differences, for the advective terms, the *upwind* scheme and the 1^{st} order centered scheme or *upwind* scheme 2^{nd} order can be combined. The large scale turbulence models are: Smagorinsky, dynamic and Yakhot. The Reynolds Stress Model, SST and DES-SST models are also available. For the integration of the motion equations of the particles, it uses the analytical model previous described in Section 4.2. Particles can be injected into faces in which the boundary condition of imposed velocity is applied. The following boundary conditions for the particles are possible: reflection, escape and frequency.

For the erosion-related problems the correlations from: Ahlert (1994), Neilson and Gilchrist (1968), Zhang et al. (2007) and Oka and Yoshida (2005) can be employed. The coefficients of restitution can be selected from: Forder et al. (1998), Sommerfeld and Huber (1999a) and Grant and Tabakoff (1975) models.

For time advance of the flow equations, the implicit Euler scheme 1^{st} and three levels in time 2^{nd} can be used. The mesh converter was developed in C language, and the solver in FORTRAN 90 language. Both flow and particles can be post processed using Paraview and VisIt tools.

Chapter 6

Particle phase algorithm

According to [Elghobashi \(1993\)](#), when starting a single-phase flow into a flow with a high particle loading, four different regimes will be achieved, and these arrangements relate to the manner in which the flow "feels" the presence of the dispersed phase (type of coupling) and the manner in which the dispersed phase interferes with the turbulence of the continuous phase (attenuating or increasing the turbulence levels).

For both Lagrangian and Eulerian approaches, it should be noted that the two-way coupling requires the description of the coupling between the phases and the particle. This interaction occurs through the tension between the phases at the particle surface. In particular, the coupling strength between the phases is the force acting on a single particle due to pressure and viscous tension caused by the disturbed fluid around. This force is equal in magnitude and opposite in direction to hydrodynamic force of the particle acting on the continuous phase. The coupling strength between the phases is the hydrodynamic forces on the surface less the contributions of the tensions of the undisturbed fluid (*e.g.*, less forces due to the pressure gradients which occur regardless of the presence of the particle).

The next section will explain the coupling procedure used in UNSCYFL3D.

6.1 Coupling procedure

The coupled solution of the continuous and particle phases is summarized as follows ([Laín and Sommerfeld \(2012\)](#)): first the steady-state solution for the fluid phase without particles is computed. Subsequently, particles are injected each timestep and tracked throughout the domain. For each control volume, the average and RMS linear and angular velocities, the particle concentration and the source-terms for the fluid momentum equation are stored.

At each timestep, the fluid flow is solved, now considering the source-terms sampled during the previous particle calculation. This process is repeated, taking the particle-to-

particle collision into account, until a converged solution for both phases is reached. It is important to bear in mind that the particle statistics must be corrected during each particle calculation. Another important detail is that the particle source term must be under-relaxed, for achieving convergence. The present work used 1.0 as under-relaxation factor for all the cases, and the quality of convergence was measured based on the standard deviation of average velocities, which should be close to 0.001. Normally, 1000 coupling iterations are sufficient for convergence of both phases. A detailed information about this method is given by [Laín and Sommerfeld \(2013\)](#).

The scheme of this procedure is presented in Fig. 34.

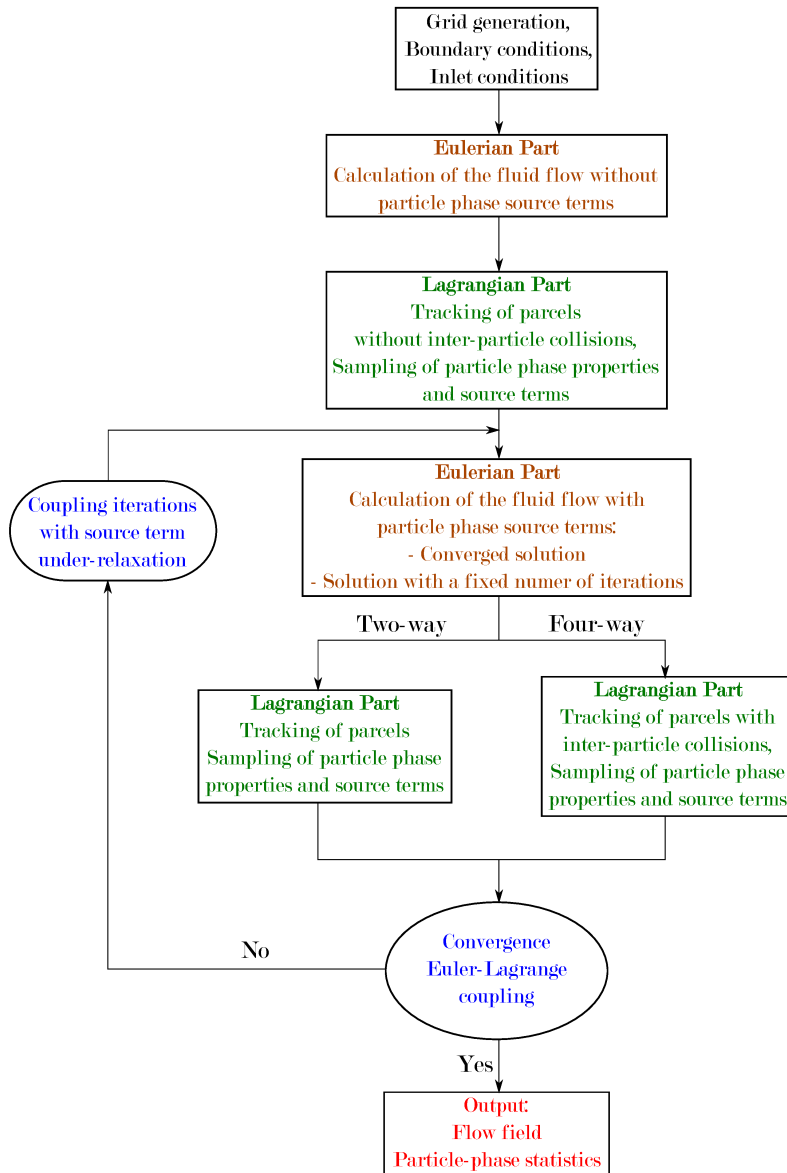


Figure 34 – Flow chart of fully coupled Euler-Lagrange calculations ([Laín and Sommerfeld \(2013\)](#)).

To solve the differential equations, it is important to know the location of each particle within the Eulerian mesh. This occurs because to calculate the variation of velocity

and position of the particles is necessary to interpolate the fluid properties to the position of its center of mass. Usually, the computational determination of the cell in which a particle is can be done quickly and efficiently by using a particle locator and a mesh mapping in cartesian uniform meshes. However, this approach can not be directly used in unstructured grids ([Peng et al. \(2009\)](#)), making the particle tracking problem an important element. Next section is dedicated to briefly explain the particle-location algorithm used in the present report.

6.2 Particle-tracking algorithm

The UNSCYFL3D code uses the algorithm proposed by [Haselbacher et al. \(2007\)](#). This choice was due to some specific features of this algorithm:

- this algorithm is robust enough to allow a particle to crosses more than one computational cell in a single step and time, in other words, the algorithm enables the particle to go through long distances, which is a limiting factor for a number of algorithms;
- the algorithm is based on distances intersection rather than time intersection, which is much more natural, once the particle tracking problem should be primarily a spatial problem, not temporal;
- the algorithm can be applied to Eulerian meshes consisting of polyhedral elements;
- according to the author, this algorithm is faster and more efficient than other published algorithms.

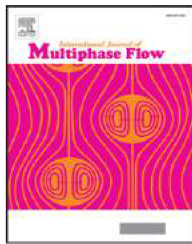
The complete procedure of particle-location as well as the algorithms used are not presented here because it differ completely from the main theme of the thesis. A detailed information about the algorithm and its implementation can be found in the publication of [Haselbacher et al. \(2007\)](#).

All the information presented until now allow the reader to familiarize themselves with the problem analyzed and the procedure used for its solution. With this in mind, will be presented in the following chapters the validation setup and procedure (Chap. 7) and the new pipe wall design (Chap. 8), respectively.

Chapter 7

The role of inter-particle collisions on elbow erosion

This chapter originates from the following publications:



Duarte, C.A.R., de Souza, F.J., Salvo, R.V., and dos Santos, V.F. The role of inter-particle collisions on elbow erosion. *International Journal of Multiphase Flow*, v. 89, p. 1-22, 2017.



Duarte, C.A.R., de Souza, F.J., and dos Santos, V.F. Effects of surface roughness and inter-particle collisions on elbow erosion. *ICMF-2016 - 9th International Conference on Multiphase Flow*, May 22nd - 27th 2016, Firenze, Italy.

Reprinted by permission from Elsevier Ltd.

7.1 Test case description

The simulation methodology was first validated based upon [Solnordal et al. \(2015\)](#) experiment. Such an experimental configuration allows insight into the complex mechanism involving the particle-erosion interaction in a 90° pipe elbow. Based on four-way coupled simulations a detailed analysis of the effects of surface roughness, coefficients of friction and mass loading influence on the erosion depth is then carried out. In this context, the role of inter-particle collisions on elbow erosion is scrutinized.

7.1.1 Description of the experimental set-up

The geometry depicted in Fig. 35 was chosen to match the experimental configuration investigated by [Solnordal et al. \(2015\)](#). They obtained a detailed three-dimensional surface map of the erosion scar occurring in a 90° pipe elbow by a Sheffield Discovery II D-8 co-ordinate measurement machine (CMM). The CMM is a profilometer capable of mapping out surface profiles in three dimensions. It consisted of a stage on which surfaces of interest could be securely mounted, and a computer controlled probe tip that could be located arbitrarily in two horizontal dimensions (x,y). The probe was then lowered onto the measurement surface and determined the vertical location (z) of the surface at that x, y position, giving a fully three dimensional map of the surface. The overall accuracy of the CMM measurement was rated as $\pm 6\mu\text{m}$, that being made up of a measurement uncertainty equal to $\pm 1\mu\text{m}$, combined with an estimated positional uncertainty of $\pm 5\mu\text{m}$.

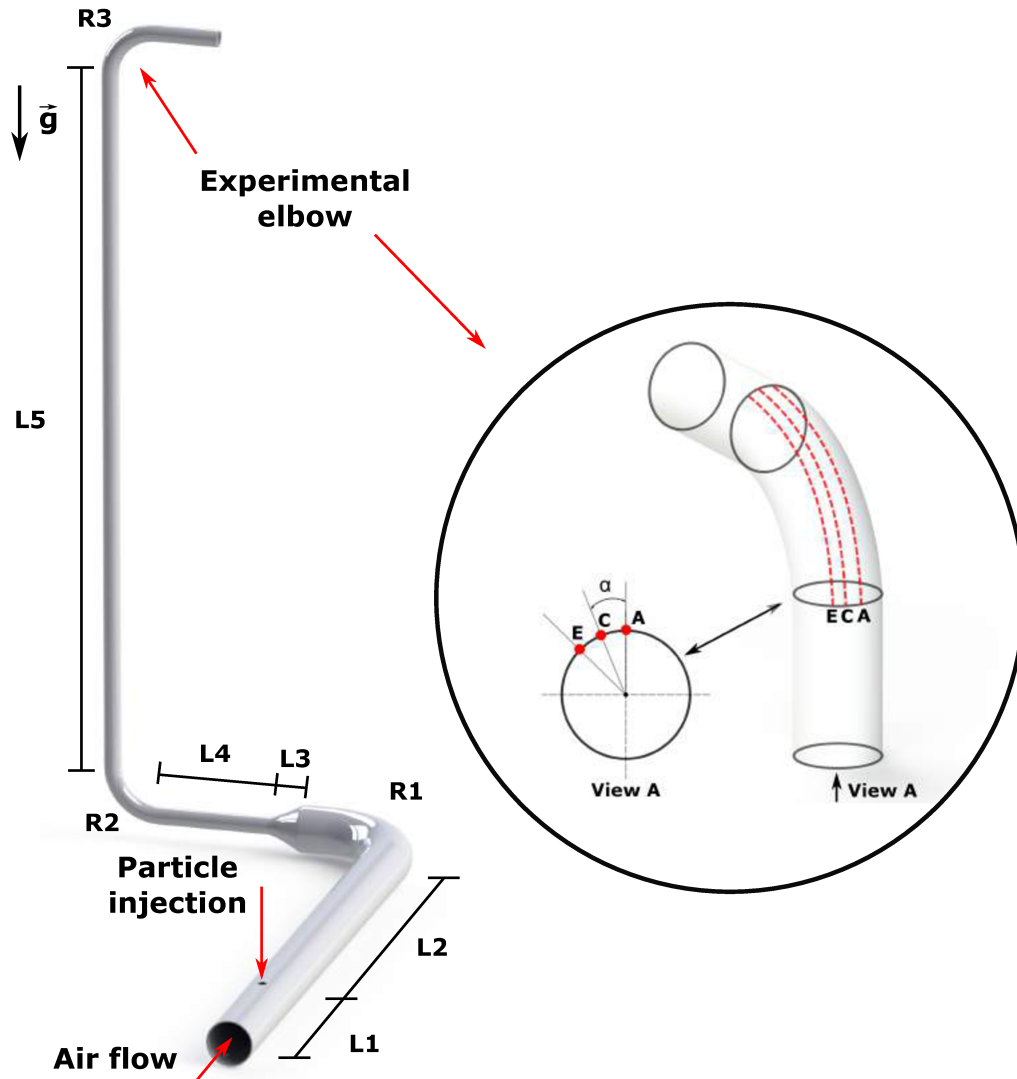


Figure 35 – Experimental configuration according to [Solnordal et al. \(2015\)](#) and the profiles used for comparison in the present work.

The flow tunnel is an open-circuit whose main test section has a diameter equal to

102.5 mm. Air enters the tunnel from a blower into a 200 mm horizontal pipe near the floor from a 75 kW blower. Sand is injected at a constant rate into this pipe and then passes through an elbow and reducer before entering another elbow that transitions to a vertical pipe. The vertical pipe has a straight section equal to $25.8D$ and ends at the experimental elbow. Downstream of the the elbow, the pipe continues to a cyclone and bag house to capture the particulates, and the air is exhausted to atmosphere.

The experimental elbow is a standard 90° elbow with $r/D = 1.5$ (where r is the bend radius and D is the pipe diameter). The elbow is machined out of aluminum blocks (Al grade 6061). Further details regarding the tunnel dimensions can be found in Table 3 and in Fig. 4 of [Solnordal et al. \(2015\)](#).

Table 3 – Experimental facility dimensions ([Solnordal et al. \(2015\)](#)).

L1	500 mm
L2	1950 mm
L3	150 mm
L4	600 mm
L5	2644 mm
R1	300 mm
R2	153 mm
R3	153 mm

Sand is introduced far upstream of the experimental elbow. Surface profile measurements were performed before the experiment, then after 200 kg of sand had passed through the flow tunnel, and again after 300 kg of sand had passed through the flow tunnel. Twenty erosion profiles labelled A to V were extracted along the left side of the elbow surface. In this study, only the profiles A, C and E for the 300 kg case were used for comparison. These profiles represent the important region of erosion and are separated by an angle $\alpha = 18.95^\circ$ (Fig. 35).

The conditions used for the experiment are outlined in Tab. 4, while the particle size distribution is given in detail in Tab. 5. The air entered the flow tunnel from outside, at an assumed ambient air temperature of 25° C. Atmospheric conditions were assumed for air pressure and density, and air viscosity was specified to be $1.8 \times 10^{-5} \text{ kg m}^{-1} \text{ s}^{-1}$. The sand was supplied by TGS Industrial Sands Pty. Ltd., and was classified as semi-sharp "70 Grand Sand". Two separate sieve sizings were performed on the sand, and the combined results of these sizings are presented in Tab. 5 numerically. The median sand size was found to be $184 \mu\text{m}$.

It is important to highlight that the experimental mass loading was $\eta = 3.846\%$. Even with low mass loading, the results which will be presented in Sec. 8.2.1 demonstrate that subtle differences are observed when the coupling between phases is considered.

Table 4 – Experimental conditions.

Air flow rate (\dot{m}_f)	0.78 kg/s
Air density (ρ_f)	1.18 kg/m ³
Air viscosity (μ_f)	1.8×10^{-5} Pa.s
Sand flow rate (\dot{m}_p)	0.030 kg/s
Sand density (ρ_p)	2650 kg/m ³
Mass loading (η)	3.846%
Amount of sand passing	300 kg
Sand median diameter (d_{50})	184 μ m
Mean volume fraction (α_p)	1.746×10^{-5}

Table 5 – Particle size distribution of sand.

Size (μ m)	Fraction (%)	Cumulative Passing (%)
> 1000	0.004	99.996
710-1000	0.002	99.994
500-710	0.030	99.963
355-500	0.242	99.722
250-355	22.014	77.708
180-250	29.377	48.331
150-180	20.085	28.246
125-150	18.774	9.472
106-125	6.077	3.395
90-106	2.530	0.865
75-90	0.489	0.376
63-75	0.264	0.112
45-63	0.108	0.016
0-45	0.004	0.004

7.1.2 Description of the numerical set-up

7.1.2.1 Domain size and grid

In order to better represent the experimental apparatus, the whole domain was solved. Despite increasing the computational cost, simulating the entire domain prevents errors associated with geometric simplifications. The grid was created using only hexahedra, which provide more stability and generate less numerical diffusion in the simulations. Gradual refinement is employed near the walls (Fig. 36b and 36c), where large velocity gradients and boundary layer exist. The stretching factor is set in order to be less than 1.1 in the whole computational domain. A mesh independence study was made to ensure the balance between quality of results and computational cost. These results are presented in Sec. 7.2.2.1.

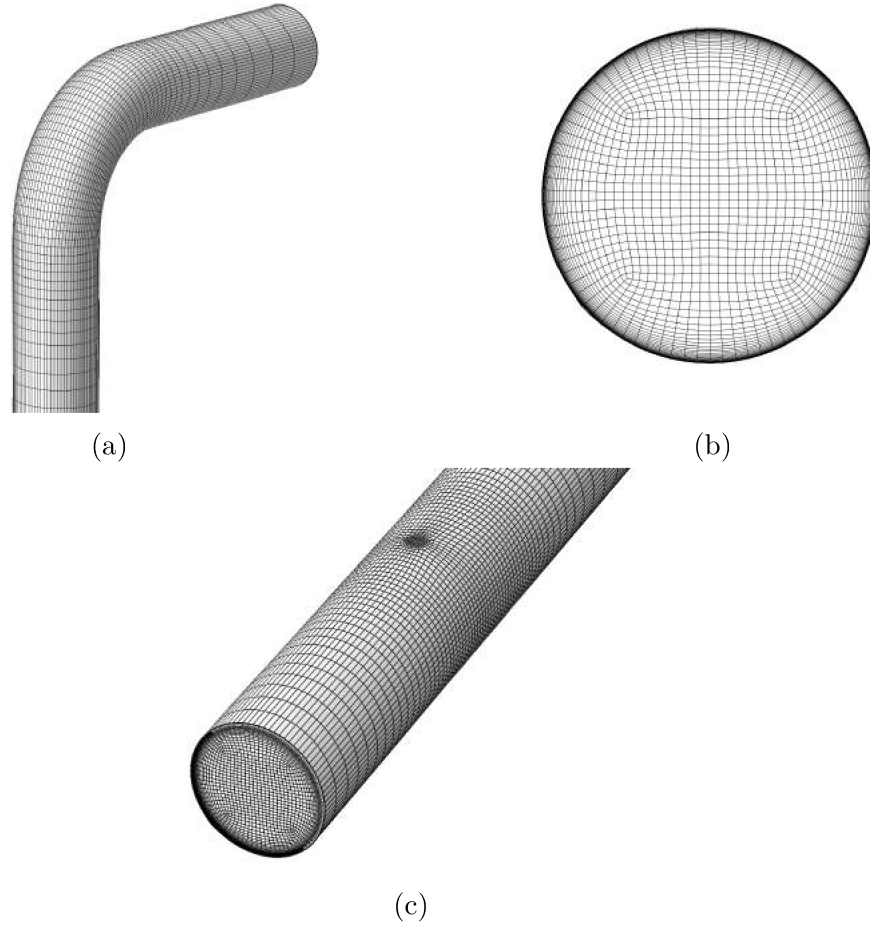


Figure 36 – (a) Grid of the elbow, perspective view. (b) Grid cross section upstream of the elbow. (c) Grid of the fluid and particle inlet regions.

7.1.2.2 Boundary conditions

The inflow conditions in the present study followed strictly the experimental conditions (Table 6). For all cases, the fluid inlet and the outlet were placed 500 mm upstream of the particle injection and 300 mm downstream the experimental elbow, respectively. The particle inlet has a diameter equal to 40 mm.

Table 6 – Simulation conditions.

Air flow rate (\dot{m}_f)	0.78 kg/s
Air density (ρ_f)	1.18 kg/m ³
Air viscosity (μ_f)	1.8×10^{-5} Pa.s
Sand flow rate (\dot{m}_p)	0.030 kg/s
Sand density (ρ_p)	2650 kg/m ³
Mass loading (η)	3.846%
Amount of sand passing	300 kg
Sand median diameter (d_{50})	184 μ m
Mean volume fraction (α_p)	1.746×10^{-5}

At the outlet a gauge pressure of 0 Pa was prescribed. At the pipe walls, the no-slip condition is applied. The inlet air flow enters the pipe with a stream velocity of $U_f = 21.01$ m/s. A turbulence intensity of 0.1% is assumed, although the results were not sensitive to this variable. Particles are fed into the domain with a velocity of $U_p = 1.0$ m/s normal to the particle inlet. Regarding the initial particle rotation, a mean of 0 and a standard deviation of 1000 s^{-1} were prescribed. The particle Stokes number (Stk) based on the mean particle diameter was 29.08. The Stokes number was defined as $\text{Stk} = \tau_p U_f / l_o$ where $\tau_p = \rho_p d_p^2 / 18 \mu_f$ was the particle relaxation time and l_o the characteristic length. The physical properties of the air are set as to match the experimental Reynolds number of 538,000.

Regarding the particle setup, at each fluid timestep, nearly 300 parcels are released, although statically converged results could be obtained with much fewer parcels. So, at "steady" state conditions, around 9.5 million parcels are tracked and used for statistics. The Courant number of the particles was set to 0.5. Lower CFL numbers did not affect the results. The fluid and particle timesteps were 1.0×10^{-4} s and 1.0×10^{-5} s, respectively. These values were obtained considering all relevant time scales.

7.1.2.3 Statistics

The region of interest is the second 102.5 mm elbow, in which erosion was measured. Due to the complexity of the measurements, the erosion experiments available in the literature frequently report the results in terms of erosion rate, penetration ratio or erosion depth. Unfortunately, these variables are not sufficient to clarify the mechanisms involved in the wearing process.

Hence, additional statistics are required to explain the physical phenomena behind the erosive wear by particle impingement. For such analysis, more fundamental variables such as particle impact velocity, particle impact angle and particle impact frequency were used in this work in order to explain the formation and the behavior of the erosion scar.

These variables are averaged for the whole domain wall allowing a statistically converged field to be obtained from the simulations.

7.2 Results and discussions

7.2.1 Two-phase flow validation

In order to show that the results obtained by the Euler/Lagrange code agree well with the experiments and hence the authors are confident about the reliability of the simulations performed, a horizontal pipe, studied experimentally by [Huber \(1991\)](#) and [Huber and Sommerfeld \(1998\)](#), was also simulated. According to [Huber and Sommerfeld](#)

(1998), the pipe diameter is 150 mm and the mean conveying velocity is $U_f = 27.0$ m/s. Vertical profiles of the mean particle velocity, particle streamwise velocity fluctuations, mean particle diameter and particle streamwise mass flux were measured in the mid-plane parallel to the axis of gravity at a distance of 8 m from the inlet. The pipe length was 10.6 m. The gas density and the dynamic viscosity were $\rho_f = 1.2$ kg/m³ and $\mu_f = 1.8 \times 10^{-5}$ Pa.s, respectively, yielding a Reynolds number of 281,250. An unstructured with a total of 585,000 hexahedral control volumes was found sufficient to produce mesh-independent results.

Regarding the two-phase flow computations, the mass loading considered in these measurements was $\eta = 70\%$. The particle phase consists of glass spheres with a density of $\rho_p = 2500$ kg/m³. The particle diameter distribution was considered according to the experiments (Huber and Sommerfeld (1998)) using 7 diameters ranging from 15 to 85 μ m. For particle-wall interactions, the wall friction coefficients $\mu_s = 0.54$ and $\mu_d = 0.18$ were adopted. The wall surface roughness has been chosen to be $\Delta\gamma = 10.0^\circ$ (the experimental pipe material was stainless steel) and the restitution coefficient linear decrease from 1.0 to 0.72 between $\alpha_1 = 0^\circ$ and $\alpha_1 = 15^\circ$, $e = e_{min} = 0.72$, for $\alpha_1 = 15^\circ$ (where α_1 is the particle impact angle with respect to the plane wall).

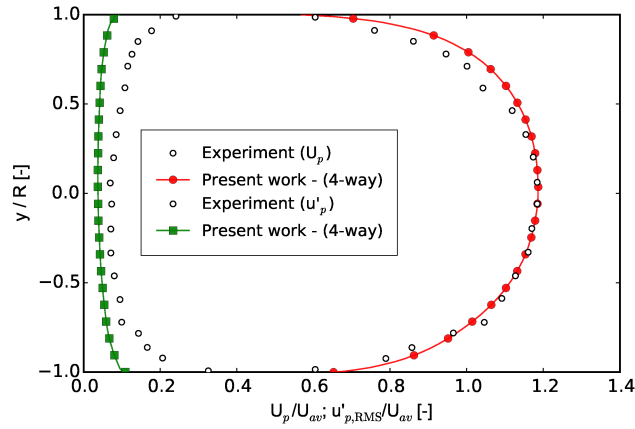


Figure 37 – Mean and RMS normalized particle velocity profiles after a conveying distance of 8 m, numerical computations versus experiments of Huber and Sommerfeld (1998).

Fig. 37 shows the mean particle velocity and the particle streamwise velocity fluctuations (root-mean-square), compared with the experiments. Both were normalized by the mean fluid velocity ($U_f = 27.0$ m/s). The quality of the numerical predictions in four-way coupling is noticeable. The mean particle velocity exhibits a better agreement with the experiments in the core flow while is slightly over-predicted near the walls. Such effects were also observed by Laín and Sommerfeld (2013). The reason is that the particles are relatively small and strongly affected by the continuous phase. This also leads to an under-prediction of the particle streamwise fluctuation, especially in the near-wall regions, which is further related to the isotropic nature of the employed turbulence model.

The particle dispersion due to the wall roughness combined with inter-particle collisions is clearly observed in Fig. 38. Although the gravitational settling is responsible for the particle concentration at lower part of the pipe, such effects cause a resuspension of the particles reducing their concentration at the bottom wall. In this case, the particle streamwise mass flux is normalized by the mean value of the extracted curve.

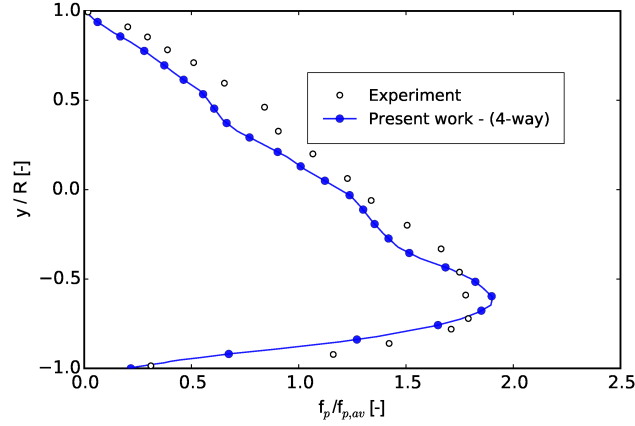


Figure 38 – Normalized particle mass flux after a conveying distance of 8 m, numerical computations versus experiments of [Huber and Sommerfeld \(1998\)](#).

Finally, the mean particle diameter (normalized by the mean value of the extracted curve) is also reported (Fig. 39). Good agreement with experiment is observed. Clearly, bigger particles slightly settled on the lower part of the pipe. This is caused by the segregation due to gravity. On the other hand, smaller particles are strongly affected by the turbulence and remain suspended in the upper part of the pipe.

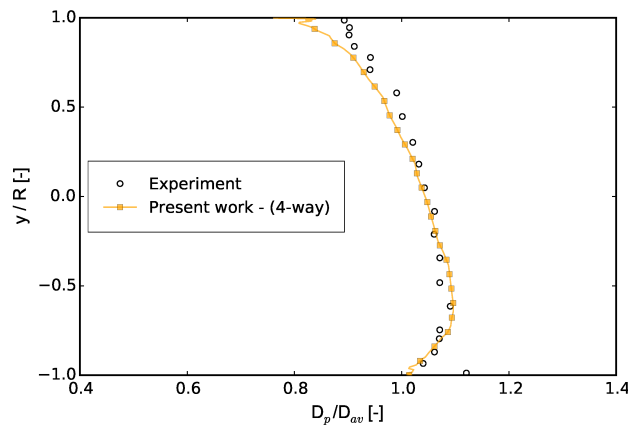


Figure 39 – Normalized particle mean diameter after a conveying distance of 8 m, numerical computations versus experiments of [Huber and Sommerfeld \(1998\)](#).

Since the simulation results depend on the correct implementation of a number of models, it can be concluded that the code is validated and further analysis on erosion can be carried out.

7.2.2 Erosion computations

7.2.2.1 Mesh independence study

To determine the mesh independence in this study, four mesh resolutions were analyzed. All the meshes were hexa-structured and generated using the ANSYS-ICEM CFD 14 meshing tool. Table 10 shows the mesh statistics including the average wall y^+ values for the mesh.

Table 7 – Mesh resolutions and y^+ average values.

Mesh number	Number of elements	Average y^+
N_1	355230	0.54073
N_2	638255	0.54189
N_3	854446	0.54210
N_4	991930	0.54223

When using the 2-layer $k-\varepsilon$ turbulence models it is important to refine the grid to ensure that $y^+ < 1$ in the first element away from the wall. This guarantees that the node of the first element is within the laminar layer so that the solution can be integrated to the wall.

To determine whether the solution is mesh independent, the fluid phase solution was computed for each mesh. The fluid velocity and the turbulent kinetic energy profiles were extracted from three different locations, producing minimal differences from grid to grid. Since the change in the velocity from N_2 and N_3 was smaller than 1%, the grid number N_2 was sufficient for achieve mesh independence while minimizing run time and memory requirements. For this reason, the rest of the simulations were carried out considering the N_2 mesh.

7.2.2.2 Erosion model validation - one, two and four-way couplings

The first test conducted in this work aims at validating the numerical model using the experiments carried out by [Solnordal et al. \(2015\)](#) which was performed at relatively low mass loading ($\eta = 3.846\%$). For this test, the static and dynamic coefficients of friction were set as $\mu_s = 0.45$ and $\mu_d = 0.30$, respectively, and the surface roughness parameter of $\Delta\gamma = 7.0^\circ$ were prescribed. These were found to be the best fit parameters, as the experimental values are not available.

In order to provide a first overview of the phase interaction effects on the elbow erosion, Fig. 40 depicts the contours for all the erosion-related variables. Quantitatively speaking, the erosion depth contours for one (Fig. 40a), two (Fig. 40b) and four-way (Fig. 40c) coupling display some differences in both pattern and magnitude. The most notable difference can be seen in the two-way solution (Fig. 40b).

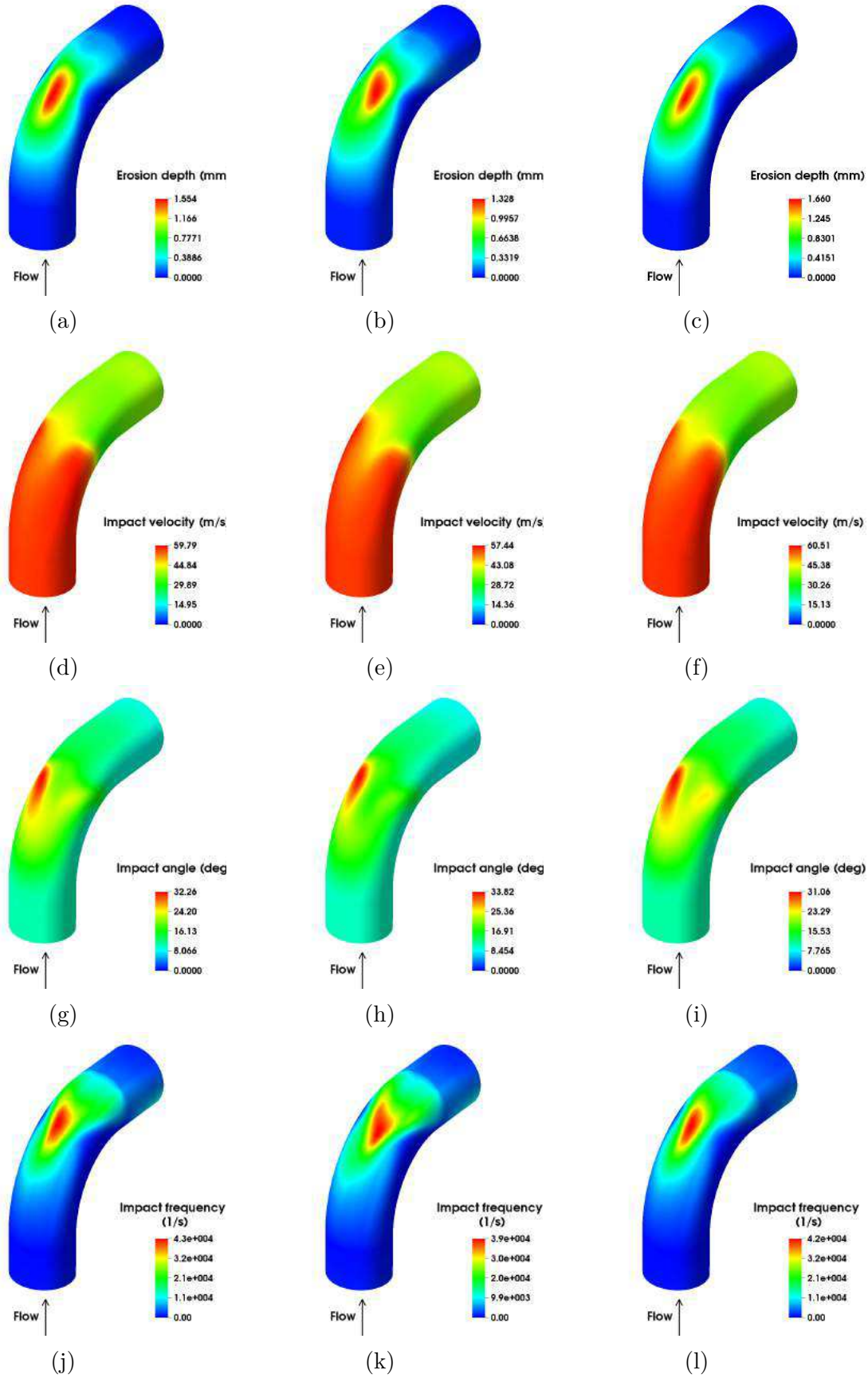


Figure 40 – Contours of the erosion-related variables for mass loading $\eta = 3.846\%$. From left to right: one-way, two-way and four-way coupling. From top to bottom: erosion depth, impact velocity, impact angle and impact frequency.

For this case, the region of maximum erosion is laterally elongated, in contrast to the contours obtained with one (Fig. 40a) and four-way (Fig. 40c) calculations. Another region displaying subtle changes depending on the phase interaction regime is located downstream of the maximum erosion region. In all cases, the erosion depth patterns considerably depart from the V-shaped erosion contours typically observed in simulations (Chen et al. (2004b), Yang and Boulanger (2012), Duarte et al. (2015), Duarte et al. (2016)). As shown by Solnordal et al. (2015), this is mainly a result of the high wall roughness, which in turn causes more particle dispersion in the radial direction along the pipe upstream of the elbow. As a result, the particle distribution in the cross section is more homogeneous as the particles hit the elbow, dramatically modifying the otherwise observed V-shaped penetration profile.

Moreover, an interesting behavior is observed when the inter-particle collisions are included in the simulation (Fig. 40c). Noticeably, the contours are rounder, with the reminiscent vee legs being attenuated, and the erosion pattern approaches the experimental result (see Fig. 6b of Solnordal et al. (2015)). As an initial result, such finding demonstrates that even for low mass loading, inter-particle collisions affect the results towards the experimental ones. By now, this result by itself is not sufficient to elucidate the real mechanism responsible for the change in the erosion behavior due to the coupling between the phases.

In this respect, the contours of the particle impact velocity in one (Fig. 40d), two (Fig. 40e) and four-way (Fig. 40f) coupling as well as the impact angle in one (Fig. 40g), two (Fig. 40h) and four-way (Fig. 40i) are presented. It is evident that for the impact velocity cases the inter-phase interactions are not contributing to significantly modify the contours. Nevertheless, the impact angle contours in two-way (Fig. 40h) suffered an attenuation in their magnitude on the right side of the elbow. This may partially explain the observed change in the erosion depth illustrated in Fig. 40b since the impact angle is recognized to remarkably influence the surface degradation in erosive environments (see, e.g., Islam and Farhat (2014)).

For completeness, the contours of the particle impact frequency against the elbow wall in one (Fig. 40j), two (Fig. 40k) and four-way (Fig. 40l) coupling are also reported. Note that the impact frequency in two-way (Fig. 40k) decreased and the maximum region displays a pattern similar to that of the erosion depth (Fig. 40b).

Before proposing explanations for the foregoing effects, a quantitative comparison with the experimental results is made. As mentioned in section 7.1.1, three profiles were extracted at the outer elbow wall as a function of the curvature angle. The origin (0°) is set at the elbow inlet, while 90° corresponds to the elbow flow outlet. Such a comparison can verify the capacity of the present models to accurately predict the erosion depth in different radial positions of the elbow.

Profile A, presented in Fig. 41, was extracted from the symmetry plane of the elbow and displays the main erosion location. Although the two-way coupling simulation demonstrates a distinct behavior in the erosion depth (Fig. 41a), the one and four-way coupling approaches exhibit very good agreement with the experiment, particularly for the curvature angle between 40° and 90° . On the other hand, the region between 0° and 40° shows a marked difference compared to the experiment. Such discrepancy has already been reported by the authors in previous works (Duarte et al. (2015), Duarte et al. (2016)) and a possible explanation is linked to the shape of the particles used in the experiment. In the present work, correlations for the forces acting on the particles are only valid for spherical particles differing from the non-spherical particles used in the experiment. As shown in works such as those by Haider and Levenspiel (1989) and Ganser (1993), the drag force on a non-spherical particle, for instance, is highly dependent on its sphericity. While this may represent a severe simplification, in view of the lack of a characterization of the particles actually used in the experiments, it was decided to simplify the numerical setup as much as possible in order to understand the inter-particle collision effects on elbow erosion.

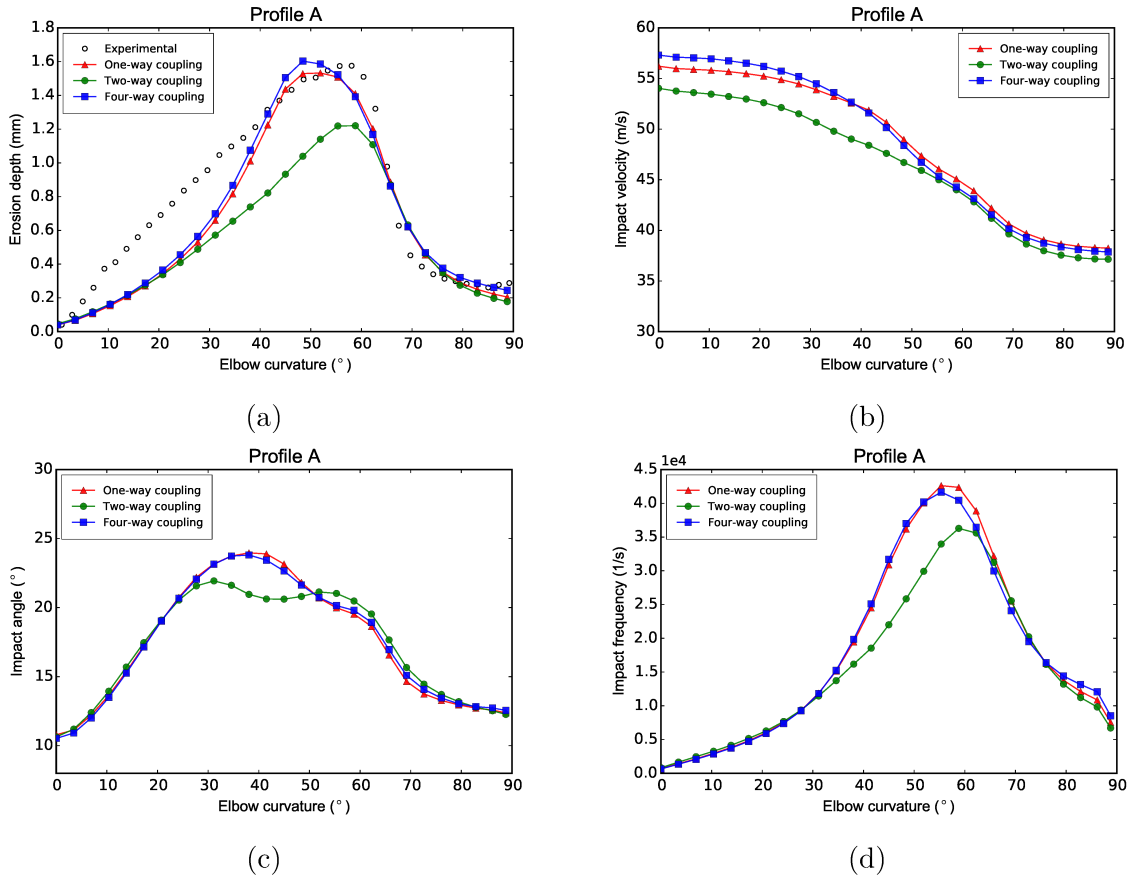


Figure 41 – Erosion-related variables extracted from profile A for one, two and four-way coupling. (a) Erosion depth, (b) impact velocity, (c) impact angle and (d) impact frequency. Mass loading $\eta = 3.846\%$.

Until now, the factor responsible for the reduction of the erosion depth in two-way

coupling would be the exchange of momentum between the particles and the fluid alone. For a given pair of materials, the erosion rate depends on the impact angle, velocity and frequency. In this sense, these three parameters, impact velocity (Fig. 41b), impact angle (Fig. 41c) and the impact frequency (Fig. 41d) are presented at the symmetry plane of the elbow. In the two-way coupling case, both the impact velocity and impact angle suffered a reduction in their magnitude for the curvature angles of $0^\circ - 50^\circ$ and $30^\circ - 50^\circ$, respectively. Nevertheless, the difference in both parameters when compared to the other interaction approaches is less than 7%. On the other hand, the impact frequency (Fig. 41d) is significantly reduced between $30^\circ - 60^\circ$. Such behavior is likely to cause the erosion depth reduction observed in Fig. 41a.

The explanation is that, after colliding with the first elbow, particles concentrate next to the pipe walls due to the focusing effect, and acquire a swirling motion. In the case of two-way calculations, the momentum exchange between the gas and the particles concentrated near the walls reduces the centrifugal force. This means that particles otherwise located in the core flow are driven radially with less strength so that wall collisions involve less energy. As a result, particle migration towards the core flow is hindered.

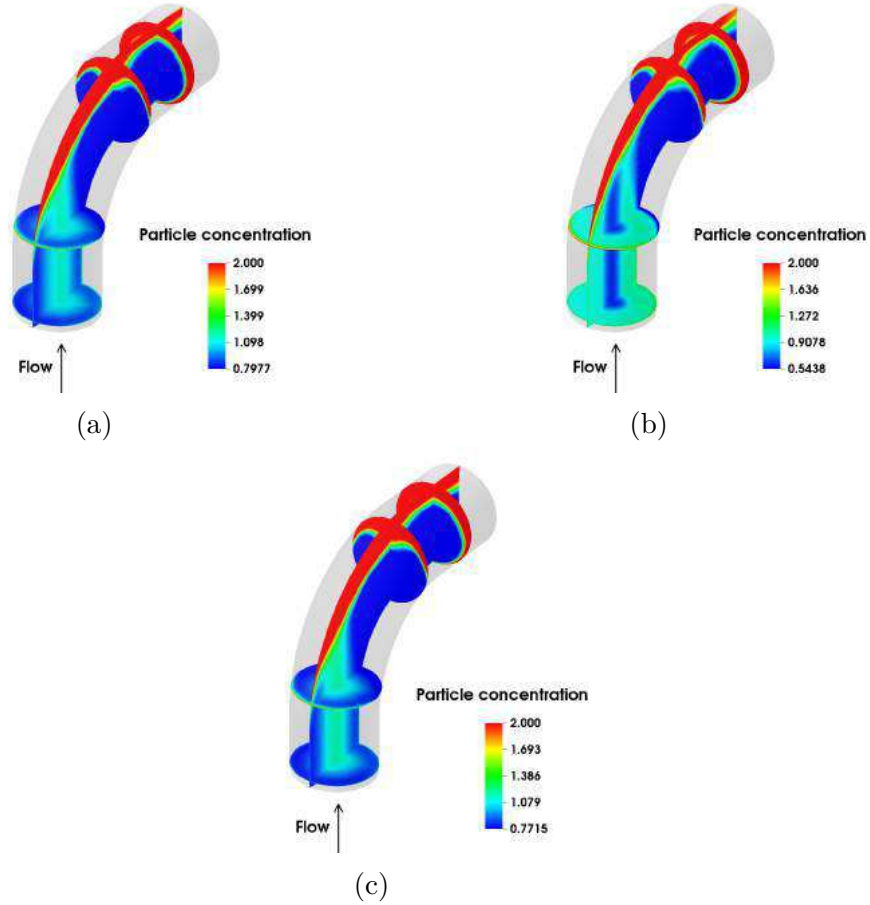


Figure 42 – Particles concentration inside the elbow for: (a) one, (b) two and (c) four-way coupling. Mass loading $\eta = 3.846\%$.

Particle momentum is lost during the wall collisions which combined with preferred regions of particle concentration also slowed down the carried phase (Fig. 41b). To provide a better overview of the particle concentration inside the elbow, Fig. 42 is presented. Clearly, the region downstream of the particles main impact location exhibits similar contours for all the cases. However, upstream of such region, a characteristic contour is observed in the two-way coupling computation (Fig. 42b). Surprisingly, for this case, the particles are segregated near the elbow entrance.

Fig. 43 illustrates the particle concentration profiles of Fig. 42 which were extracted from a line in the symmetry plan of the elbow entrance. As expected, the differences between the one-way and four-way coupled cases is minor, suggesting that the role of inter-particle collisions is of less importance at this location. According to Sommerfeld (1996) and Sommerfeld (2000), large particles (i.e. $> 100 \mu\text{m}$) are less affected by the surface roughness. However, due to their inertia, they need more time to adjust to the flow after the rebound. The effect of wall roughness on particle distribution in a horizontal pipe was investigated by Laín and Sommerfeld (2012). They concluded that conveying of particles in a horizontal pipe with higher wall roughness results in the so-called "focusing effect", whereby the particles colliding with the curved walls are bounced back towards the core of the pipe. This reinforces the similarity of the particle concentration in the core flow in one-way and four-way coupling simulations.

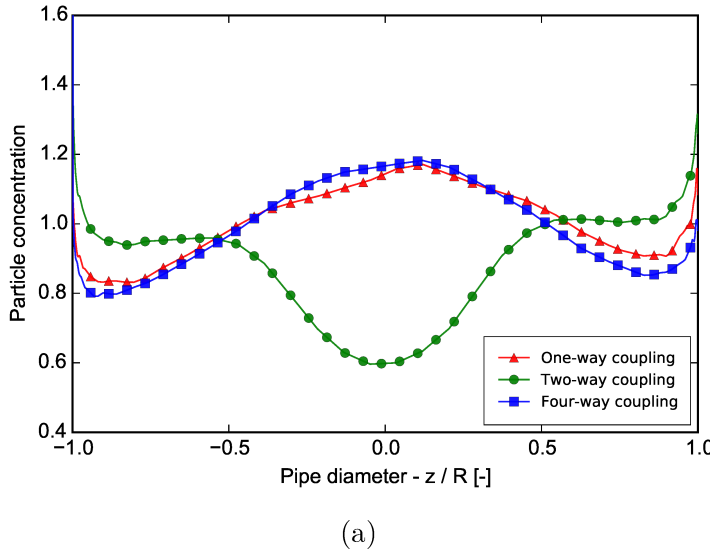


Figure 43 – Particle concentration upstream of the elbow. Mass loading $\eta = 3.846\%$.

On the contrary, the influence of the particles on the fluid is of major interest. For this case, a pronounced reduction in the particle concentration at the elbow centre can be observed while it is augmented near the wall. A particularly unexpected feature is the high particle concentration near the vertical pipe walls observed in the two-way calculations. This is due to the Saffman force, as shown by the plots in Fig. 44. Because of their high inertia, particles are driven towards the pipe walls by the swirl generated in the second

elbow. Although the collisions with the pipe walls tend to redisperse them, a region of preferential concentration exists near the wall in two-way calculations. Upstream of the third elbow, it can be shown that the Saffman force points outwards in the radial direction, as the product of the particle slip velocity and vorticity in cylindrical coordinates is positive. This force was augmented in two-way calculations, because of the local modifications in the fluid velocity and vorticity. As a consequence, and in the absence of interparticle collisions, the Saffman force partly compensates for the effect of particle-to-wall collisions and causes the particle to concentrate near the pipe walls rather than the core flow.

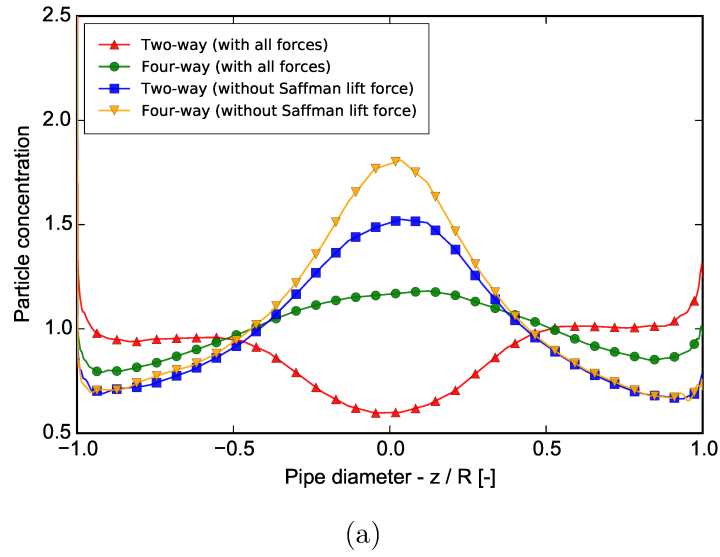


Figure 44 – Particle concentration upstream of the elbow with and without Saffman lift force. Mass loading $\eta = 3.846\%$.

By observing the erosion profile C, some discrepancies with respect to the experiment are observed (see Fig. 45a). Again, the erosion magnitude provided by the two-way coupling simulation is below the other approaches, and the erosion depth profiles for all the cases becomes flatter between 35° and 60° .

To explain such effect, Fig. 46 is presented. A normal view of the elbow with the lines where each profile was extracted is shown. According to [Solnordal et al. \(2015\)](#), the experimental erosion contour on the outer surface of the elbow was close to symmetrical. However, the predictions for one (Fig. 46a), two (Fig. 46b) and four-way (Fig. 46c) indicate a marginal displacement of the maximum erosion region to the right side of the elbow. This, in turn, quantifies the flattening behavior observed in profile C (Fig. 45a). It is important to mention that all the experimental curves were extracted from the left side of the elbow, according to [Solnordal et al. \(2015\)](#).

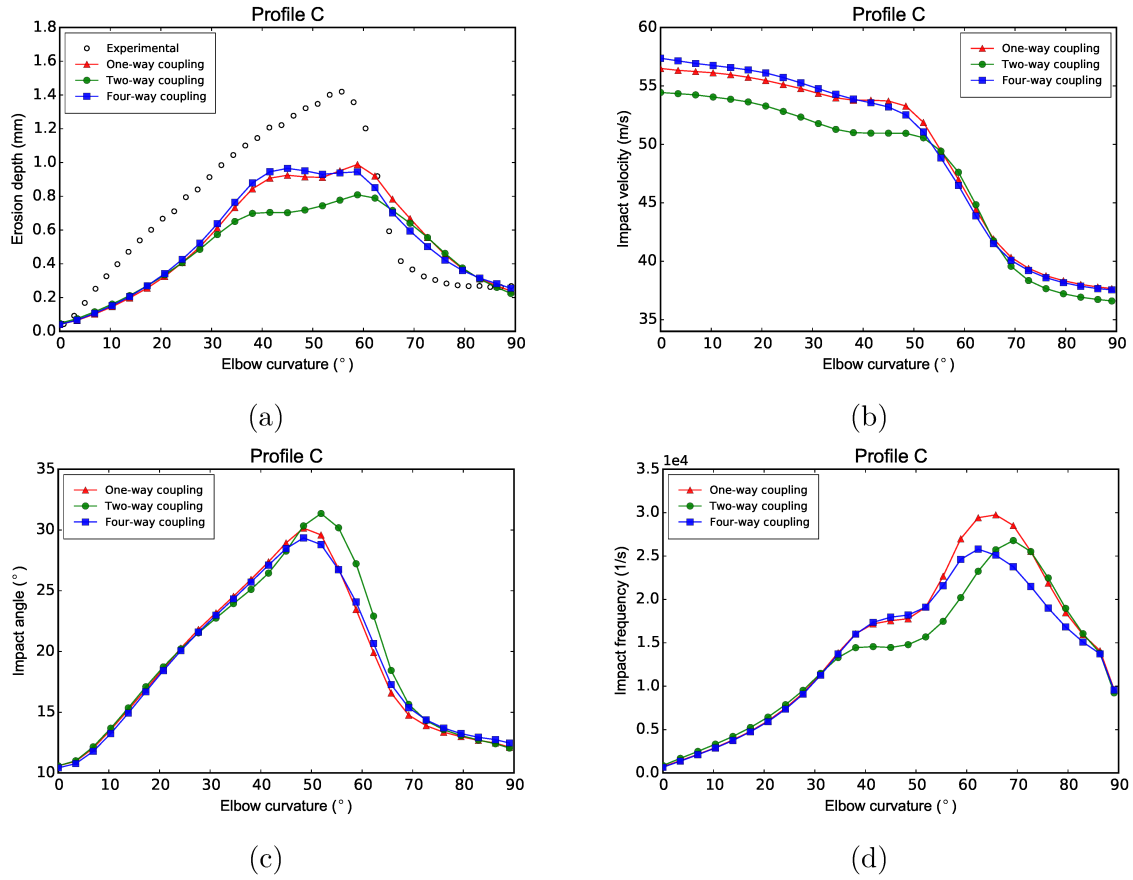


Figure 45 – Erosion-related variables extracted from profile C for one, two and four-way coupling. (a) Erosion depth, (b) impact velocity, (c) impact angle and (d) impact frequency. Mass loading $\eta = 3.846\%$.

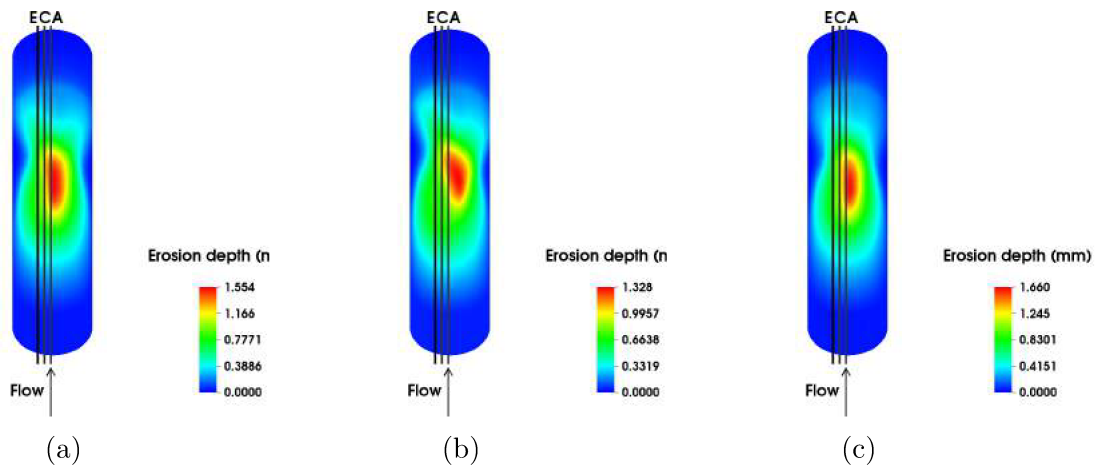


Figure 46 – Location of extracted profiles for mass loading $\eta = 3.846\%$. (a) One-way, (b) two-way and (c) four-way coupling.

For curvature angles between 60° and 90° , the erosion depth was overpredicted (Fig. 45a). The impact velocity profiles (Fig. 45b) behave similarly to those shown in profile A (Fig. 41b) although a more accentuated inflexion close to 60° is displayed on the first. This trend is clearly visible from the velocity impact contours (see Figs. 40d, 40e and 40f), which show higher impact velocities in the first half of the elbow. At this region, particles lose energy due to the collisions with the walls and reach the downstream part of the elbow with lower speeds.

Interestingly, the impact angle (Fig. 45c) for all the coupling approaches increased between 30° and 60° when compared to profile A (Fig. 41c). This is in agreement with the contours presented in Figs. 40g, 40h and 40i which demonstrate higher impact angles on the left side of the elbow. Generally, the high roughness leads to a redistribution of the particles after the first impact against the outer elbow wall. Consequently, the particles tend to rebound with lower impact angles to the right side of the elbow. It is important to highlight that the inter-particle collisions are not the main mechanism to cause the above-mentioned effect on the impact angle for the actual mass loading, so no significant variations are observed among the coupling approaches (Fig. 45c).

Finally, the changes in the impact frequencies (Fig. 45d) must be pointed out. Higher impact frequencies are predicted between 55° and 75° , although such increase is not contributing to an increase in the erosion depth (Fig. 45a). This observation contradicts the trend observed for profile A (Figs. 41a and 41d) where regions with the highest impact frequency resulted in greater depths of erosion. This likely occurs due to the location where profile C was extracted. Since profile A represents the main impact location, it is expected that the particle impact frequency defines the erosion process (see Fig. 41d). However, profile C was taken from a location that essentially experiences the secondary impacts from the main impact area (profile A). This explains the higher frequency of impact for larger curvature angles in profile C. More specifically, the four-way simulation reduced the particle impact frequency in profile C. Obviously, the inter-particle collisions after the main impact spot are redirecting the particles to new locations. This causes the attenuation of the impact frequency in regions away from the elbow symmetry plane.

For further validation of the erosion model, comparison is also provided for profile E (Fig. 64). This comparison allows the understanding of the erosive mechanisms farther from the symmetry plane as well as the investigation of the sensitivity of the erosion model.

Although the erosion depth between 0° and 60° is underpredicted, the erosion model was capable of capturing the actual erosion magnitude at 60° and 90° . In addition, the four-way coupled simulation predicted an erosion pattern that most closely resemble the experimental measurement between the above-mentioned curvature angles. This supports the assumption that particle-to-particle interactions gradually diminish the V-shaped

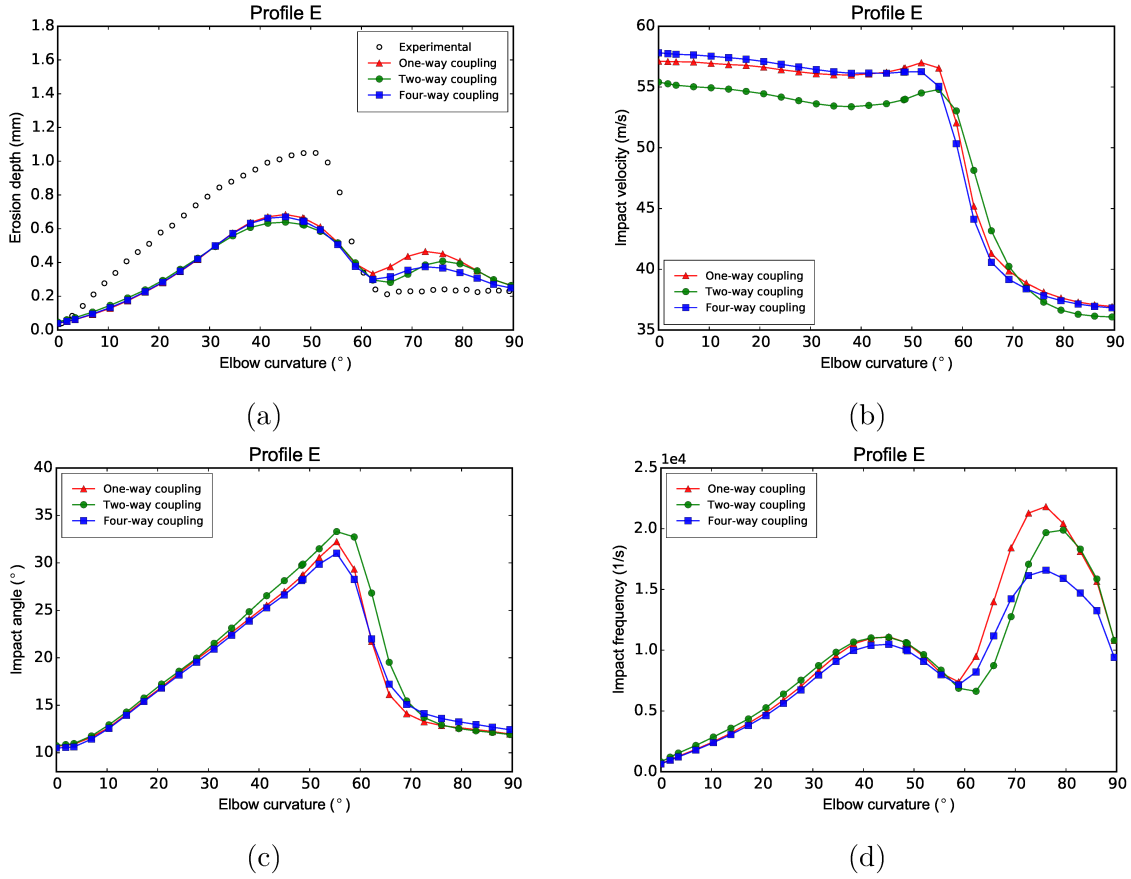


Figure 47 – Erosion-related variables extracted from profile E for one, two and four-way coupling. (a) Erosion depth, (b) impact velocity, (c) impact angle and (d) impact frequency. Mass loading $\eta = 3.846\%$.

erosion scar even at low mass loadings.

Note that the impact velocity (Fig. 47b) and the impact angle (Fig. 47b) exhibit the same trends as profile C (see Figs. 45b and 45c). On the other hand, the impact frequency (Fig. 47d) follows the patterns of the erosion depth (Fig. 47a), in which a slight reduction is visible in the four-way coupling case.

Based on these considerations, there are two different ways particles can cause wear in elbows: they can either directly drive the erosive process by consecutive stresses exerted on the wall (curvature angles smaller than 60°) or by indirect stresses after the first impact (curvature angles larger than 60°). Such mechanisms propagate along the radial position of the elbow as demonstrated by the present analysis (see Figs. 41a, 45a and 47a).

In view of the complexity of the phenomenon, the erosion depth predictions for the present validation are in reasonable agreement with experiments for all the profiles. The final results depend on secondary impacts, which in turn require detailed information on the particle shape and the interaction among themselves and with the walls. Different calibrations for such parameters might improve the agreement for one or another specific

profile, although with a penalty for the overall match. It is important to bear in mind that the erosion model proposed by [Oka and Yoshida \(2005\)](#) can take into account, for instance, the particle shape (see Eqs. 3.49 and 3.50) and diameters (see Eq. 3.51), differing from other models ([Bitter \(1963a\)](#), [Finnie and McFadden \(1978\)](#), [Ahlert \(1994\)](#), [Neilson and Gilchrist \(1968\)](#), [Zhang et al. \(2007\)](#), [Meng and Ludema \(1995\)](#), [Tilly \(1973\)](#), [Haugen et al. \(1995\)](#), [Huang et al. \(2008\)](#)). In this sense, the authors believe that this erosion model will be able to accurately reproduce complex erosive situations once improvements on non-spherical particle modeling interactions are feasible.

7.2.2.3 Influence of the surface roughness on the penetration depth

Although the particle behavior on rough walls has been widely investigated ([Sommerfeld and Huber \(1999a\)](#), [Sommerfeld and Kussin \(2004\)](#), [Benson et al. \(2004\)](#), [Laín and Sommerfeld \(2008\)](#)), its effects on elbow erosion has received little attention ([Solnordal et al. \(2015\)](#)). In this regard, the effect of wall roughness on particle-wall interactions, and its subsequent effect on particle trajectories and hence predicted erosion distribution was investigated.

In order to account for such impact, five cases with $\Delta\gamma$ equal to 3.0° , 5.0° , 7.0° and 9.0° respectively, were then run to assess their effects on the erosion depth. To avoid additional parameter interference, all the cases were simulated with $\eta = 3.846\%$ and the static and dynamic coefficients of friction were constant with $\mu_s = 0.45$ and $\mu_d = 0.30$ respectively. For the sake of brevity, only four-way coupling cases will be presented from now.

Fig. 48 shows the erosion depth contour from the lowest (Fig. 48a) to the highest (Fig. 48d) wall roughness. The contours that most resemble the one measured in the experiment (see Fig. 6b of [Solnordal et al. \(2015\)](#)) occur for higher roughness (Figs. 48c and 48d). It is evident that the increase of the wall roughness is contributing to the particles dispersion preventing the formation of the vee-shaped erosion scar. Furthermore, the region of maximum erosion are qualitatively similar for all the cases but its magnitude is decreasing with the roughness augmentation. This means that the particle-wall interactions with rougher walls extracts more momentum from the particles during the whole course to the elbow which is consistent with the lower magnitude presented for higher roughnesses. This, in turn, causes particles to hit the elbow surface with less energy, thereby reducing the erosion.

To identify the eroding mechanisms on the elbow wall and relate them with the roughness variation, all the erosion-related variables (impact velocity, impact angle and impact frequency) are presented for each profile discussed in Section 7.1.1.

Fig. 49a shows the erosion depth at the profile A location. For the smoother pipe walls ($\Delta\gamma = 3.0^\circ$ and 5.0°), a slight increase in the erosion depth is observed. In all cases,

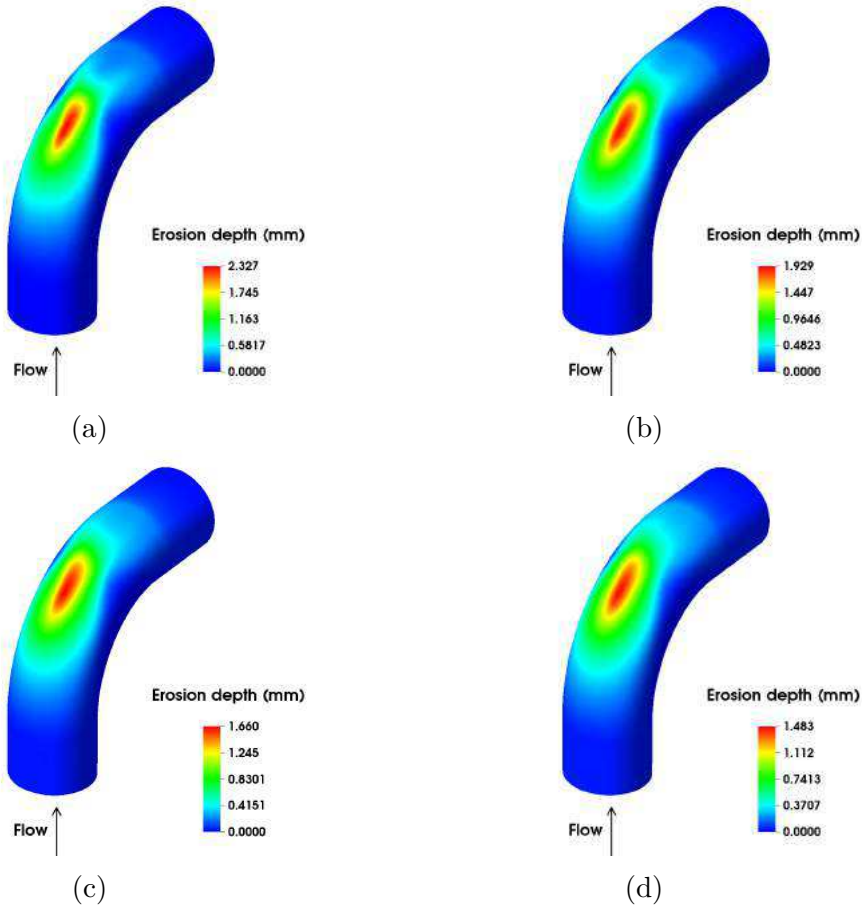


Figure 48 – Erosion depth contours for mass loading $\eta = 3.846\%$ for four-way coupling. (a) $\Delta\gamma = 3.0^\circ$, (b) $\Delta\gamma = 5.0^\circ$, (c) $\Delta\gamma = 7.0^\circ$ and (d) $\Delta\gamma = 9.0^\circ$.

the erosion magnitude is monotonically decreased for curvature angles between 30° and 65° with the roughness increase. Such behavior was expected since smoother walls lead to less particle dispersion. Consequently, the mean distance traveled by the particle after successive wall collisions are longer and the momentum lost by the particle to the wall are smaller. This is in accordance to work of [Sommerfeld and Huber \(1999a\)](#) which found that the wall roughness considerably alters the rebound behavior of the particles causing a re-dispersion.

Generally, the particle impact velocity (Fig. 49b) against the elbow wall decreases with the roughness increase whereas the impact angle (Fig. 49c) presents the opposite trend. Since the inter-particle collisions are of minor importance due to the low mass loading, it is obvious that the impact velocity reduction is influenced by the wall roughness. Consequently, severe particle dispersion by rougher walls induces more wall-normal collisions. This causes the particle impact angle (Fig. 49c) to become greater in rough walls than in perfectly smooth ones. As already mentioned in the validation section, the impact frequency (Fig. 49d) plays a decisive role on the erosion patterns (Fig. 49a) at the profile A region.

For convenience, profiles C and E will be omitted from the presented analysis. For

both profiles, the surface roughness effect is towards reducing the erosion depth. Although a better match is obtained for profile A, the trends are the same with regard to impact frequency, impact angle and impact velocity.

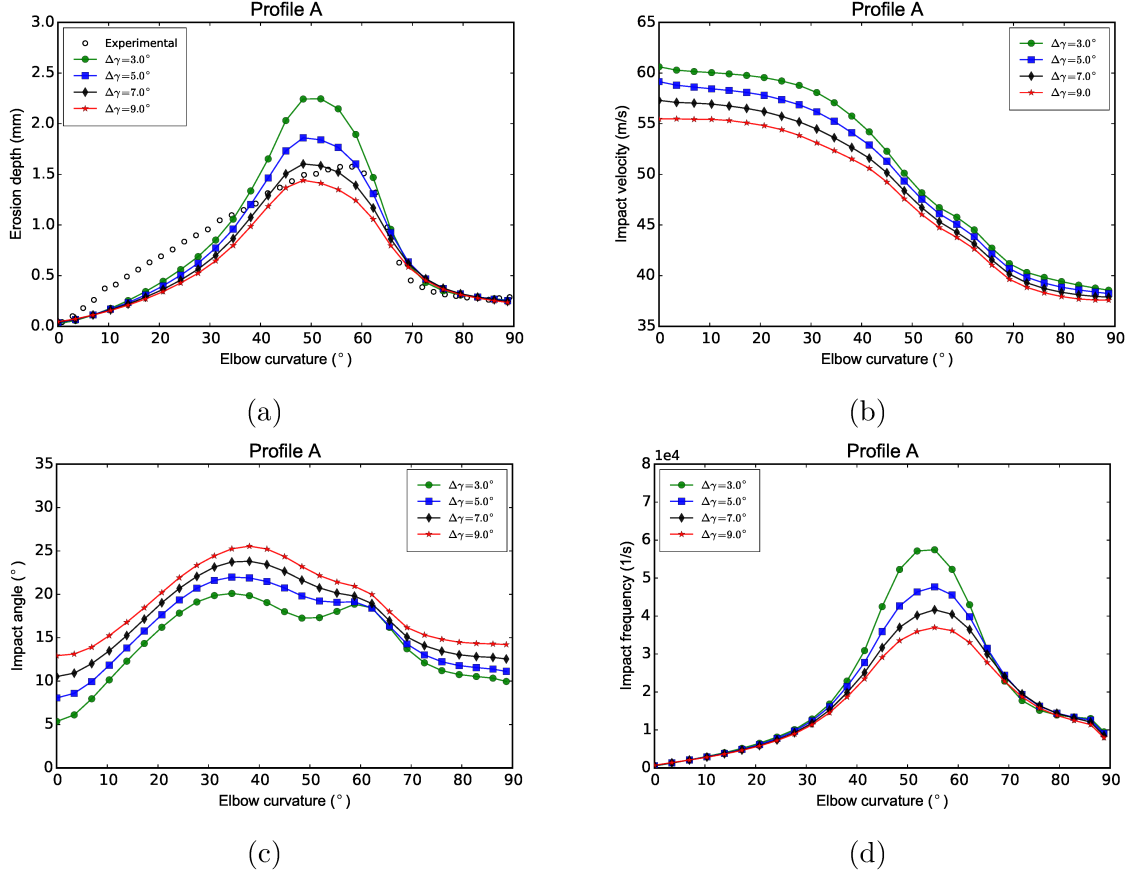


Figure 49 – Erosion-related variables extracted from profile A for four-way coupling. (a) Erosion depth, (b) impact velocity, (c) impact angle and (d) impact frequency. Mass loading $\eta = 3.846\%$.

7.2.2.4 Influence of the static and dynamic coefficients of friction in the penetration depth

The coefficients of friction are dimensionless parameters which express the relationship between two contact materials when one slides towards the other. Their values are characteristic for each pair of materials and it is not an intrinsic property of the material. Therefore, it depends on factors such as surface finish, the relative velocity between the surfaces, temperature, for instance. The dynamic coefficient of friction is always smaller than the static coefficient of friction.

In order to investigate the effects of the static and dynamic coefficients of friction on elbow erosion, four cases abbreviated as denoted in Table 8 were simulated. For all these cases, a surface roughness of $\Delta\gamma = 7.0^\circ$ were prescribed and the mass loading was kept constant ($\eta = 3.846\%$).

Table 8 – Abbreviation of the computed cases.

Case abbreviation	Static coefficient (μ_s)	Dynamic coefficient (μ_d)
S60D45	0.60	0.45
S45D30	0.45	0.30
S15D30	0.15	0.30
S15D15	0.15	0.15

Fig. 50 displays the erosion depth contours for the above-mentioned cases. Generally, the erosion contours show a substantial augmentation of the erosion depth magnitude with both coefficients decreasing. Curiously, none of the cases displayed the vee-shaped erosion scar. This indicates that the coefficients of friction are not considerably affecting the particle-wall interaction downstream of the elbow.

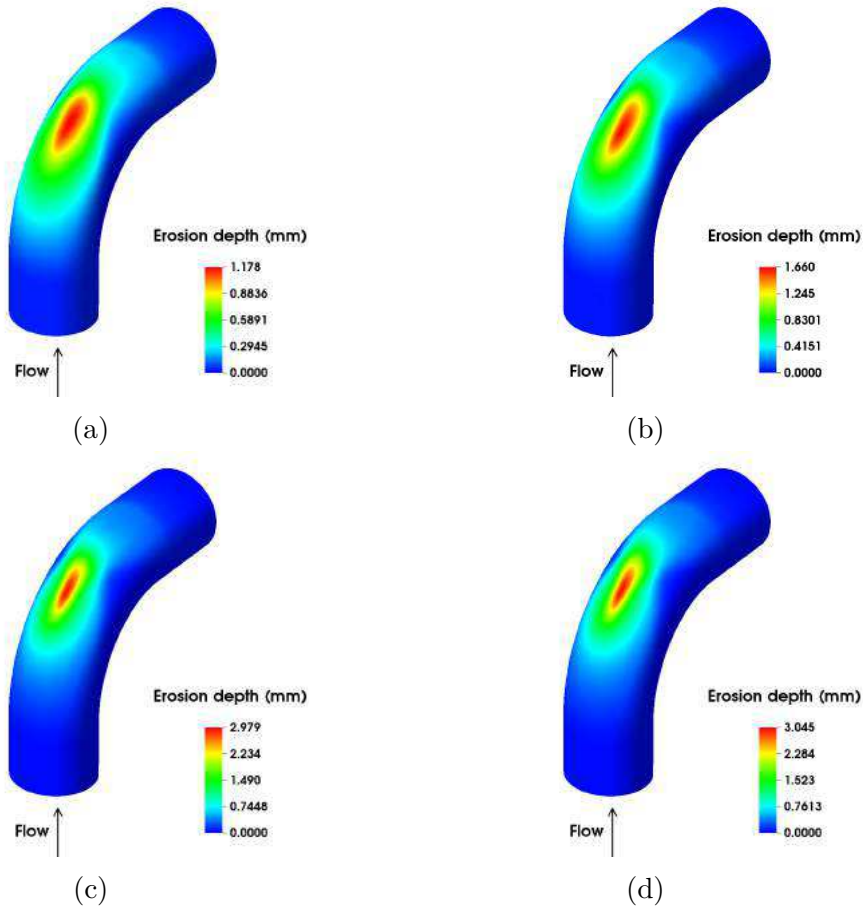


Figure 50 – Erosion depth contours for mass loading $\eta = 3.846\%$ for four-way coupling. (a) $\mu_d = 0.45$ and $\mu_s = 0.6$, (b) $\mu_d = 0.3$ and $\mu_s = 0.45$, (c) $\mu_d = 0.3$ and $\mu_s = 0.15$, (d) $\mu_d = 0.15$ and $\mu_s = 0.15$.

Although not physically coherent, when setting the static coefficient lower than the dynamic (case S30D15, Fig. 50c) or both equal (case S15D15, Fig. 50d) the erosion depth (Fig. 51a) for profile A does not display any significant discrepancy between each other. The same happens for the impact velocity (Fig. 51b) and impact angle (Fig. 51c). In

addition, both cases show greater magnitudes of erosion depth. Such behavior was expected since, by reducing the static and dynamic coefficients of friction, the static and dynamic friction forces are also reduced. This directly affects the resistance particles experience when interacting with the walls and results in higher impact frequencies (Fig. 51d).

For the dynamic coefficient smaller than the static (cases S60D45 and S45D30, Figs. 50a and 50b respectively) a visible difference on the erosion depth is observed (Fig. 51a). For both situations, the increase in the coefficients of friction increases the resistance to particle motion along the wall. As a consequence, the particle impact velocity (Fig. 51b) is considerably reduced. Note that the static coefficient of friction contributes to determine whether a collision against the wall will behave as sliding or nonsliding. In this sense, cases S60D45 and S45D30 are more susceptible to the occurrence of nonsliding collisions which explains, in turn, the erosion reduction in such cases. Nonsliding and sliding collisions dictate whether a particle will be ejected from the wall with more or less energy. This clarifies the amplification of the maximum erosion region observed in the contours of Figs. 50a and 50b.

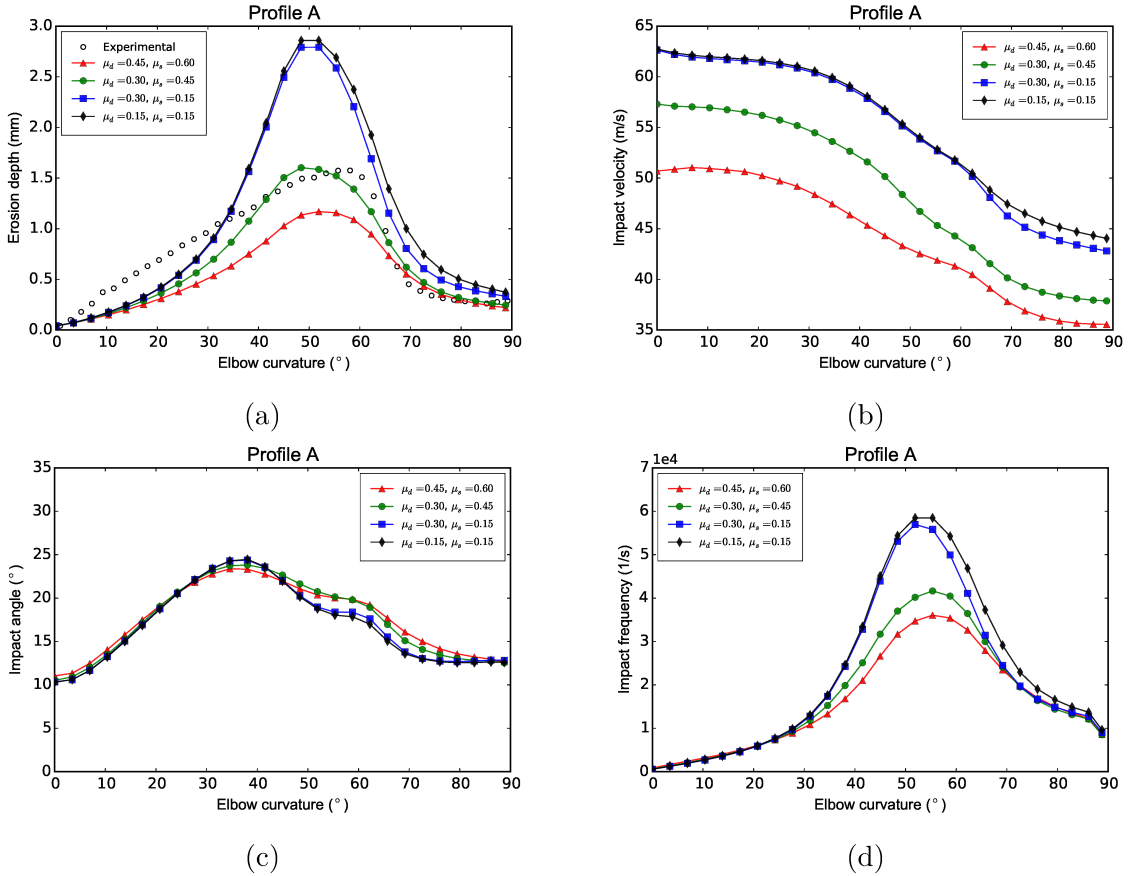


Figure 51 – Erosion-related variables extracted from profile A for four-way coupling. (a) Erosion depth, (b) impact velocity, (c) impact angle and (d) impact frequency. Mass loading $\eta = 3.846\%$.

It is noteworthy that no sudden change was observed in the impact angle that the

particles reach the elbow wall (Fig. 51c). This result confirms that the alteration in the impact angle preferably occur by changes in the surface roughness rather than the friction coefficients.

The numerical results for profile C can be seen in Fig. 52. One characteristic is readily apparent from the erosion depth plot (Fig. 52a). The region between 35° and 65° shows a clear difference in shape among all the cases. Cases with higher coefficients (S60D45 and S45D30) exhibit less flattening in the aforesaid region compared to the lower ones (S15D30 and S15D15). Although the latter seems to better fit the experimental result, it is important to bear in mind that they are non-physical parameters. Additionally, these cases produced two peaks at 45° and 60° , unlike the experiment. Naturally, the impact velocity (Fig. 52b) and impact angle (Fig. 52c) followed the same tendency of profile A. In fact, the modification of the coefficients of friction are not affecting the impact angle.

The impact frequency (Fig. 52d) resembles the profile obtained in the validation section (Fig. 45d) and reveals that, independent of the coefficients of friction, the impact frequency is not the leading erosion process at such location.

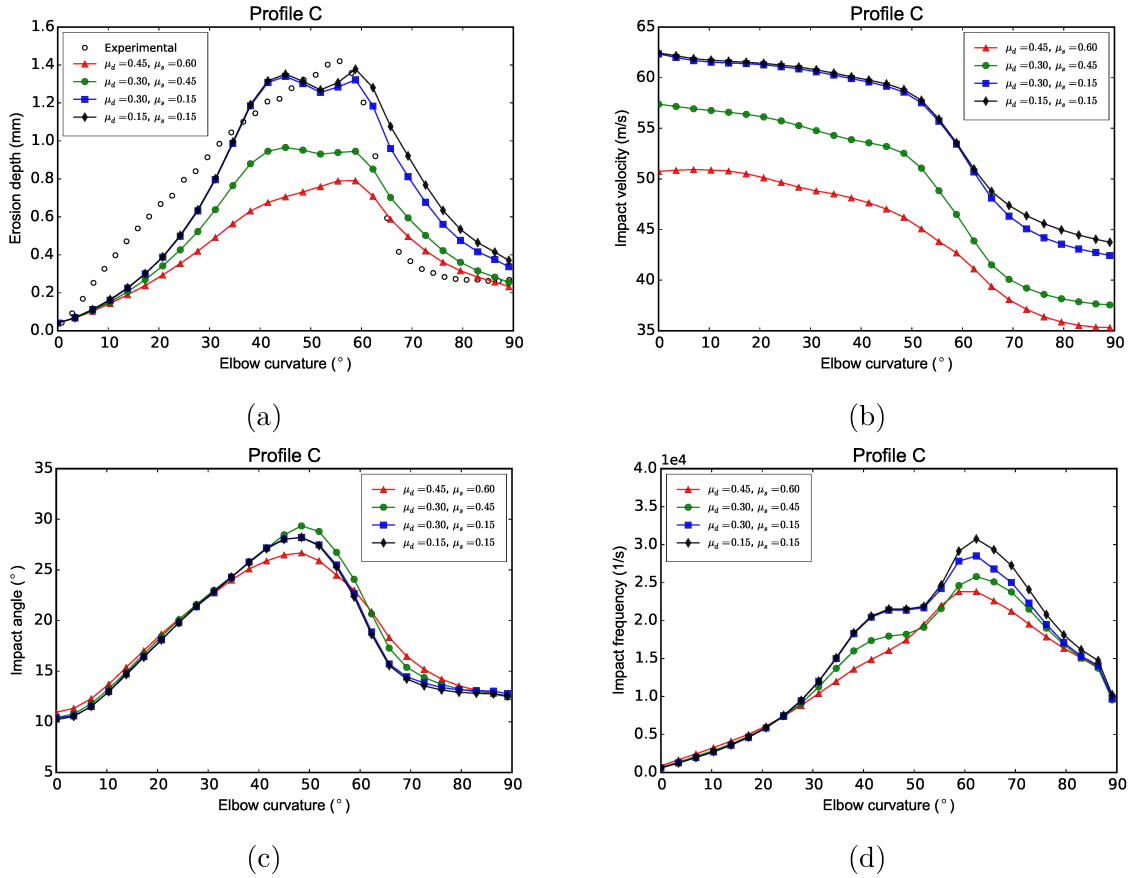


Figure 52 – Erosion-related variables extracted from profile C for four-way coupling. (a) Erosion depth, (b) impact velocity, (c) impact angle and (d) impact frequency. Mass loading $\eta = 3.846\%$.

For the sake of brevity, profile E will not be presented, as the results followed the

same trend of the erosion-related variables for profiles farther from the symmetry plane.

As they refer to highly dependent parameters of the material pair and environmental conditions, the coefficients of friction should be adjusted and there is no database providing the relationship for sand and aluminum.

7.2.2.5 Influence of the mass loading in the penetration depth

Mass loading is a variable that has been explored in a few works on erosion. In this respect, the influence of the mass loading on elbow erosion was investigated. Six cases with η equal to 3.846%, 10%, 30%, 50%, 70% and 90%, respectively, were simulated to assess their effects in the penetration depth. All the cases considered inter-particle collisions (4-way-coupled simulations). Fig. 53 displays the erosion depth contours for the six cases studied.

Clearly, the erosion depth pattern is modified with the mass loading increase. For the lower mass loading cases (Figs. 53a, 53b and 53c) the erosion contour retains certain symmetry along the outer elbow wall. On the other hand, higher mass loadings (Figs. 53d, 53e and 53f) lead to a stretching of the maximum erosion region. Besides, the profile is slightly shifted to the left, producing a teardrop-shaped erosion pattern. To the best of the authors knowledge, this is the first time that such behavior is captured by simulations. To clarify such behavior, the particle concentration contour for each mass loading is presented in Fig. 54. Cases with lower mass loadings (Figs. 54a, 54b and 54c) show an almost symmetric distribution on the outer elbow wall. In the remaining (Figs. 54d, 54e and 54f), the particle concentration contour rotates counterclockwise. Somehow, the inter-particle collisions downstream of the main impact region are forcing the particles path to the left side of the elbow. Therefore, for higher mass loadings the inter-phase interaction far upstream of the elbow are extremely important and reflect on how the particles will enter the elbow.

Another important effect is observed in the erosion depth. Visually speaking, its maximum is diminishing with the mass loading increase. [Bikbaev et al. \(1972\)](#) report experimental results that demonstrate such effect (reduction of the erosion rate with mass loading increase). In fact, mining companies employ such effect to design process equipment ([Utikar et al. \(2010\)](#)). Numerically, previous publications ([Duarte et al. \(2015\)](#), [Duarte et al. \(2016\)](#)), predicted the cushioning effect based on the experimental configuration of [Mazumder et al. \(2005\)](#) but the lack of details about the experimental setup restricted the analysis to the elbow centerline of the outer radius.

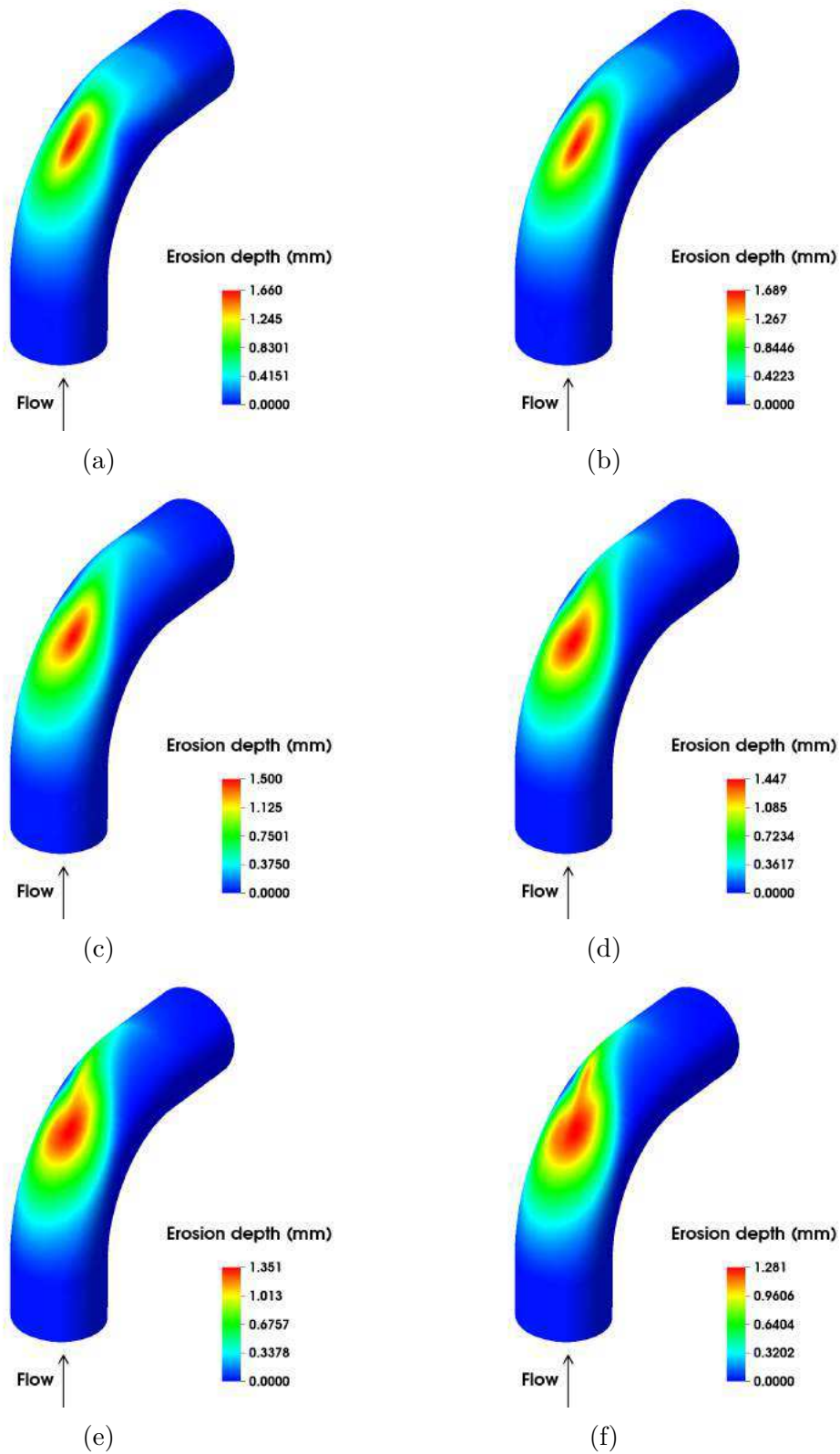


Figure 53 – Erosion depth contours for mass loadings: (a) $\eta = 3.846\%$, (b) $\eta = 10.0\%$, (c) $\eta = 30.0\%$, (d) $\eta = 50.0\%$, (e) $\eta = 70.0\%$ and (f) $\eta = 90.0\%$.

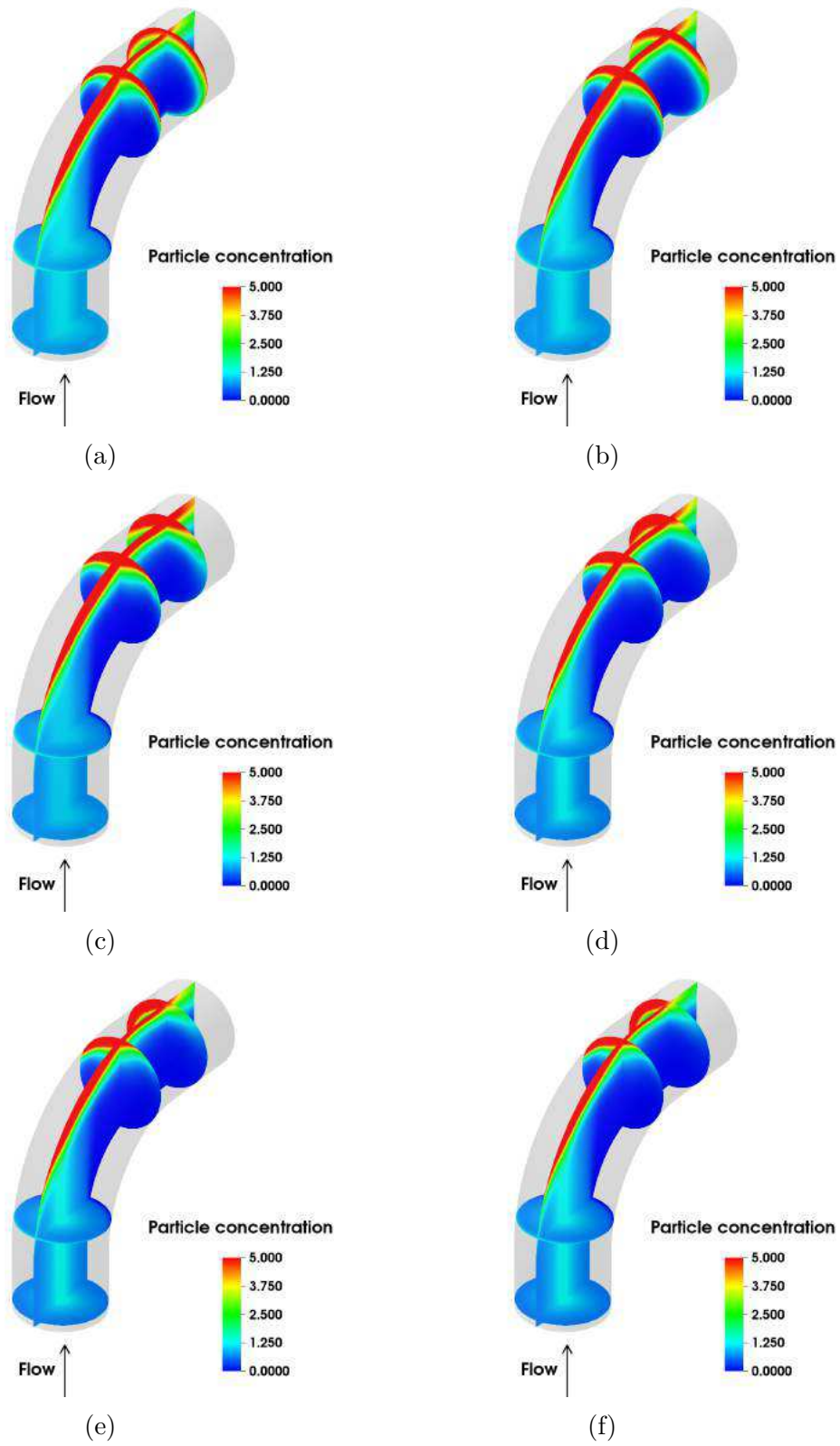


Figure 54 – Particle concentration contours for mass loadings: (a) $\eta = 3.846\%$, (b) $\eta = 10.0\%$, (c) $\eta = 30.0\%$, (d) $\eta = 50.0\%$, (e) $\eta = 70.0\%$ and (f) $\eta = 90.0\%$.

Contrary to common sense, increasing the particle concentration is actually reducing the erosion depth. To show this reduction, Fig. 55 depicts all the erosion-related variables for profile A. Quantitatively speaking, the erosion depth (Fig. 55a) is gradually reduced with the mass loading increase. This proves that the cushioning effect is occurring at this location and can only be predicted because inter-particle collisions were considered in the simulations. In fact, if particle-to-particle interactions were neglected in the computations the erosion depth would present similar patterns for all the cases.

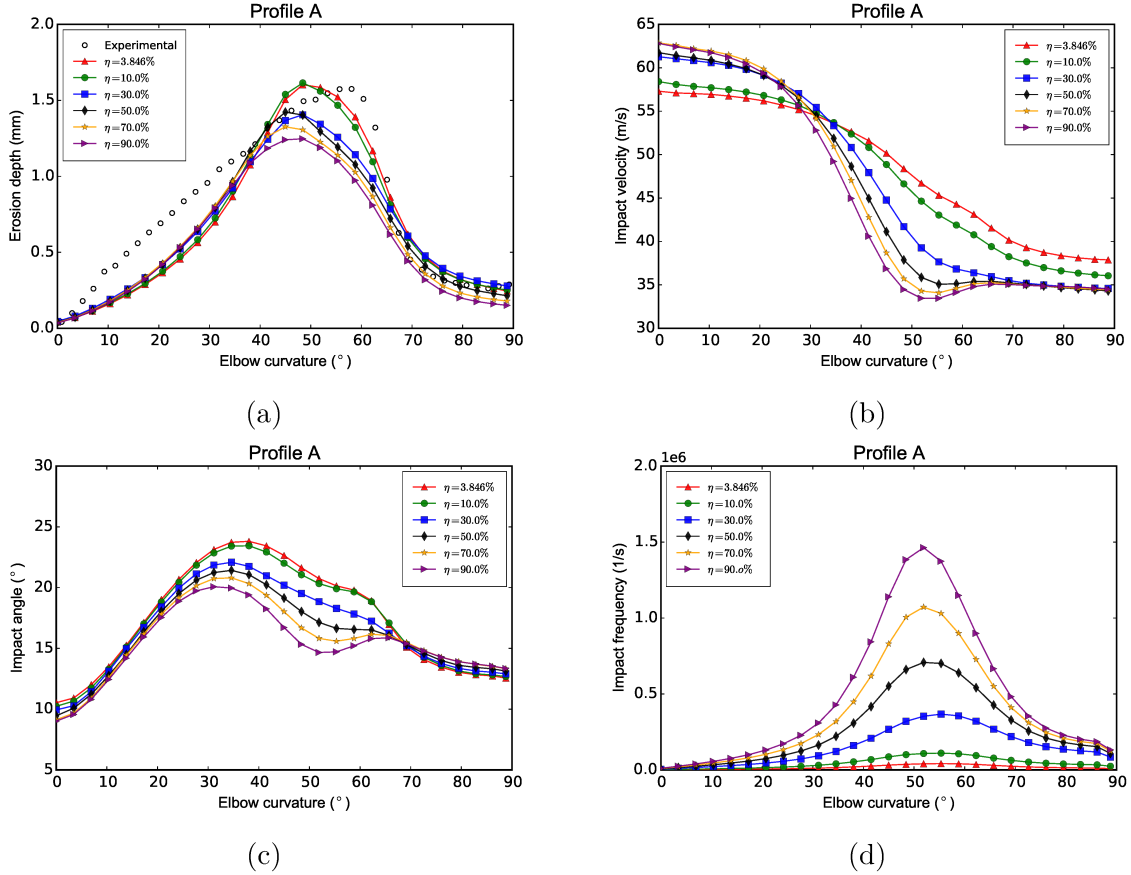


Figure 55 – Erosion-related variables extracted from profile A for four-way coupling. (a) Erosion depth, (b) impact velocity, (c) impact angle and (d) impact frequency.

To support this statement, a mechanism of erosion reduction at profile A is proposed by the authors and is schematically presented in Fig. 56. The cushioning process is divided into three steps: (1st step) Particles enter the elbow carried by the fluid stream. At this stage, both the inter-particle collisions and particle-wall interactions are not relevant to the process. (2nd step) Since the particles are very inertial ($Stk = 29.08$) their motion is decoupled from the fluid. Hence they tend to go straight to the outer elbow wall. After the collisions against the elbow wall, the particles are forced to change their direction. This deviation begins for curvature angles larger than 25° and causes the particles to move towards the core flow or new near wall locations. At this step, inter-particle interactions become important. (3rd step) The cushioning effect takes place for curvatures angles larger

than 40° . At this location, a larger amount of particles are ejected from the elbow wall and the collisions between them are of major importance. At this stage, the particles adjacent to the wall create a "virtual barrier" which damps the surrounding particles to directly hit the elbow wall (see Fig. 56, zoomed region). As the mass loading increases, such effect is enhanced and the erosion depth is significantly reduced (Fig. 55a).

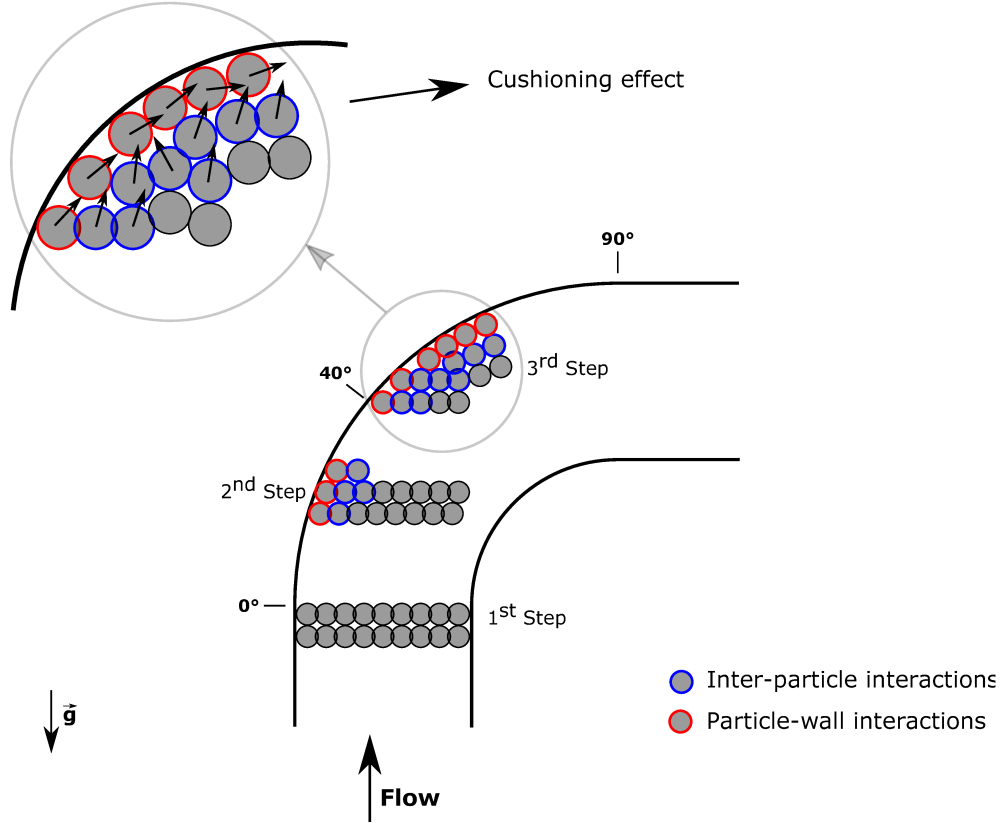


Figure 56 – Scheme representing the cushioning effect caused at high mass loadings.

Uuemõis and Kleis (1975) suggested that inter-particle collisions prevent other particles to reach the surface. According to them, the inter-particle collisions create a protective barrier that reduces erosion. Interestingly, the particle impact frequency (Fig. 55d) increased for curvature angles between 40° and 60° with the mass loading augmentation. This is in accordance to Sommerfeld and Laín (2015) which found that inter-particle collisions actually increase the number of particle-wall collisions in the elbow. However, this contradicts the notion of a protective barrier proposed by Uuemõis and Kleis (1975) and states that the inter-particle collisions are indeed reducing the energy of the incoming particles. Although the impact frequency increases, the energy per particle is lower which results in the erosion reduction. Since no physical barrier is formed to protect the elbow surface, the authors prefer to consider the cushioning effect as a consequence of a "virtual barrier". Such term is reasonable since the dynamic motion of the particles is the main factor to initiate the cushioning effect.

Additionally, the particle impact velocity (Fig. 55b) shows a visible reduction for

curvature angles between 40° and 60° with mass loading increase. This suggests that the inter-particle collisions at this location are corroborating to the velocity reduction of the approaching particles. In case of the impact angle (Fig. 55c), the increase of the mass loading also leads to a decrease in the impact angles, especially for curvature angles lower than 65° . The reason is that near wall particles at higher mass loading cases are forced to drift towards regions with high particle concentration. This region of particle concentration extracts momentum from the incoming particles and redirects them to the wall with lower impact angles. The combined effect of the reduction of the impact velocity as well as the impact angle of wall colliding particles is the most reasonable explanation to the maximum erosion depth decrease at profile A.

The results of profile C are presented on Fig. 57. The erosion depth (Fig. 57a) is slightly reduced for curvature angles between 25° and 50° . On the other hand, the cases with $\eta = 70\%$ and $\eta = 90\%$ showed a pronounced peak at 65° . Such behavior reproduced the left shifted erosion depth of Figs. 53e and 53f. In general, the impact velocity (Fig. 57b), impact angle (Fig. 57c) and impact frequency (Fig. 57d) resemble the ones presented for profile A. This indicates that the cushioning effect is still present on locations other than the elbow symmetry plane.

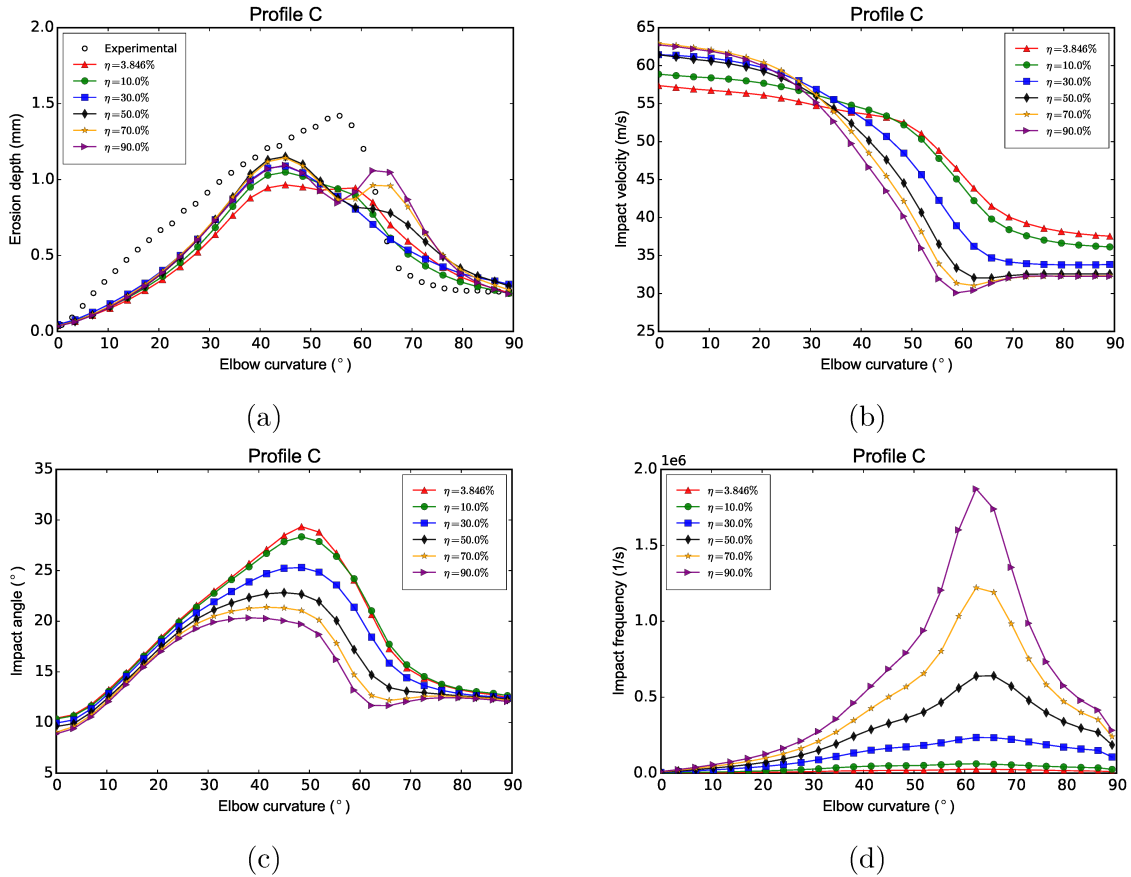


Figure 57 – Erosion-related variables extracted from profile C for four-way coupling. (a) Erosion depth, (b) impact velocity, (c) impact angle and (d) impact frequency.

The same cannot be assigned to profile E (Fig. 58). At this location, the increase of the mass loading also increased the erosion depth (Fig. 58a). Remarkable increase of the erosion depth is observed for higher mass loading cases and curvature angles larger than 60° . Note, however, that both impact velocity (Fig. 58b) and impact angle (Fig. 58c) are slightly influenced by the mass loading variation. Since no attenuation of the above-mentioned variables exists between 40° and 60° it is safe to assume that the cushioning effect is unlikely to occur at profile E location.

It is evident that the impact frequency (Fig. 58d) has a drastic effect on the erosion depth (Fig. 58a) at this location. The reason is that the incoming particles rebounded from profiles A and C regions are preferably concentrating on curvature angles larger than 60° .

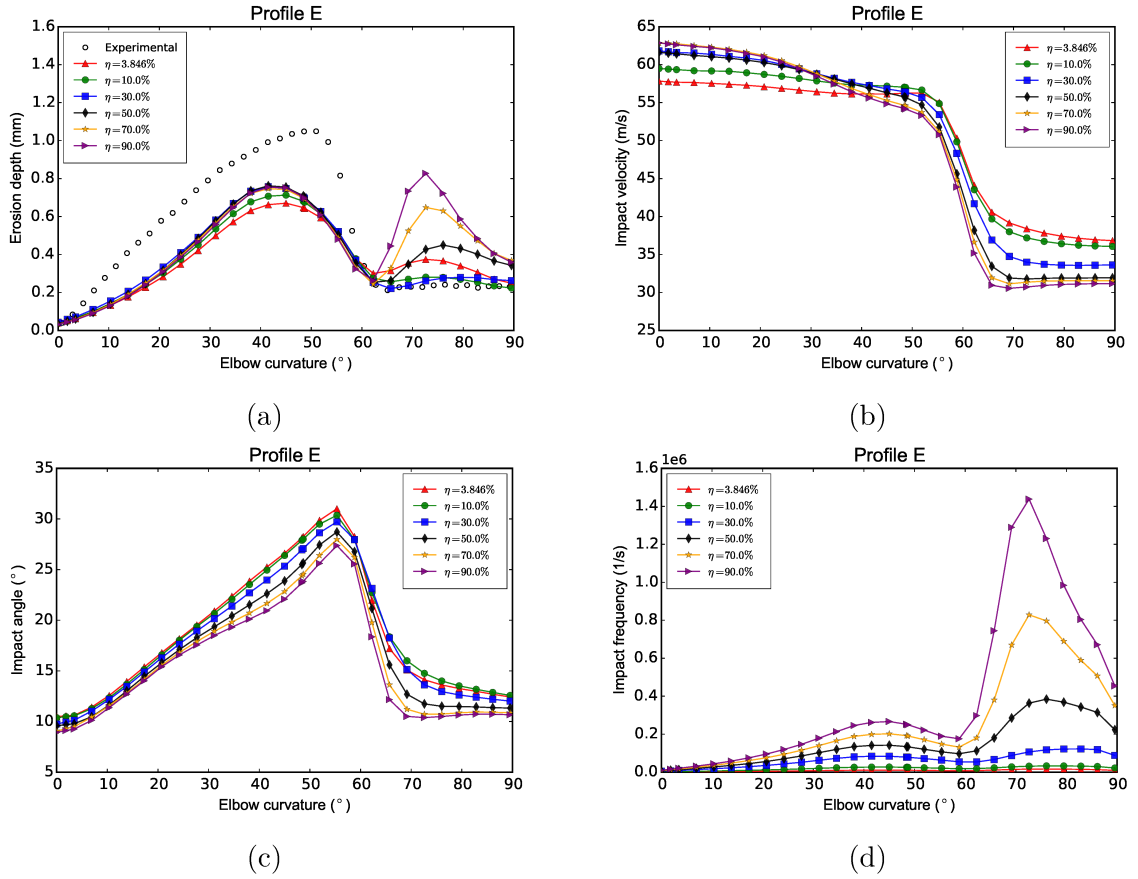


Figure 58 – Erosion-related variables extracted from profile E for four-way coupling. (a) Erosion depth, (b) impact velocity, (c) impact angle and (d) impact frequency.

7.3 Chapter conclusions

A substantial amount of work undertaken in this chapter was to elucidate further understanding of the erosion process on a 90° elbow pipe and to evaluate the fundamental characteristics during the particle-wall surface interaction. In this sense, the present work

tries to shed some light on the dynamics governing particle-laden flows in elbow erosion by means of a four-way coupled URANS combined with a Lagrangian approach for the particles. In order to validate the erosion model and to add confidence to the results, the erosion profiles were compared with experimental data. In a second step, several values of wall roughness and coefficients of friction were experimented with and compared with experimental measurements. Furthermore, the role of inter-particle collisions was enlightened for six different values of mass loading.

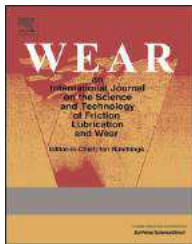
The main results of this study are:

- A significant difference exists between the phase interactions for the low mass loading case ($\eta = 3.846\%$). Although one-way coupling and four-way coupling were found to be similar, the two-way coupling case showed a characteristic drift of the particles to the wall.
- For $\eta = 3.846\%$ the inter-particle collisions was found to play a major role at profile E location. Such interactions suppress the erosion contours, found in previous works, bringing results closer to the experiments. This proves that even at low mass loading cases, the inter-particle collisions positively affect the numerical results.
- For $\eta = 3.846\%$, the predictions demonstrate that particles can cause wear in elbows in two different ways. Particles can directly drive the erosive process by consecutive stresses exerted on the wall (curvature angles smaller than 60°) or by indirect stresses after the first impact (curvature angles larger than 60°).
- A parametric variation of the surface roughness showed that the erosion depth monotonically diminishes with the roughness increase.
- The impact angle was not affected by the modification of the coefficients of friction. This proves that the alteration of the impact angle primarily occurs by changes in the surface roughness rather than the friction coefficients.
- The cushioning effect was captured by the simulations and the mechanisms involved in the process were proposed by the authors.
- For all different mass loading cases, the cushioning effect is restricted to regions near profiles A and C, whereas at the profile E such effect is unlikely to occur.
- Higher mass loading cases require a four-way coupled approach in order to accurately predict the above-mentioned effects.

Chapter 8

Innovative pipe wall design to mitigate elbow erosion

This chapter originates from the following publication:



Duarte, C.A.R., and de Souza, F.J. Innovative pipe wall design to mitigate elbow erosion: A CFD analysis. *Wear*, v. ??, p. ??-??, 2017 (Accepted for publication).

Reprinted by permission from Elsevier Ltd.

8.1 Pipe wall design proposal

The new pipe wall designs are presented in Figs. 59 and 60 with 4 and 8 undulations, respectively. Visibly, the pipe wall concept is simple. Based on the untwisted pipe diameter (D , where D is equal to 102.5 mm), smaller circles (with radius equal to $D/4$) are inscribed and rotated by an angle α_1 (Fig. 59c) and α_2 (Fig. 60c). For the present cases, $\alpha_1 = 90^\circ$ leads to a wall with 4 undulations (4 inscribed circles) whereas $\alpha_2 = 45^\circ$ provides an 8-undulation (8 inscribed circles) pipe wall. It is important to bear in mind that depending on the value of α , the swirl generated by the undulations will be more intense or not. In this sense, the above-mentioned cases were intentionally chosen in order to cover both situations.

Once the undulations are set, they are turned along the axial direction. For both cases, the undulations were turned once (360°) along 1333.5 mm ($13D$) according to Figs. 59b and 60b. The twisted wall length is also important to determine the swirl generated. In fact, a correct combination of the undulations with the twisted length will dictate how

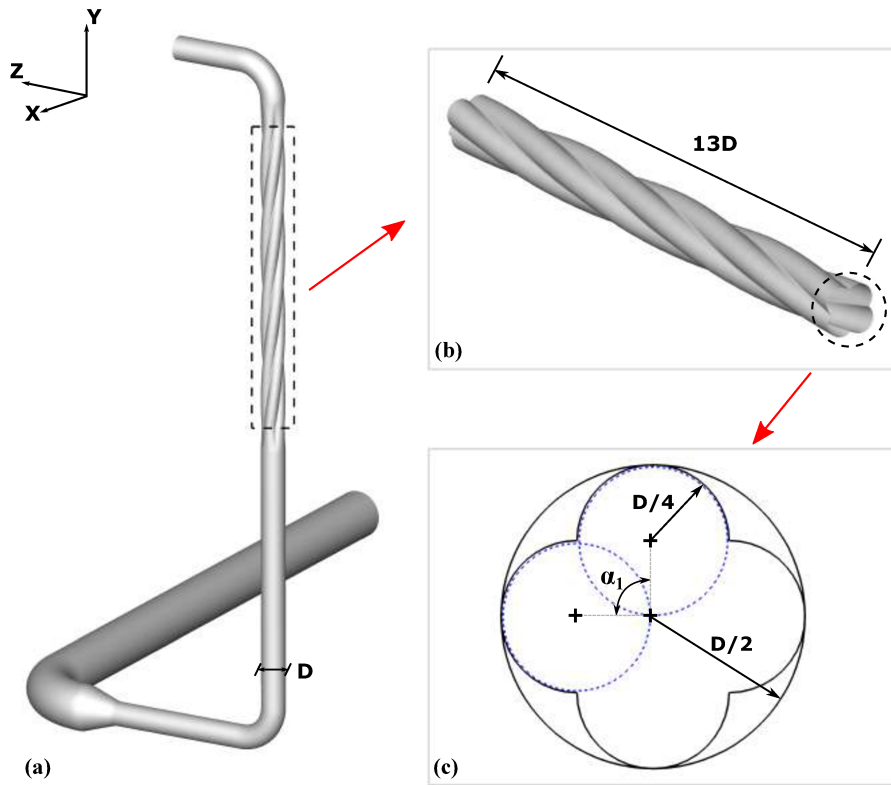


Figure 59 – Schematics of the proposed pipe wall with 4 undulations.

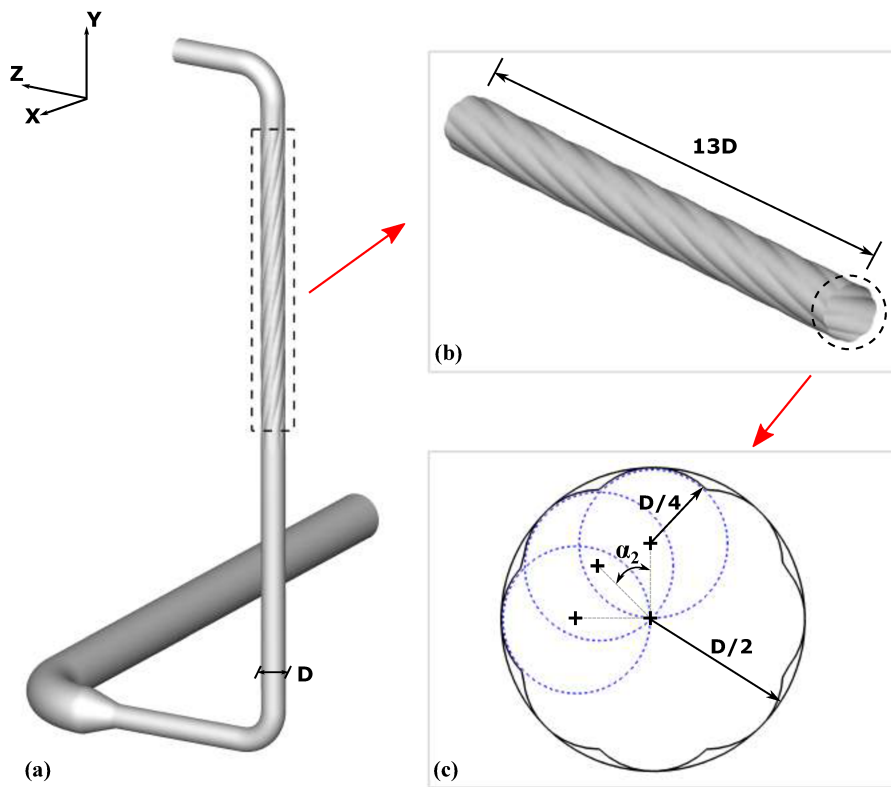


Figure 60 – Schematics of the proposed pipe wall with 8 undulations.

strongly the fluid interacts with the walls. For instance, fewer undulations in a short space can generate the same swirl as a long twisted wall with more undulations. Such parameters are strictly related to each pipeline plant and should be defined according to the desired erosion reduction to be achieved at the elbow.

To add confidence to the proposed wall design on the elbow erosion reduction, the twisted pipe is placed upstream the experimental elbow analyzed by [Solnordal et al. \(2015\)](#) (Figs. 59a and 60a). A soft transition between the untwisted pipe and the twisted wall pipe is made through a pipe of length D (Figs. 61b and 61c). Such transition is important to avoid geometrical discontinuities.

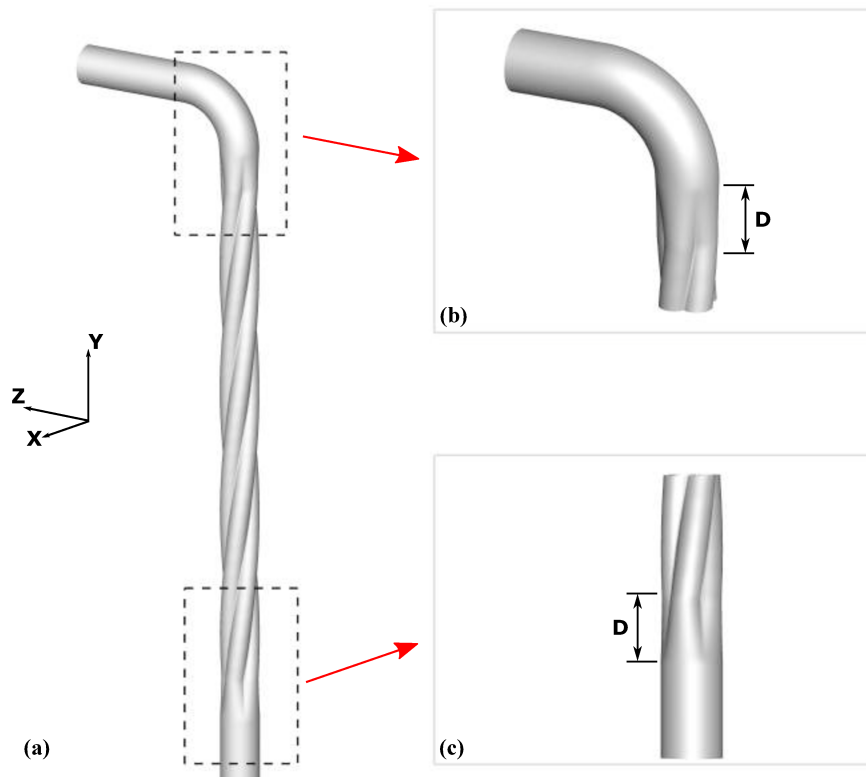


Figure 61 – Schematic representation of the transition between the untwisted and twisted wall pipe.

After a detailed revision in the literature, the authors are convinced that the twisted pipe wall has never been used as an alternative to mitigate erosion. With this in mind, the present study aims to contribute to the scientific community by proposing a new pipe concept to reduce elbow erosion when particles are to be conveyed.

8.1.1 Geometries and grids

The calculations were performed with grids containing hexahedral cells (Figs. 62a, 63a and 64a). Near wall refinement is necessary (Figs. 62c, 63c and 64c), since the boundary layers are very thin. In all simulations, the first element away from the wall was positioned

so that the dimensionless wall distance y^+ lower than one. To generate the twisted wall pipe (Figs. 63b and 64b), 8 blocks were extruded and rotated in the axial direction. Such operation did not distort the elements and provided good fit to the actual geometry.

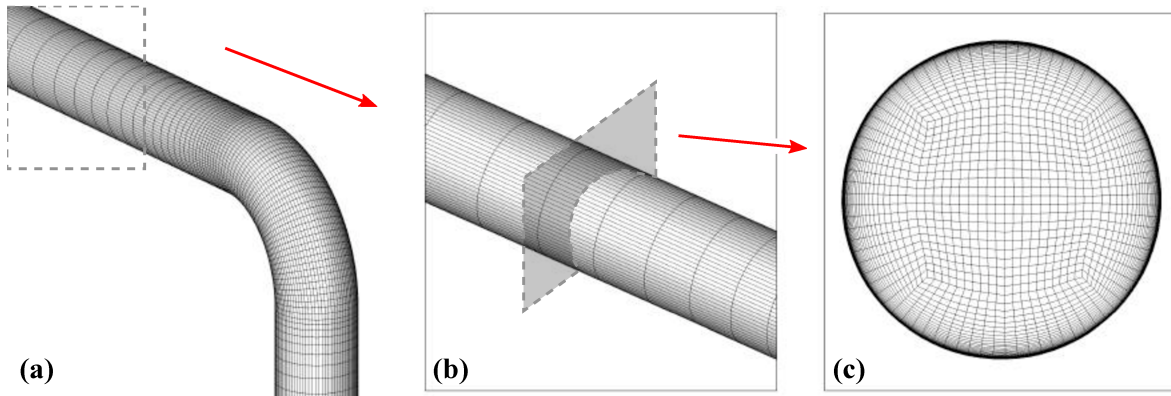


Figure 62 – (a) Grid of the untwisted pipe, perspective view. (b) Detail view of the untwisted pipe. (c) Grid cross section upstream of the elbow.

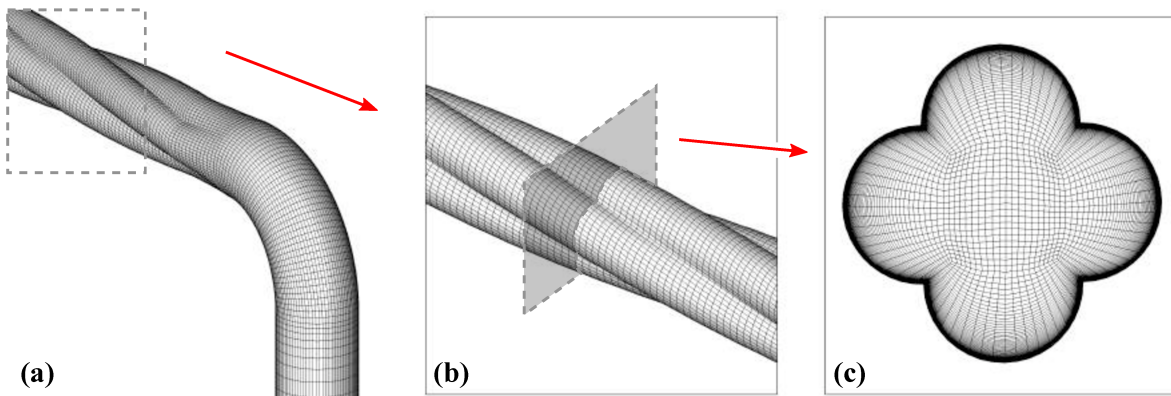


Figure 63 – (a) Grid of the twisted wall pipe with 4 undulations, perspective view. (b) Detail view of the twisted pipe. (c) Grid cross section upstream of the elbow.

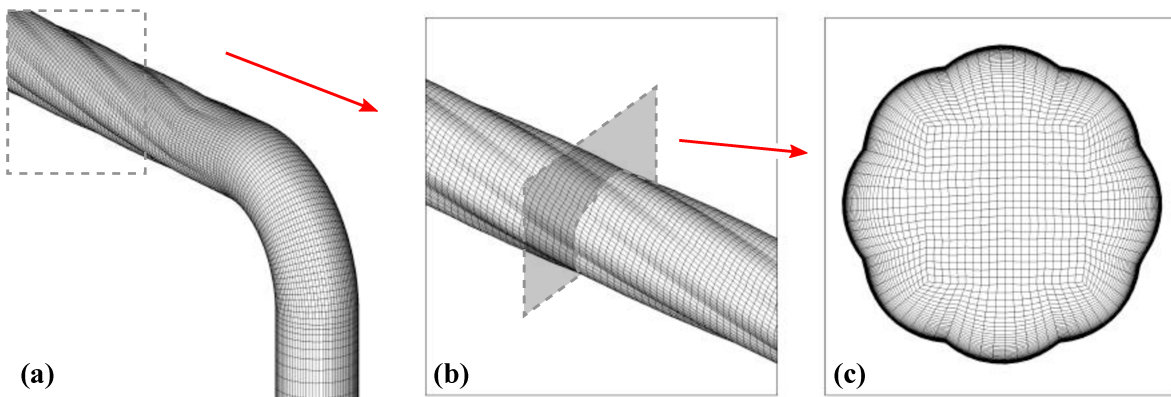


Figure 64 – (a) Grid of the twisted wall pipe with 8 undulations, perspective view. (b) Detail view of the twisted pipe. (c) Grid cross section upstream of the elbow.

Table 9 shows the wall y^+ values for the meshes that produced grid-independent results.

Table 9 – Parameters for the erosion model.

Pipe type	Number of elements	Average y^+
untwisted pipe	1,165,742	0.5436
4-spiral pipe	1,658,592	0.6547
8-spiral pipe	1,706,172	0.6559

8.1.2 Boundary conditions

The boundary conditions used in this investigation were as those used in the experiments of [Solnordal et al. \(2015\)](#) (Table 10).

Table 10 – Simulation conditions.

Air flow rate (\dot{m}_f)	0.78 kg/s
Air density (ρ_f)	1.18 kg/m ³
Air viscosity (μ_f)	1.8×10^{-5} Pa.s
Sand flow rate (\dot{m}_p)	0.030 kg/s
Sand density (ρ_p)	2650 kg/m ³
Mass loading (η)	3.846%
Amount of sand passing	300 kg
Mean volume fraction (α_p)	1.746×10^{-5}

The air velocity at the inlet is prescribed as $U_f = 21.01$ m/s with a turbulence intensity of 0.1%. A gauge pressure of 0 Pa is set at the domain exit. The diameter for particle inlet is 40 mm. The sand particles are introduced with a velocity of $U_p = 1.0$ m/s in crossflow with the air. Their size distribution was represented by 21 classes following the experimental distribution (see Table 2 of [Solnordal et al. \(2015\)](#)), with a mean diameter of 184 μm . 550 parcels are injected at each timestep. Under "steady" state conditions, nearly 11 million particles were used for the statistics. The fluid and particle timesteps were 1.0×10^{-4} s and 1.0×10^{-5} s, respectively.

8.2 Results and discussions

8.2.1 Erosion model validation - Standard 90° elbow pipe

As previously mentioned, the computational results are validated based on the experiments by [Solnordal et al. \(2015\)](#). Fig. 65 shows the contours of the erosion depth (Fig. 65a), particle impact velocity (Fig. 65b), particle impact angle (Fig. 65c) and particle impact frequency (Fig. 65d), with perspective and normal views of the elbow. Quantitatively

speaking, the erosion depth contours (Fig. 65a) resemble the ones obtained experimentally by Solnordal et al. (2015) both in shape and magnitude.

Although only the erosion depth is available from the experiments, additional erosion-related variables (e.g., impact angle, impact velocity and impact frequency) are used for further understanding the phenomenon. The particle impact velocity contours (Fig. 65b) show higher impact velocities halfway of the elbow curvature. In this case, particles are less affected by the turbulence effects and their response to the changes in the fluid direction is reduced. This also explains the sudden impact velocity reduction observed downstream of the elbow.

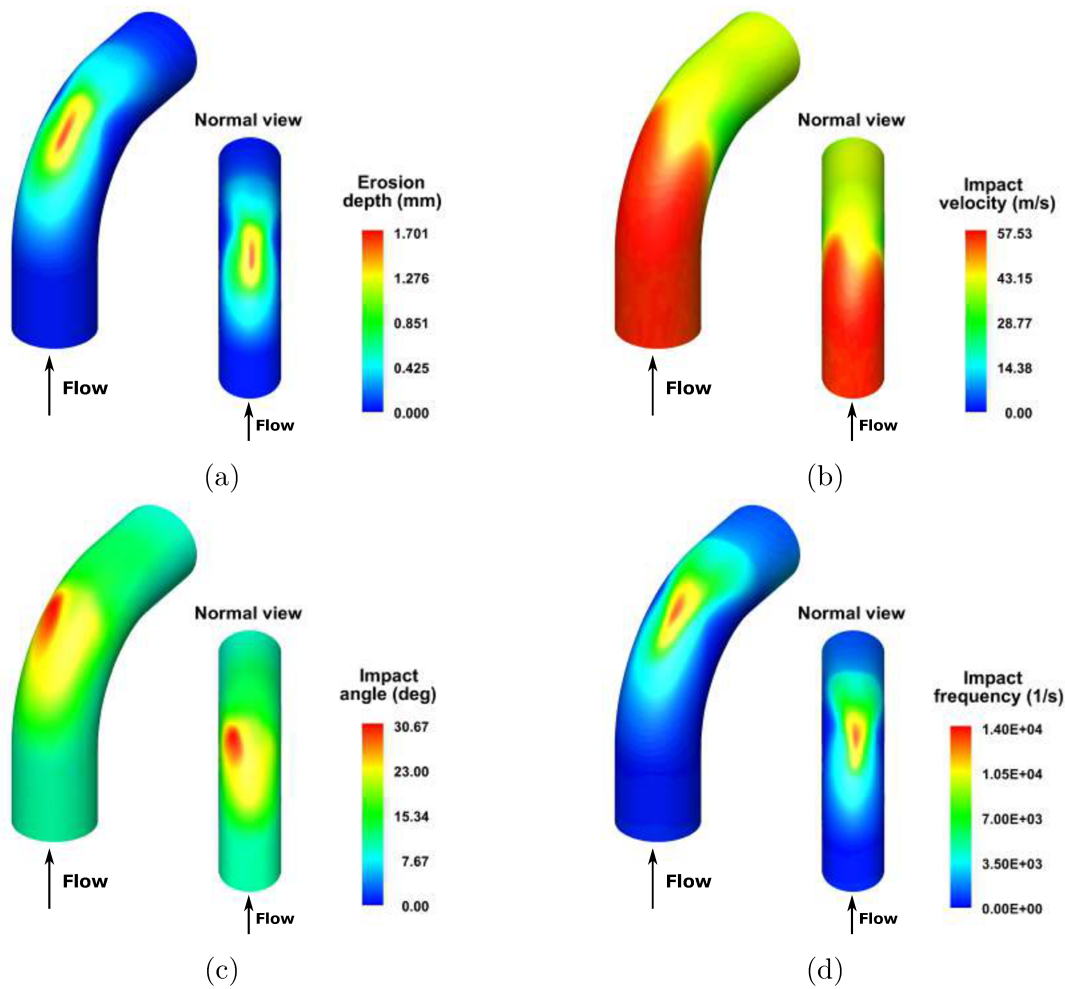


Figure 65 – Contours of the erosion-related variables for the untwisted pipe. (a) Erosion depth, (b) impact velocity, (c) impact angle and (d) impact frequency.

The contours of particle impact angle is presented in Fig. 65c. Higher magnitude can be found on the left side of the elbow. Such preferential increase of the impact angle is related to the particle dynamics upstream of the elbow. Since the entire experimental facility is considered in the simulations, the changes promoted by the other elbows are responsible for modifying the particle path, avoiding them to reach the final elbow with a

uniform profile. This justifies, at least partly, the non-symmetrical contours obtained for both impact velocity (Fig. 65b) and impact angle (Fig. 65c).

At this point, we highlight the importance of simulating the entire experimental facility. If only the vertical pipe section and the elbow were simulated, inlet conditions for both fluid and particles would have to be assumed. Because these conditions are highly dependent on the particle behavior upstream of experimental elbow, such geometric simplification, although attractive in terms of computational costs, can compromise the erosion pattern and its derived variables. Caution should be taken when simulating the erosive wear by particle impact as the flow may not be fully developed before particles collide with the surface of interest.

For completeness, particle impact frequency contours against the elbow wall are presented in Fig. 65d. Note that the region with higher impact frequency matches the maximum erosion depth location (Fig. 65a). This confirms that both impact angle (Fig. 65c) and impact velocity (Fig. 65b) are suppressed by the impact frequency, which is the most important mechanism to generate spots of erosion in this case.

To quantitatively compare the erosion depth profile with the experiments, the origin (0°) is set at the elbow inlet, whereas 90° corresponds to the elbow outlet. All erosion-related variables are presented in Fig. 66. As previously mentioned, these profiles were extracted from the outer wall which contains the symmetry plane of the elbow. Clearly, the numerical results exhibit very good agreement with the experiment (Fig. 66a), especially for curvature angles between 40° and 90° . On the other hand, the simulation shows an underprediction between 0° and 40° . This marginal difference had already been observed by the authors in previous works (Duarte et al. (2015), Duarte et al. (2016)) and is believed to be related to the particle shape actually used in the experiment. Since the erosion process also depends on such parameter, the present particle motion model was not capable of predicting such erosion region once all the forces exerted on the particles are derived for spherical particles. Because no characterization of the particles sphericity used in the experiment was available, the authors decided to simplify the numerical setup considering only spherical particles.

One interesting fact can be observed from the impact angle (Fig. 66b) and impact velocity (Fig. 66c) plots. The former increases up to an elbow curvature equal to 45° . The explanation is that, smaller elbow curvatures ($0^\circ - 10^\circ$) are eroded by particles that are mainly moving tangent to the surface. Naturally, increasing the elbow curvature will also increase the impact angle. The impact angle limit is achieved at a location where the elbow experiences direct particle impact (elbow curvature equal to 45°). After such region, particles interact with the elbow wall by secondary impacts which explains the impact angle reduction for elbow curvature greater than 45° (Fig. 66b). A similar behavior can be observed with the particle impact velocity (Fig. 66c). Basically, at the direct

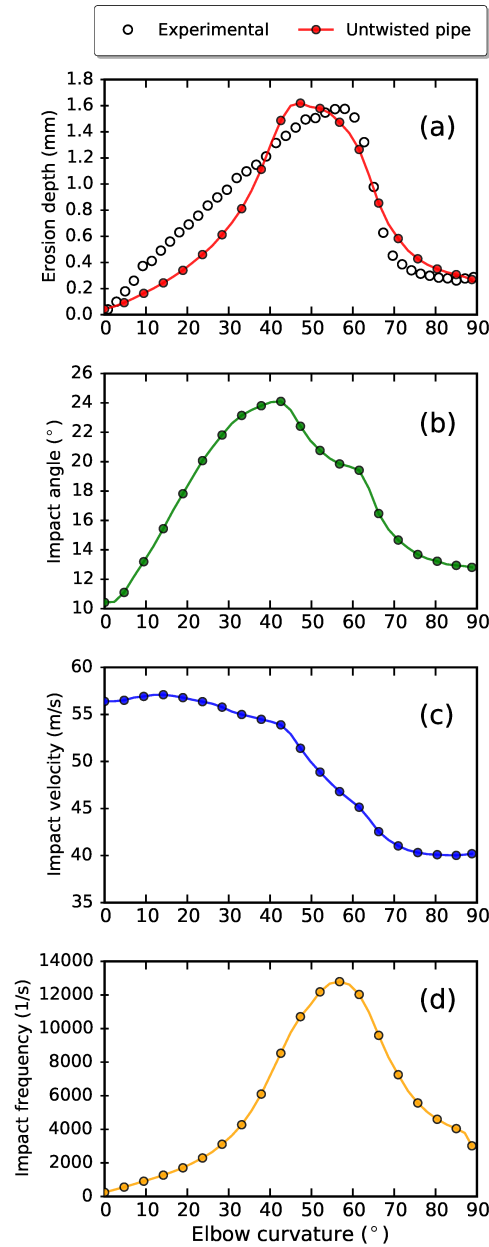


Figure 66 – Erosion-related variables extracted from the elbow extrado of symmetry plane. (a) Erosion depth, (b) impact angle, (c) impact velocity and (d) impact frequency.

impact location (elbow curvature between 0° and 45°), the impact velocity remains high whereas it is gradually reduced after that. One might think that the combination of higher velocities (> 55 m/s) and relatively small impact angle (between 10° and 24°) would produce higher erosion depth, especially because the ductile nature of the surface material. Such contradiction to the common sense can be explained by the particle impact frequency on the elbow wall (Fig. 66d).

Clearly, although both impact angle and impact velocity corroborate to the erosion depth augmentation on elbow curvature angles smaller than 45°, the impact frequency at

the respective location is low. This proves that the erosion depth on the present study is preferably caused by an increase on the particles impact frequency rather than the combined effect of impact angle and impact velocity. This explains why regions with higher impact frequencies are more prone to erosion (Fig. 65a and Fig. 65d).

Since the simulation results show a good agreement with the experiment, it can be concluded that the code is validated and further analysis considering the new pipe wall design can be carried out.

8.2.2 Influence of the pipe design on the fluid flow

Before analyzing the erosion depth patterns, we present the fluid flow patterns in each pipe design. Fig. 67 shows the streamlines for the clean air flow. As expected, no considerable variation of the flow path can be seen in the untwisted pipe (Fig. 67a). On the other hand, the 4-spiral pipe (Fig. 67b) noticeably promotes the fluid rotation. In this case, the streamlines show that the induced rotation actually begins after the first fourth of the twisted region. This indicates that the fluid at the twisted entrance takes some time to respond to the geometric modification. Finally, the 8-spiral pipe (Fig. 67c) is presented. The streamlines show minor disturbances of the fluid flow in the core region of the pipe while some marginal interactions with the near wall region are observed.

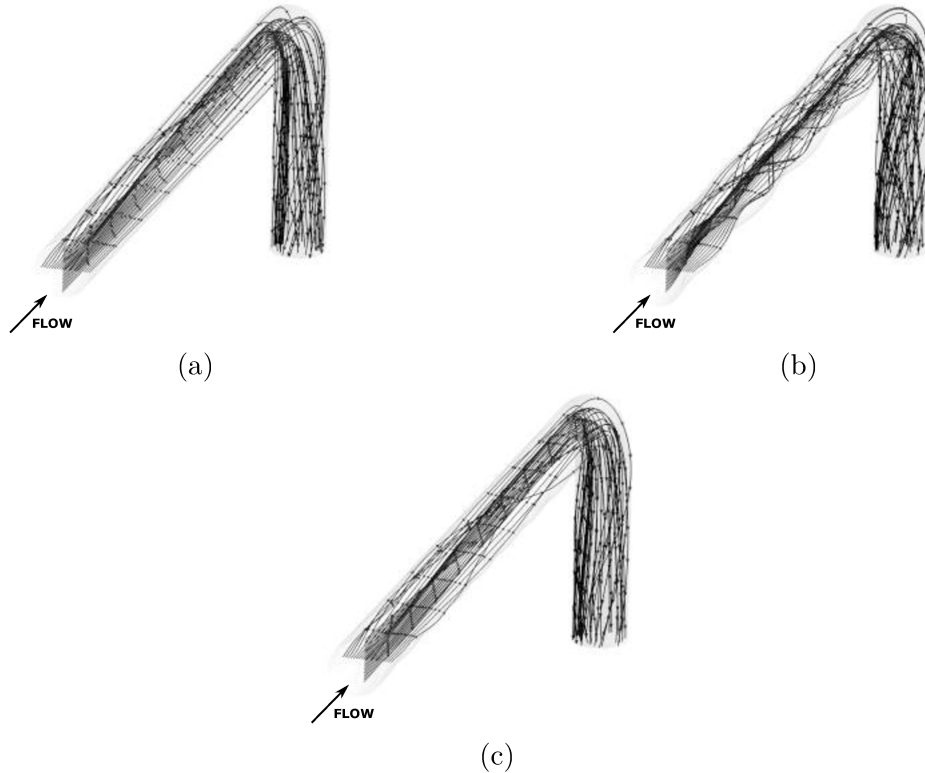


Figure 67 – Streamlines of the velocity field. (a) Untwisted pipe, (b) 4-spiral pipe and (c) 8-spiral pipe.

The contours of the velocity magnitude along each pipe can be observed in Fig. 68. Additionally, three slices (i.e., start, middle and end) were extracted from the pipe with the respective tangential streamlines. Such visualization gives a general idea of the structures formed by the fluid along each pipe. The untwisted pipe (Fig. 68a) shows two vortices at the first position of the pipe. These vortices are generated by the second elbow since no wall-induced rotation is produced for this configuration. After some distance (e.g., second slice of Fig. 68a), one of the recirculations becomes weaker. At the elbow entrance (e.g., third slice of Fig. 68a), this structure is dissipated, giving rise to a single vortex. Interestingly, the 8-spiral pipe (Fig. 68c) prevents the formation of these two vortices at the first portion of the twisted pipe wall. Otherwise, a single vortex structure takes place along the whole 8-spiral pipe. For this case, the spirals inhibit the formation of larger structures near the wall, explaining the above-mentioned single vortex.

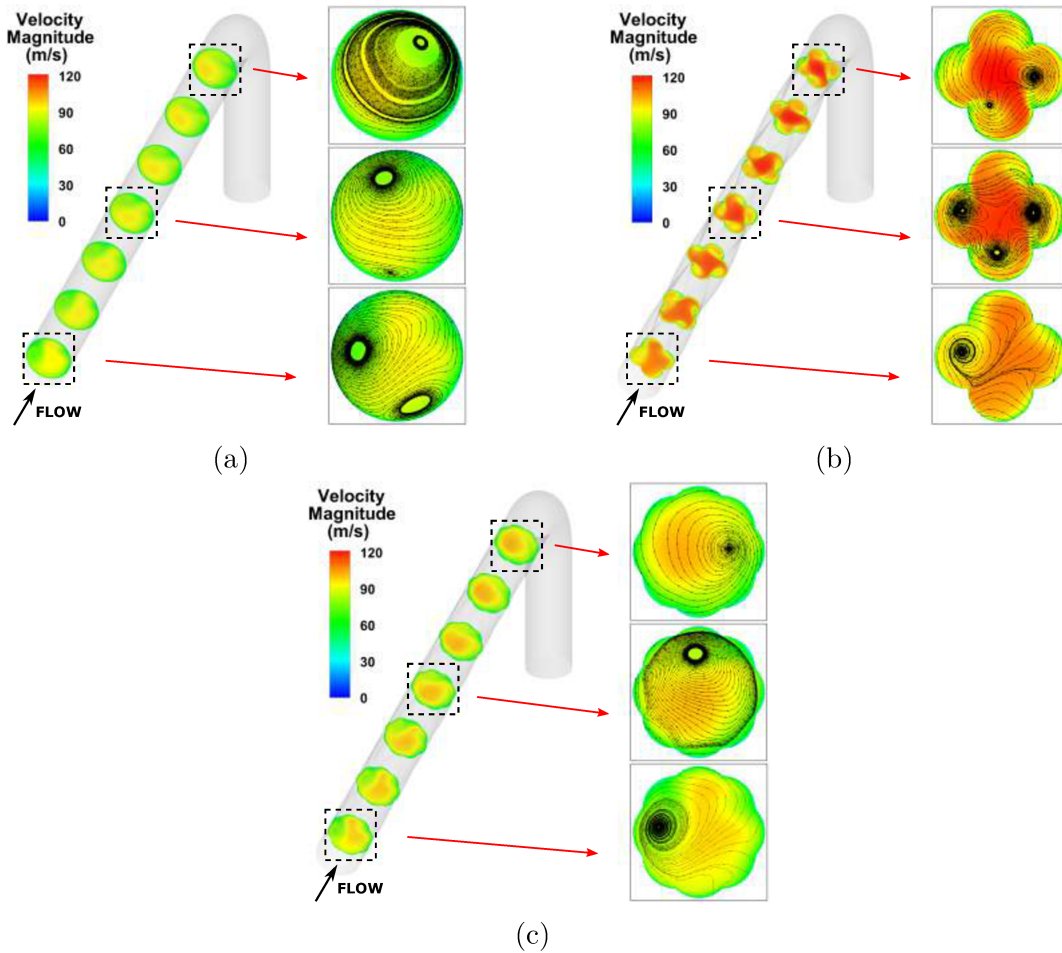


Figure 68 – Velocity magnitude along each pipe type. (a) Untwisted pipe, (b) 4-spiral pipe and (c) 8-spiral pipe.

The 4-spiral pipe shows a peculiar behavior of the fluid (Fig. 68c). Initially, only one vortex is observed at the twisted pipe entrance. After that, three well-defined vortices are generated inside the twisted pipe. The spirals are so strong, geometrically speaking,

that these structures become evident. At the end, two vortices are still present before reaching the final elbow. Another interesting observation is that the mean fluid velocity increases in the core region of the 4-spiral pipe when compared to the others. Such increase is explained by the continuity equation. Since the cross-sectional area of the 4-spiral pipe is smaller than the 8-spiral pipe, higher axial velocities are required by the former in order to maintain the same flow rate of the fluid upstream of the twisted region. In fact, this will also affect the static pressure in the entire pipeline but the details regarding the pressure inside each pipe will be discussed in section 8.2.3.

This overview of the fluid flow inside each pipe design demonstrated how significant these pipe concepts are in the flow behavior. Such flow modification will be crucial on the particle dynamics which shall lead to new mechanisms reducing the erosion depth at the elbow.

8.2.3 Influence of the pipe design on the elbow erosion

The goal of this numerical experiment is to assess the erosion patterns for both 4-spiral and 8-spiral pipes. Fig. 69 shows all the erosion-related variables for the 4-spiral pipe. When compared to the untwisted pipe case (Fig. 65a), the erosion depth contours for the 4-spiral pipe (Fig. 69a) shows a shift of the maximum erosion region to the right side of the elbow. The same trend can be seen for the 8-spiral pipe (Fig. 70a), but with less intensity. In fact, this displacement of the maximum erosion spot to the right side of the elbow was expected since both pipes were twisted clockwise. The opposite behavior in the erosion profile would possibly be observed if the pipes were twisted counter-clockwise. Moreover, the maximum value of the erosion depth for both twisted pipes is lower than the one obtained for the untwisted pipe. This is the first evidence that the proposed pipe acts positively towards mitigating the elbow erosion.

The contours of the particle impact velocity for the 4-spiral pipe and 8-spiral pipe are presented in Figs. 69b and 70b, respectively. In both cases, the impact velocity was substantially reduced in the central part of the elbow. Notwithstanding, this reduction is also present in the untwisted pipe case (Fig. 65b), but to a lesser extend. In the latter, such impact velocity reduction is achieved by the constant interactions between the particles and the outer elbow wall. Such effect has been studied by the authors ([Duarte et al. \(2015\)](#)) and is named cushioning effect. Basically, the inter-particle collisions become so important in regions of high particle concentration that a "virtual barrier" is created near the eroded wall, reducing the frequency at which the particles interact with it. As a consequence, the impact velocity is also reduced. In both twisted pipes, besides the cushioning effect, the swirling motion upstream of the elbow contributes to the impact velocity reduction at the central part of the elbow. These combined effects also cause modification in the impact angle. A slight reduction of the impact angle on the right side of the elbows for both

twisted pipes can be observed (see, e.g., Figs. 69c and 70c) while higher impact angles are concentrated on the left side of them. Such contours resemble the one obtained for the untwisted pipe (Fig. 65a).

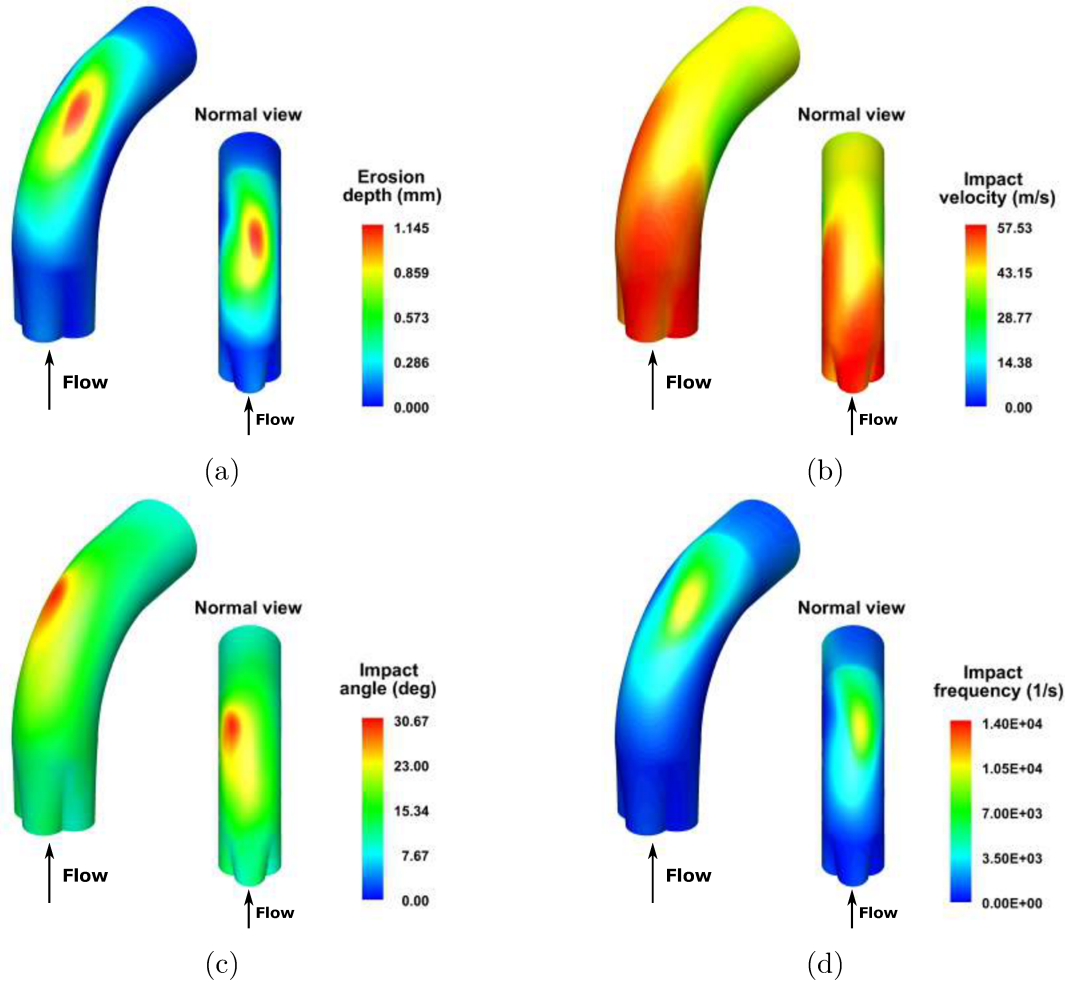


Figure 69 – Contours of the erosion-related variables for the 4-spiral pipe. (a) Erosion depth, (b) impact velocity, (c) impact angle and (d) impact frequency.

The contours of the particle impact frequency for both pipe designs are shown in Figs. 69d and 70d. Again, locations with higher impact frequency are defining the erosion depth patterns although less impacts occur on elbows with the twisted pipes. In fact, the twisted region is redirecting the particles to new locations (e.g. elbow intrados), preventing them to focus onto a single spot at the elbow.

In order to better visualize the erosion depth reduction for each pipe design, the erosion depth magnitude for the untwisted pipe was set as a reference, and the results for the other pipes were plotted in Fig. 71.

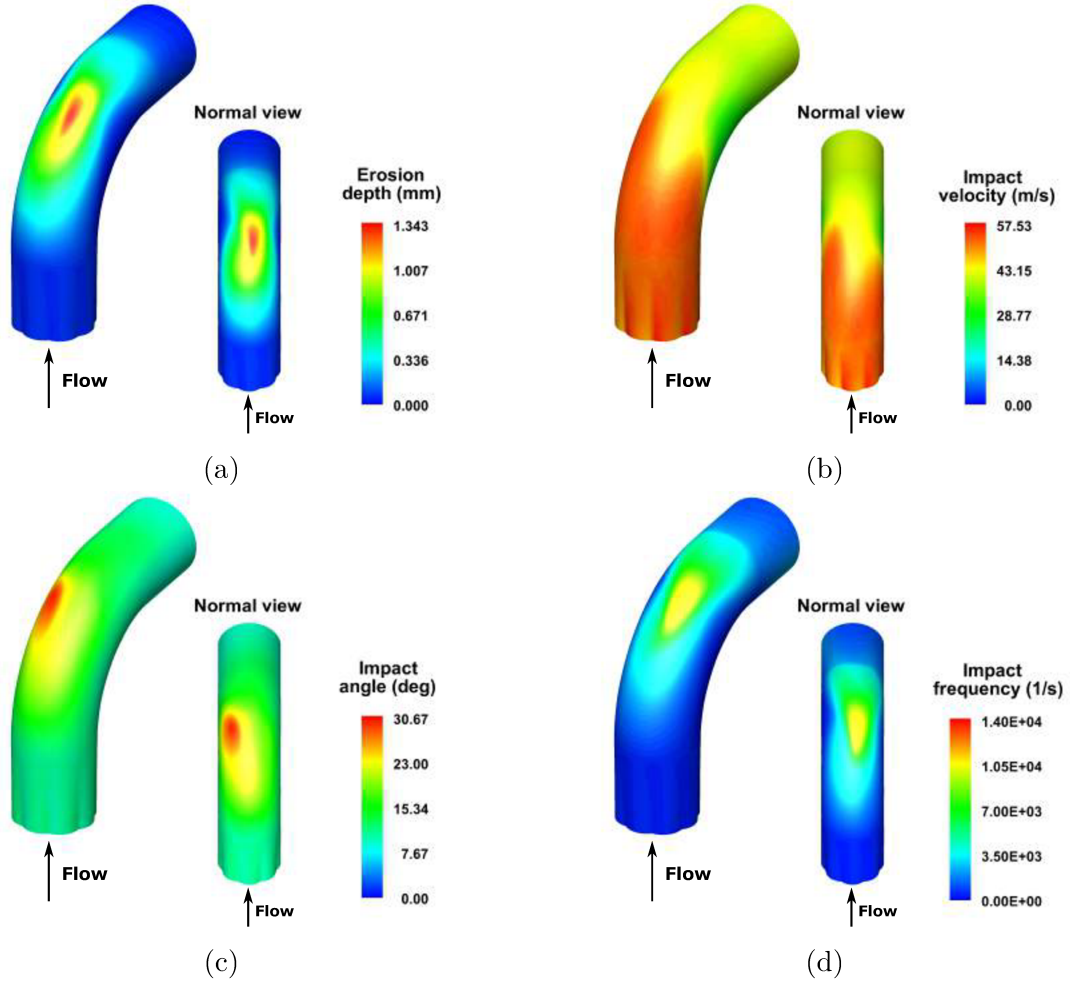


Figure 70 – Contours of the erosion-related variables for the 8-spiral pipe. (a) Erosion depth, (b) impact velocity, (c) impact angle and (d) impact frequency.

Both 4-spiral (Fig. 71b) and 8-spiral (Fig. 71c) pipes display lower erosion contours when compared to the untwisted pipe (Fig. 71a). This shows the efficacy of using twisted pipe in reducing elbow erosion. The erosion peak in the untwisted pipe (Fig. 71a) is decreased in the other pipe configurations. This proves that the particles are better distributed before effectively hitting the elbow wall.

To quantify the erosion depth on the elbow wall and relate it to each pipe type, all the erosion-related variables are presented in Fig. 72. As described in Section 7.1.1, the profile in the symmetry plane of the elbow was extracted for each case.

The erosion depth profile (Fig. 72a) confirms the reduction observed in the contours. For both 4-spiral and 8-spiral pipes, the erosion magnitude is decreased for curvature angles between 30° and 65° . On the other hand, a slight increase for the 4-spiral pipe is observed for curvature angles higher than 65° . Such behavior can be explained by the stronger swirl experienced by the particles in this case. From an industrial stand point, the 4-spiral pipe would be more attractive, despite such increase. In terms of the elbow

lifetime, this configuration would ensure greater durability compared to the others because it has the lowest peak of erosion depth. The 4-spiral pipe reduced the peak of erosion by approximately 33% when compared to the untwisted pipe.

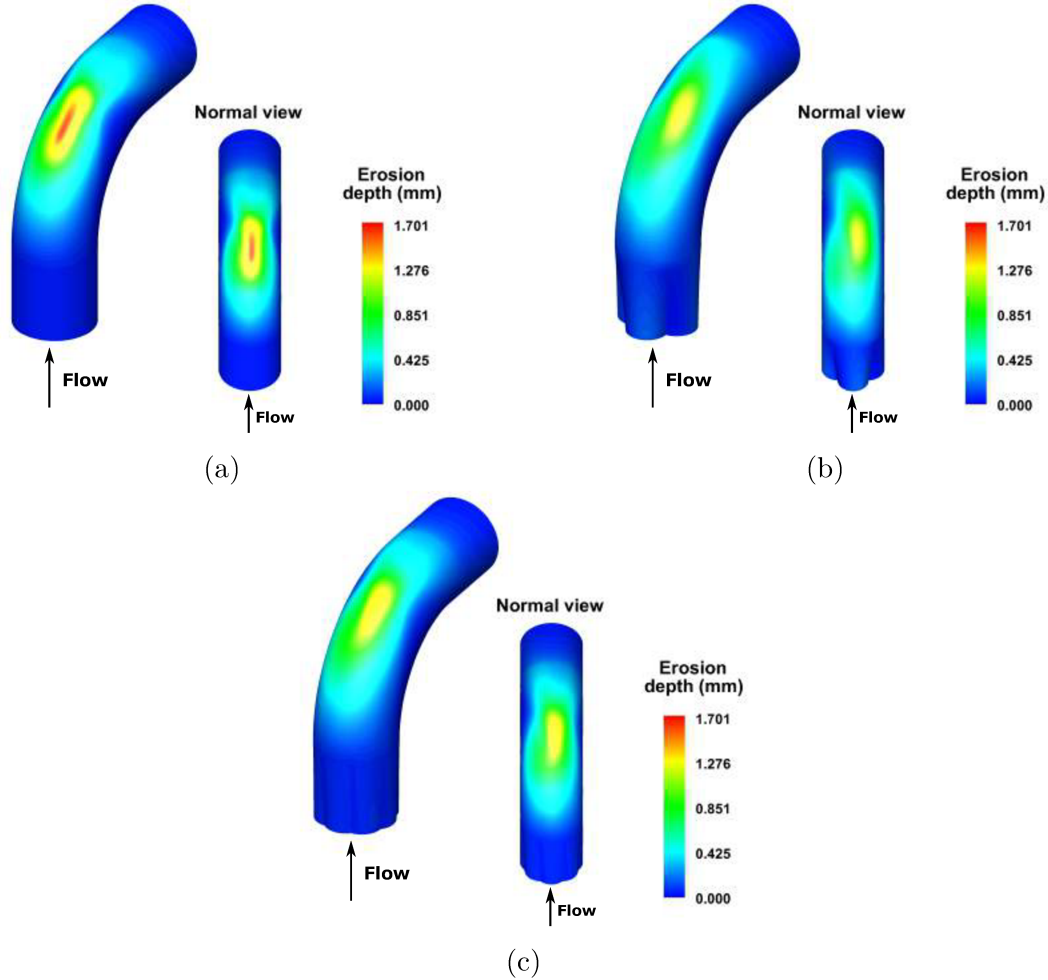


Figure 71 – Erosion depth contours for each pipe type with the magnitude fixed for the untwisted pipe.

In order to represent each erosion depth profile by only one characteristic value, we integrate each curve using the trapezoidal rule and normalized the result by the maximum curvature angle ($\pi/2$). This mean value can clarify, for instance, if the increase in larger elbow curvature angles in the 4-spiral case could suppress the reduction for smaller curvature angles.

Table 11 provides the integral value for each elbow, including the experimental case. The difference between the experiment ($IV = 0.798$) and the untwisted pipe ($IV = 0.729$) confirms the underprediction of the latter for curvature angles between 0° and 40° as reported in the validation section. On the other hand, the difference between the untwisted ($IV = 0.729$) and 4-spiral pipe ($IV = 0.623$) is remarkable. This result reinforces the effectiveness of the new pipe design to reduce the erosion at the elbow and makes it clear that even increasing it in some regions, it is still a viable alternative. Moreover, a

slight difference is observed between the twisted pipes. It is important to bear in mind that although these values were calculated from only one line at the elbow, they globally represent the mean amount of erosion, since they were extracted from the maximum erosion location of each case.

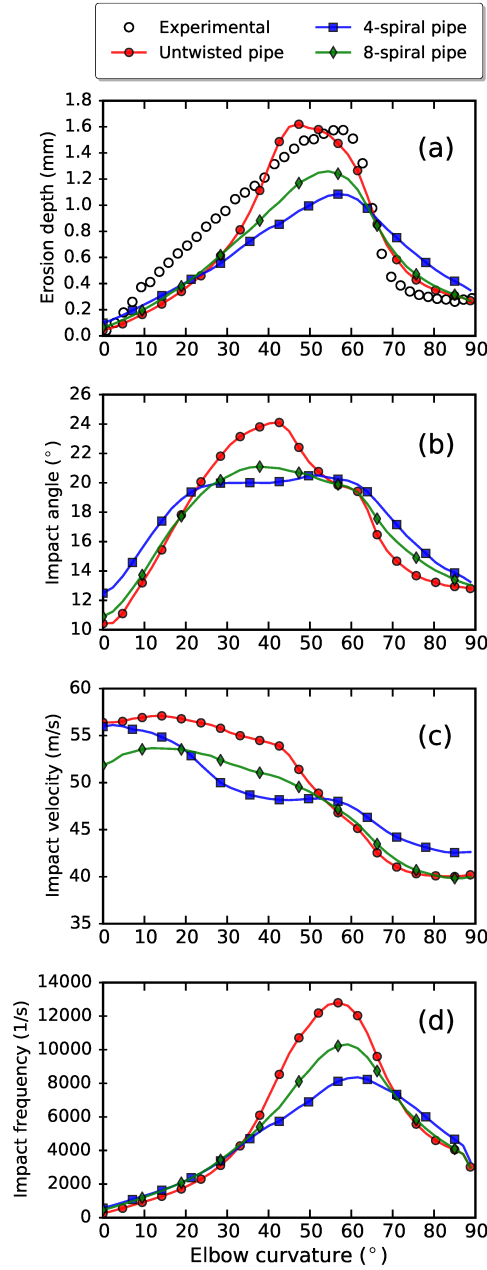


Figure 72 – Influence of the pipe wall type on the erosion-related variables. (a) Erosion depth, (b) impact angle, (c) impact velocity and (d) impact frequency. Profiles extracted from the elbow extrados of symmetry plane.

To further understand the mechanisms of erosion reduction in the simulated cases, the impact angle and impact velocity are presented in Figs. 72b and 72c, respectively. For both twisted pipes, the impact angle profile was flattened for curvature angles between 20° and 65° when compared to the untwisted pipe (Fig. 72b). Additionally, the impact

Table 11 – Integral value of each erosion depth curve normalized by the maximum curvature angle ($\pi/2$).

Pipe type	Integral value (IV)
Experimental	0.79874
untwisted pipe	0.72920
4-spiral pipe	0.62357
8-spiral pipe	0.64348

velocity (Fig. 72c) for both cases was reduced for curvature angles between 0° and 50° while an augmentation for curvature angles larger than 55° is clearly visible for the 4-spiral pipe. Such increase in the impact velocity is partially related to the erosion depth increase at the same location. However, the impact frequency (Fig. 72d), again, contributes in defining the erosion depth profile. The combined effect of both for curvature angles larger than 70° reflects in the erosion accretion on the 4-spiral pipe.

Despite part of the erosion reduction can be explained by the previous graphs, any final conclusion would be incomplete since the particle dynamics upstream of the elbow be the main factor in changing the erosion profile and its associated variables. With this in mind, the following section presents the particle dynamics in each pipe configuration.

8.2.4 Particle dynamics inside each pipe design

Fig. 73 shows the particle concentration for all the studied pipes. As expected, the particle concentration contours for all pipes remain similar up to approximately half length. Naturally, up to this location, the particles are only responding to the fluid flow and no geometric modification affects them. Downstream of this point, the particle concentration is strongly influenced by the pipe wall design.

In the untwisted pipe (Fig. 73a), the particles tend to concentrate in the core flow. No additional momentum is transferred to the particles by the walls. Consequently, the most important mechanisms to redirect the particles to the center are the particle-wall interaction due to the surface roughness and particle-to-particle collisions.

On the other hand, the particle concentration on both twisted pipes (Figs. 73b and 73c) presents an opposite behavior. Visibly, the swirl applied on the particles suppresses the natural mechanisms mentioned for the untwisted pipe, avoiding the central concentration. Such increase in the particle concentration at the near wall region upstream of the elbow helps to understand the impact frequency for both cases (see, Fig. 72d).

To quantitatively compare the particle concentration inside each pipe, a centerline was extracted from the second elbow outlet to the third elbow inlet. Fig. 74 displays the results, a dashed line represents the beginning of the spiral pipes. Upstream of this location, the particle concentration remains similar for all pipe configuration. Immediately after the

start of the twisted pipes, the particles are strongly influenced by the flow changes imposed by the twisted walls, generating a pronounced peak of concentration for the 4-spiral pipe. Since the transition from the untwisted region to the 8-spiral pipe is slightly softer, such peak was not observed in the 8-spiral pipe. Downstream of this transition, both twisted pipes experience the particle concentration reduction whereas in the untwisted pipe it is constantly increasing.

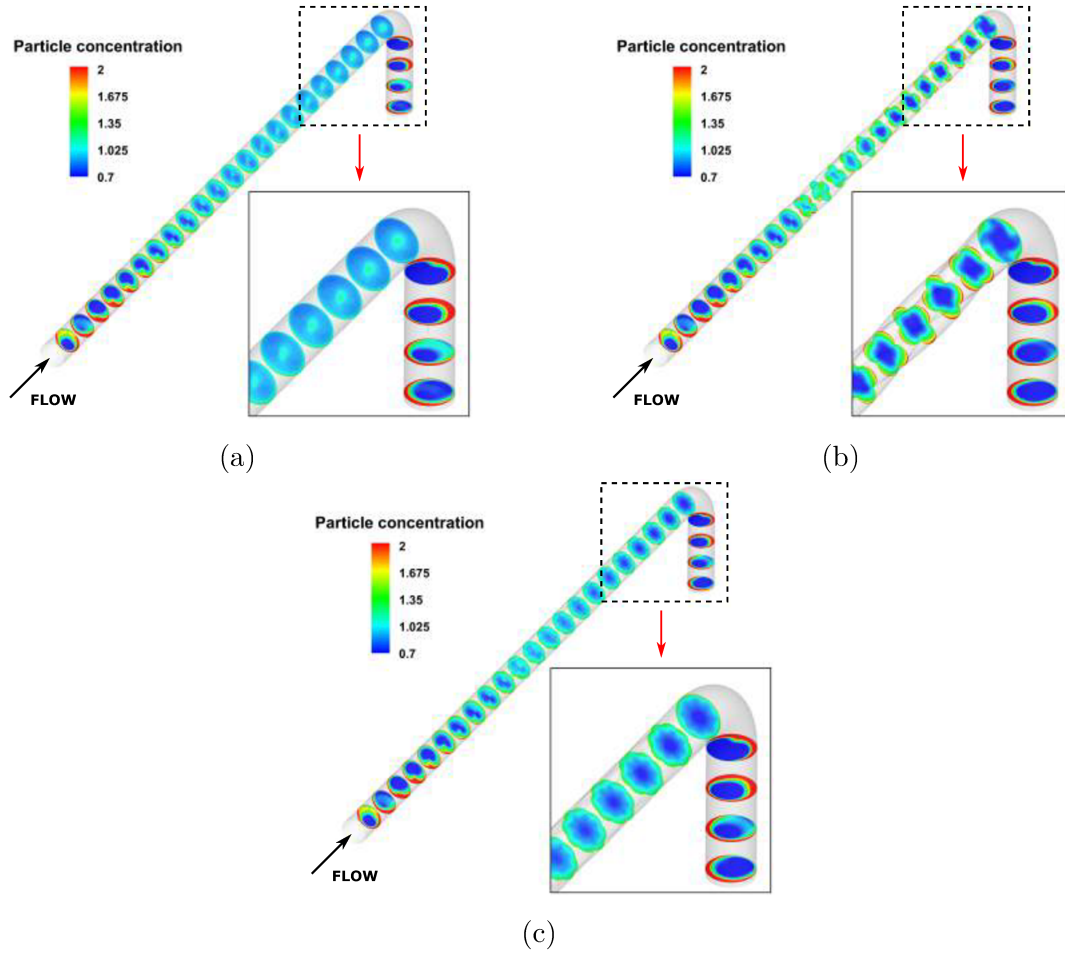


Figure 73 – Influence of the pipe wall type on the particle concentration. (a) Untwisted pipe, (b) 4-spiral pipe and (c) 8-spiral pipe.

In fact, the authors proposed these twisted pipes for this purpose. Preventing the particles from concentrating in the core flow while being conveyed avoids the formation of a focus point at the elbow. As a consequence, both impact velocity and frequency are reduced. Obviously, one negative point may arise from this modification. Increasing the particle concentration near the wall will also promote constant particle-wall interactions which can result, for instance, in new spots of erosion on the twisted pipe walls. With this in mind, a detailed analysis about such effects on the twisted pipe walls will be addressed in section 8.2.5.

The effect of particle size on the erosion rate has drawn the attention of many

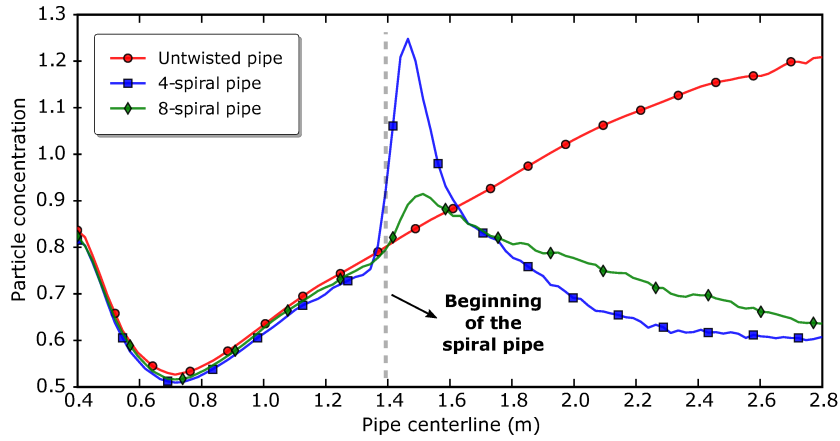


Figure 74 – Particle concentration along the center line of each pipe wall type.

authors (Clark (1992), Lynn et al. (1991), Clark and Hartwich (2001), Nguyen et al. (2016)). To analyze the effects of the particle size on the erosion mechanism, the contours of the particle mean diameter for each pipe design are presented in Fig. 75. In general, both untwisted (Fig. 75a) and 8-spiral (Fig. 75c) pipes segregate the particles in a similar way. Larger particles ($> 215 \mu\text{m}$) are preferably located near the walls. The underlying reason for this is that larger particles take longer to respond to the fluid motion, specially after the particle rebound. Besides that, the mean particle velocity near the wall is higher than the fluid velocity which, in turn, makes larger particles less affected by the Saffman lift force, for instance. Due to their inertia, they are not significantly impacted by the surface roughness as a large body force exists. In the case of 4-spiral pipe, this migration mechanism of the larger particles to the wall is interrupted by the intense swirl generated. At the beginning of the 4-spiral pipe, the particle-wall interactions are still present, however, at the elbow entrance (see, Fig. 75b, zoomed region), such relation is no longer observed.

To further understand this effect, a centerline, as described for the particle concentration, was extracted considering the particle mean diameter along each pipe type (Fig. 76). By the beginning of the twisted region, the mean diameter is the same for all the cases. Upstream this region, it is augmented for both twisted pipes and slightly decreased for the untwisted pipe. In the former, the combination of lower particle concentration (Fig. 74) and higher particle mean diameter (Fig. 76) at the central part of the pipe contribute to the erosion reduction at the elbow. This is in accordance to the finds of Nguyen et al. (2016) who performed experiments to analyze the effects of particle size on the erosion pattern and conclude that the erosion rate increases with the particle size until reaches a maximum value of $150 \mu\text{m}$. Above this value, the erosion rate gradually decreased as the particle size becomes bigger. In the present study, by increasing the size of the particles conveyed in the central part of the pipe (Fig. 76), the inter-particle collisions extracts additional momentum upstream of the elbow which results in an impact velocity reduction during the collisions on the elbow surface (see, Fig. 51c, curvature angles between 0° and

50°).

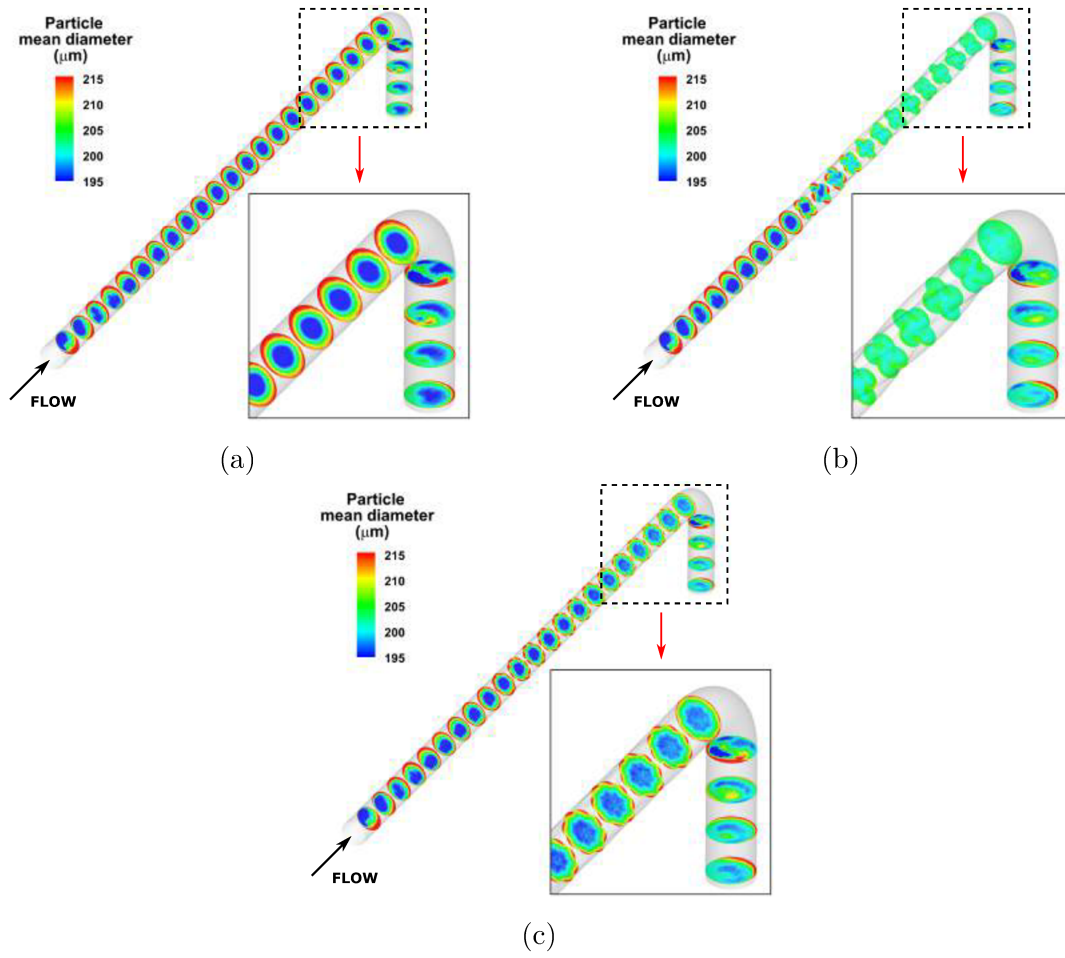


Figure 75 – Influence of the pipe wall type on the particle mean diameter. (a) Untwisted pipe, (b) 4-spiral pipe and (c) 8-spiral pipe.

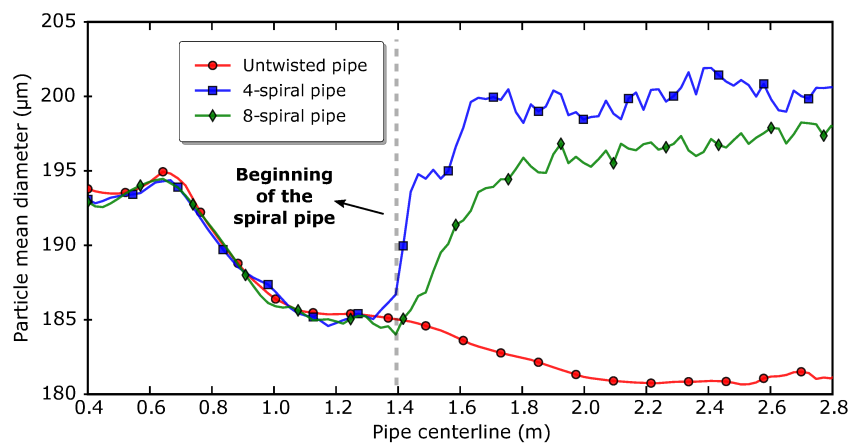


Figure 76 – Particle mean diameter along the center line of each pipe wall type.

The impact frequency reduction on both twisted pipes (Fig. 72d) can also be partially explained by the same principle. Enhancing the particle-to-particle interactions

upstream of the elbow increases the probability of deflecting the particle to new spots on the elbow which reduce the focus effect and consequently the impact frequency.

Up to this point, the benefits of the new pipe design have been addressed and the mechanisms responsible to the erosion reduction on the elbow were explained. From an industrial point of view, such erosion reduction in an entire pipeline plant could drastically reduce maintenance costs. However, other variables should be taken into account to ensure a good applicability of this new pipe concept. In this regard, the pressure drop inside each pipe type is presented in Fig. 77. The pressure drop for the single-phase flow (continuous line) and two-phase flow (dashed line) shows a small deviation. In fact, a slight increase in the latter was expected. Due to inter-particle collisions and particle-wall interactions, the particles reach the twisted region at a velocity which is lower than their steady-state velocity. The energy required to re-accelerate the particles manifests itself as an additional pressure loss along the pipe. Obviously, such small difference is related to the small mass loading ($\eta = 3.846\%$) in the present study. Higher mass loadings will consequently increase the pressure drop. As shown in Fig. 77, the static pressure decreases linearly in the center of the untwisted pipe. However, in both twisted pipes, the static pressure is higher upstream of the beginning of the spiral region. For both configurations, the twisted wall generates radial velocities components that were not present in the untwisted pipe. Such components tends to retard the flow in the axial direction. To compensate for this, higher pressure is required upstream. As a consequence, the static pressure along the twisted region is visibly reduced, been smaller than that in the untwisted pipe.

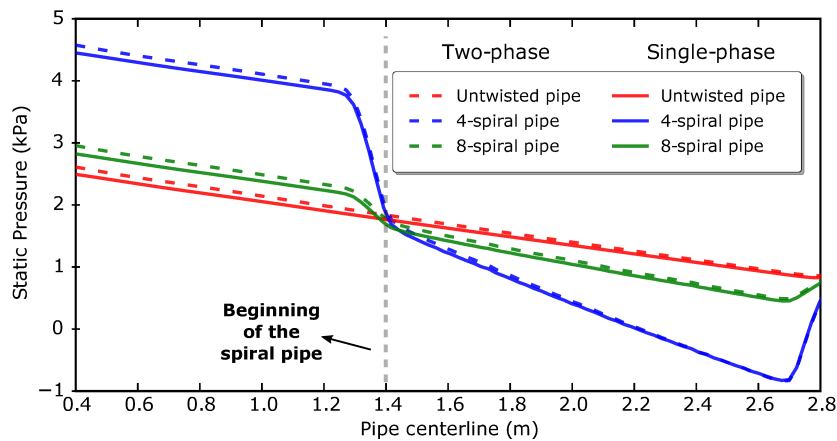


Figure 77 – Static pressure profile extracted from the center line of each pipe type. Continuous line is the single phase flow and dashed line is the two-phase flow.

8.2.5 Erosion analysis

As stated in the previous section, a swirling motion of the multiphase flow upstream of the elbow is beneficial to changing the particle dynamics and consequently reduce the

elbow erosion. However, new particle-wall interactions may become relevant, inducing the erosion process on the twisted walls. With this concern, such effects are analyzed below.

Fig. 78 shows the erosion depth contour for each pipe type. The untwisted pipe wall (Fig. 78a) exhibits nearly an uniform erosion contour. As expected, for this case, no significant erosion spots are observed since the particle motion inside the pipe have similar mechanisms of particle-wall interactions along the axial direction. Conversely, the 4-spiral pipe (Fig. 78b) presented peaks of erosion equally spaced right before the elbow. Similarly, but less intensively, such behavior can also be observed in the 8-spiral pipe (Fig. 78c). In both cases, this effect is noticeably present in the second half of these pipes. Initially, it was observed that larger particles enter the twisted region with highest concentration on the wall due to the natural fluid flow. With the swirl generated by the spiral walls, the particle separation process begins and the larger particles are driven to the center of the pipe while the smaller ones, which in turn are more sensitive to turbulent fluctuations, remain in constant contact with the walls.

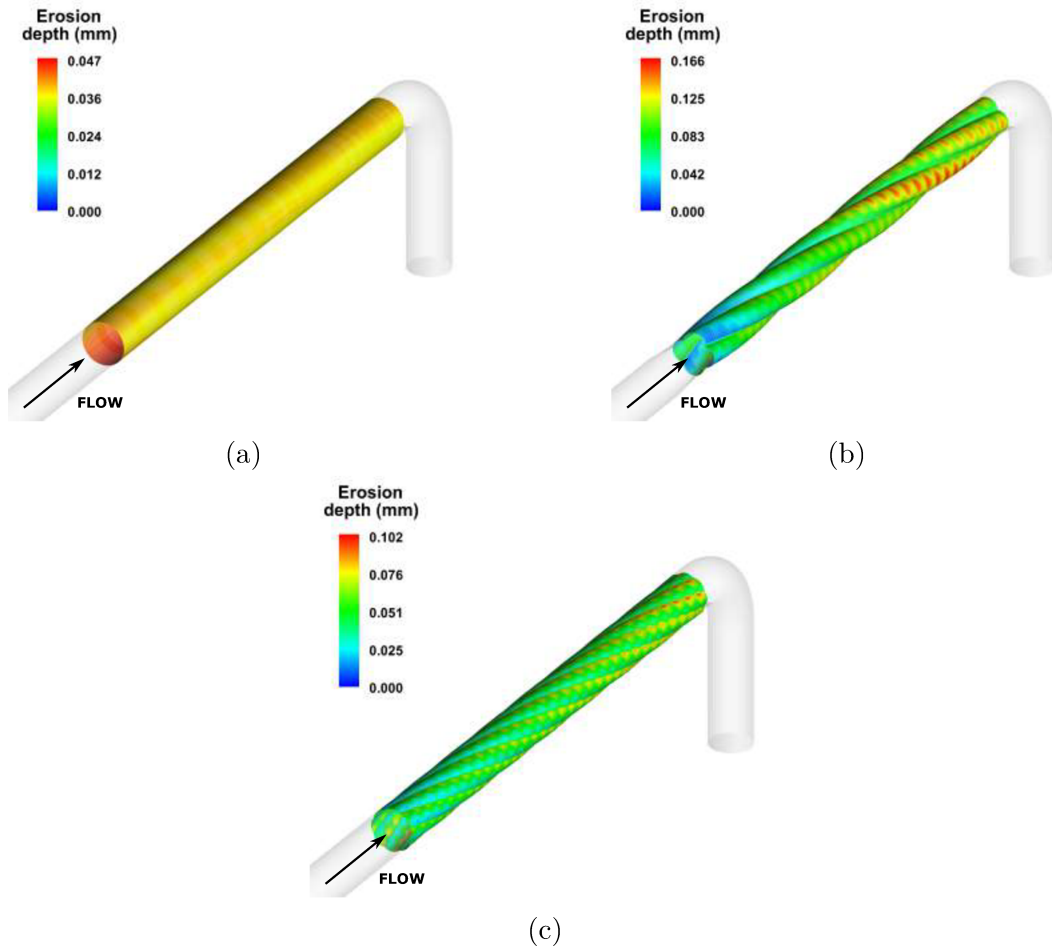


Figure 78 – Erosion depth contours for each pipe wall type. (a) Untwisted pipe, (b) 4-spiral pipe and (c) 8-spiral pipe.

Naturally, this process is intensified over the twisted pipes, which explains the

greater erosion rate at the final part. Meanwhile, the equally spaced erosion scars can be explained by the particle saltation mechanisms (Cabrejos and Klinzing (1994)). As the simulations have been performed considering the particle distribution size of the experiment, different mechanisms may influence the behavior of each isolated particle. This behavior is directly linked to the particle response time and the collisions between them. Thus some particles have their trajectory forced radially more intensively by the spirals, but the fluid flow in the axial direction causes this range of particles diameters to jump from one region to another. In other words, the centrifugal motion of some particles is interrupted by the fluid flow, which inhibits the sliding movement of them towards the spiral wall. Thereby, the saltation mechanism becomes evident from the erosion patterns formed in the twisted pipes (Figs. 78b and 78c).

In addition, it is worth mentioning how important it is to simulate the particle distribution depending on the case under investigation. Clearly, the size distribution might not noticeably affect the untwisted pipe results, but when looking at the particle dynamics at the twisted pipes, erroneous conclusions about the erosion profile could be drawn if only one particle diameter were simulated.

In order to measure the erosion in each pipe wall configuration, a profile was extracted according to the scheme presented in Fig. 79. The "view A" of Fig. 79 shows the 4-spiral pipe sliced at $y = 2.71$ m where the blue line defines the location that all the erosion-related variables were extracted. The same procedure was adopted to extract such variables from both untwisted and 8-spiral pipes. After the extraction, each profile was planned and plotted in the same graph (Fig. 80). This region was chosen because, according to the erosion contours of Fig. 78, it is the site of most erosive activity in the twisted pipes. Thus, an overall conclusion about the mechanisms acting in the twisted pipes can be made. Furthermore, a direct comparison to the reduction achieved in the elbow can be performed to actually check the benefits by the use of twisted pipes.

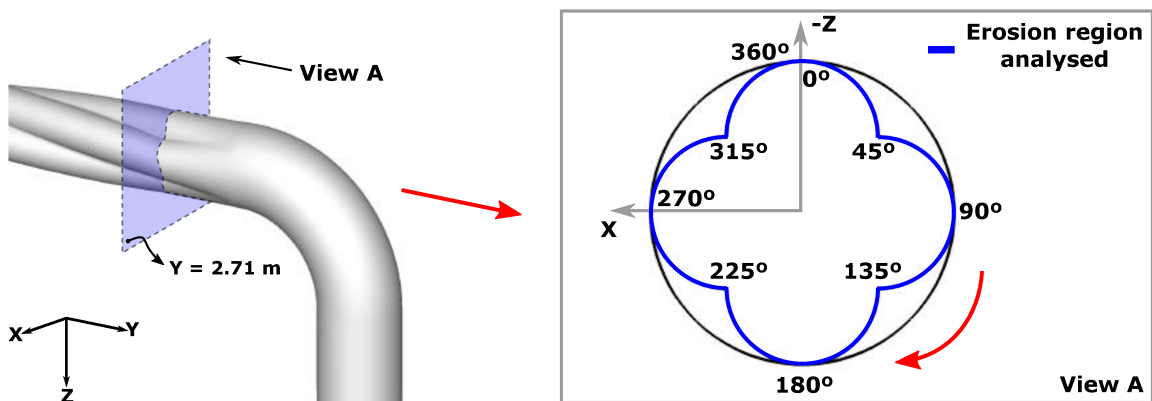


Figure 79 – Schematic representation of the location where the erosion-related variables were extracted at the pipe wall.

Fig. 80 shows all the erosion-related variables for each pipe design. In order to better visualize the results and associate them to the correct location at each pipe, the wall shape is additionally presented in Fig. 80a.

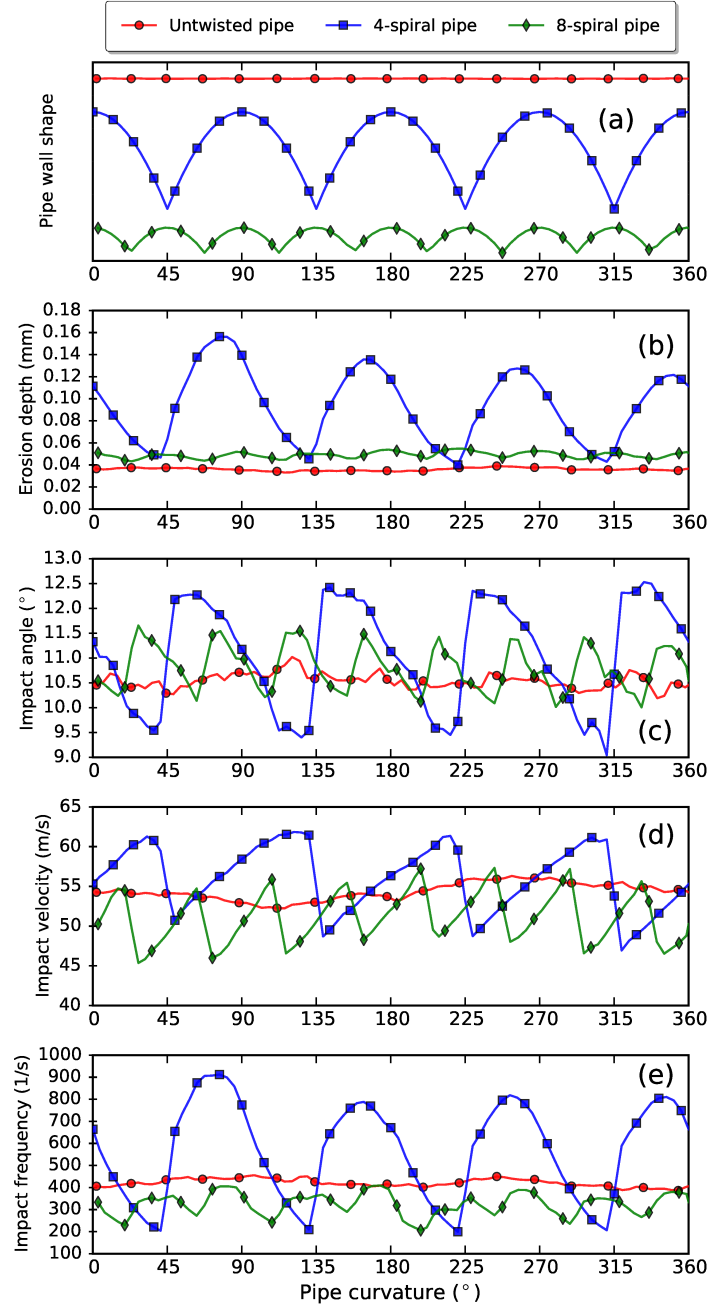


Figure 80 – Erosion-related profiles comparing each pipe wall type.

Fig. 80b shows the erosion depth for each configuration. The 4-spiral pipe has greater erosion depth compared with the others. The erosion depth peaks are not uniformly distributed throughout the spirals. Due to the rotational motion, the erosion depth is transferred to the left side of the spirals. To better understand this effect, let us look at the first spiral that starts at pipe curvature of 45° and ends at 135° . For this location, the erosion depth is higher between 45° - 90° than 90° - 135° . The same trend prevails for

the others spirals. This proves that one side of each spiral will suffer more or less erosive wear and this side will be defined by the sense of rotation in which the pipe is twisted. Although the 4-spiral pipe presents a higher erosion reduction on the elbow, the swirl applied to the multiphase flow is so considerable that its walls are exposed to high erosion rates which may not be interesting in terms of industrial application.

On the other hand, the 8-spiral pipe shows a drastically erosion reduction when compared to the 4-spiral pipe. This reduction caused the erosion profile to almost achieve the one obtained for the untwisted pipe. Such result is remarkable and indicates that the 8-spiral pipe operates better, in terms of pipe erosion, than the 4-spiral pipe. It is important to bear in mind that the erosion transferred to the twisted pipes must not overlap the reduction achieved in the elbow. If this occurs, the twisted pipe design is no longer a viable alternative. Clearly, the present results demonstrates that the 8-spiral pipe would be a better option the 4-spiral ones considering the lifetime of the pipe and elbow together. Obviously, such result could change depending on the flow characteristics (e.g., fluid velocity, mass loading, etc), elbow orientation and other factors related to the pipeline dimensions (e.g., elbow curvature, pipe diameter, etc).

Figs. 80c and 80d show the impact angle and impact profiles, respectively. For both twisted pipes, regions with higher impact angles have lower impact velocities. On average, the impact velocity of the 8-spiral pipe is smaller than the untwisted pipe (Fig. 80d). Interestingly, the impact frequency (Fig. 80e) observed in the 8-spiral pipe contradicts the statement that increasing the impact frequency will also increase the erosion depth. Actually, this is true for the elbow erosion process, however, other mechanisms takes place for the twisted walls. Overall, the impact frequency of the 8-spiral pipe is smaller than the untwisted pipe although the erosion depth is higher in the former. This is explained by the fact that the 8-spiral pipe swirl is not sufficient to "trap" the particles near the spiral wall region. Accordingly, this re-dispersion causes particles to return to the walls with larger impact angles (Fig. 80c), explaining the erosion depth increase when compared to the untwisted pipe. An opposite behavior is observed for the 4-spiral pipe. In this case, the impact frequency increase is conducting the erosive process. Considering a fixed point at the pipe wall (e.g., pipe curvature angle equal to 45°) it is clear that despite the impact frequency for the 4-spiral pipe be smaller than the others, the erosion depth is larger at the same location.

8.2.6 Practicality of the twisted pipe wall for fabrication and testing

This CFD investigation results mainly in a potential pipe design that can mitigate elbow erosion which requires further fabrication and testing steps. The following considerations are made to check the practicality of this design:

- Tube drawing produces high-quality tubing with precise dimensions and good surface finish. This manufacturing method is considered by the authors as the most suitable for the twisted pipe production.
- As recommended, a soft transition between the untwisted pipe and the twisted one is required to avoid geometrical discontinuities.
- The mechanical resistance increases when using twisted pipe walls. This indicates that this pipe design can be used in long pipe lines, especially oriented horizontally.

8.3 Chapter conclusions

The gas-solid flow in a new pipe wall design was investigated herein. Its influence on the flow was analyzed and related to the elbow erosion reduction. In this sense, the present work highlights the benefits of the twisted pipe wall design in order to mitigate elbow erosion. Furthermore, two pipe designs considering 4 and 8 spirals were evaluated in order to quantify the swirl intensity on the elbow erosion reduction and the pipe lifetime.

The main results of this study are:

- The flow modifications brought about by the twisted pipe walls are crucial on the particles dynamics.
- The maximum value of the erosion depth at the elbow for both twisted pipes are lower than the one obtained for the untwisted pipe.
- The 4-spiral pipe reduced the peak of erosion on the elbow by approximately 33% when compared to the untwisted pipe.
- The present results demonstrates that the 8-spiral pipe would be a better option than the 4-spiral ones considering the lifetime of the pipe and elbow together.

Chapter 9

Thesis conclusions

The current study has focused on the behavior of erosion considering a new pipe wall design in order to increase the 90 ° elbow lifetime. The validation of the erosion model supported the creation of a decent simulation setup, after which the resulting setup was employed for simulating the twisted pipe wall cases. The current study has produced a simulation setup that is able to predict erosion phenomena inside pipe fittings with sufficient accuracy. Moreover it has revealed that including the twisted pipe geometry has a positive effect on the elbow erosion depth reduction.

Below a more elaborate discussion is presented concerning the separate phases in the research, i.e. the standard elbow and the cushioning effect in the validation phase and the twisted pipe wall simulations in the analysis phase.

Validation phase

By using accurate CFD models for the gas-particle flow within a ninety-degree-elbow, it was possible to better understand the particle behavior and its consequences on the erosion. A major feature of this validation has been the numerical investigation of the surface roughness, static and dynamic coefficients and mass loadings on the erosion depth.

Based on the simulation results, it can be concluded that even at low mass loadings, the effects of inter-particle collisions on the penetration ratio cannot be disregarded. The first contribution of this work is the prediction and evaluation of the cushioning effect in elbow erosion. It is noteworthy that such effect has been noticed experimentally and can be present in several industrial situations. It may also be the key to understanding erosion-related problems.

The decay of the erosion depth with increasing the mass loading was found to be due to particle-to-particle collisions through a so called "virtual barrier". Although this phenomenon may appear as beneficial, it is important to bear in mind that equipment regions not subject to erosion at low particle concentrations might become susceptible at

higher concentrations.

The simulations also revealed that the impact angle was not affected by the modification of the coefficients of friction. This proves that the alteration of the impact angle primarily occurs by changes in the surface roughness rather than the friction coefficients. In addition, a parametric variation of the surface roughness showed that the erosion depth monotonically diminishes with the roughness increase.

For the case with lower mass loading ($\eta = 3.846\%$), the predictions demonstrate that particles can cause wear in elbows in two different ways. Particles can directly drive the erosive process by consecutive stresses exerted on the wall (curvature angles smaller than 60°) or by indirect stresses after the first impact (curvature angles larger than 60°).

Analysis phase

Since many industrial processes requires the transportation of solid particles, the twisted pipe wall appears as a very interesting alternative to mitigate elbow erosion. Based on the simulation results, it can be concluded that the elbow equipped with a twisted pipe show its full potential towards reduce elbow erosion.

Due to the excellent agreement of the numerical computations obtained with the validation phase in combination with all required models for the erosion prediction, it may be concluded that the models presented here are capable for supporting the optimization and the design of pneumatic conveying systems. In addition, with the knowledge of the inter-particles collision effects it will be now also possible to predict erosion rates in the different pipe elements.

Among the benefits obtained with the use of the twisted pipe, the main finding is that the maximum value of the erosion depth at the elbow for both twisted pipes (4 and 8 undulations) are lower than the one obtained for the untwisted pipe. Additionally, the 4-spiral pipe configuration reduced the peak of erosion on the elbow by approximately 33% when compared to the untwisted pipe. Such reduction in the erosion depth is closely related to the flow modifications brought by the twisted wall, which are crucial on the particle dynamics. From an industrial point of view, such erosion reduction in an entire pipeline plant could drastically reduce maintenance costs.

On the other hand, it was observed that the swirling motion of the multiphase flow upstream of the elbow acts positively to changing the particle dynamics and consequently reduce the elbow erosion. However, new particle-wall interactions may become relevant, inducing the erosion process on the twisted walls. Therefore, it is important to bear in mind that the erosion transferred to the twisted pipes must not overlap the reduction achieved in the elbow. If this occurs, the twisted pipe design is no longer a viable alternative.

Finally, this thesis contributes to the development of a new geometry that can

benefit from such effects.

Chapter 10

Future research

In the current research it was only possible to study the erosion process isolated. Although the outcome was satisfying, some topics may be interesting for future research. These topics are listed below:

- change the twisted pipe configuration (length and number of undulations);
- change fluid and particles properties;
- add corrosion models to work alongside with erosion models.

Bibliography

AGARWAL, V. K. .; KULKARNI, N.; MILLS, D. Influence of expanded bends on wear and particle degradation in pneumatic conveying system pipelines. In: *Proc IMechE Conf on Powder and Bulk Solids Handling*. London: [s.n.], 2000. p. 307–317. Cited on page 55.

AGARWAL, V. K. .; MILLS, D. The use of inserts for reducing bend wear in pneumatic conveying system pipelines. In: *Proc 14th Powder and Bulk Solids Conf*. [S.l.: s.n.], 1989. Cited 2 times on pages 52 and 53.

AHLERT, K. R. *Effects of particle impingement angle and surface wetting on solid particle erosion of AISI 1018 Steel*. [S.l.]: University of Tulsa, 1994. Cited 3 times on pages 68, 94, and 117.

ASKELAND, D.; FULAY, P.; WRIGHT, W. *The Science and Engineering of Materials*. [S.l.]: Cengage Learning, 2010. ISBN 9780495296027. Cited on page 37.

BAYER, R. G. Fundamentals of Wear Failures. *ASM Handbook, Volume 11: Failure Analysis and Prevention*, v. 11, p. 901–905, 2002. Cited on page 30.

BENSON, M.; TANAKA, T.; EATON, J. K. Effects of Wall Roughness on Particle Velocities in a Turbulent Channel Flow. *Journal of Fluids Engineering*, v. 127, n. 2, p. 250–256, dec 2004. ISSN 0098-2202. Cited 2 times on pages 88 and 117.

BHUSHAN, B. *Introduction to Tribology*. [S.l.: s.n.], 2013. ISBN 1118403223. Cited 3 times on pages 13, 37, and 39.

BIKBAEV, F. A.; KRASNOV, V. I.; MAKSIMENKO, M. Z.; BEREZIN, V. L.; ZHILINSKI, I. B.; OTROSHKO, N. T. Main factors affecting gas abrasive wear of elbows in pneumatic conveying pipes. *Chemical and Petroleum Engineering*, Springer, v. 9, n. 1, p. 73–75, 1973. Cited on page 29.

BIKBAEV, F. A.; MAKSIMENKO, M. Z.; BEREZIN, V. L.; KRASNOV, V. I.; ZHILINSKII, I. B. Wear on branches in pneumatic conveying ducting. *Chemical and Petroleum Engineering*, Springer, v. 8, n. 5, p. 465–466, 1972. Cited 5 times on pages 14, 29, 56, 57, and 123.

BITTER, J. A study of erosion phenomena: Part I. *Wear*, v. 6, n. 1, p. 5–21, jan 1963. ISSN 00431648. Cited 2 times on pages 60 and 117.

BITTER, J. A study of erosion phenomena part II. *Wear*, v. 6, n. 3, p. 169–190, may 1963. ISSN 00431648. Disponível em: <<http://www.sciencedirect.com/science/article/pii/0043164863900735>>. Cited 3 times on pages 14, 61, and 62.

BOURGOYNE, A. Experimental Study of Erosion in Diverter Systems Due to Sand Production. *SPE/IADC Drilling Conference*, 1989. Disponível em: <<https://www.onepetro.org/conference-paper/SPE-18716-MS>>. Cited 2 times on pages 14 and 57.

BOUSSINESQ, J. *Essai sur la théorie des eaux courantes*. [S.l.]: Imprimerie Nationale, 1877. (Mémoires présentés par divers savants à l'Académie des sciences de l'Institut national de France). Cited on page 80.

BRACH, R. M. Impact dynamics with applications to solid particle erosion. *International Journal of Impact Engineering*, v. 7, n. 1, p. 37–53, jan 1988. ISSN 0734743X. Disponível em: <<http://linkinghub.elsevier.com/retrieve/pii/0734743X88900115>>. Cited on page 68.

BREUER, M.; ALLETTO, M.; LANGFELDT, F. Sandgrain roughness model for rough walls within Eulerian–Lagrangian predictions of turbulent flows. *International Journal of Multiphase Flow*, v. 43, p. 157–175, jul 2012. ISSN 03019322. Cited on page 86.

CABREJOS, F. J.; KLINZING, G. E. Pickup and saltation mechanisms of solid particles in horizontal pneumatic transport. *Powder Technology*, v. 79, n. 2, p. 173–186, 1994. ISSN 00325910. Cited on page 152.

CHEN, D.; SARUMI, M.; AL-HASSANI, S. Computational mean particle erosion model. *Wear*, v. 214, n. 1, p. 64–73, 1998. ISSN 00431648. Cited on page 69.

CHEN, D.; SARUMI, M.; AL-HASSANI, S.; GAN, S.; YIN, Z. A model for erosion at normal impact. *Wear*, v. 205, n. 1-2, p. 32–39, apr 1997. ISSN 00431648. Disponível em: <<http://linkinghub.elsevier.com/retrieve/pii/S0043164896073152>>. Cited on page 69.

CHEN, X.; MCLAURY, B. S.; SHIRAZI, S. A. Application and experimental validation of a computational fluid dynamics (CFD)-based erosion prediction model in elbows and plugged tees. *Computers and Fluids*, v. 33, n. 10, p. 1251–1272, 2004. ISSN 00457930. Cited on page 57.

CHEN, X.; MCLAURY, B. S.; SHIRAZI, S. A. Application and experimental validation of a computational fluid dynamics (CFD)-based erosion prediction model in elbows and plugged tees. *Computers & Fluids*, v. 33, n. 10, p. 1251–1272, dec 2004. ISSN 00457930. Cited on page 109.

CLARK, H. M. The influence of the flow field in slurry erosion. *Wear*, v. 152, n. 2, p. 223–240, 1992. ISSN 00431648. Cited on page 148.

CLARK, H. M.; HARTWICH, R. B. A re-examination of the 'particle size effect' in slurry erosion. *Wear*, v. 248, n. 1-2, p. 147–161, 2001. ISSN 00431648. Cited on page 148.

COFFIN, L. A study of the effects of cyclic thermal stresses on a ductile metal. *Trans. AIME*, v. 76, p. 931–950, 1954. ISSN 0011-3395. Cited on page 73.

COUSENS, A. K. *The Erosion of Ductile Metals by Solid Particle Impact*. [S.l.]: University of Cambridge, 1984. Cited on page 29.

CROWE, C. T. *Multiphase Flow Handbook*. [S.l.]: CRC Press, 2005. (Mechanical and Aerospace Engineering Series). ISBN 9781420040470. Cited on page 86.

CROWE, C. T.; SCHWARZKOPF, J. D.; SOMMERFELD, M.; TSUJI, Y. *Multiphase Flows with Droplets and Particles*. [S.l.]: Taylor & Francis, 1997. ISBN 9780849394690. Cited on page 86.

DENG, T.; PATEL, M.; HUTCHINGS, I.; BRADLEY, M. S. A. Effect of bend orientation on life and puncture point location due to solid particle erosion of a high concentration flow in pneumatic conveyors. *Wear*, v. 258, n. 1-4 SPEC. ISS., p. 426–433, 2005. ISSN 00431648. Cited on page 59.

DENNIS, S. C. R.; SINGH, S. N.; INGHAM, D. B. The steady flow due to a rotating sphere at low and moderate Reynolds numbers. *Journal of Fluid Mechanics*, v. 101, n. 02, p. 257–279, 1980. ISSN 1469-7645. Cited on page 86.

DHODAPKAR, S.; SOLT, P.; KLINZING, G. Understanding Bends In Pneumatic Conveying Systems. *Solids Processing*, p. 53–60, 2009. Cited 4 times on pages 14, 54, 55, and 56.

DOSANJH, S.; HUMPHREY, J. A. C. The influence of turbulence on erosion by a particle-laden fluid jet. *Wear*, v. 102, n. 4, p. 309–330, apr 1985. ISSN 00431648. Disponível em: <<http://linkinghub.elsevier.com/retrieve/pii/0043164885901759>>. Cited 2 times on pages 13 and 42.

DUARTE, C. A. R.; SOUZA, F. J. de; SALVO, R. d. V.; SANTOS, V. F. dos. The role of inter-particle collisions on elbow erosion. *International Journal of Multiphase Flow*. No citation in the text.

DUARTE, C. A. R.; SOUZA, F. J. de; SANTOS, V. F. dos. Numerical investigation of mass loading effects on elbow erosion. *Powder Technology*, v. 283, p. 593–606, oct 2015. ISSN 00325910. Cited 7 times on pages 47, 75, 109, 110, 123, 137, and 141.

DUARTE, C. A. R.; SOUZA, F. J. de; SANTOS, V. F. dos. Mitigating elbow erosion with a vortex chamber. *Powder Technology*, v. 288, p. 6–25, jan 2016. ISSN 00325910. Cited 8 times on pages 14, 29, 54, 55, 109, 110, 123, and 137.

DUTTA, P.; SAHA, S. K.; NANDI, N.; PAL, N. Numerical study on flow separation in 90 pipe bend under high Reynolds number by k- ϵ modelling. *Engineering Science and Technology, an International Journal*, v. 19, n. 2, p. 904–910, 2016. ISSN 22150986. Cited on page 49.

ELGHOBASHI, S. On predicting particle-laden turbulent flows. *Applied Scientific Research*, Kluwer Academic Publishers, v. 52, n. 4, p. 309–329, 1993. ISSN 0003-6994. Cited on page 95.

EVANS, a. G.; GULDEN, M. E.; ROSENBLATT, M. Impact Damage in Brittle Materials in the Elastic-Plastic Response Regime. *Proceedings of the Royal Society A: Mathematical, Physical and Engineering Sciences*, v. 361, n. 1706, p. 343–365, 1978. ISSN 1364-5021. Cited 2 times on pages 58 and 65.

EYLER, R. L. Design and Analysis of a Pneumatic Flow Loop. 1987. Cited on page 59.

FERZIGER, J. H.; PERIC, M. *Computational methods for fluid dynamics*. [S.l.]: Springer, 2002. Cited 4 times on pages 89, 90, 92, and 93.

FINNIE, I. Erosion of surfaces by solid particles. *Wear*, v. 3, n. 2, p. 87–103, mar 1960. ISSN 00431648. Cited 8 times on pages 14, 29, 39, 40, 60, 61, 62, and 63.

FINNIE, I. Erosion by Solid Particles in a Fluid Stream. *ASTM International*, 1962. Disponível em: <www.astm.org>. Cited on page 46.

FINNIE, I. Some observations on the erosion of ductile metals. *Wear*, v. 19, n. 1, p. 81–90, jan 1972. ISSN 00431648. Disponível em: <<http://linkinghub.elsevier.com/retrieve/pii/S0043164872904449>>. Cited on page 63.

FINNIE, I.; MCFADDEN, D. On the velocity dependence of the erosion of ductile metals by solid particles at low angles of incidence. *Wear*, v. 48, n. 1, p. 181–190, may 1978. ISSN 00431648. Cited 3 times on pages 13, 46, and 117.

FORDER, A.; THEW, M.; HARRISON, D. A numerical investigation of solid particle erosion experienced within oilfield control valves. *Wear*, v. 216, n. 2, p. 184–193, 1998. ISSN 00431648. Disponível em: <<http://www.sciencedirect.com/science/article/pii/S0043164897002172>>. Cited 2 times on pages 75 and 94.

FRÖHLICH, J.; TERZI, D. von. Hybrid LES/RANS methods for the simulation of turbulent flows. *Progress in Aerospace Sciences*, v. 44, n. 5, p. 349–377, 2008. ISSN 0376-0421. Cited 2 times on pages 15 and 78.

GAHR, K. H. Z. *Microstructure and Wear of Materials*. [S.l.]: Elsevier, 1987. v. 10. v – vi p. (Tribology Series, v. 10). ISSN 0167-8922. Cited on page 37.

GANSER, G. H. A rational approach to drag prediction of spherical and nonspherical particles. *Powder Technology*, v. 77, n. 2, p. 143–152, nov 1993. ISSN 00325910. Cited on page 110.

GIBSON, M. M.; LAUNDER, B. E. Ground Effects on Pressure Fluctuations in the Atmospheric Boundary Layer. *Journal of Fluid Mechanics*, v. 86, n. 3, p. 491–511, 1978. Cited on page 83.

GOODWIN, J. E.; SAGE, W.; TILLY, G. P. Study of erosion by solid particles. *ARCHIVE: Proceedings of the Institution of Mechanical Engineers 1847-1982 (vols 1-196)*, v. 184, n. 1969, p. 279–292, 2006. ISSN 0020-3483. Cited 2 times on pages 45 and 46.

GRANT, G.; TABAKOFF, W. Erosion Prediction in Turbomachinery Resulting from Environmental Solid Particles. *Journal of Aircraft*, v. 12, n. 5, p. 471–478, 1975. ISSN 0021-8669, 1533-3868. Disponível em: <<http://arc.aiaa.org/doi/abs/10.2514/3.59826>>. Cited 3 times on pages 75, 76, and 94.

GUIDE, F. *Fluent 6.2 User Guide*. Centerra Resource Park, 10 Cavendish Court, Lebanon, NH 03766, USA, 2005. Cited on page 89.

HAIDER, A.; LEVENSPIEL, O. Drag coefficient and terminal velocity of spherical and nonspherical particles. *Powder Technology*, v. 58, n. 1, p. 63–70, may 1989. ISSN 00325910. Cited on page 110.

HASELBACHER, A.; NAJJAR, F.; FERRY, J. An efficient and robust particle-localization algorithm for unstructured grids. *Journal of Computational Physics*, v. 225, n. 2, p. 2198–2213, aug 2007. ISSN 00219991. Cited 2 times on pages 88 and 97.

HAUGEN, K.; KVERNVOLD, O.; RONOLD, A.; SANDBERG, R. Sand erosion of wear-resistant materials: Erosion in choke valves. *Wear*, v. 186-187, p. 179–188, jul 1995. ISSN 00431648. Cited 2 times on pages 69 and 117.

HESS, L. W. *Short radius, low wear elbow*. Google Patents, 1991. Disponível em: <<https://www.google.ch/patents/US5060984>>. Cited on page 54.

HOJO, H.; TSUDA, K.; YABU, T. Erosion damage of polymeric material by slurry. *Wear*, v. 112, n. 1, p. 17–28, oct 1986. ISSN 00431648. Disponível em: <<http://linkinghub.elsevier.com/retrieve/pii/0043164886901973>>. Cited 3 times on pages 13, 41, and 42.

HUANG, C.; CHIOVELLI, S.; MINEV, P.; LUO, J.; NANDAKUMAR, K. A comprehensive phenomenological model for erosion of materials in jet flow. *Powder Technology*, v. 187, n. 3, p. 273–279, nov 2008. ISSN 00325910. Cited 2 times on pages 73 and 117.

HUBER, N. *Zur Phasenverteilung von Gas-Feststoff-Strömungen in Rohren*. Tese (Doutorado) — Universität Erlangen-Nürnberg, 1991. Cited on page 104.

HUBER, N.; SOMMERFELD, M. Modelling and numerical calculation of dilute-phase pneumatic conveying in pipe systems. *Powder Technology*, Elsevier, v. 99, n. 1, p. 90–101, sep 1998. ISSN 00325910. Cited 4 times on pages 15, 104, 105, and 106.

HUTCHINGS, I. M. A model for the erosion of metals by spherical particles at normal incidence. *Wear*, v. 70, n. 3, p. 269–281, aug 1981. ISSN 00431648. Disponível em: <<http://linkinghub.elsevier.com/retrieve/pii/0043164881903471>>. Cited 3 times on pages 65, 67, and 69.

HUTCHINGS, I. M. *Tribology: friction and wear of engineering materials*. [S.l.]: Edward Arnold, 1992. (Metallurgy and materials science). Cited 3 times on pages 13, 37, and 40.

HUTCHINGS, I. M.; WINTER, R. E.; FIELD, J. E. Solid Particle Erosion of Metals: The Removal of Surface Material by Spherical Projectiles. *Proceedings of the Royal Society of London A: Mathematical, Physical and Engineering Sciences*, The Royal Society, v. 348, n. 1654, p. 379–392, 1976. ISSN 0080-4630. Disponível em: <<http://rspa.royalsocietypublishing.org/content/348/1654/379>>. Cited on page 64.

ISLAM, M. A.; FARHAT, Z. N. Effect of impact angle and velocity on erosion of API X42 pipeline steel under high abrasive feed rate. *Wear*, v. 311, n. 1-2, p. 180–190, mar 2014. ISSN 00431648. Cited on page 109.

JENNINGS, W. H.; HEAD, W. J.; MANNING, C. R. A mechanistic model for the prediction of ductile erosion. *Wear*, v. 40, n. 1, p. 93–112, 1976. ISSN 00431648. Cited on page 64.

JOHANSSON, S.; ERICSON, F.; SCHWEITZ, J.-Å. Solid particle erosion — a statistical method for evaluation of strength properties of semiconducting materials. *Wear*, v. 115, n. 1-2, p. 107–120, mar 1987. ISSN 00431648. Disponível em: <<http://linkinghub.elsevier.com/retrieve/pii/004316488790202X>>. Cited on page 67.

JOHNSON, G. R.; COOK, W. H. Fracture characteristics of three metals subjected to various strains, strain rates, temperatures and pressures. *Engineering Fracture Mechanics*, v. 21, n. 1, p. 31–48, jan 1985. ISSN 00137944. Disponível em: <<http://linkinghub.elsevier.com/retrieve/pii/0013794485900529>>. Cited on page 69.

JONES, W. P.; LAUNDER, B. E. The prediction of laminarization with a two-equation model of turbulence. *International Journal of Heat and Mass Transfer*, v. 15, n. 2, p. 301–314, 1972. ISSN 0017-9310. Cited on page 81.

KESANA, N. R. Erosion in Multiphase Pseudo Slug Flow with Emphasis on Sand Sampling and Pseudo Slug Characteristics. 2013. Cited on page 59.

LAÍN, S.; SOMMERFELD, M. Euler/Lagrange computations of pneumatic conveying in a horizontal channel with different wall roughness. *Powder Technology*, v. 184, n. 1, p. 76–88, may 2008. ISSN 00325910. Cited on page 117.

LAÍN, S.; SOMMERFELD, M. Numerical calculation of pneumatic conveying in horizontal channels and pipes: Detailed analysis of conveying behaviour. *International Journal of Multiphase Flow*, v. 39, p. 105–120, mar 2012. ISSN 03019322. Cited 2 times on pages 95 and 112.

LAÍN, S.; SOMMERFELD, M. Characterisation of pneumatic conveying systems using the Euler/Lagrange approach. *Powder Technology*, v. 235, p. 764–782, 2013. ISSN 00325910. Cited 3 times on pages 15, 96, and 105.

LAIN, S.; SOMMERFELD, M.; KUSSIN, J. Experimental studies and modelling of four-way coupling in particle-laden horizontal channel flow. *International Journal of Heat and Fluid Flow*, v. 23, n. 5, p. 647–656, 2002. ISSN 0142-727X. Cited on page 88.

LAUNDER, B. Second-moment closure and its use in modelling turbulent industrial flows. *International Journal for Numerical Methods in Fluids*, v. 9, p. 963–985, 1989. Cited on page 83.

LAUNDER, B.; SHARMA, B. Application of the energy-dissipation model of turbulence to the calculation of flow near a spinning disc. *Letters in Heat and Mass Transfer*, v. 1, n. 2, p. 131–137, nov 1974. ISSN 00944548. Cited 2 times on pages 80 and 81.

LEVEQUE, R. J. Finite-volume methods for non-linear elasticity in heterogeneous media. *International Journal for Numerical Methods in Fluids*, John Wiley & Sons, Ltd., v. 40, n. 1-2, p. 93–104, 2002. ISSN 1097-0363. Cited on page 89.

LEVIN, B. F.; VECCHIO, K. S.; DUPONT, J. N.; MARDER, a. R. Modeling solid-particle erosion of ductile alloys. *Metallurgical and Materials Transactions A*, v. 30, n. July, p. 1763–1774, 1999. ISSN 1073-5623. Cited on page 70.

LEVY, A. V.; HICKEY, G. Liquid-solid particle slurry erosion of steels. *Wear*, v. 117, n. 2, p. 129–146, jun 1987. ISSN 00431648. Disponível em: <<http://linkinghub.elsevier.com/retrieve/pii/0043164887902511>>. Cited on page 41.

LEVY, A. V.; JEE, N.; YAU, P. Erosion of steels in coal-solvent slurries. *Wear*, v. 117, n. 2, p. 115–127, 1987. ISSN 00431648. Cited on page 41.

LIEN, F. S.; LESCHZINER, M. A. Assessment of turbulence-transport models including non-linear RNG eddy-viscosity formulation and second-moment closure for flow over a backward-facing step. *Computers & Fluids*, v. 23, n. 8, p. 983–1004, 1994. ISSN 00457930. Disponível em: <<http://www.sciencedirect.com/science/article/pii/0045793094900019>>. Cited on page 83.

- LUN, C.; LIU, H. Numerical simulation of dilute turbulent gas-solid flows in horizontal channels. *International Journal of Multiphase Flow*, v. 23, n. 3, p. 575–605, jun 1997. ISSN 03019322. Cited on page 85.
- LYNN, R. S.; WONG, K. K.; CLARK, H. M. On the particle size effect in slurry erosion. *Wear*, v. 149, n. 1-2, p. 55–71, 1991. ISSN 00431648. Cited on page 148.
- MAMOUN, M. M. *Analytical Models for the Erosive-Corrosive Wear Process*. [S.l.], 1975. Cited on page 67.
- MANSON, S. S. Behavior of Materials Under Conditions of Thermal Stress. *Technical Report No. 1170, National Advisory Committee for Aeronautics, NACA.*, 1953. Cited on page 73.
- MATHUR, S. R.; MURTHY, J. Y. A pressure-based method for unstructured meshes. *Numerical Heat Transfer, Part B: Fundamentals*, v. 31, n. 2, p. 195–215, 1997. Cited 2 times on pages 89 and 91.
- MAZUMDER, Q.; SHIRAZI, S.; MCLAURY, B.; SHADLEY, J.; RYBICKI, E. *Development and validation of a mechanistic model to predict solid particle erosion in multiphase flow*. 203–207 p. Tese (Doutorado) — The University of Tulsa, 2005. Cited on page 123.
- MAZUMDER, Q. H.; SHIRAZI, S. a.; MCLAURY, B. Experimental Investigation of the Location of Maximum Erosive Wear Damage in Elbows. *Journal of Pressure Vessel Technology*, v. 130, n. 1, p. 011303, 2008. ISSN 00949930. Cited 2 times on pages 14 and 58.
- MCKETTA, J. J. *Encyclopedia of Chemical Processing and Design: Volume 52 - Solid-Liquid Separation: Clarifiers and Thickeners Selection to Specific Gravity and Specific Heats*. Taylor & Francis, 1995. (Chemical Processing and Design Encyclopedia). ISBN 9780824726034. Disponível em: <<https://books.google.com.br/books?id=wzbhurfbZygC>>. Cited on page 51.
- MEI, R. An approximate expression for the shear lift force on a spherical particle at finite reynolds number. *International Journal of Multiphase Flow*, v. 18, n. 1, p. 145–147, jan 1992. ISSN 03019322. Cited on page 85.
- MENG, H.; LUDEMA, K. Wear models and predictive equations: their form and content. *Wear*, v. 181-183, p. 443–457, mar 1995. ISSN 00431648. Cited on page 117.
- MEYER, E. Contribution to the knowledge of hardness and hardness testing. *Zeitschrift Des Vereines Deutscher Ingenieure*, v. 52, p. 740–835, 1908. Cited on page 63.
- MILLS, D. Pneumatic Conveying Design Guide. *Pneumatic Conveying Design Guide*, p. 570–594, 2004. Disponível em: <<http://www.sciencedirect.com/science/article/pii/B9780750654715500265>>. Cited 11 times on pages 13, 14, 30, 43, 44, 45, 48, 50, 51, 52, and 53.
- MILLS, D.; MASON, J. The erosive wear of hardened and tempered steels in pneumatic conveying system pipelines. In: *Proc 7th ELSI Conf. Paper 81*. [S.l.: s.n.], 1987. p. 81. Cited 3 times on pages 13, 46, and 47.
- MILLS, D.; MASON, J. S. Particle size effects in bend erosion. *Wear*, v. 44, n. 2, p. 311–328, 1977. ISSN 00431648. Cited on page 47.

NEILSON, J.; GILCHRIST, A. Erosion by a stream of solid particles. *Wear*, v. 11, n. 2, p. 111–122, feb 1968. ISSN 00431648. Cited 4 times on pages 29, 62, 94, and 117.

NGUYEN, V. B.; NGUYEN, Q. B.; ZHANG, Y. W.; LIM, C. Y. H.; KHOO, B. C. Effect of particle size on erosion characteristics. *Wear*, v. 348–349, p. 126–137, 2016. ISSN 00431648. Cited on page 148.

NSOESIE, S.; LIU, R.; CHEN, K. Y.; YAO, M. X. Analytical modeling of solid-particle erosion of Stellite alloys in combination with experimental investigation. *Wear*, v. 309, n. 1-2, p. 226–232, 2014. ISSN 00431648. Cited 3 times on pages 15, 73, and 74.

OESTERLE, B.; PETITJEAN, A. Simulation of particle-to-particle interactions in gas solid flows. *International Journal of Multiphase Flow*, v. 19, n. 1, p. 199–211, feb 1993. ISSN 03019322. Cited on page 87.

OKA, Y. I.; OKAMURA, K.; YOSHIDA, T. Practical estimation of erosion damage caused by solid particle impact: Part 1: Effects of impact parameters on a predictive equation. *Wear*, v. 259, n. 1-6, p. 95–101, 2005. ISSN 00431648. Cited 3 times on pages 70, 71, and 72.

OKA, Y. I.; YOSHIDA, T. Practical estimation of erosion damage caused by solid particle impact: Part 2: Mechanical properties of materials directly associated with erosion damage. *Wear*, v. 259, n. 1-6, p. 102–109, jul 2005. ISSN 00431648. Cited 6 times on pages 19, 72, 74, 75, 94, and 117.

ONO, A.; KIMURA, N.; KAMIDE, H.; TOBITA, A. Influence of elbow curvature on flow structure at elbow outlet under high Reynolds number condition. *Nuclear Engineering and Design*, v. 241, n. 11, p. 4409–4419, 2011. ISSN 00295493. Cited on page 49.

PAULSON, J. I. *Elbow fitting for pneumatic transport system*. Google Patents, 2005. Disponível em: <<https://www.google.com/patents/US6951354>>. Cited on page 55.

PAULSON, J. I.; HESS, L. W. *Short radius, low wear elbow*. Google Patents, 1983. Disponível em: <<http://www.google.com/patents/US4387914>>. Cited on page 54.

PENG, K.; SHUGUANG, Z.; JIANGHAO, W.; CHUNXIN, Y. An improved known vicinity algorithm based on geometry test for particle localization in arbitrary grid. *Journal of Computational Physics*, v. 228, n. 24, p. 9001–9019, 2009. ISSN 0021-9991. Cited on page 97.

PEREIRA, G. C.; SOUZA, F. J. de; de Moro Martins, D. A. Numerical prediction of the erosion due to particles in elbows. *Powder Technology*, v. 261, p. 105–117, jul 2014. ISSN 00325910. Cited 2 times on pages 39 and 75.

REDDY, A. V.; SUNDARARAJAN, G. Erosion behaviour of ductile materials with a spherical non-friable erodent. *Wear*, v. 111, n. 3, p. 313–323, sep 1986. ISSN 00431648. Disponível em: <<http://linkinghub.elsevier.com/retrieve/pii/0043164886901900>>. Cited on page 67.

REYNOLDS, O. On the Dynamical Theory of Incompressible Viscous Fluids and the Determination of the Criterion. *Philosophical Transactions of the Royal Society of London A: Mathematical, Physical and Engineering Sciences*, The Royal Society, v. 186, p. 123–164, 1895. ISSN 0264-3820. Cited on page 79.

RUBINOW, S. I.; KELLER, J. B. The transverse force on a spinning sphere moving in a viscous fluid. *Journal of Fluid Mechanics*, v. 11, n. 03, p. 447–459, 1961. ISSN 1469-7645. Cited 2 times on pages 85 and 86.

SAFFMAN, P. G. The lift on a small sphere in a shear flow. *Journal of Fluid Mechanics*, v. 22, p. 385–400, 1965. Cited on page 85.

SANTOS, V. F. dos; SOUZA, F. J. de; DUARTE, C. A. R. Reducing bend erosion with a twisted tape insert. *Powder Technology*, v. 301, p. 889–910, 2016. ISSN 00325910. Cited 3 times on pages 14, 49, and 52.

SCHILLER, L.; NAUMANN, Z. A drag coefficient correlation. *Z.Ver.Deutsch.Ing*, v. 77, n. 13-14, p. 318–320, 1935. ISSN 00179310. Disponível em: <<http://dx.doi.org/10.1016/j.ijheatmasstransfer.2009.02.006>>. Cited on page 84.

SHELDON, G. L.; KANHERE, A. An investigation of impingement erosion using single particles. *Wear*, v. 21, n. 1, p. 195–209, aug 1972. ISSN 00431648. Disponível em: <<http://linkinghub.elsevier.com/retrieve/pii/0043164872902578>>. Cited 3 times on pages 63, 73, and 74.

SOLNORDAL, C. B.; WONG, C. Y.; BOULANGER, J. An experimental and numerical analysis of erosion caused by sand pneumatically conveyed through a standard pipe elbow. *Wear*, v. 336-337, p. 43–57, aug 2015. ISSN 00431648. Cited 16 times on pages 9, 11, 14, 15, 19, 59, 99, 100, 101, 107, 109, 113, 117, 133, 135, and 136.

SOMMERFELD, M. *Modellierung und numerische Berechnung von partikelbeladenen turbulenten Strömungen mit Hilfe des Euler/Lagrange-Verfahrens*. [S.l.]: Shaker, 1996. (Berichte aus der Strömungstechnik). ISBN 3-8265-1951-5. Cited on page 112.

SOMMERFELD, M. Theoretical and Experimental Modelling of Particulate Flows. In: . [S.l.: s.n.], 2000. cap. Overview a, p. 63. Cited on page 112.

SOMMERFELD, M. Validation of a stochastic Lagrangian modelling approach for inter-particle collisions in homogeneous isotropic turbulence. *International Journal of Multiphase Flow*, v. 27, n. 10, p. 1829–1858, oct 2001. ISSN 03019322. Cited 2 times on pages 84 and 87.

SOMMERFELD, M.; HUBER, N. Experimental analysis and modelling of particle-wall collisions. *International Journal of Multiphase Flow*, v. 25, n. 6-7, p. 1457–1489, sep 1999. ISSN 03019322. Cited 4 times on pages 88, 94, 117, and 118.

SOMMERFELD, M.; HUBER, N. Experimental analysis of modelling of particle-wall collisions. *International Journal of Multiphase Flow*, v. 25, n. 6-7, p. 1457–1489, 1999. ISSN 03019322. Cited on page 75.

SOMMERFELD, M.; KUSSIN, J. Wall roughness effects on pneumatic conveying of spherical particles in a narrow horizontal channel. *Powder Technology*, v. 142, n. 2-3, p. 180–192, apr 2004. ISSN 00325910. Cited on page 117.

SOMMERFELD, M.; LAÍN, S. Parameters influencing dilute-phase pneumatic conveying through pipe systems: A computational study by the Euler/Lagrange approach. *The Canadian Journal of Chemical Engineering*, v. 93, n. 1, p. 1–17, 2015. ISSN 1939-019X. Cited on page 127.

STACHOWIAK, G.; BATCHELOR, A. *Engineering tribology*. Elsevier Butterworth-Heinemann, 2013. 801 p. ISBN 9780750678360. Disponível em: <https://www.google.com/books?hl=en&lr=&id={_}wVoTz1pDlwC{&}oi=fnd{&}pg=PR1{&}dq=engineering+tribology{&}ots=J0KLperVZq{&}sig=Yef>. Cited 3 times on pages 13, 37, and 38.

STORF, R.; LANG, K. P. *90 degree elbow for pneumatic transport pipes*. Google Patents, 1994. Disponível em: <<https://www.google.com/patents/US5288111>>. Cited on page 56.

SUNDARARAJAN, G. A comprehensive model for the solid particle erosion of ductile materials. *Wear*, v. 149, n. 1-2, p. 111–127, 1991. ISSN 00431648. Cited on page 68.

SUNDARARAJAN, G.; SHEWMON, P. G. A new model for the erosion of metals at normal incidence. *Wear*, v. 84, n. 2, p. 237–258, 1983. ISSN 00431648. Cited on page 66.

TABAKOFF, W.; KOTWAL, R.; HAMED, A. Erosion study of different materials affected by coal ash particles. *Wear*, v. 52, n. 1, p. 161–173, 1979. ISSN 00431648. Cited on page 65.

TABOR, D. *The hardness of metals*. Oxford: Clarendon Press, 1951. Cited on page 66.

TILLY, G. Erosion caused by airborne particles. *Wear*, v. 14, n. 1, p. 63–79, jul 1969. ISSN 00431648. Disponível em: <<http://linkinghub.elsevier.com/retrieve/pii/0043164869900350>>. Cited 2 times on pages 13 and 45.

TILLY, G. A two stage mechanism of ductile erosion. *Wear*, v. 23, n. 1, p. 87–96, jan 1973. ISSN 00431648. Cited 3 times on pages 63, 64, and 117.

TILLY, G. Erosion caused by impact of solid particles. *Treatise on materials science and technology*, v. 13, p. 287–317, 1979. Cited 2 times on pages 13 and 43.

TILLY, G. P.; SAGE, W. The interaction of particle and material behaviour in erosion processes. *Wear*, v. 16, n. 6, p. 447–465, dec 1970. ISSN 00431648. Disponível em: <<http://linkinghub.elsevier.com/retrieve/pii/0043164870901717>>. Cited 2 times on pages 13 and 44.

TOLLE, G. C.; GREENWOOD, D. R. Design of Fittings to Reduce Wear Caused by Sand Erosion. 1977. Cited on page 57.

TONG, K. N.; MILLS, D.; MASON, J. S. The influence of bend radius on the erosion of pipe bends in pneumatic conveying systems. In: *Proc 5th Powder and Bulk Solids Conf*. Chicago: [s.n.], 1980. Cited 3 times on pages 13, 49, and 50.

TORO, E. F. *Riemann Solvers and Numerical Methods for Fluid Dynamics: A Practical Introduction*. [S.l.]: Springer, 2009. ISBN 9783540498346. Cited on page 89.

UTIKAR, R.; DARMAWAN, N.; TADE, M.; LI, Q.; EVANS, G.; GLENNY, M.; PAREEK, V. Hydrodynamic Simulation of Cyclone Separators. *Computational Fluid Dynamics*, n. January, p. 241–266, 2010. ISSN ISBN: 978-953-7619-59-6. Cited on page 123.

UUEMÖIS, H.; KLEIS, I. A critical analysis of erosion problems which have been little studied. *Wear*, v. 31, n. 2, p. 359–371, feb 1975. ISSN 00431648. Cited on page 127.

V. Patankar, S. *Numerical Heat Transfer and Fluid Flow*. [S.l.: s.n.], 1980. 211 p. ISSN 0142727X. ISBN 987-0-89116-522-3. Cited on page 92.

VERSTEEG, H. K.; MALALASEKERA, W. *An Introduction to Computational Fluid Dynamics: The Finite Volume Method*. [S.l.]: Pearson Education Limited, 2007. ISBN 9780131274983. Cited on page 89.

VIEIRA, R. E.; KESANA, N. R.; MCLAURY, B. S.; SHIRAZI, S. A.; TORRES, C. F.; SCHLEICHER, E.; HAMPEL, U. Experimental investigation of the effect of 90 degree standard elbow on horizontal gas–liquid stratified and annular flow characteristics using dual wire-mesh sensors. *Experimental Thermal and Fluid Science*, v. 59, n. 0, p. 72–87, 2014. ISSN 0894-1777. Cited on page 48.

VIEIRA, R. E.; MANSOURI, A.; MCLAURY, B. S.; SHIRAZI, S. A. Experimental and computational study of erosion in elbows due to sand particles in air flow. *Powder Technology*, v. 288, p. 339–353, 2016. ISSN 1873328X. Cited on page 56.

WILCOX, D. C. *Turbulence Modeling for CFD*. [S.l.]: DCW Industries, Incorporated, 1994. ISBN 9780963605108. Cited on page 80.

YANG, H.; BOULANGER, J. The Whole Annulus Computations of Particulate Flow and Erosion in an Axial Fan. *Journal of Turbomachinery*, ASME, v. 135, n. 1, p. 11040, oct 2012. ISSN 0889-504X. Cited on page 109.

ZAHEDI, P.; KARIMI, S.; MAHDAVI, M.; MCLAURY, B. S.; SHIRAZI, S. A. *Parametric Analysis of Erosion in 90 Degree and Long Radius Bends*. 2016. V01AT06A003 p. Disponível em: <<http://dx.doi.org/10.1115/FEDSM2016-7735>>. Cited on page 49.

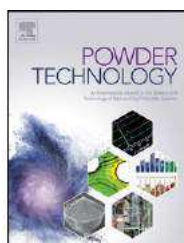
ZHANG, Y.; REUTERFORS, E.; MCLAURY, B.; SHIRAZI, S.; RYBICKI, E. Comparison of computed and measured particle velocities and erosion in water and air flows. *Wear*, v. 263, n. 1-6, p. 330–338, sep 2007. ISSN 00431648. Cited 3 times on pages 69, 94, and 117.

Appendix

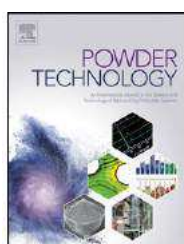
APPENDIX A

List of Publications

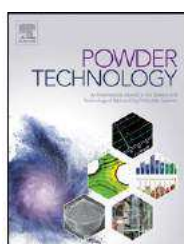
Publication in Journals



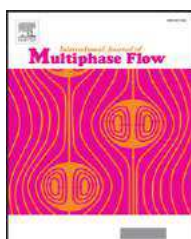
Duarte, C.A.R., de Souza, F.J., and dos Santos, V.F. Numerical investigation of mass loading effects on elbow erosion. *Powder Technology*, v. 283, p. 593-606, 2015.



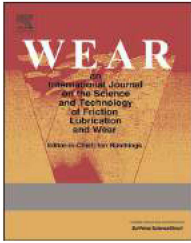
Duarte, C.A.R., de Souza, F.J., and dos Santos, V.F. Mitigating elbow erosion with a vortex chamber. *Powder Technology*, v. 288, p. 6-25, 2016.



dos Santos, V.F., de Souza, F.J., and Duarte, C.A.R. Reducing bend erosion with a twisted tape insert. *Powder Technology*, v. 301, p. 889-910, 2016.



Duarte, C.A.R., de Souza, F.J., Salvo, R.V., and dos Santos, V.F. The role of inter-particle collisions on elbow erosion. *International Journal of Multiphase Flow*, v. 89, p. 1-22, 2017.



Duarte, C.A.R., and de Souza, F.J. Innovative pipe wall design to mitigate elbow erosion: A CFD analysis. *Wear*, v. ??, p. ??-??, 2017 (Accepted for publication).

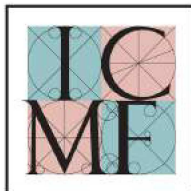
Publication in conference proceedings



Duarte, C.A.R., de Souza, F.J., and dos Santos, V.F. Numerical erosion prediction comparing standard and vortex chamber elbows. *POSMEC-2014 - Simpósio do Programa de Pós-Graduação em Engenharia Mecânica*, November 26th - 28th 2014, Uberlândia, Brazil.



Duarte, C.A.R., de Souza, F.J., and dos Santos, V.F. Mitigating elbow erosion with a vortex chamber. *THMT-15 - 8th International Symposium on Turbulence, Heat and Mass Transfer*, September 15th - 18th 2015, Sarajevo, Bosnia and Herzegovina.



2016

Duarte, C.A.R., de Souza, F.J., and dos Santos, V.F. Effects of surface roughness and inter-particle collisions on elbow erosion. *ICMF-2016 - 9th International Conference on Multiphase Flow*, May 22nd - 27th 2016, Firenze, Italy.

APPENDIX B

Curriculum Vitae

Carlos Antonio Ribeiro Duarte was born on January 9th 1989 in Patrocínio, MG, Brazil. After accomplishing his high school education at hometown in 2008, he started his study in Mechanical Engineering at the Federal University of Uberlândia. In April 2012, he went to study Mechanical Engineering at the Technische Universität Berlin (Germany), and received his Bachelor's degree in December 2013. In March 2015, he graduate with Master's degree at the Federal University of Uberlândia, and his dissertation was entitled "Numerical investigation of the erosion reduction in elbows promoted by a vortex chamber", under the supervision of Prof. Dr. Francisco José de Souza. In April 2015, he started his Ph.D. study. His research focuses on Computational Fluid Dynamics (CFD) of gas-solid flows using an "in-house" CFD code UNCSYFL3D.